Computational and Experimental Study of Sprays from the Breakup of Water Sheets

Madsen, Jesper

Publication date:
2007

Document Version
Publisher's PDF, also known as Version of record

Link to publication from Aalborg University

Citation for published version (APA):
Madsen, J. (2007). Computational and Experimental Study of Sprays from the Breakup of Water Sheets. Esbjerg: Esbjerg Institute of Technology, Aalborg University.

Computational and Experimental Study of Sprays from the Breakup of Water Sheets

Ph.D. thesis

Submitted by

Jesper Madsen

to The Faculty of Engineering and Science, Aalborg University
for the degree of Doctor of Philosophy.

Group for Chemical Fluid Flow Processes
Esbjerg Institute of Technology
Aalborg University Esbjerg
Niels Bohrs Vej 8
DK-6700 Esbjerg, Denmark

October 2006

Jesper Madsen
Computational and Experimental Study of Sprays from the Breakup of Water Sheets
Ph.D. thesis Aalborg University Esbjerg, 2006.

ISBN 87-7606-016-0

Published by Aalborg University Esbjerg, Niels Bohrs Vej 8,
DK-6700 Esbjerg, Denmark.
http://www.aaue.dk/
Cover design by Martin Helsing.
Typeset with Word

Abstract

This thesis presents an Eulerian multi-fluid CFD model for sprays, which is able to describe droplet breakup and coalescence and size polydispersion as well as the associated size-conditioned dynamics. In order to model the evolution of the polydisperse droplet phase, the population balance equation (PBE) is coupled to the continuity and momentum balance equations. The direct quadrature method of moments (DQMOM) is implemented to simulate the evolution of the droplet size distribution (DSD) due to breakup and coalescence.

The DQMOM-multi-fluid model uses source terms for the first $2N$ moments of the droplet number distribution as parameters to determine the source terms of the transport equations of the N droplet volume fractions and the N droplet diameters. Transport equations are also solved for phase-average velocities for each droplet phase. Submodels are designed to capture the effects of droplet breakup and droplet-droplet collisions.

The model is applied to calculate local values of droplet sizes and velocities produced by diesel-type, Y-jet, and hollow-cone sprays. The droplet velocity results for the diesel-type spray are well predicted. The droplet size and velocity results for the Y-jet water sprays are less accurate, although this is considered to be due to inaccuracies in the boundary conditions at the nozzle, rather than an error in the model. The collapse of the hollow-cone spray is evident in the predictions, and droplet sizes and velocities are in good agreement with experimental data.

The model has successfully predicted the main features of the sprays, but there are aspects of the model in which improvements can be made.

A computational study of the internal flow field of a large-scale Danfoss pressure-swirl atomizer is also presented. The two-phase flow is modeled using three approaches: 1) a volume of fluid (VOF) method using laminar viscosity only, 2) a VOF method using subgrid-scale turbulence modeling, and 3) a two-fluid Euler/Euler method using the laminar viscosity only. The primary focus of the analysis is on the internal flow characteristics in the swirl chamber. The CFD results compare favorably with experimental data of tangential and axial velocity distributions in the swirl chamber and static wall pressure.

Experiments are carried out in order to obtain local quantities in water sprays from production-scale pressure-swirl and Y-jet atomizers. A two-component phase Doppler anemometry (PDA) system is used for obtaining local values of droplet velocities and sizes. Experimental studies are conducted in sprays produced by nine different single-hole Y-jet atomizers with different operating conditions. Experiments concerned with the effects of atomizer geometry on the spray show that the mixing length should be approximately four times the mixing chamber diameter. Other geometrical variables have relatively little effect, except for the way in which they affect air and water gauge pressures. The investigation into the effects of operating conditions shows that increasing the liquid flow rate or the mass loading ratio both reduce the mean diameters and increase the axial velocity of the spray. The liquid flow rate is the key parameter determining the spray characteristics of the Y-jet atomizers. The spray is less affected by different mass loading ratios.

In supplement, to the PDA measurements, interferometric particle imaging (IPI) measurements are carried out in a hollow-cone spray from a Danfoss pressure-swirl atomizer. IPI is a technique for determining the diameter of transparent and spherical particles in a whole field from out-of-focus particle images. The velocity of each particle is simultaneously determined using particle tracking velocimetry (PTV) on focused images. Results are compared to PDA measurements. In shape and trends the data acquired with IPI and PDA are very similar, however due to different sampling methods employed by the two measuring techniques, IPI yields consistently smaller mean diameters than PDA. The IPI/PTV technique has some advantages over the PDA system as it measures droplet sizes and velocities in a whole field. The main limitation of the IPI/PTV technique is that it cannot be used at high droplet concentrations.

Synopsis

I denne afhandling præsenteres en Eulerian multi-fluid CFD model til simulering af sprays. Modellen kan beskrive opbrydning og sammenklumpning af dråber samt de dråbestørrelses-afhængige hastigheder. Metoden "Direct Quadrature Method of Moments" (DQMOM) er implementeret for at simulere ændringen af dråbestørrelsesfordelingen pga. opbrydning og sammenklumpning.

I DQMOM-multi-fluid modellen anvendes kildeled for de første $2N$ momenter af dråbestørrelsesfordelingen som parametre til at bestemme kildeled i transportligningerne for de N dråbevolumenfaktioner og de N dråbediametre. For hver dråbefase løses desuden en impulsbalance. Effekterne af opbrydning og sammenklumpning af dråber er implementeret ved hjælp af undermodeller.

I denne afhandling anvendes modellen til at beregne lokale dråbestørrelser og hastigheder i diesel-type, Y-jet og tryk-hvirvelkammer sprays. Beregningerne af diesel-type sprayen viser god overensstemmelse med de eksperimentelle data for dråbehastigheder. Overensstemmelsen mellem simulerede og målte dråbestørrelser og hastigheder i Y-jet sprayen er mindre god, men dette anses for at være pga. usikkerhed i grænsebetingelserne ved dysen og ikke en fejl ved modellen. Kollapset af sprayen fra tryk-hvirvelkammer dysen er tydelig, og dråbestørrelser og hastigheder er i god overensstemmelse med målinger.

Resultaterne viser at modellen kan beregne de væsentligste egenskaber ved de simulerede sprays, men der er stadig aspekter ved modellen der kan forbedres.

CFD-beregninger af flowet inde i en opskaleret Danfoss tryk-hvirvelkammer dyse præsenteres også. Gas-væske flowet modelleres ved hjælp af tre metoder: 1) en "Volume of Fluid" (VOF) model under antagelse af laminart flow, 2) en VOF model kombineret med "Large Eddy Simulation" (LES), og 3) en to-fluid Euler/Euler model under antagelse af laminart flow. Der fokuseres primært på det indre flow i hvirvelkammeret. CFD-beregningerne giver god overensstemmelse med eksperimentelle data for tangentielle og aksiale hastighedsprofiler i hvirvelkammeret samt trykket ved væggen.

Der er udført eksperimenter, for at bestemme lokale værdier i vandsprays fra produktionsskala tryk-hvirvelkammer og Y-jet dyser. Et 2D "Phase Doppler Anemometry" (PDA) system benyttes til at måle lokale værdier af dråbehastigheder og størrelser. Der er udført eksperimenter i sprays produceret fra ni forskellige et-huls Y-jet dyser med varierende driftstilstande. Eksperimenter omhandlende effekterne af dysegeometri viser at længden af blandekammeret skal være ca. fire gange dets diameter. Øvrige dimensioner har relativ lille effekt, undtagen på de krævede luft- og vanddriftstryk. Undersøgelsen af effekterne af forskellige driftstilstande viser at både stigende væskeflow og stigende gasflow giver faldende middeldråbediametre og stigende aksiale hastigheder i sprayen. Væskeflowet er den vigtigste parameter, der kontrollerer sprayen fra Y-jet dyserne. Sprayen er mindre påvirket af gasflowet.

Udover PDA målingerne, er der udført "Interferometric Particle Imaging" (IPI) målinger i en spray fra en Danfoss tryk-hvirvelkammer dyse. IPI er en måleteknik til bestemmelse af diameteren af transparente og sfæriske partikler i et helt felt ud fra ikke-fokuserede billeder. Hver partikels hastighed bestemmes samtidigt ved hjælp af "Particle Velocimetry Tracking" (PTV) på fokuserede billeder. Resultaterne sammenlignes med PDA målinger. Tendenserne i dataene fra IPI og PDA er meget ens, men pga. de forskellige samplingsmetoder der anvendes i de to måleteknikker, giver IPI konsistent mindre middeldiametre end PDA. IPI/PTV teknikken har forskellige fordele i forhold til PDA teknikken, da den giver mulighed for at måle dråbestørrelser og hastigheder i et helt felt (i modsætning til PDA der måler i et punkt). Den væsentligste begrænsning ved IPI/PTV teknikken er, at den ikke kan anvendes ved høje dråbekoncentrationer.

Acknowledgements

This work has been carried out at Esbjerg Institute of Technology, Aalborg University Esbjerg, Denmark.

I would like to express my sincere gratitude to my supervisors, Prof. Bjørn H. Hjertager and Prof. Tron Solberg, for their expert guidance and constructive criticism as well as being a constant source of inspiration, throughout this study.

I would like to thank my colleagues Ville Alopaeus, Stefano Bove, Kim G. Hansen, Rolf Hansen, Claus H. Ibsen, Lene K. H. Osenbroch, and Jørgen Osenbroch for their support and helpful comments and suggestions during the course of this study.

Grateful acknowledgements are due to Carsten Andreasen, Henry Enevoldsen, and other support staff at Aalborg University Esbjerg for their assistance.

Discussions with Dr. Graham Wigley concerning the PDA system have been very helpful. I am also grateful for assistance provided by Dantec Dynamics in various stages of the experimentation.

Thanks are also due to Dr. Daniele Marchisio, who introduced me to population balance methods and DQMOM. I am also grateful to Prof. Rodney O. Fox for making invaluable comments and suggestions concerning the DQMOM-multi-fluid model. Furthermore, the advice of Adam Anderson of Fluent Europe has been very helpful in the implementation of the DQMOM scheme in Fluent.

I would like to acknowledge the financial support provided by Danfoss A/S and Aalborg Industries A/S. Furthermore, EXSIM consultants AS is acknowledged for financing the last nine months of my Ph.D. study. I would also like to thank Otto Mønsteds Fond for their financial support to my conference expenses.

Finally, a great thanks to my family and my friends, with whom I shared good and bad times throughout the duration of this study.

Contents

Nomenclature

A_{gl}	mixture area density	[m^2/m^3]
a_q	breakup kernel	[s^{-1}]
B	non-dimensional impact parameter	[-]
B_0	WAVE breakup model constant	[-]
B_1	WAVE breakup model constant	[-]
$b\left(d\middle\|d_q\right)$	breakup daughter distribution function	[-]
$\bar{b}_q^{(k)}$	moment transform of $b\left(d\middle\|d_q\right)$	[m^k]
C	constant	[-]
C_D	drag coefficient	[-]
C_f	friction coefficient	[kg/m^3·s]
c	speed of light	[m/s]
c_{pq}	coalescence kernel	[m^3/s]
D	diameter	[m]
d	droplet diameter	[m]
d_a	aperture diameter	[m]
d_{jk}	mean droplet diameter	[m]
$\mathbf{e}$	unit vector	[-]
E	coalescence efficiency	[-]
e_{pq}	collision-induced breakup kernel	[m^3/s]
F	force	[m/s^2]
$F_{i,pq}$	interfacial momentum transfer	[kg/m^2·s^2]
f	frequency	[s^{-1}]
$f_0\left(d\right)$	droplet number distribution	[m^{-1}]
$f_3\left(d\right)$	droplet volume distribution	[m^{-1}]
$f\left(d\middle\|d_p,d_q\right)$	collision-induced breakup daughter distribution	[-]
$\bar{f}_{pq}^{(k)}$	moment transform of $f\left(d\middle\|d_p,d_q\right)$	[m^k]
G_k	production of turbulence kinetic energy	[kg/m·s^3]
g	gravity	[m/s^2]

h	sheet half-thickness	[m]
I	turbulence intensity	[%]
K	sheet thickness parameter	[m^2]
K_S	most unstable sheet wave number	[-]
k	wave number (Chapter 2)	[-]
k	turbulent kinetic energy	[m^2/s^2]
k_v	velocity coefficient	[-]
L	length	[m]
ℓ	turbulent length scale	[m]
MFR	momentum flux ratio	[-]
MLR	mass loading ratio	[%]
m	relative refractive index	[-]
$\dot{m}$	mass flow rate	[kg/s]
$\dot{m}_{pq}$	mass transfer	[kg/m^3·s]
m_k	k^{th} moment of the DSD	[m^k/m^3]
N	number of droplet phases (nodes)	[-]
N_f	number of fringes	[-]
$n(d)$	droplet number density distribution	[m^{-4}]
Oh	Ohnesorge number	[-]
P	pressure	[Pa]
Pr	Prandtl number	[-]
p	parameter of size distribution	[-]
Q	density ratio	[-]
q	parameter of size distribution	[-]
Re	Reynolds number	[-]
r	radius	[m]
S	modulus of the mixture mean strain rate tensor	[s^{-1}]
S_{ij}	mean rate of strain tensor	[s^{-1}]
S	source term	
$\overline{S}_{m_k}$	source term for the k^{th} moment	[m^k/m^3]
T_{bu}	dimensionless breakup time	[-]
Ta	Taylor number	[-]
t	time	[s]
U	average velocity	[m/s]
u	instantaneous velocity	[m/s]
u'	fluctuating velocity	[m/s]
We	Weber number	[-]
x	coordinate	[m]
z	distance to lightsheet	[m]

Greek Letters

α	volume fraction	[-]
β_{pq}	collision coefficient	[m^3/s]
δ_0	film thickness	[m]
δ_q	weighted diameter	[m/m^3]
ε	turbulent kinetic energy dissipation rate	[m^2/s^3]
ϕ	off-axis angle	[°]
γ	droplet size ratio	[-]
η	wave amplitude	[m]
κ	geometric factor	[m^{-1}]
Λ	most unstable wave length	[m]
λ	wave length	[m]
μ	dynamic viscosity	[kg/m·s]
ν	kinematic viscosity	[m^2/s]
ρ	density	[kg/m^3]
ρ_{pq}	correlation coefficient	[-]
θ	sheet half-angle	[°]
σ	surface tension coefficient	[N/m]
τ	time scale	[s]
τ_{ij}	stress tensor	[kg/m·s^2]
Ω	maximum growth rate	[m]
ω	wave growth rate	[s^{-1}]
ω_q	weight (droplet number density)	[m^{-3}]

Subscripts

0	initial
1	larger droplet
2	smaller droplet
boun	bounce
bu	breakup
c	characteristic
coal	coalescence
coll	collision
crit	critical
D	droplet
dr	drift
frag	fragments
g	gas

inj	injection
L	ligament
l	liquid
m	mixture
p	p^{th} droplet phase
q	q^{th} droplet phase
rel	relative
S	sheet
st	stable
t	turbulent

Abbreviations

CFD	Computational Fluid Dynamics
DDM	Discrete Droplet Method
DQMOM	Direct Quadrature Method of Moments
DSD	Droplet Size Distribution
IPI	Interferometric Particle Imaging
LES	Large Eddy Simulation
LISA	Linearized Instability Sheet Atomization
LT	Li and Tankin
MEF	Maximum Entropy Formalism
PBE	Population Balance Equation
PD	Product-Difference
PDA	Phase Doppler Anemometry
PDF	Probability Density Function
PIV	Particle Image Velocimetry
PTV	Particle Tracking Velocimetry
QLES	Quasi-LES
QMOM	Quadrature Method of Moments
RR	Rosin-Rammler
SMD	Sauter Mean Diameter
VOF	Volume of Fluid

Chapter 1

Introduction

Sprays are widely used in several applications, e.g. spray combustion, spray-painting, crop spraying, and many other applications. For the different applications a wide range of spray devices have been developed and they are generally designated as atomizers or nozzles. For combustion in domestic heating burners, the pressure-swirl atomizer has been found to be the most reliable type of atomizer. In industrial heat generation equipment, the Y-jet atomizer is typically used.

This thesis deals with a numerical and experimental investigation of the atomization processes in sprays produced by pressure-swirl and Y-jet atomizers.

1.1 The Pressure-Swirl Atomizer

Figure 1.1 shows a cross-section of the Danfoss pressure-swirl atomizer used in heating burners. Liquid is fed tangentially into a swirl chamber giving it a high angular velocity, thereby creating an air-cored vortex. The outlet from the swirl chamber is the final orifice, and the rotating liquid flows through this orifice under both axial and radial forces to emerge from the atomizer in the form of a hollow conical sheet, the actual cone angle being determined by the relative magnitude of the tangential and axial velocity components at the exit.

Danfoss atomizers of this type are designed for oil flow rates from 1.46 kg/h up to 6.55 kg/h, with spray angles from $2\theta = 30° - 90°$, and a wide range of spray patterns. The simplicity of the design, with very few components, gives a relatively low price.

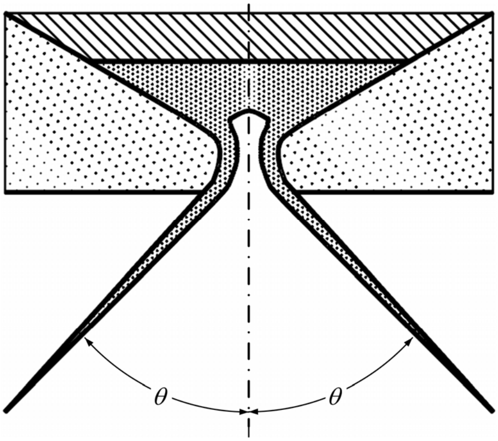

Figure 1.1: Schematic view of a Danfoss pressure-swirl atomizer.

1.2 The Y-Jet Atomizer

Figure 1.2 shows a cross-section of a typical Y-jet atomizer, showing the distinctive crossing of the liquid and gas paths, whereby gas passes through the centre of the atomizer and is distributed from an array of drilled holes. In each individual hole, liquid is injected into the gas flow at an angle, which gives penetration across the gap and formation of a liquid film on the walls inside the hole. The mixing of the liquid with the atomizing gas also gives partial breakup into droplets. The gas/liquid mixture completes the breakup in the combustion chamber. The required spray angle to fit the application is achieved by placement of multiple orifices. When incorporated into a particular burner, such as the Aalborg Industries KBSA burner (see Figure 1.3) for steam or hot water generation applications, the corresponding burner can provide firing capacities from 1.7 – 46.9 MW (heavy fuel oil consumption from 150 – 4,200 kg/h) and high turn-down capability.

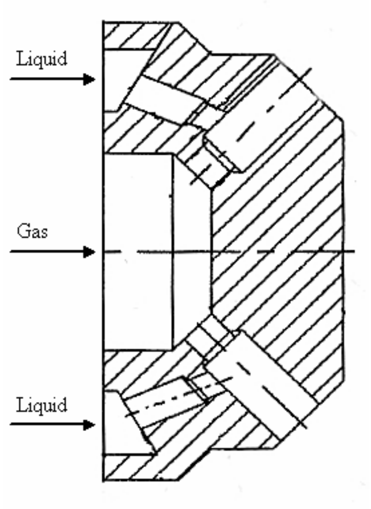

Figure 1.2: Typical Y-jet atomizer.

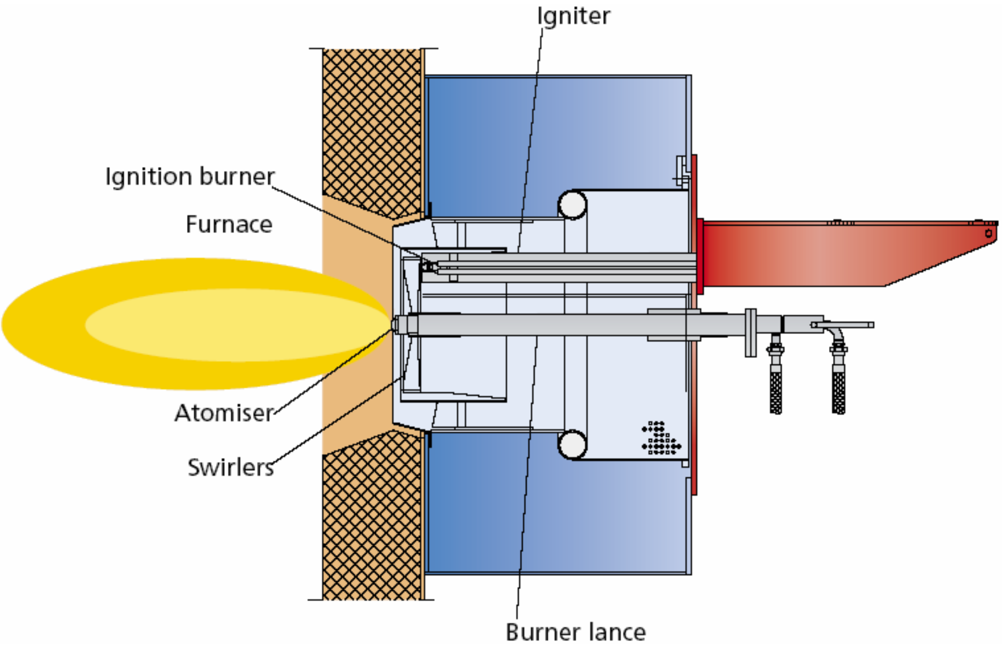

Figure 1.3: Aalborg Industries KBSA burner with Y-jet atomizer.

A deficiency of this type of atomizer arises from the fundamental asymmetry of the Y-jet configuration itself. The liquid has a tendency to attach to one side of the orifice whilst mixing with the gas and is forced into coarse droplets and ligaments on that side, whilst relatively fine droplets are produced in the leaner mixture diametrically opposite.

1.3 Atomization Mechanism

The mechanism of pressure-swirl and Y-jet atomizers is a formation of a liquid film on the walls inside the atomizer. When the liquid is issued from the atomizer a sheet is generated, and further downstream the sheet breakup into droplets. The way that this liquid sheet is formed is different for the pressure-swirl and Y-jet atomizers, but the key factors that govern the breakup downstream are assumed to be the same.

The atomization of sprays can be divided into two main processes, primary and secondary breakup. The former takes place in the region close to the nozzle. It is not only determined by the interaction between the liquid and gaseous phases but also by internal nozzle phenomena like turbulence. Atomization that occurs further downstream in the spray due to hydrodynamic interaction processes, and which is largely independent of the nozzle type, is called secondary breakup.

1.4 Droplet Size Distribution (DSD)

The droplet size distribution (DSD) in sprays is the crucial parameter needed for the fundamental analysis of the transport of mass, momentum and heat in engineering systems. Moreover, the DSD determines the quality of the spray and consequently influences to a significant extent the processes of fouling and undesired emissions in oil combustion. The evaporation and combustion of droplets and sprays have been extensively investigated, and several reviews are available (Faeth, 1983; Sirignano, 1983; Faeth, 1987; Faeth, 1996; Chiu, 2000). In certain applications, the DSD must have a particular form (narrow, wide, few large droplets, few small droplets, etc.) for optimal operation (Babinsky and Sojka, 2002). Consequently, it is important to have reliable models and numerical methods in order to be able to describe precisely the physics of sprays constituted of a cloud of droplets of various sizes which can breakup, coalesce, or vaporize and which have their own inertia and size-conditioned dynamics.

Surface tension will tend to minimize the droplet surface area, given its volume, resulting in a spherical shape for sufficiently small droplets. The size of a spherical droplet is represented by its diameter d. In most sprays, droplets of many sizes will exist. Droplet breakup, droplet coalescence, vaporization, and condensation will cause a temporal variation in droplet sizes. A distribution of the instantaneous diameter $f\left(d\right)$ is typically used to describe a spray. The number distribution $f_0\left(d\right)$ gives the frequency of droplets possessing a certain diameter. Another approach to describing size distribution is to use the droplet volume (or mass) instead of the number as the dependant variable and this is known as the volume distribution and identified as $f_3\left(d\right)$. In practice, $f\left(d\right)$ will not be a continuous function. However, for a spray with many droplets the function is well approximated as a continuously varying function. The continuous version of $f\left(d\right)$ is the probability density function (PDF) of the droplet size, or the droplet size distribution (DSD). See Figure 1.4 for an example of a measured distribution. The volume distribution is skewed to the right due to the weighting effect of the larger droplets.

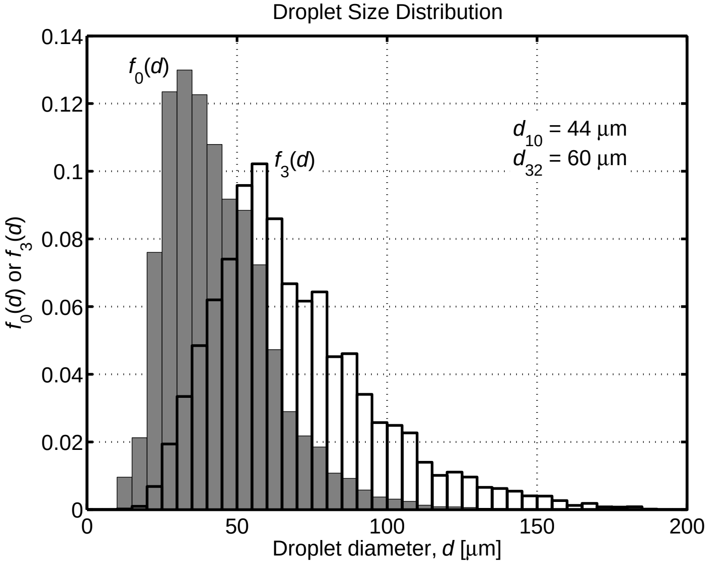

Figure 1.4: Discrete droplet size frequency distributions based on number, $f_0(d)$, and volume, $f_3(d)$.

For a droplet PDF to be physically valid, it is necessary that the following conditions hold (Babinsky and Sojka, 2002)

$$\lim_{d \to 0} \int_0^d f(d)\,\mathrm{d}d = 0 \tag{1.1}$$

$$\lim_{d \to \infty} \int_d^\infty f(d)\,\mathrm{d}d = 0 \tag{1.2}$$

i.e., the total number (or volume) of droplets below some minimum diameter and above some maximum diameter should vanish. Furthermore, a distribution must satisfy the following properties

$$f(d) \geq 0 \tag{1.3}$$

$$\int_0^\infty f(d)\,\mathrm{d}d = 1 \tag{1.4}$$

i.e., the distribution must be positive and normalized.

Multiplying the droplet number PDF by the total number density, N_t, gives the number density distribution:

$$n(d) = N_t f_0(d) \tag{1.5}$$

Moments of the number density distribution can be calculated in the following manner:

$$m_k = \int_0^\infty d^k n(d)\,\mathrm{d}d \tag{1.6}$$

Moments of a DSD typically use positive values of k, but there is no reason not to include negative and fractional values. Some moments have particular physical meaning. For example, $m_0 = N_t$ represents the total droplet density, and m_3 is related to the total droplet volume fraction.

Often an average droplet diameter d_{jk} is taken to represent a spray. A general mean diameter is (Lefebvre, 1989)

$$d_{jk} = \left[\frac{\int_0^\infty d^j n(d)\,\mathrm{d}d}{\int_0^\infty d^k n(d)\,\mathrm{d}d}\right]^{1/(j-k)} = \left[\frac{m_j}{m_k}\right]^{1/(j-k)} \tag{1.7}$$

An example is the Sauter mean diameter (SMD) d_{32}, which is proportional to the ratio of the total liquid volume to the total droplet surface area. d_{10} is the arithmetic mean diameter, sometimes referred to as length mean diameter.

The performance of a given spray combustion system depends not only on the DSD but on the spray spatial distribution. For this reason, spatially-resolved information on the mean droplet size and DSD as well as velocities needs to be determined in order to understand the most favorable spray conditions for optimal performance of its appliances.

1.5 Experimental Investigations

The geometries of the pressure-swirl and the Y-jet atomizers and the formed liquid sheets are somewhat complex and difficult to investigate experimentally. Therefore, research in planer liquid sheets is popular. Several experimental studies have been devoted to droplet formation from planer liquid sheets (Dombrowski and Fraser, 1954; Mansour and Chigier, 1990 and 1991; Stapper, *et al.*, 1992; Lozano and Barreras, 2001; Lozano, *et al.*, 2001; Scholz, *et al.*, 2003). Studies on the mechanisms of sheet breakup have been made using different experimental techniques, e.g. high-speed photography, phase Doppler anemometry (PDA), particle image velocimetry (PIV), and planer laser-induced fluorescence (PLIF). As a result of these studies, many features of the breakup are understood reasonably; but, there is still a lack of experimental data to fully understand the breakup process.

Phase Doppler anemometry (PDA) is widely used for the measurement of drop size and velocity in sprays (Tolpadi, *et al.*, 1995; Sommerfeld, 1998; Wigley, *et al.*, 2004). PDA combines the measurement of scattered light intensity with laser Doppler anemometry (LDA) to obtain simultaneous droplet size and velocity measurements. PDA is most favorable for measurement of spray evolution. The breakup of liquid sheets and the dense spray region is normally not considered here.

PDA is a point measurement technique and cannot be used to obtain instantaneous spatial information on velocity, droplet size and concentration. With a relatively new imaging technique, called interferometric particle imaging (IPI), these instantaneous spatial informations can be obtained. IPI has been developed into a commercial product by Dantec Dynamics. It is a technique for determining the diameter of transparent and spherical particles in a whole field from out-of-focus particle images. The velocity of each particle is simultaneously determined using particle tracking velocimetry (PTV) on focused images. The IPI/PTV technique is tested on hollow-cone water sprays produced by pressure-swirl atomizers in Madsen, *et al.* (2003) and Damaschke, *et al.* (2005). The main limitation of the technique is that it cannot be used at high droplet concentrations.

1.6 Numerical Simulation of Sprays

Computational fluid dynamics (CFD) of single- and multi-phase flows has been a rapidly developing research topic over the last years. At this point, advanced CFD codes are a valuable complement to experimental investigations, since they allow a detailed local analysis of the flow. Engineering flow prediction of single-phase flows is standard application of CFD and is widely used nowadays. However, there remain a number of challenges that arise in multi-phase CFD analysis beyond those present in single-phase methods. Among these are large constituent density ratios, the presence of discrete interfaces, and interfacial dynamics. A spray is one type of multi-phase flow. It involves a liquid as a dispersed phase in form of droplets and air or gas as the continuous phase.

Currently the most common spray description is based on the Lagrangian discrete droplet method (DDM) (e.g., Rüger, *et al.*, 2000). While the continuous phase is described by the standard Eulerian conservation equations, the transport of the dispersed phase is calculated by tracking the trajectories of a certain number of representative parcels (particles). A parcel consists of a number of droplets and it is assumed that all the droplets within one parcel have the same physical properties and behave equally when they move, breakup, or evaporate. The coupling between the liquid and the gaseous phases is achieved by source term exchange for mass, momentum, energy, and turbulence. Various submodels account for the effects of turbulent dispersion, coalescence, evaporation, and droplet breakup. The Lagrangian method is especially suitable for dilute sprays, but has shortcomings with respect to modeling of dense sprays. Further problems are reported connected with bad statistical convergence and also with dependence of the spray on grid size (Schmidt and Rutland, 2000).

These drawbacks make the use of an Eulerian formulation for the description of the disperse phase attractive. In comparison to the Lagrangian approach, the Eulerian approach treats spray as an interacting and interpenetrating continuum and the tracking of individual particles is avoided, but transport properties for the dispersed phase must be defined.

A single-fluid Eulerian (mixture model) representation of the gas/liquid mixture close to the atomizer is used in Vallet, *et al.* (2001), Beheshti and Burluka (2004), and Beau, *et al.* (2005) for jet atomization. Transport equations for the mean mixture velocity of the two-phase flow and for the mean liquid mass fraction are used to describe the flow, and atomization is considered as turbulent mixing in a flow with variable density. The mean size of the liquid droplets is calculated from a balance equation for the mean area per unit volume of the liquid-gas interface.

An Euler/Euler (two-fluid) modeling approach for predicting the velocities and the volume fractions of the continuous and the dispersed phase is used by Deux and Sommerfeld (2004) for the flow inside the nozzle and in the dense part of the spray. In order to obtain the droplet size distribution, a model using the maximum entropy formalism (Alhassid, *et al.*, 1978) is used. The Sauter SMD and the DSD depend only on the known nozzle diameter and a characteristic velocity. This model predicts only one DSD and is not a function of distance from the nozzle. The results of the two-fluid model and the DSD are used as inlet conditions for a Lagrangian calculation of further breakup, coalescence, and spray dispersion.

Iyer and Abraham (2003 and 2005) employed an Eulerian two-fluid model to study Diesel sprays. Their work considers droplet collisions and breakup as well as mass and energy transfer between the droplets and the gas. To know the SMD of the droplets, a transport equation for the liquid surface area density is solved and the "blob"-atomization model (Reitz, 1987) is employed to simulate atomization and liquid breakup.

The DSD is necessary for judging the performance of different atomizers. However, it cannot be predicted with the two-fluid model. An alternative approach is based upon adopting the Eulerian multi-fluid method treating different size classes of the spray droplets as separate phases and solving conservation equations for each of them. Hallmann, *et al.* (1995) have presented an Eulerian model for turbulent evaporating sprays, but their work focused relatively dilute sprays not accounting for droplet collisions and breakup. von Berg, *et al.* (2005) developed an Eulerian model for polydisperse sprays accounting for droplet breakup. A disadvantage of the multi-fluid method is that the number of equations to be solved increases when the droplet size distribution becomes wider and therefore the number of droplet size classes increases. If the size distributions in the spray are to be fully captured, this leads to a computationally expensive scheme.

Several authors have proposed dispersed phase transport models that involve transportation of moments of the particle size distribution (Beck and Watkins, 2002; Yue and Watkins, 2004; Archambault, *et al.*, 2003; Marchisio, *et al.*, 2003*a*). These techniques are broadly known as "moment method" models. Moment transport models attempt to model polydispersed flow by transporting statistical moments of the particle distribution (size, velocity, etc.) through physical space. When a moment approach is adopted to solve the phase space transport equation, problems are encountered because the governing equations for the k^{th} moment also depends on the $(k + 1)^{\text{th}}$ moment. Previous work in this area has adopted two different methods for the reconstruction of the PDF. Beck and Watkins (2002) approximate the DSD using a presumed Gamma distribution, parameterized by two transported moments. Yue and Watkins (2004) extended the method by transporting four moments; however, a presumed size distribution is still needed to evaluate higher order moments. Archambault, *et al.* (2003) outline the use of the maximum entropy formulation to calculate the higher order moments, required for closure, using the transported moments of the droplet size-velocity joint-PDF.

As an alternative, McGraw (1997) developed the so-called quadrature method of moments (QMOM), which is based on the product-difference (PD) algorithm formulated by Gordon (1968). QMOM has been validated for small particles in the study of aerosols in chemical engineering. It provides a precise and efficient numerical method in order to follow the size distribution of particles, without inertia, experiencing some aggregation-breakage phenomena (Marchisio, *et al.*, 2003*b*). One of the main limitations of QMOM is that since the dispersed phase is represented through the moments of the size distribution, the phase-average velocity of different solid phases must be used to solve the transport equations for the moments. Thus, in order to use this method in the context of sprays for which the inertia determines the dynamical behavior of the droplets, it is necessary to extend QMOM to handle cases where each droplet size is convected by its own velocity. In order to address these issues, the direct quadrature method of moments (DQMOM) has been formulated and validated (Marchisio and Fox, 2005). However, the extension of such methods to sprays has not yet been reported.

1.7 Objectives of the Current Work

The overall objective is to compute sprays from the breakup of liquid sheets with adequate accuracy. The specific goals of this project are

- To apply the IPI and PTV techniques for measuring droplet sizes and velocities in a hollow-cone spray from a Danfoss pressure-swirl atomizer and verify the results against PDA measurements.
- To investigate sprays from Y-jet atomizers and examine the effect of geometrical and operational variables by using PDA.
- To simulate the flow through a large-scale pressure-swirl atomizer using the Fluent CFD code and compare with measured velocity profiles.
- To implement the DQMOM in the Fluent 6.2 CFD code for non-evaporating polydisperse sprays.
- To develop a stable numerical scheme for computing polydisperse sprays using the Eulerian multi-fluid model.
- To incorporate models for atomization and breakup and collisions and coalescence of droplets in the DQMOM-multi-fluid approach for polydisperse sprays.
- To compare computed steady droplet size and velocity profiles with measurements in Y-jet water sprays and a hollow-cone spray from a Danfoss pressure-swirl atomizer.

1.8 Organization of the Thesis

In this chapter, the investigated atomizers and the atomization mechanisms of the atomizers were presented. The chapter also includes information on definition of DSDs, moments of a DSD, and mean diameters. Background coverage of measurement techniques and modeling methods is also provided.

Chapter 2 provides an introduction to the manner in which a liquid sheet emerging from an atomizer is broken down into droplets. A model of sheet breakup is presented. This model, known as the LISA model, is based on a linearized instability analysis of a free sheet.

In Chapter 3, models for droplet breakup and collisions are presented.

In Chapter 4, a theoretical background for PDA is given. Furthermore the IPI and PTV techniques for droplet flows are introduced and applied to a hollow-cone spray. The experimental part closes with an experimental characterization of Y-jet sprays obtained with a PDA system.

In Chapter 5, the volume of fluid (VOF), the Lagrangian, and the Eulerian models for simulating multiphase flows are presented.

Chapter 6 presents the DQMOM-multi-fluid polydisperse spray modeling approach. The DQMOM conservation equations are derived. Implementation of spray submodels describing droplet breakup and collisions between droplets are also presented. Finally, the solution procedure for solving the DQMOM equations is described.

In Chapter 7, results from two-phase computations of internal flow in a large-scale pressure-swirl atomizer, obtained with VOF and two-fluid Euler/Euler models, are presented.

In Chapter 8, results from DQMOM-multi-fluid computations of non-evaporating diesel-type sprays are presented and the computed steady velocity profiles are compared with measurements.

In Chapter 9, results from DQMOM-multi-fluid computations of Y-jet water sprays are presented and the computed profiles of steady droplet axial velocity and SMD are compared with measurements.

In Chapter 10, results from DQMOM-multi-fluid and DDM computations of a hollow-cone spray from a Danfoss pressure-swirl atomizer are presented and the computed profiles of steady droplet sizes and velocities are compared with measurements.

In Chapter 11, a summary and conclusions are presented and possibilities for future work are discussed.

Chapter 2

Breakup of Liquid Sheets

2.1 Introduction

In pressure-swirl and Y-jet atomizers the liquid is introduced through an annular orifice and exits under relatively low pressure in the form of a conical or an annular sheet. In the Y-jet atomizer high-velocity air is passed along the inside of the liquid sheet to produce a shear force at the air/liquid interface. Whereas increasing relative air/liquid velocity has shown to produce smaller droplets, the mechanism for breakup is not clearly established. The common notion is that the shear causes spanwise waves to form on the surface of the sheet, and the waves grow and separate from the sheet in the form of ligaments, which subsequently fragment into droplets as shown in Figure 2.1.

In most of the experiments conducted to study atomization particular attention has been paid to the atomization of planar liquid sheets because of their simplicity (Dombrowski and Hooper, 1962; Dombrowski and Johns, 1963). These sheets can be produced in a variety of ways by the impingement of liquid streams or their impact on a solid stationary or rotating surface. A simple method is to use the fan nozzle, a device that enables the properties and dimensions of the sheet to be easily controlled by varying the approach passages to the orifice (Dombrowski, *et al.*, 1960). During a study of single-hole fan-spray nozzles, Dombrowski and Fraser (1954) found that the spraying of liquids results in a network of unstable threads caused by perforations in the sheet. They established that the history of the perforation determines the stage of growth at which the threads break up.

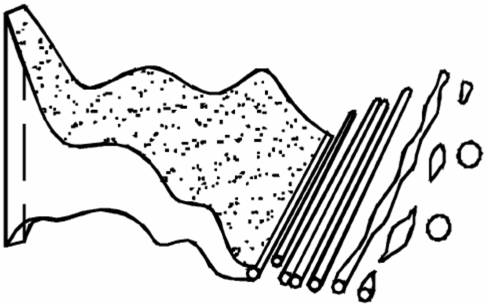

Figure 2.1: Sheet disintegration and drop formation process as proposed by Dombrowski and Johns (1963).

All early experimental studies focused on flat liquid sheets issuing into stagnant air. Later sheet disintegration research has been performed on sheet sprays issuing from two-dimensional air-blast nozzles (Mansour and Chigier, 1990; Beck, *et al.*, 1991; Stapper, *et al.*, 1992). Mansour and Chigier (1990) reported that the air flow is responsible for formation of both large, ordered, and small, chaotic "cell" structures. There were thin membranes bounded by relatively large-diameter ligaments. Stapper, *et al.* (1992) identified two primary mechanisms of disintegration, i.e. the cellular breakup and the stretched streamwise ligament breakup.

Theoretical studies also have been conducted on the hydrodynamic instability and the breakup process of liquid sheets for various cases: inviscid or viscous liquid, linear or nonlinear approaches, two-dimensional (plane or axisymmetric) or three-dimensional geometries, and swirling and diverging annular sheets (Sirignano and Mehring, 2000). The studies based on the linear assumption mainly reported that the aerodynamic instabilities cause the liquid sheet to be wavy and broken up into ligaments, followed by further disintegration into fine droplets (Squire, 1953; Dombrowski and Hooper, 1962; Dombrowski and Johns, 1963; Li and Tankin, 1991). The breakup process essentially originates from Kelvin-Helmholtz-type instability due to the velocity difference between the two fluids. The results from linear analyses are consistent with experimental data, at least qualitatively, and show quite good agreement, especially when the relative velocity is low (Dombrowski and Hooper, 1962; Dombrowski and Johns, 1963).

Whereas the linear stability analysis can help to understand the aerodynamic interaction between the liquid and the gas, leading to unstable growth on the sheet surface, the influence of the flow inside the nozzle on the disintegration of a liquid sheet is more difficult to analyze and requires a tool which solves the full Navier-Stokes-equations without linearization or the neglection of some material properties. Whereas several investigations treat periodic shear layers (Zaleski, *et al.*, 1997; Tryggvason, *et al.*, 2001; Fulgosi, *at al.*, 2003), there are only a few DNS studies concerned with the primary breakup of a spatially developing liquid sheet. Couderc and Estivalezes (2004) presented numerical simulations of a spatially developing liquid sheet surrounded by co-flowing air streams at moderate velocities (U_g = 20 and 40 m/s). The interface was captured by a Level-Set method. Klein (2005) investigated a liquid water film ejected into air. A VOF scheme was used to advect the interface, and good agreement with experimental data was obtained. To extend these types of analyses further to include the interaction of high-velocity air with the liquid sheet (to model Y-jet atomization) or very thin liquid sheets (to model pressure-swirl atomization), very fine grid resolution would be required to capture the atomization near the tip of the nozzle, the dispersion of the resulting spray field, and the air velocity field. This level of analysis is currently not possible at acceptable computational times.

2.2 Sheet Breakup Model

It is generally accepted that an aerodynamic instability causes the sheet to break up. The mathematical analysis below assumes that Kelvin-Helmholtz waves grow on the sheet and eventually break the liquid into ligaments. It is then assumed that the ligaments break up into droplets due to varicose instability.

The model used in this study is called the Linearized Instability Sheet Atomization (LISA) model of Schmidt, *et al.* (1999). The commercial

CFD code Fluent provides a variation of this model for their discrete phase modeling.

2.2.1 Sheet Breakup

The model includes the effects of the surrounding gas, liquid viscosity, and surface tension on the breakup of the liquid sheet. Details of the theoretical development of the model are given in Senecal, *et al.* (1999) and are only briefly presented here.

Linear Stability Analysis

The model assumes that a two-dimensional, viscous, incompressible liquid sheet of thickness $2h$ moves with relative velocity U through an inviscid, incompressible gas medium. The liquid and gas have densities of ρ_l and ρ_g, respectively, the viscosity of the liquid is μ_l, and surface tension is σ. A coordinate system is used that moves with the sheet, and a spectrum of infinitesimal disturbances of the form

$$\eta = \eta_0 \exp\left(ikx + \omega t\right) \tag{2.1}$$

is imposed on the initially steady, motion-producing fluctuating velocities, and pressures for both the liquid and the gas. In Eq. (2.1) η_0 is the initial wave amplitude, $k = 2\pi/\lambda$ is the wave number, and $\omega = \omega_r + i\omega_i$ is the complex growth rate. The most unstable disturbance has the largest value of ω_r, denoted here by Ω_S, and is assumed to be responsible for sheet breakup. Thus, it is desired to obtain a dispersion relation $\omega = \omega(k)$ from which the most unstable disturbance can be deduced.

Squire (1953) has shown that two solutions, or modes, exist that satisfy the liquid governing equations subject to the boundary conditions at the upper and lower interfaces. For the first solution, called the sinuous mode, the waves at the upper and lower interfaces are in exactly phase. On the other hand, for the varicose mode, the waves are π radians out of phase (see Figure 2.2). It has been shown by numerous authors, e.g. Senecal, *et al.*, (1999), that the sinuous mode dominates the growth of varicose waves for low velocities and low gas-to-liquid density ratios. In addition, it can be shown that the sinuous and varicose modes become indistinguishable for high-velocity flows. As a result, the present discussion focuses on the growth of sinuous waves on the liquid sheet.

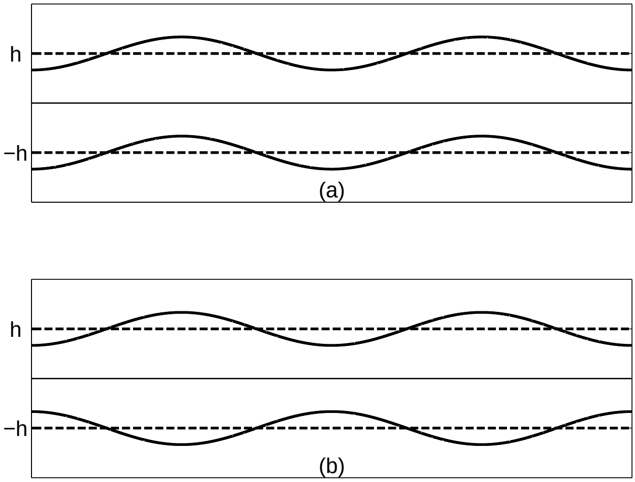

Figure 2.2: Schematic of (a) antisymmetric or sinuous waves and (b) symmetric or varicose waves.

As derived in Senecal, *et al.* (1999), the dispersion relation for the sinuous mode is given by

$$\begin{aligned}&\omega^2\left[\tanh(kh)+Q\right]+\omega\left[4\nu_l k^2\tanh(kh)+2iQkU\right]\\&\quad+4\nu_l^2k^4\tanh(kh)-4\nu_l^2k^3\ell\tanh(\ell h)-QU^2k^2+\frac{\sigma k^3}{\rho_l}=0\end{aligned}\qquad(2.2)$$

where $Q=\rho_g/\rho_l$, $\ell=k^2+\omega/\nu_l$, $\nu_l=\mu_l/\rho_l$, and U is the relative velocity between the liquid and gas.

Li and Tankin (1991) derived a dispersion relation similar to Eq. (2.2) for a viscous sheet from a linear analysis with a stationary coordinate system. Whereas Li and Tankin's relation is quite general, a simplified relation has been presented in Senecal, *et al.* (1999). First, an order-of-magnitude analysis using typical values from inviscid solutions shows that the terms of the second order in viscosity can be neglected in comparison to the other terms in Eq. (2.2). The resulting expression for the growth rate is given by

$$\omega_r = -\frac{2\nu_l k^2 \tanh(kh)}{\tanh(kh)+Q} + \frac{\sqrt{4\nu_l^2 k^4 \tanh^2(kh) - Q^2U^2k^2 - \left[\tanh(kh)+Q\right]\left[-QU^2k^2 + \frac{\sigma k^3}{\rho_l}\right]}}{\tanh(kh)+Q} \tag{2.3}$$

We are interested in the waves that grow most rapidly for a sheet of liquid in air. Squire (1953) assumed that long waves grow on the sheet. For long waves, the wavelengths, $\lambda = 2\pi/k$, are large compared with the sheet thickness so that $\tanh(kh) \approx kh$. In addition, the density ratio, Q, is on the order of 10^{-3} in typical applications, so if it is further assumed that $Q \ll kh$, Eq. (2.3) reduces to

$$\omega_r = -2\nu_l k^2 + \sqrt{4\nu_l^2 k^4 + \frac{QU^2k}{h} - \frac{\sigma k^2}{\rho_l h}} \tag{2.4}$$

Furthermore, if short waves are assumed for high-speed sheets, $\tanh(kh) \approx 1$ and $Q \ll 1$, Eq. (2.3) reduces to

$$\omega_r = -2\nu_l k^2 + \sqrt{4\nu_l^2 k^4 + QU^2k^2 - \frac{\sigma k^3}{\rho_l}} \tag{2.5}$$

Comparisons of Eqs. (2.4) and (2.5) with the sinuous mode solution, Eq. (2.3), are given in Figure 2.3 and Figure 2.4 for gas Weber numbers, $\mathrm{We}_g = \rho_g U^2 h/\sigma$, of 0.5 and 5.0, respectively. The results indicate that the long wave assumption is in good agreement with the general sinuous analysis for a We_g of 0.5, whereas the short wave assumption predicts the maximum growth rate of the general analysis well for a We_g of 5.0.

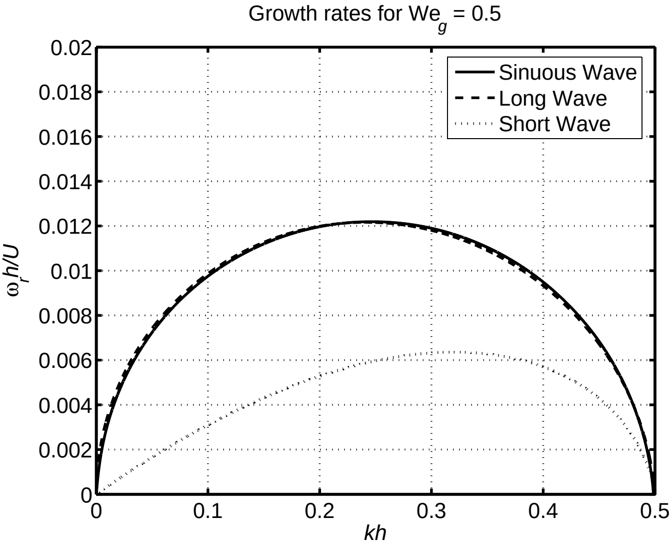

Figure 2.3: Dimensionless growth rate $\omega_r h/U$ as function of dimensionless wave number *kh* for $\mathrm{We}_g = 0.5$.

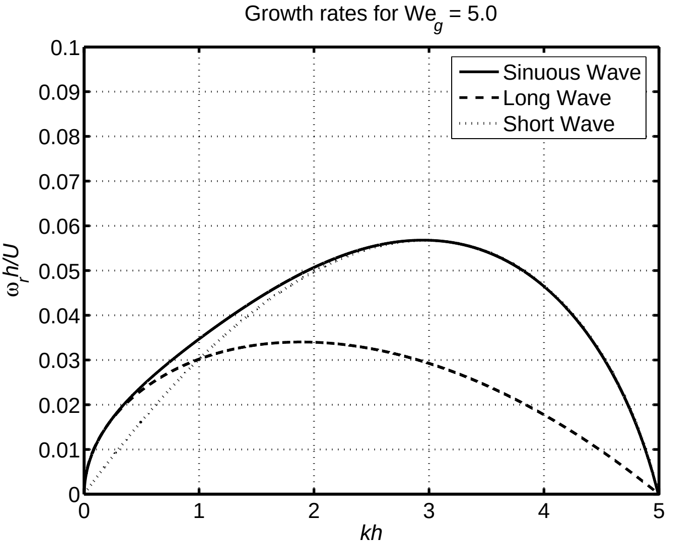

Figure 2.4: Dimensionless growth rate $\omega_r h/U$ as function of dimensionless wave number *kh* for $\mathrm{We}_g = 5.0$.

Inviscid Sheets

If viscosity is neglected, Eq. (2.4) for long waves reduces to

$$\omega_r = \sqrt{\frac{QU^2k}{h} - \frac{\sigma k^2}{\rho_l h}} \tag{2.6}$$

and Eq. (2.5) for short waves reduces to

$$\omega_r = \sqrt{QU^2k^2 - \frac{\sigma k^3}{\rho_l}} \tag{2.7}$$

Equations (2.6) and (2.7) are presented in Figure 2.5 and Figure 2.6 with their viscous counterparts for a We_g of 0.5 and 5.0, respectively. From these figures it is seen that the inclusion of viscosity reduces both the maximum growth rate and the corresponding wave number. The effect of viscosity is minimal for long wave growth, whereas inclusion of the viscous terms is necessary to accurately predict the wave growth of short waves.

If the maximum growth rate for the inviscid long wave analysis Eq. (2.6), which occurs at a dimensionless wave number of $K_S h = 1/2\,\mathrm{We}_g$, is equated with the dimensionless maximum growth rate for the short wave analysis, Eq. (2.7), which occurs at $K_S h = 2/3\,\mathrm{We}_g$, it can be shown that a critical Weber number (based on the relative velocity U, the gas density ρ_g, and the sheet half-thickness h) is given by $\mathrm{We}_g = 27/16$. Above $\mathrm{We}_g = 27/16$, the fastest growing waves are short, and below $27/16$, the wavelengths are long compared to the sheet thickness.

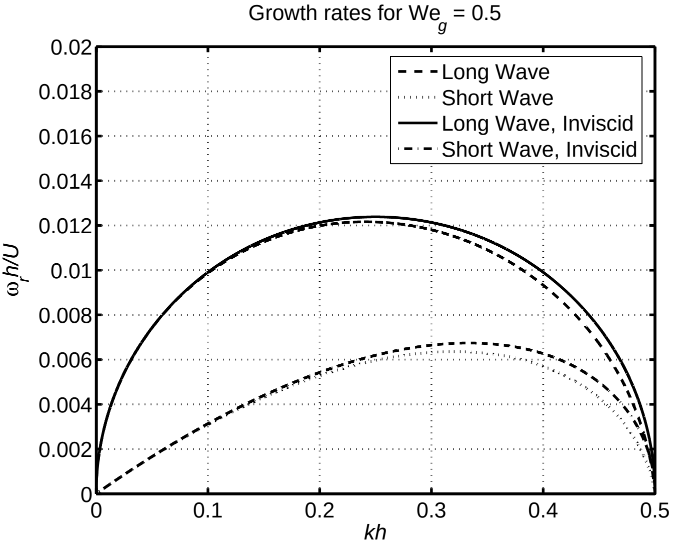

Figure 2.5: Viscous and inviscid dimensionless growth rate $\omega_r h/U$ as function of dimensionless wave number *kh* for $\mathrm{We}_g = 0.5$

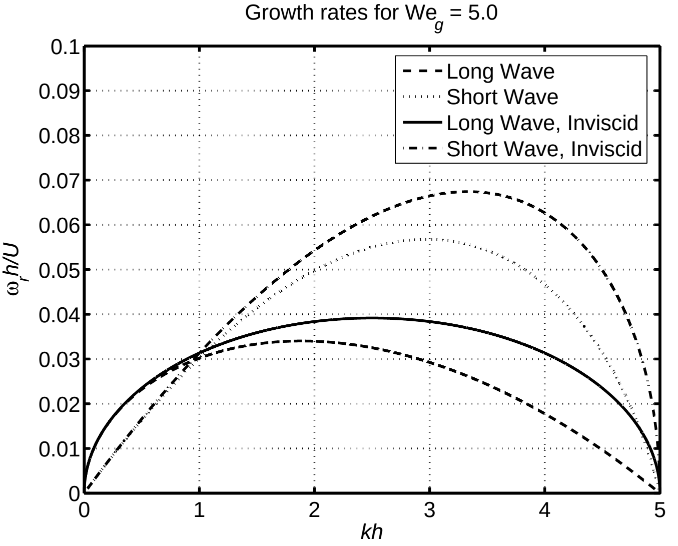

Figure 2.6: Viscous and inviscid dimensionless growth rate $\omega_r h/U$ as function of dimensionless wave number *kh* for $\mathrm{We}_g = 5.0$.

Sheet Breakup

The physical mechanism of sheet disintegration proposed by Dombrowski and Johns (1963) is adopted in order to predict the drop sizes produced from the primary breakup process. As shown in Figure 2.1, ligaments are assumed to form from the sheet breakup process once the unstable waves reach critical amplitude.

Equations (2.4) and (2.5) indicate that whereas the growth rate of long waves depends on sheet thickness, the growth rate of short waves is independent of the thickness of the sheet.

Since the growth rate for short waves are independent of the sheet thickness, the onset of ligament formation, or breakup length, can be formulated based on an analogy with the breakup length of cylindrical jets, e.g. see Reitz and Bracco (1982). If the surface disturbance has reached a value of η_{bu} at breakup, a breakup time, τ_{bu}, can be evaluated:

$$\eta_{bu} = \eta_0 \exp\left(\Omega_S \tau_{bu}\right) \quad \Rightarrow \quad \tau_{bu} = \frac{1}{\Omega_S} \ln\left(\frac{\eta_{bu}}{\eta_0}\right) \tag{2.8}$$

where Ω_S, the maximum growth rate, is found by numerically maximizing Eq. (2.5) as a function of k. The sheet breaks up and ligaments will be formed at a length given by

$$L_{bu} = U_l \tau_{bu} = \frac{U_l}{\Omega_S} \ln\left(\frac{\eta_{bu}}{\eta_0}\right) \tag{2.9}$$

where the quantity $\ln\left(\eta_{bu}/\eta_0\right)$ is given the value 12 in the present study based on the work of Dombrowski and Hooper (1962). The quantity U_l in Eq. (2.9) is the absolute velocity of the sheet.

For long waves, the breakup length depends on the sheet thickness. For a parallel-sided sheet, the half-thickness is not a function of radial position and thus the above formulation can be used directly to determine the maximum growth rate and corresponding wave number for long waves from Eq. (2.4).

However, for attenuating sheets the thickness is inversely proportional to the radial distance from the injector nozzle. The sheet half-thickness, h, can be calculated from the sheet length L, the sheet half-angle θ, the radial distance from the center line to the mid-line of the sheet at the atomizer exit r_0, and the sheet half-thickness at atomizer exit h_0 (Figure 2.7):

$$h = \frac{r_0 h_0}{r_0 + L \sin\theta} \tag{2.10}$$

If the substitution $L = U_l t$ is made and if it is assumed that $r_0 \ll L \sin\theta$, Eq. (2.10) reduces to

$$h = \frac{K}{U_l t} \tag{2.11}$$

where $K = r_0 h_0 / \sin\theta$ is a dimensional constant which represents the variation of the sheet thickness with distance from the nozzle.

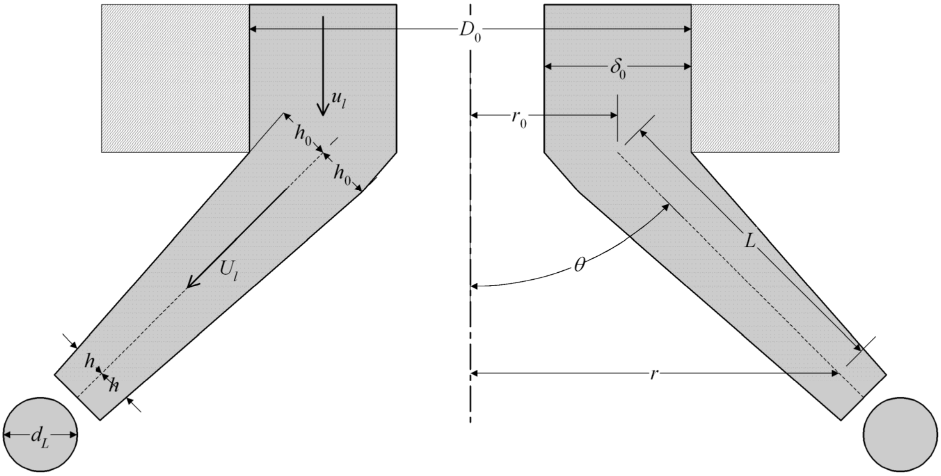

Figure 2.7: Schematic showing the conceptual liquid flow at the nozzle exit.

Equation (2.8) can be applied to an attenuating sheet if it is assumed that the wave growth at any point depends solely upon the values of the local parameters. The growth rate then becomes time-dependent and the growth rate must be integrated over time. Thus, Eq. (2.8) may be rewritten as

$$\ln\left(\frac{\eta_{bu}}{\eta_0}\right)=\int_0^{\tau_{bu}}\omega_r \mathrm{d}t \tag{2.12}$$

It was shown in Figure 2.5 that viscosity has a minor effect on wave growth in the long wave regime. As a result, Eq. (2.6) can be used in Eq. (2.12) for simplicity. The most unstable wave number is then given by

$$K_S=\frac{\rho_g U^2}{2\sigma} \tag{2.13}$$

The integration of Eq. (2.12) results in the following expression for the breakup length $L_{bu}=U_l\tau_{bu}$ of the sheet:

$$L_{bu}=\left[3U_l\ln\left(\frac{\eta_{bu}}{\eta_0}\right)\right]^{2/3}\left[\frac{K\sigma}{Q^2U^4\rho_l}\right]^{1/3} \tag{2.14}$$

where U_l and U are the absolute sheet velocity and liquid/gas relative velocity, respectively.

Ligament Formation

The diameter of ligaments formed at the point of breakup can be obtained from a mass balance. For the case of long waves it is assumed that the ligaments are formed from tears in the sheet twice per wavelength, and the resulting diameter is given by

$$d_L=\sqrt{\frac{8h_{bu}}{K_S}} \qquad \text{for long waves} \tag{2.15}$$

where h_{bu} and K_S is determined from Eqs. (2.11) and (2.13), respectively.

For short waves, Senecal, *et al.* (1999) assumes that the ligaments are formed from tears in the sheet once per wavelength, and the resulting diameter is given by

$$d_L = \sqrt{\frac{16h_{bu}}{K_S}} \quad \text{for short waves} \tag{2.16}$$

where h_{bu} is now given by Eq. (2.10), and K_S is the wave number corresponding to the maximum growth rate, Ω_S, determined from Eq. (2.5). In the Fluent pressure-swirl atomizer model, the ligament diameter is assumed to be linearly proportional to the wavelength, Λ_S, which breaks up the sheet (Fluent, 2005):

$$d_L = C_L \Lambda_S = \frac{2\pi C_L}{K_S} \tag{2.17}$$

where C_L is a ligament constant.

Drop Formation

In either the short wave or the long wave case, the breakup from ligaments to droplets is assumed to behave according to Weber's analysis for capillary instability (Dombrowski and Johns, 1963). The wave number, K_L, corresponding to the maximum growth rate for the breakup of a cylindrical, viscous column is determined from

$$K_L d_L = \left[\frac{1}{2} + \frac{3\mu_l}{2\left(\rho_l \sigma d_L\right)}\right]^{-1/2} \tag{2.18}$$

If it is assumed, as in Dombrowski and Johns (1963), that breakup occurs when the amplitude of the unstable waves is equal to the radius of the ligament; one drop will be formed per wavelength. Thus by mass balance the relation between drop size and wave number is given by

$$d_D^3 = \frac{3\pi d_L^2}{K_L} \tag{2.19}$$

for the drop size d_D, which on combination with Eq. (2.18) gives

$$d_D = 1.88 d_L \left(1 + 3\mathrm{Oh}\right)^{1/6} \tag{2.20}$$

where Oh is the Ohnesorge number, which is a combination of Reynolds number and Weber number:

$$\mathrm{Oh} = \frac{\sqrt{\mathrm{We}_l}}{\mathrm{Re}_l} = \frac{\mu_l}{\sqrt{\rho_l \sigma d_L}} \tag{2.21}$$

2.2.2 Sheet Formation

The way that the liquid sheet is formed is different for the pressure-swirl and Y-jet atomizers. Sheet formation models for the pressure-swirl atomizer and the Y-jet atomizer is described below.

Pressure-Swirl Atomizer

The centrifugal motion of the liquid within the injector creates an air core surrounded by a liquid film. The thickness of the film, δ_0, is related to the mass flow rate by

$$\dot{m}_l = \pi \rho_l u_l \delta_0 \left(D_0 - \delta_0 \right) \tag{2.22}$$

where D_0 is the atomizer exit diameter, and $\dot{m}_l$ is the liquid mass flow rate. The other unknown in Eq. (2.22) is u_l, the axial component of velocity at the exit. This quantity depends on internal details of the injector and is difficult to calculate from first principles. Instead, the approach of Han, *et al.* (1997) is used. The total velocity, U_l, is assumed to be related to the injector pressure drop, ΔP, by

$$U_l = k_v \sqrt{\frac{2\Delta P}{\rho_l}} \tag{2.23}$$

Lefebvre (1989) has noted that k_v is a function of the injector design and injection pressure. If the swirl ports are treated as nozzles, Eq. (2.23) is then an expression for the coefficient of discharge for the swirl ports, assuming that the majority of the pressure drop through the injector occurs at the ports. The coefficient of discharge for single-phase nozzles with sharp inlet corners and an L/D of 4 is typically 0.78 or less

(Schmidt, *et al.*, 1999). Reducing k_v by 10% to allow for other momentum losses in the injector gives an estimate of 0.7.

Physical limits on k_v are such that it must be less than unity by conservation of energy, and it must be large enough to permit sufficient mass flow. To guarantee that the size of the air core is non-negative, the following expression is used:

$$k_v = \max\left(0.7, \frac{4\dot{m}_l}{\pi D_0^2 \rho_l \cos\theta}\sqrt{\frac{\rho_l}{2\Delta P}}\right) \tag{2.24}$$

where θ is the spray half-angle.

Assuming that the pressure drop is known, Eq. (2.23) can be used to find U_l. Once U_l is determined, u_l is found from

$$u_l = U_l \cos\theta \tag{2.25}$$

The initial half-thickness h_0 can be related to the film thickness within the discharge orifice δ_0, by the expression

$$h_0 = \frac{1}{2}\delta_0 \cos\theta \tag{2.26}$$

Consequently the sheet thickness parameter K is found from

$$K = \frac{r_0 h_0}{\sin\theta} = \frac{\dot{m}_l}{4\pi\rho_l U_l \sin\theta} \tag{2.27}$$

Depending on the spray angle, θ, and the geometry of the atomizer, D_0, the sheet thickness parameter for Danfoss pressure-swirl atomizers lies in the range $1000\ \mu m^2 < K < 10000\ \mu m^2$. These conditions found in Danfoss pressure-swirl atomizers lead to thin low-speed sheets. As a consequence of the low Weber numbers, it is assumed that the sheet breakup is always due to long waves. Hence the ligament diameter is determined from Eqs. (2.11), (2.13), and (2.15).

With the preceding expressions, Eq. (2.15) can be used in Eq. (2.20), yielding the results shown in Figure 2.8 for water ($\nu_l = 1.0\times10^{-6}\ m^2/s$, $\sigma = 0.072$ N/m, and $\rho_l = 998\ kg/m^3$), depicting the droplet diameter vs.

pressure drop for different values of the sheet thickness parameter K for a spray half-angle of $\theta = 30°$. At a given K the droplet sizes decrease first with increasing pressure drop and sheet velocity, but then as the pressure drop exceeds about 20 bar, only very slight decrease in droplet size is gained by increasing the pressure drop more.

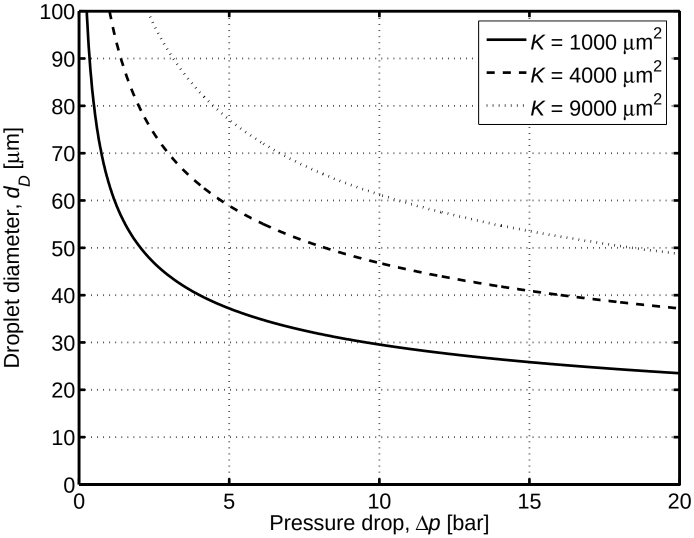

Figure 2.8: Droplet diameter vs. pressure drop for different sheet thickness parameters.

Y-jet Atomizer

In a typical Y-jet atomizer, the liquid, on entering the mixing chamber, is pushed against the wall by the incoming atomizing gas and a liquid film is generated. This liquid film is then ejected from the discharge orifice nearly as an annular sheet, $\theta \approx 0$.

The liquid sheet velocity is related to the liquid mass flow rate $\dot{m}_l$ by

$$U_l = \frac{\dot{m}_l}{\pi \rho_l \delta_0 \left(D_0 - \delta_0 \right)} \tag{2.28}$$

and the gas velocity inside the liquid sheet is given by

$$U_g = \frac{MLR\dot{m}_l}{\pi\rho_g\left(\frac{D_0}{2}-\delta_0\right)^2} \tag{2.29}$$

where *MLR* is mass loading ratio

$$MLR = \frac{\dot{m}_g}{\dot{m}_l} \tag{2.30}$$

Another useful non-dimensional number relevant to the liquid sheet atomization in a co-flowing gas stream is the momentum flux ratio (Lasheras, *et al.*, 1998)

$$MFR = \frac{\rho_g U_g^2}{\rho_l U_l^2} \tag{2.31}$$

It is to be noted that the *MFR* also corresponds to the ratio of dynamic pressures.

Then from Eqs. (2.28), (2.29), and (2.31) one has

$$\delta_0 = \frac{D_0}{2}\left(1-\sqrt{\frac{MLR\left(MLR\rho_l-\sqrt{MFR\rho_l\rho_g}\right)}{MLR^2\rho_l-MFR\rho_g}}\right) \tag{2.32}$$

In the present work, an annular sheet is assumed to be formed from the final discharge orifice. As the liquid moves as an annular sheet from the nozzle tip with constant velocity U_l, the half-thickness at any section is considered to be constant and given by $h=\delta_0/2$.

For the relative gas-liquid velocity *U*, a mean value is chosen as an average between relative velocities on both sides of the sheet:

$$U = \sqrt{\frac{\left(U_{g,i}-U_l\right)^2+\left(U_{g,o}-U_l\right)^2}{2}} \tag{2.33}$$

where $U_{g,i}$ and $U_{g,o}$ are the gas velocities on the inside and outside of the sheet, respectively (Dombrowski and Johns, 1963).

Figure 2.9 gives the model predictions of gas (air: ρ_g = 1.2 kg/m^3), liquid (water: ρ_l = 998 kg/m^3, ν_l = 1.0×10^{-6} m^2/s, σ = 0.072 N/m), and relative velocities, and the half-thickness of the liquid sheet at the exit of the nozzle, varying with the mass loading ratio *MLR* for a liquid mass flow rate of $\dot{m}_l$ = 190 kg/h and an exit diameter of D_0 = 3.7 mm and for *MFR* = 1. As the mass loading ratio increases, the velocities increase and the sheet half-thickness decreases.

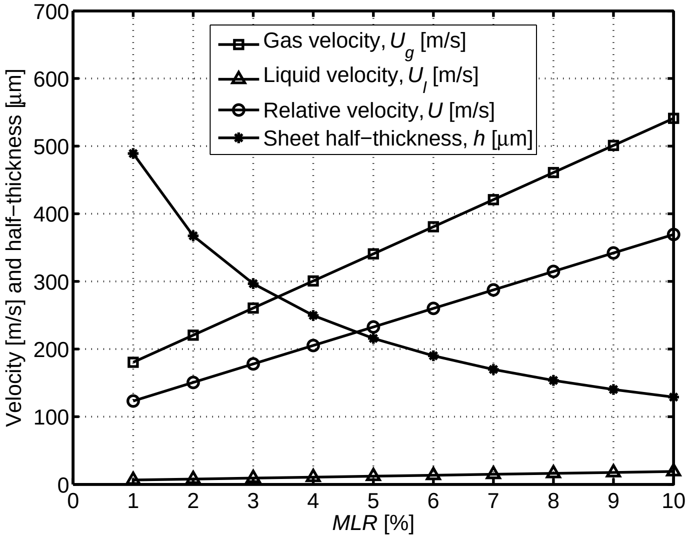

Figure 2.9: Prediction of gas velocity, liquid velocity, and sheet half-thickness at the nozzle exit.

For Y-jet atomizers it is assumed that the sheet breakup is always due to short waves. This assumption is a consequence of the greater sheet thickness and higher relative velocity found in Y-jet atomizers. Hence the ligament diameter is determined from Eqs. (2.5) and (2.16) with $h_{bu} = \delta_0/2$.

Figure 2.10 illustrates the droplet diameter d_D predicted by the model, varying with the momentum flux ratio *MFR*, for mass loading ratios of *MLR* = 3.75, 5.00, and 6.25%. As the momentum flux ratio increases for a given mass loading ratio, the droplet diameter first increases until a maximum value is reached. When the momentum flux ratio increases further the droplet diameter decreases gradually.

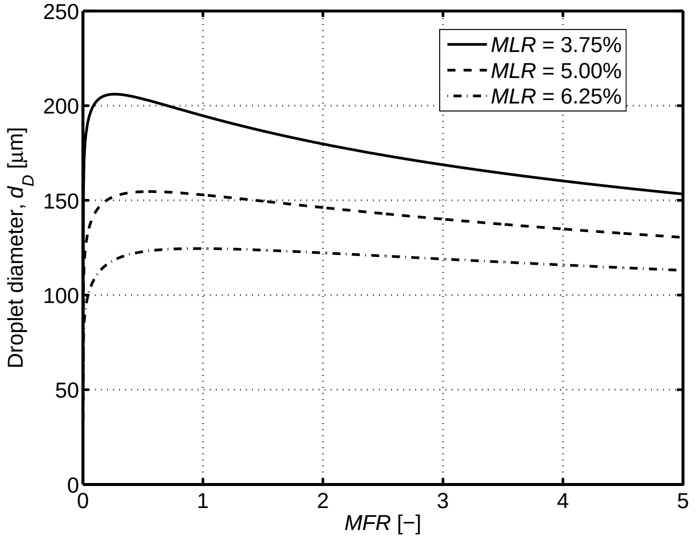

Figure 2.10: Predicted droplet diameter.

2.2.3 Secondary Droplet Breakup

The droplets formed after the primary breakup of the liquid sheet, may undergo secondary breakup. The modeling of secondary droplet breakup and droplet-droplet collision and coalescence is discussed in the following chapter.

Chapter 3

Droplet Breakup and Coalescence

3.1 Introduction

The mechanisms determining the evolution of the droplet size distribution (DSD) of the spray is discussed in this chapter, and various models for the droplet breakup and droplet-droplet collision are presented.

3.2 Droplet Breakup

Liquid drops detached from the liquid sheet, continuing their motion through the gas may, under certain conditions, be disintegrated into smaller droplets. This phenomenon is known in the literature as droplet breakup or secondary atomization. The exact mechanisms behind the droplet breakup, despite numerous experimental and theoretical works, are still not completely understood. As a result of this, there are many uncertainties in the quantitative description of the process.

The relative motion between a droplet and the surrounding gas causes a non-uniform distribution of pressure and shear stress on the droplet surface. These external forces deform the droplet and cause it to disintegrate when they overcome the opposing force of surface tension. The new droplets may undergo further breakup until a stable diameter is reached for which the surface tension force is stronger than the external forces. A literature review on this subject can be found in Faeth, *et al.* (1995) and Faeth (2002).

Dimensionless numbers, expressing the ratio of the aforementioned forces, are used in correlations of the various breakup regimes. Faeth, *et al.* (1995) reported that the breakup regime transitions are mainly functions of the gas Weber number, We_g, and the Ohnesorge number, Oh. The former represents the ratio of drag forces to surface tension forces, whereas the latter represents the ratio of viscous forces to surface tension forces. Their mathematical expressions are respectively given by:

$$\mathrm{We}_g = \frac{\rho_g U_{rel}^2 d}{\sigma} \tag{3.1}$$

$$\mathrm{Oh} = \frac{\mu_l}{\sqrt{\rho_l d \sigma}} \tag{3.2}$$

Here ρ_g is the surrounding gas density, ρ_l is the liquid density, U_{rel} is the relative velocity between the gas and the droplet, d is the droplet diameter, σ is the surface tension, and μ_l is the liquid molecular viscosity.

3.2.1 Pilch-Erdman' Correlations

Pilch and Erdman (1987) collected data in a wide literature search for various fluids and categorized droplet breakup into five distinct mechanisms described below and illustrated schematically in Figure 3.1:

1. **Vibrational breakup** ($\mathrm{We}_g \leq 12$): A few large fragments are produced. The overall breakup time is long compared to the other breakup mechanisms. Hence, this mechanism is usually not considered important in droplet breakup studies.
2. **Bag breakup** ($12 < \mathrm{We}_g \leq 50$): A thin hollow bag is blown downstream while it is attached to a more massive toroidal rim. The bag forms a large number of small fragments, whereas the rim, a short time later, produces a small number of large fragments.

3. **Bag-and-stamen** ($50 < \mathrm{We}_g \leq 100$): This mode is similar to bag breakup. A thin bag is blown downstream while being anchored to a massive toroidal rim. A column of liquid (stamen) is formed along the droplet axis parallel to the approaching flow. The bag bursts first and the disintegration of rim and stamen follows.

4. **Sheet stripping** ($100 < \mathrm{We}_g \leq 350$): A thin sheet is continuously drawn from the periphery of the deforming droplet. The sheet disintegrates a short distance downstream from the droplet because of Kelvin-Helmholtz (K-H) instabilities. A coherent residual droplet exists during the entire breakup process.

5. **Wave crest stripping followed by catastrophic breakup** ($\mathrm{We}_g > 350$): Waves with large amplitude and small wavelength related with K-H instabilities are formed on the windward surface of the droplet. The wave crests are continuously eroded by the action of the flow field over the surface of the droplet. Waves with large amplitude and long wavelength related with Rayleigh-Taylor (R-T) instabilities ultimately penetrate the droplet creating several large fragments. This is referred to as catastrophic breakup.

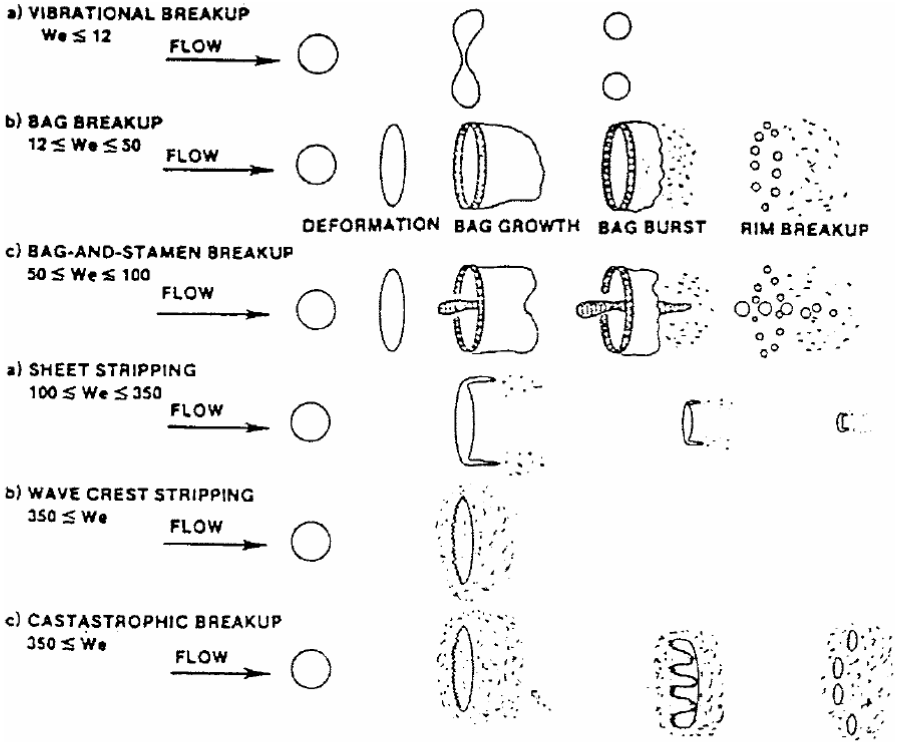

Figure 3.1: Breakup mechanisms, adapted from Pilch and Erdman (1987).

The characteristic breakup time is given by

$$\tau_{bu} = T_{bu} \frac{d}{U_{rel}} \sqrt{\frac{\rho_l}{\rho_g}} \tag{3.3}$$

where T_{bu} is called the dimensionless breakup time and for each breakup regime, it is estimated from the following correlations:

$$T_{bu}=\begin{cases}6\left(\mathrm{We}_g-12\right)^{-0.25} & \text{for } 12\le \mathrm{We}_g\le 18\\ 2.45\left(\mathrm{We}_g-12\right)^{0.25} & \text{for } 18\le \mathrm{We}_g\le 45\\ 14.1\left(\mathrm{We}_g-12\right)^{-0.25} & \text{for } 45\le \mathrm{We}_g\le 351\\ 0.766\left(\mathrm{We}_g-12\right)^{0.25} & \text{for } 351\le \mathrm{We}_g\le 2670\\ 5.5 & \text{for } \mathrm{We}_g\ge 2670\end{cases} \tag{3.4}$$

The variation of T_{bu} with We_g is illustrated in Figure 3.2.

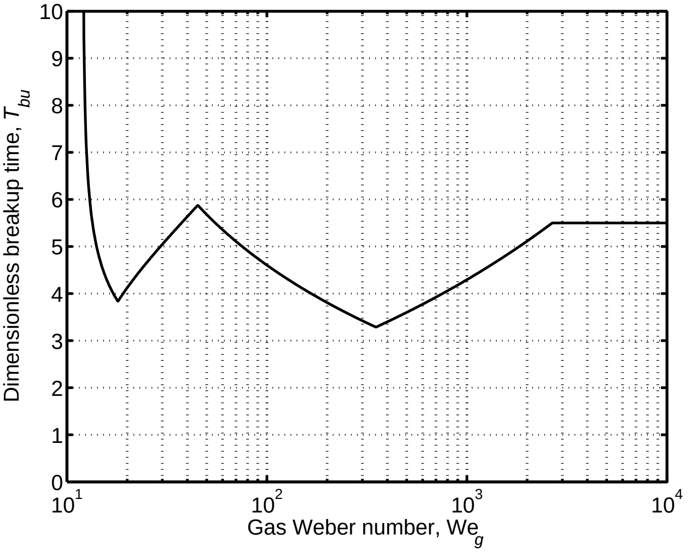

Figure 3.2: Dimensionless breakup time.

The stable diameter is estimated, for all the above mentioned regimes by the following expression:

$$d_{st}=\mathrm{We}_{g,crit}\frac{\sigma}{\rho_g U_{rel}^2} \tag{3.5}$$

where $\mathrm{We}_{g,crit}$ is the critical Weber number below which breakup does not occur. An empirical correlation for this, for gas-liquid systems, is given by:

$$\mathrm{We}_{g,crit} = 12\left(1 + 1.077\,\mathrm{Oh}^{1.6}\right) \tag{3.6}$$

The critical Weber number is approximately 12 when the Ohnesorge number is small (Oh < 0.1), as depicted in Figure 3.3.

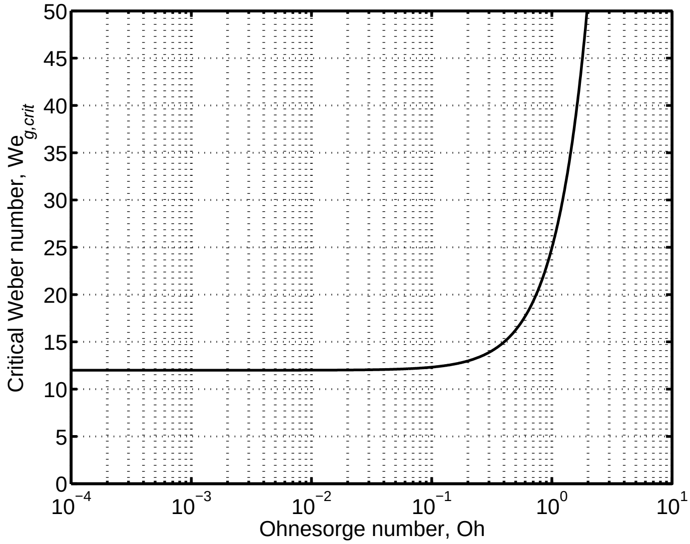

Figure 3.3: Critical Weber number.

3.2.2 Breakup Models

In the past a number of different breakup models have been proposed, based on different physical mechanisms.

The TAB (O'Rourke and Amsden, 1987) and the DDB (Ibrahim, *et al.*, 1993) models are based on the dynamics of single droplets and can therefore be considered as secondary breakup models. In the first the breakup is due to the amplification of droplet deformation resulting from vibrational resonance of the surface and therefore is well suited for low-Weber-number sprays. The latter is a deformation-induced secondary breakup model and is appropriate in the bag breakup regime. The WAVE (Reitz, 1987) model considers K-H instabilities effects and is appropriate for the breakup of secondary droplets in the stripping regime. The RT (Patterson and Reitz, 1998; Beale and Reitz, 1999) model considers R-T instabilities that arise on a very high-speed droplet surface and therefore can be adopted to model droplet secondary breakup in the catastrophic regime.

It is not easy to decide which breakup model to choose for a specific simulation task. It turns out that practically all the breakup models are capable of reproducing measured data, as long as model constants are properly chosen.

For droplet breakup rate, the approach from the standard WAVE model has been implemented. Details of the model are presented below.

3.2.3 WAVE Model

Based on the Reitz and Bracco (1982) stability analysis of round liquid jets, Reitz (1987) derived a general breakup model describing the stripping breakup of droplets. When applied to large liquid drops at the nozzle exit, the model also simulates the breakup of a liquid jet.

Droplet breakup in the WAVE model is due to the unstable growth of waves on a liquid surface, subjected to an infinitesimal axisymmetric displacement. The maximum growth rate, Ω, and its corresponding wavelength, Λ, are related to the relevant properties of the liquid and gas by

$$\Lambda = 9.02 r \frac{\left(1 + 0.45\,\mathrm{Oh}^{0.5}\right)\left(1 + 0.4\,\mathrm{Ta}^{0.7}\right)}{\left(1 + 0.87\,\mathrm{We}_g^{1.67}\right)^{0.6}} \tag{3.7}$$

and

$$\Omega = \frac{0.34 + 0.38\,\mathrm{We}_g^{1.5}}{\left(1 + \mathrm{Oh}\right)\left(1 + 1.4\,\mathrm{Ta}^{0.6}\right)} \sqrt{\frac{\sigma}{\rho_l r^3}} \tag{3.8}$$

Here, $\mathrm{Ta} = \mathrm{Oh}\sqrt{\mathrm{We}_g}$ is the Taylor number, $\mathrm{We}_g = \rho_g U_{rel}^2 r / \sigma$ is the gas Weber number, and $\mathrm{Oh} = \mu_l / \sqrt{\rho_l r \sigma}$ is the Ohnesorge number. $r = d/2$ refers to the radius of the parent liquid drop and U_{rel} is the relative velocity between the gas and the drop.

Liquid breakup is modeled by postulating that new droplets of diameter d_{st} are formed from the parent drop, with diameter d, with

$$d_{st} = 2B_0\Lambda \tag{3.9}$$

where B_0 is a model constant set equal to 0.61 based on the work of Reitz (1987).

The characteristic diameter d of an unstable parent drop changes continuously with time following the rate equation:

$$\frac{\mathrm{d}d}{\mathrm{d}t} = -\frac{d - d_{st}}{\tau_{bu}}, \quad d_{st} < d \tag{3.10}$$

The breakup time τ_{bu} is calculated from

$$\tau_{bu} = 3.726 B_1 \frac{r}{\Lambda\Omega} \tag{3.11}$$

where the constant B_1 is subject to further debate. It is shown in the limits We → 0 and We → ∞ that the characteristic breakup time takes the form

$$\tau_{bu} = 1.72 B_1 \sqrt{\frac{\rho_l r^3}{2\sigma}} \qquad \text{for We} \to 0 \qquad \text{(bag breakup)} \tag{3.12}$$

$$\tau_{bu} = B_1 \frac{r}{U_{rel}} \sqrt{\frac{\rho_l}{\rho_g}} \qquad \text{for We} \to \infty \qquad \text{(stripping breakup)} \tag{3.13}$$

The conditions of bag and stripping breakup are taken from experiments to be $\mathrm{We}_g > 6$ and $\mathrm{We}_g / \sqrt{\mathrm{Re}_g} > 0.5$, respectively. Based on comparisons to the TAB model (O'Rourke and Amsden, 1987), B_1 has been set as $B_1 = \sqrt{3} = 1.73$. In the case of We → ∞, B_1 can be estimated from Eqs. (3.3) and (3.4) to be $B_1 = 2T_{bu} = 11$. B_1 accounts for differences in the drop breakup time due to unknown initial conditions for the drop, and in the literature B_1 has been set as high as 80 for some calculations.

3.2.4 Comparison of the WAVE Model and the Pilch-Erdman' Correlations

Predictions of Eq. (3.11) with different values of B_1 are compared with the correlations of Pilch and Erdman (1987) in Figure 3.4. The various peaks and valleys seen in dimensionless breakup time plot (Figure 3.2) appear as slope changes in real time; however, the WAVE model predicts a continuously decreasing breakup time with the Weber number, and whereas the Pilch-Erdman' correlations predicts that the breakup time goes to infinity in the vicinity of the critical Weber number ($\mathrm{We}_g = 12$), the WAVE model predicts a small value of τ_{bu}. The value of $B_1 = 10$ allows the WAVE model to approach the Pilch-Erdman correlations.

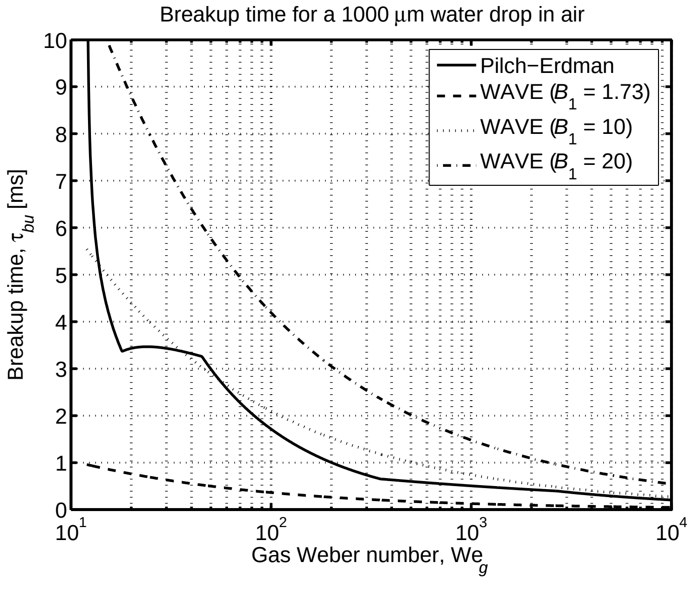

Figure 3.4: Comparison of breakup time predicted by the WAVE model with various values of the droplet breakup time constant B_1 and the correlations proposed by Pilch and Erdman (1987) as function of the gas Weber number for a 1 mm water drop in air.

With $B_0 = 0.61$ and in the limit of large We_g and $\mathrm{Oh} = 0$ (inviscid liquid), Eq. (3.9) is the same as Eq. (3.5). The ratio of the stable/parent droplet diameters d_{st}/d, as computed with Eqs. (3.5) and (3.9), is plotted in Figure 3.5 as a function of the gas Weber number for a 1 mm water drop in air. As expected, the stable droplet diameters for both models decrease with increasing Weber number, and the ratio is almost the same for the two models throughout the entire range.

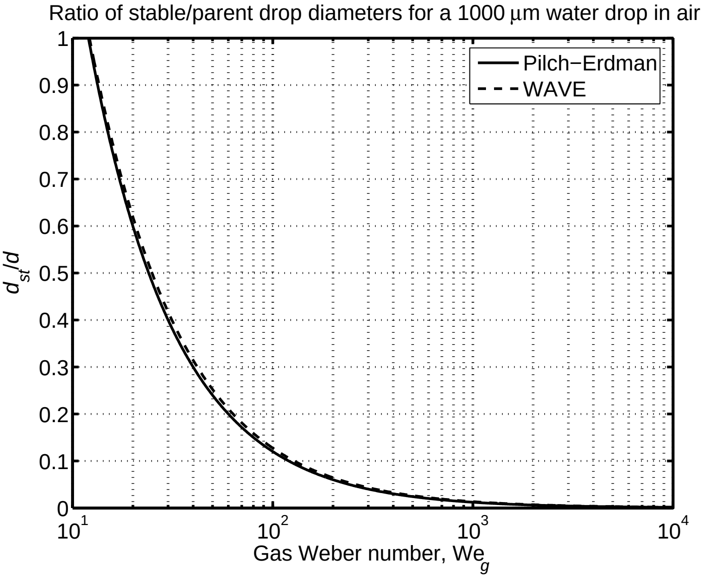

Figure 3.5: Comparison of ratio of the stable/parent droplet diameters predicted by the WAVE model and the correlations proposed by Pilch and Erdman (1987) as function of the gas Weber number for a 1 mm water drop in air.

3.2.5 Breakup Outcome

A second aspect of modeling droplet breakup is to determine the results. Faeth, *et al.* (1995) use a physical argument to determine the resultant drop sizes, although they suggest that the value should be taken as a resultant SMD rather than the exact diameter of all droplets. Han, *et al.* (1997) showed that a Rosin-Rammler distribution applied to newly created child drops improved the drop size distribution predictions. When breakup occurs in the WAVE model, the parent drop changes diameter and a collection of new droplets is formed. In general, these new droplets are subject to a size distribution function, which depends on the breakup mechanism. However, in the present study a uniform product size distribution has been assumed.

The breakup of an unstable parent drop with diameter d_q produces γ droplets of diameter d_{st} and one drop of diameter $\left(d_q^3 - \gamma d_{st}^3\right)^{1/3}$. The daughter distribution function $b\left(d \middle| d_q\right)$, which contains information on the fragments produced by a breakup event, corresponding to this breakup mechanism is

$$b\left(d \middle| d_q\right) = \begin{cases} \gamma & \text{if } d = d_{st} \\ 1 & \text{if } d = \left(d_q^3 - \gamma d_{st}^3\right)^{1/3} \\ 0 & \text{otherwise} \end{cases} \tag{3.14}$$

This daughter distribution function corresponds to an erosion type breakup mechanism. But, this mechanism may lead to an abundance of small droplets.

If symmetric fragmentation is considered, the breakup of an unstable droplet with diameter d_q produces two droplets of diameter $2^{-1/3} d_q$. The daughter distribution function corresponding to this breakup mechanism is

$$b\left(d \middle| d_q\right) = \begin{cases} 2 & \text{if } d = 2^{-1/3} d_q \\ 0 & \text{otherwise} \end{cases} \tag{3.15}$$

With this breakup mechanism, no small droplets are produced. However, the new droplets may undergo further breakup until the stable diameter is reached.

3.3 Droplet-Droplet Collision

It was shown by e.g. Wu, *et al.* (1986) that collision processes are important in sprays, especially in regions with high droplet number density. Collision is responsible for the growth of the droplets, due to the coalescence and the exchange of momentum between droplets. In this sense, the collision and breakup processes can be seen as two competing mechanisms whose outcomes determine the local DSD.

3.3.1 Collision Rate

The droplet-droplet collision model is semi-empirical and has two stages. The first stage is to determine collision rate between droplets. Collision rates are expressed by a collision coefficient β_{12} defined such that $\beta_{12} n(d_1) n(d_2)$ is the number of collisions per unit volume and time of droplets having number densities $n(d_1)$ and $n(d_2)$. According to the kinetic theory (Delichatsios and Probstein, 1975; Gidaspow, 1984), the collision coefficient is given by

$$\beta_{12} = \pi d_{12}^2 U_{rel} \tag{3.16}$$

where $d_{12} = (d_1 + d_2)/2$ and $U_{rel} = \overline{|\vec{u}_1 - \vec{u}_2|}$ is the average relative velocity between the two droplet classes. The following form for the relative velocity between colliding droplets is assumed:

$$U_{rel} = \sqrt{(U_1 - U_2)^2 + (V_1 - V_2)^2 + (W_1 - W_2)^2 + 3\overline{u_1'^2} + 3\overline{u_2'^2} - 6\overline{u_1' u_2'}} \tag{3.17}$$

where U, V, and W are the mean velocities in the x, y, and z directions, respectively. For isotropic turbulence $\overline{u'^2} = \overline{v'^2} = \overline{w'^2}$ is the mean-squared value of the velocity component. $\overline{u_1' u_2'} = \overline{v_1' v_2'} = \overline{w_1' w_2'}$ is the correlation between fluctuating velocities.

The velocities of the droplets at two points are closely related if the two points are close together, but become independent from each other if the two points are far apart. The correlation coefficient $\rho_{12}(r)$, describing the correlation of velocities as a function of the separation r, thus varies from 1 at a point-to-point distance $r = 0$, to 0 as $r \to \infty$. Provided the Reynolds number of the flow producing the turbulence is sufficiently large, an internal range of eddies will be developed whose velocities will be solely dependent on scale, r, and turbulent energy dissipation rate, ε. From Kolmogorov's theory of the internal range, and from experiment, it has been found (see, for example, Mathieu and Scott (2000)) that

$$\rho(\vec{r}) = \frac{\overline{u'(\vec{x})u'(\vec{x}+\vec{r})}}{\overline{u'^2}} = 1 - \frac{1.2(\varepsilon r)^{2/3}}{\overline{u'^2}} \tag{3.18}$$

Considering two droplets separated by d_{12} (for two droplets in contact) the correlation coefficient is assumed to be

$$\rho_{12} = 1 - \frac{2.4\left(\frac{\varepsilon_1+\varepsilon_2}{2}d_{12}\right)^{2/3}}{\overline{u_1'^2}+\overline{u_2'^2}} = 1 - \frac{3.6\left(\frac{\varepsilon_1+\varepsilon_2}{2}d_{12}\right)^{2/3}}{k_1+k_2} \tag{3.19}$$

where $k = \frac{3}{2}\overline{u'^2}$ is the turbulent kinetic energy. Thus the relative velocity between two droplets is obtained from

$$U_{rel} = \sqrt{(U_1-U_2)^2+(V_1-V_2)^2+(W_1-W_2)^2+2(1-\rho_{12})(k_1+k_2)} \tag{3.20}$$

3.3.2 Outcome of Collision

The binary droplet collision phenomenon is discussed in this section. The outcome of collisions can be described by three non-dimensional parameters: the collisional Weber number, the impact parameter, and the droplet size ratio (Orme, 1997; Post and Abraham, 2002; Ko and Ryou, 2005*b*).

The collisional Weber number is defined as

$$\mathrm{We}_{coll} = \frac{\rho_l U_{rel}^2 d_2}{\sigma} \tag{3.21}$$

where U_{rel} is the relative velocity of the interacting droplets and d_2 is the diameter of the smaller droplet.

The dimensional impact parameter b is defined as the distance from the center of one droplet to the relative velocity vector, $\vec{u}_{rel}$, placed on the center of the other droplet. This definition is illustrated in Figure 3.6. The non-dimensional impact parameter is calculated as

$$B = \frac{2b}{d_1 + d_2} = \sin\theta \tag{3.22}$$

where d_1 is the diameter of the larger droplet and θ is the angle between the line of centers of the droplets at the moment of impact and the relative velocity vector.

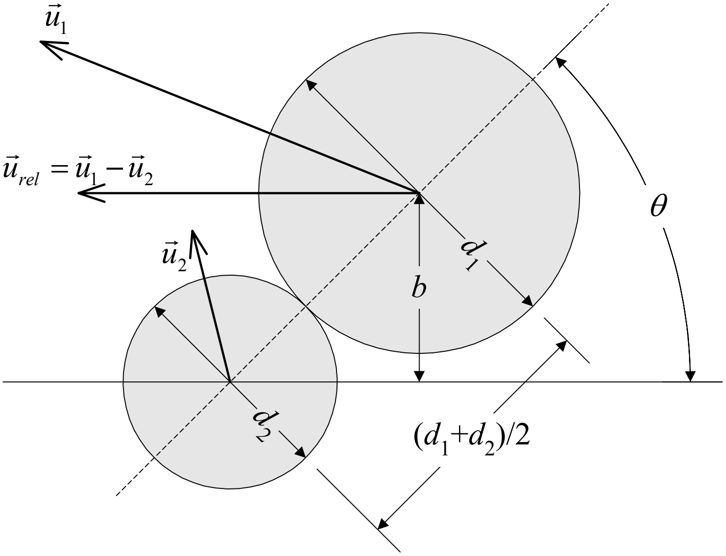

Figure 3.6: Illustration of the definition of geometric parameters of the droplet collision.

The droplet size ratio is given by

$$\gamma = \frac{d_1}{d_2} \tag{3.23}$$

The possible outcomes of collisions are illustrated in Figure 3.7. Droplet bounce will occur if there is not enough time for the gas trapped between the droplets to escape and the surfaces of the droplets do not make contact due to the intervening gas film. When the relative velocity of the droplets is higher and the collisional kinetic energy is sufficient to expel the intervening layer of gas, the droplets will coalesce. If the collisional energy exceeds the value for permanent coalescence, then temporary coalescence occurs. Temporary coalescence may result in either disruption or fragmentation. In disruption, the collision product separates into the same number of droplets which existed prior to the collision. In fragmentation, the coalesced droplet breaks up into numerous satellite droplets (Orme, 1997).

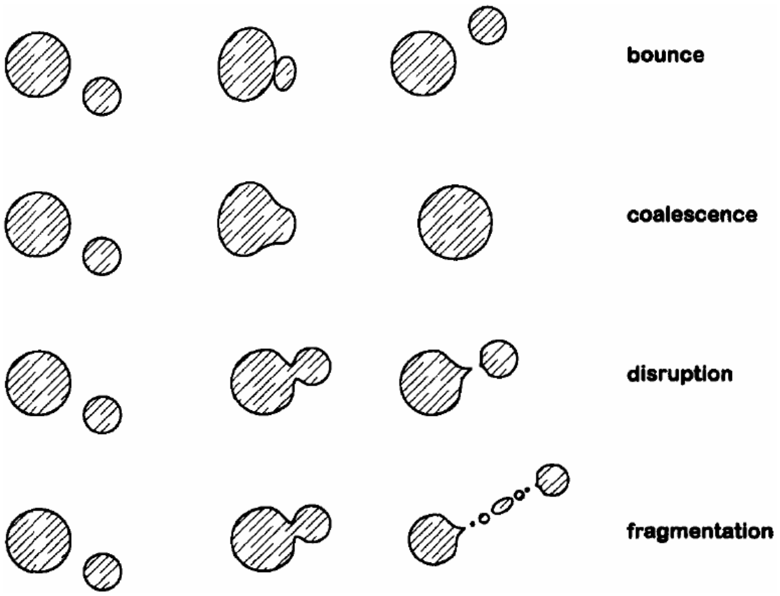

Figure 3.7: Types of collision (Orme, 1997).

Bounce affects droplet trajectory, but it does not modify droplet size. Coalescence followed by disruption does not have any significant influence on droplet size. Even if some mass transfer occurs, the droplet diameters are not changed in any observable way. However, other types of collision outcomes may influence the DSD, because the sizes of post-collision droplets are different from those of the pre-collision droplets. During fragmentation, a number of small satellite droplets are formed with the accompanying decrease in size. Fragmentation occurs when the relative velocity of colliding droplets is high. This regime could be important in high-velocity sprays, e.g. in Y-jet sprays. Coalescence results in one droplet of a larger size than that of the pre-collision droplets. Since these phenomena appear at low relative velocity, it is expected that their effect is significant in low-velocity regions of the spray where this causes an increase in droplet size.

Coalescence Efficiency

The experiment of Brazier-Smith, *et al.* (1972) showed that when two droplets of nearly equal size collide and the impact parameter B exceeds some critical value, the droplets will break up (disruption or fragmentation). The probability that a collision event will result in permanent coalescence is given by the coalescence efficiency:

$$E_{coal} = \min\left[1, \frac{4.8 f(\gamma)}{\mathrm{We}_{coll}}\right] \tag{3.24}$$

where the complex function $f(\gamma)$ is approximated by a polynomial for simplicity (Amsden, *et al.*, 1989)

$$f(\gamma) = \gamma^3 - 2.4\gamma^2 + 2.7\gamma \tag{3.25}$$

The regime boundary between coalescence and disruption or fragmentation is determined by $B^2 = E_{coal}$. Therefore, coalescence occurs if impact parameter B^2 is less than E_{coal}. Brazier-Smith, *et al.* (1972) observed droplet bounce when the equal sized water droplets collide at low relative velocity. They suggested a critical Weber number We_{coll} of 4.24 below which bouncing is possible and a bouncing efficiency determined by (Ko and Ryou, 2005*b*)

$$E_{boun} = \min\left[1, \left(\frac{\mathrm{We}_{coll}}{4.8 f(\gamma)}\right)^{1/3}\right] \tag{3.26}$$

above which, $B^2 > E_{boun}$, the bounce collision takes place.

Figure 3.8 shows the boundaries between the regimes obtained from Eqs. (3.24) and (3.26) for the collision of equal-sized droplets.

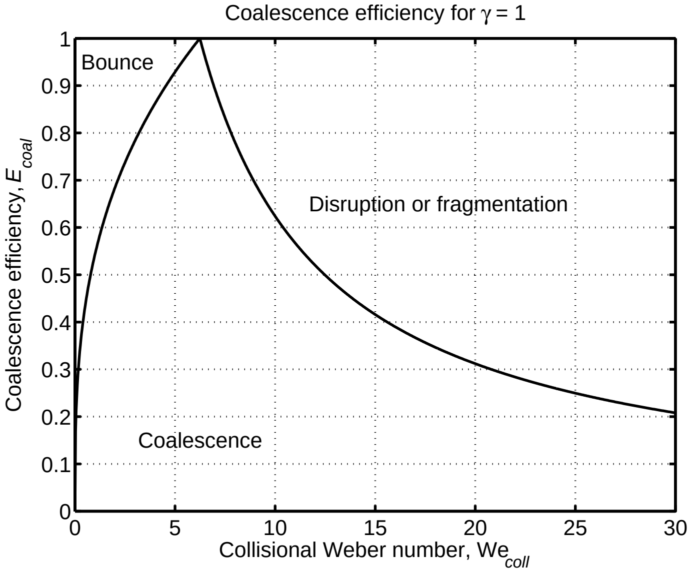

Figure 3.8: Boundaries between collision regimes for $\gamma = 1$.

Fragmentation

One possible outcome of droplet-droplet collisions is the breakup of the original droplets into smaller droplets. Georjon and Reitz (1999) proposed a model for "shattering" collisions between droplets. They assumed that after the droplets collide they form a ligament, which stretches due to the inertia of the collision. An estimation for the diameter of the droplet fragments d_{frag} is given by a correlation of Post and Abraham (2002)

$$d_{frag} = \frac{1.89\left(d_1^3 + d_2^3\right)^{1/3}}{\sqrt{2.81\,\mathrm{We}_{coll}^{2/7}\left(1+\gamma^3\right)^{2/21} + 1}} \tag{3.27}$$

Figure 3.9 shows the predicted diameter of droplet fragments as a function of the collisional Weber number for two droplets colliding. Three values of the droplet size ratio γ are presented: 1, 2, and 3. The larger the value of γ, the smaller is the diameter of fragments.

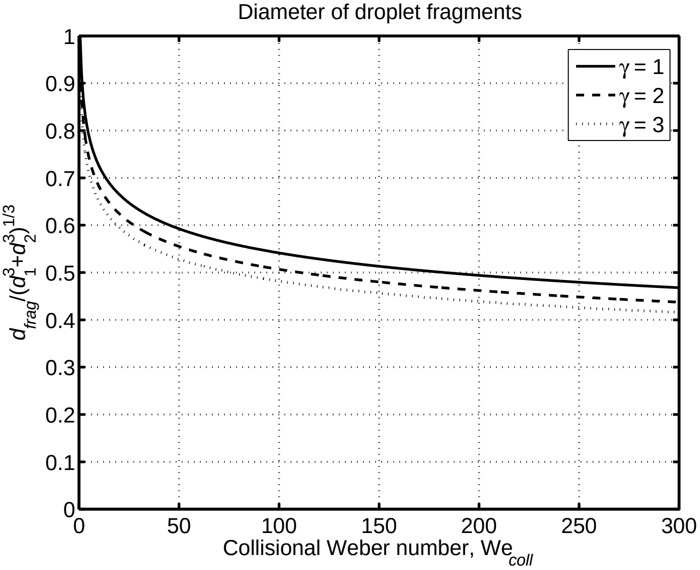

Figure 3.9: Predicted diameter of droplet fragments normalized by $\left(d_1^3 + d_2^3\right)^{1/3}$ for binary collision of two droplets for different values of γ.

One limitation of this correlation is that it is assumed that all the satellite droplets have the same size, whereas experimental works (Qian and Law, 1997; Brenn, *et al.*, 2001) indicate that the satellite droplets are usually much smaller than the parent droplets.

A composite collision outcome model that takes into account of also stretching separation, reflexive separation, and satellite droplet formation phenomena has been proposed by Ko and Ryou (2005*b*).

Composite Collision Outcome Model

The composite coalescence model, applied in the present study, takes coalescence and bounce into account, as well as fragmentation. This composite model is formulated by first using Eqs. (3.24) and (3.26) to calculate the probability of coalescence, with the Weber number and droplet size ratio known. Then Eq. (3.24) is employed to determine the probability of fragmentation as $E_{frag} = 1 - E_{coal}$. If fragmentation occurs, Eq. (3.27) is employed to determine the diameter of the droplet fragments.

Figure 3.10 shows the predicted number of post-collision droplets in the case of binary collision of droplets for different values of the droplet size ratio γ. In the bouncing regime, the number of droplets decreases with increasing Weber number, until the Weber number reaches $\mathrm{We}_{coll} = 4.8 f(\gamma)$. When the Weber number is above this value, the number of droplets increases because of increased probability of droplet fragmentation.

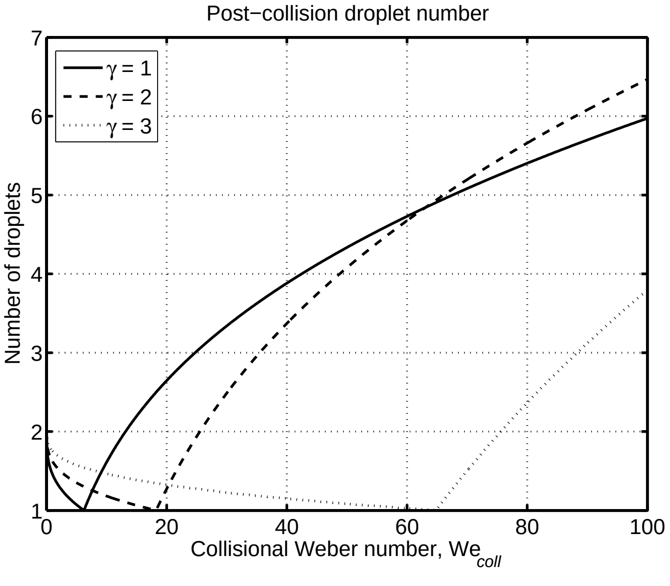

Figure 3.10: Number of post-collision droplets for binary collision of two droplets for different values of γ.

In Figure 3.11, the normalized mean diameter (d_{10} and d_{32}) is presented as function of Weber number. Over the range of low Weber numbers, the model predicts an increase of mean diameters after collision because of droplet coalescence. However, as the Weber number increases the mean diameters decrease gradually, indicating that the droplet fragmentation via collision increases with Weber number.

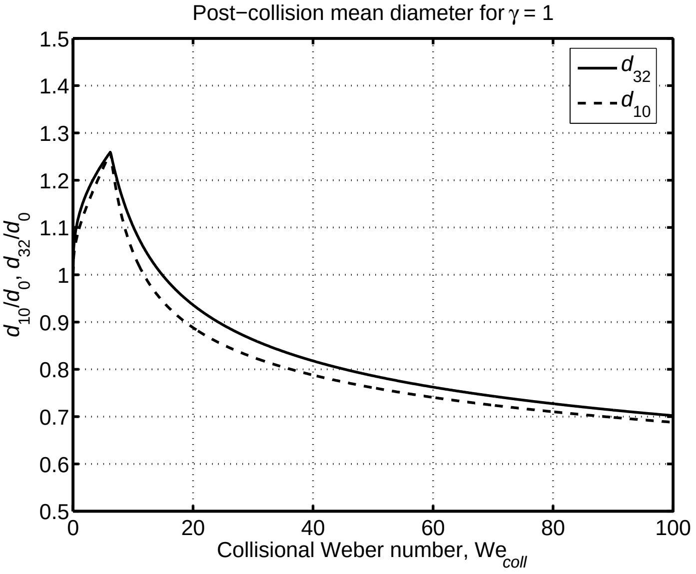

Figure 3.11: Prediction of the d_{10} and d_{32} normalized by the initial droplet diameter d_0 for the binary collision of equal-sized droplets.

Chapter 4

Experiments

4.1 Introduction

This chapter introduces the theory behind the laser based measurement techniques used, i.e. phase Doppler anemometry (PDA) and Interferometric Particle Imaging (IPI) combined with particle tracking velocimetry (PTV). The laser based measurement techniques have the advantage that they are non-intrusive and therefore do not disturb the flow.

The PDA system has a good spatial and temporal resolution and provides information in one point. Mean droplet velocity and diameter profiles are obtained by traversing the measuring device stepwise in the desired direction taking data for each point.

The combination of IPI with PTV can provide instantaneous information on droplet size and velocity in a whole plane. The disadvantage with the current technology is a low maximum droplet concentration. The maximum droplet concentration can be improved but new limitations are often introduced to the acquisition of data. The limitation can be a reduction of the field of view of the system and thereby loosing information on the large-scale flow phenomena.

In Section 4.2 a theoretical background for PDA is given.

In Section 4.3 the theory behind IPI combined with PTV is introduced, and the techniques are applied for measuring droplet sizes and velocities in a spray from a Danfoss pressure-swirl atomizer. The results are verified against PDA measurements.

In Section 4.4, sprays from Y-jet atomizers are investigated, and the effect of geometrical and operational variables is examined experimentally by using PDA.

4.2 Phase Doppler Anemometry (PDA)

4.2.1 The Laser Doppler Anemometer

Velocities of particles or droplets in fluids can be measured optically by the Doppler Effect. This method is called laser Doppler anemometry (LDA) or laser Doppler velocimetry (LDV). Some of the characteristics of LDA are:

- Point measurement, the size of the measuring volume can be from about 20 μm to several millimeters depending on optical configuration.
- Non-intrusive measurements.
- Measures remotely, typical distances from 1 mm to 2 m.
- Measures velocities in the range 0 – 1000 m/s.
- Measures one, two, or three velocity components at the same time.
- No calibration required (only measurement of angle between laser beams).

In the following a brief introduction to the principles of LDA is given. The introduction is based on material from Albrecht, *et al.* (2003) and Dantec (2003*a*). The references can be consulted for a more detailed description of LDA.

Doppler Effect

The physical principle underlying LDA and PDA for velocity measurements is the Doppler Effect, which relates the interaction of sound or light waves with a moving observer or the modulation of sound or light waves received by a stationary observer from a moving emitter. In LDA this principle is used in such a way that a laser emits plane light waves, which are transmitted from a moving emitter, the particle. Hence, the frequency or wavelength of the light received by the particle is already modulated. Since the moving particle scatters the light into space, an additional Doppler shift occurs when the scattered light is received at a stationary observer. The Doppler Effect is illustrated in Figure 4.1. Incident light with unit vector $\mathbf{e}_i$ illuminates the particle. The observed scattered light has unit vector $\mathbf{e}_s$. It can be shown that the frequency of light received at the photo detector is (Albrecht, *et al.*, 2003)

$$f_s = f_i + f_s \frac{\mathbf{U} \cdot (\mathbf{e}_s - \mathbf{e}_i)}{c} = f_i + \frac{\mathbf{U} \cdot (\mathbf{e}_s - \mathbf{e}_i)}{\lambda_i} \tag{4.1}$$

where f_i is the frequency and λ_i is the wavelength of the incident light, **U** is the velocity of the moving particle, and c is the speed of light.

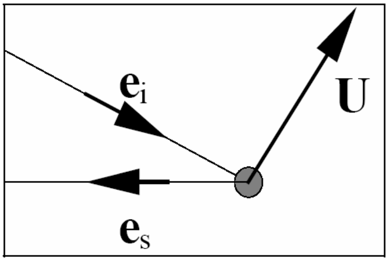

Figure 4.1: Doppler Effect for particle with velocity vector **U** in a light beam with unit vector $\mathbf{e}_i$. The scattered light is observed in the direction of unit vector $\mathbf{e}_s$ (Dantec, 2003*a*).

The second term of Eq. (4.1) contains the Doppler shift of the incident wave frequency. The Doppler shift is usually much smaller than the light frequency and thus virtually impossible to resolve directly. More frequently, the dual-beam system is used for LDA measurements. Here the moving particle is illuminated by two laser beams from different directions as shown in Figure 4.2. In this case, the Doppler frequency of the scattered light is obtained from the difference of the contributions from two incident beams:

$$f_D = f_{s,2} - f_{s,1} \tag{4.2}$$

Using Eq. (4.1) and $f_1 = f_2 = f_I$, where subscript I refer to incident light, gives

$$f_D = \frac{\mathbf{U}\cdot(\mathbf{e}_1 - \mathbf{e}_2)}{\lambda_I} \tag{4.3}$$

The Doppler shift is therefore proportional to the dot product between the velocity, **U**, and the difference between the two incident unit vectors, $\mathbf{e}_1$ and $\mathbf{e}_2$. For the velocity component perpendicular to the bisector of the two incident beams Eq. (4.3) becomes

$$f_D = \frac{2\sin(\theta/2)}{\lambda_I} u_x \tag{4.4}$$

where θ is the angle between the two incident beams.

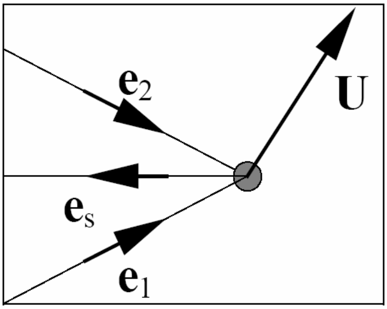

Figure 4.2: Scattering of two incoming laser beams (Dantec, 2003*a*).

The Fringe Model

There is another way to explain the signal received by the detector. The two laser beams will create an interference pattern at their intersection. The pattern will consist of planes with high light intensity separated by planes with low light intensity as shown in Figure 4.3. This pattern of light planes is called fringes. A particle passing through the fringe pattern will emit light modulated with a frequency proportional to its velocity component perpendicular to the light planes.

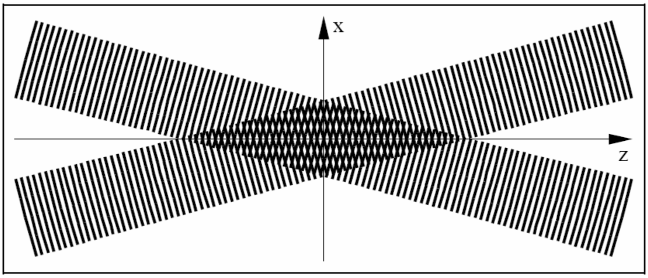

Figure 4.3: Fringes from where two coherent laser beams cross (Dantec, 2003*a*).

The distance δ_f between the fringes in a dual-beam LDA system is determined by the angle θ between the beams and the wavelength λ of the light:

$$\delta_f = \frac{\lambda}{2\sin(\theta/2)} \tag{4.5}$$

The relation between the velocity component u_x perpendicular to the fringes and the measured Doppler frequency (Doppler shift) is then simply

$$u_x = \delta_f f_D \tag{4.6}$$

Note that Eqs. (4.5) and (4.6) can be combined to Eq. (4.4).

The size of the measuring volume is an important parameter in measurements. The intensity of a laser beam has normally a Gaussian profile. The thickness d_l of the laser beam is often defined by the borders where the intensity is $1/e^2$ (= 14%) of full intensity. When a laser beam is focused by a lens with a focal length F, the minimum beam thickness called beam waist d_f is found in the focal point of the lens as

$$d_f = \frac{4}{\pi} \frac{F\lambda}{d_l} \tag{4.7}$$

The size of the region with the fringe pattern created by the two intersecting, focused laser beams can be defined in a similar way as the region bounded by the $1/e^2$-contour of the modulation depth. The measurement volume defined this way is an ellipsoid. This is illustrated in Figure 4.4.

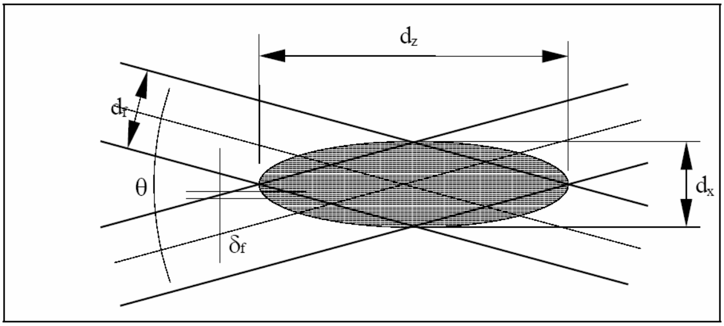

Figure 4.4: The measurement volume and its dimensions (Dantec, 2003*a*).

A coordinate system is defined with z-direction in the optical axis of the focusing lens and the x-direction in the plane formed by the two laser beams. The dimensions of the measuring volume can be expressed as

$$
\begin{aligned}
d_x &= \frac{d_f}{\cos(\theta/2)} \\
d_y &= d_f \\
d_z &= \frac{d_f}{\sin(\theta/2)}
\end{aligned}
\tag{4.8}
$$

To create a small measuring volume, the beam waist d_f should be small. Eq. (4.7) indicates that this can be obtained by using a short focal length and a large beam diameter before the lens. In some applications a beam expander is therefore used to expand the laser beam before the front lens. A short length of the measuring volume depends on having a large angle θ between the two laser beams.

It is important that the fringes have a uniform separation throughout the measuring volume. This is the case when the intersection between the two laser beams takes place at the beam waist of both beams. If the laser beams before the front lens are not parallel with the optical axis of the lens or are slightly divergent or convergent, the beam waist will not be located at the focal point of the front lens. As a consequence, the measured Doppler frequency will also depend on particle position, and as such it will no longer be directly proportional to the particle velocity.

The dual-beam LDA system has several advantages. Noteworthy is the fact that the Doppler frequency is independent of the receiver position. This implies that the observation angle and solid angle of scattered light collection may be selected for convenience according to the desired application. A typical optical setup of an LDA system operated in the backward scattering mode is shown in Figure 4.5. This so-called backscatter LDA allow for the integration of transmitting and receiving optics in a common housing. The transmitting optics consists of the laser, a beam splitter, a Bragg cell, and a transmitting lens. The receiving optics consists of an imaging lens and a photodetector (receiver) with a mask in front of it.

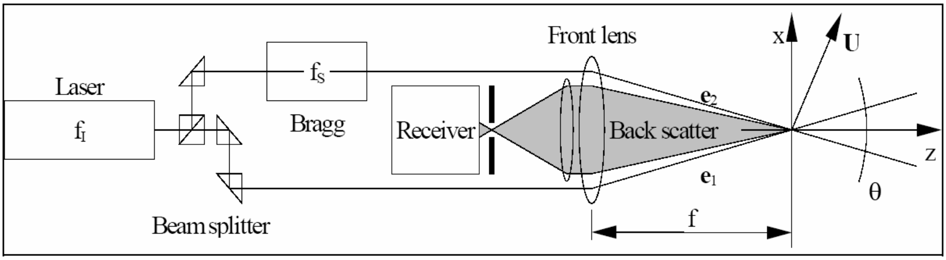

Figure 4.5: Dual-beam backscatter LDA configuration (Dantec, 2003*a*).

Bragg Cell

The Bragg cell introduce a frequency difference between the two incident beams whereby it is possible to detect the direction of particle motion in the measurement volume (see, for example, Albrecht, *et al.*, 2003). The shift in frequency for one of the laser beams causes the fringe pattern to be no longer stationary. Instead the fringe pattern is moving with a velocity equal to the fringe spacing multiplied with the Bragg cell frequency. The velocity component can therefore be found by subtracting the Bragg cell frequency f_s from the detected Doppler shift:

$$f_D = f_s + \frac{2\sin(\theta/2)}{\lambda} u_x \tag{4.9}$$

4.2.2 The Phase Doppler Anemometer

A typical optical setup of a two detector PDA system is shown in Figure 4.6. This technique determines the droplet velocity by standard fringe mode LDA (see section 4.2.1), and establishes the droplet size by measuring the phase shift of light encoded in the spatial variation of the fringes reaching two detectors after traveling paths of different lengths through the droplets (Figure 4.7). The phase shift is measured by two detectors, each looking at a spatially distinct portion of the collection lens.

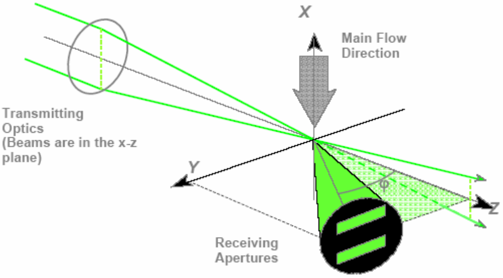

Figure 4.6: Optical arrangement of a two detector PDA system (Dantec, 2003*a*).

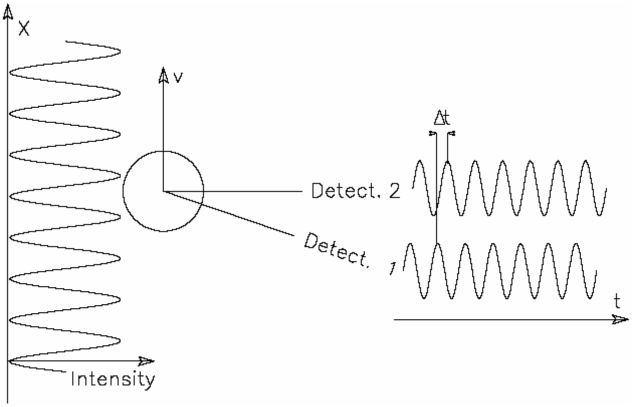

Figure 4.7: The phase shift between two detectors (Dantec, 2003*a*).

By recording the Doppler signals from the two detectors the phase shift, $\Delta\Phi_{12}$, is determined from the time lag, Δt, between the two signals as

$$\Delta\Phi_{12} = 2\pi f_D \Delta t \tag{4.10}$$

where f_D is the Doppler frequency. The measured phase shift is related linearly to the droplet diameter, d_p, by a so-called phase factor, F_Φ, which is determined by the geometry of the optical arrangement of the PDA system, the refractive index between the droplet and the medium, the wavelength of the laser light, and the mechanism of light scattering (reflection or refraction):

$$d_p = F_\Phi \Delta\Phi_{12} \tag{4.11}$$

Only a phase shift between zero and 2π (= 360°) can be distinguished with a two detector PDA system. To eliminate the ambiguity associated with spatial shifts of over 2π, an additional detector may be added.

The specific instrument employed here is a three-detector PDA system.

4.2.3 Operating Conditions

A PDA system from Dantec Dynamics is used in the present study. The light source is a multi-line argon ion air-cooled laser (Spectra-Physics Model 177) operating at 488 nm and 514.5 nm with approximately output of 300 mW. In the transmitter unit, the laser light is color separated (514.5 nm for the axial component and 488 nm for the radial component) and the two beams are split into four and coupled into single mode glass fibers, which conducts them to the transmitting optics unit. One beam of each color is frequency shifted by 40 MHz through a Bragg cell for the purpose of direction recognition of the velocities. The polarization direction is adjusted perpendicular to the scattering plane. The scattering light is collected by a receiving lens where it is coupled into multimode fibers. After color separation by filters, the light reaches the photomultipliers and is transformed into electrical signals. The signals are processed by a covariance-processor (Dantec 58N80) of the PDA system. With this processor, the frequency and the phase shift of the filtered and amplified signals are determined. The signals are processed if the signal-to-noise of the burst of a droplet fulfills a minimum criterion.

4.3 Interferometric Particle Imaging (IPI) and Particle Tracking Velocimetry (PTV)[*]

Interferometric Particle Imaging (IPI) is a relatively new technique for determining the diameter of transparent spherical particles from out-of-focus images, though its origins can be traced to a number of sources (König, *et al.*, 1986; Glover, *et al.*, 1995). The strength of the IPI technique lies in its ability to measure the instantaneous size and velocity of spatially distributed droplets.

4.3.1 Interferometric Particle Imaging (IPI)

In the focused field the incident light scattered by a transparent spherical particle produces two glare points (as seen from the receiver) on the particle's surface. According to geometric optics, one glare point represents the reflected ray, the other the refracted ray (Figure 4.8). The existence of both glare points is contingent on the light scattering properties of the particle-medium and the off-axis angle of the receiver. In the out-of-focus field the scattered light from the glare points interferes to produce measurable fringes on a CCD array, as seen in Figure 4.9. The particle size can then be directly determined from the fringe number and spacing. The velocity of each particle is then separately determined using particle-tracking (PTV) techniques.

---

[*] Partly based on Madsen, *et al.* (2003).

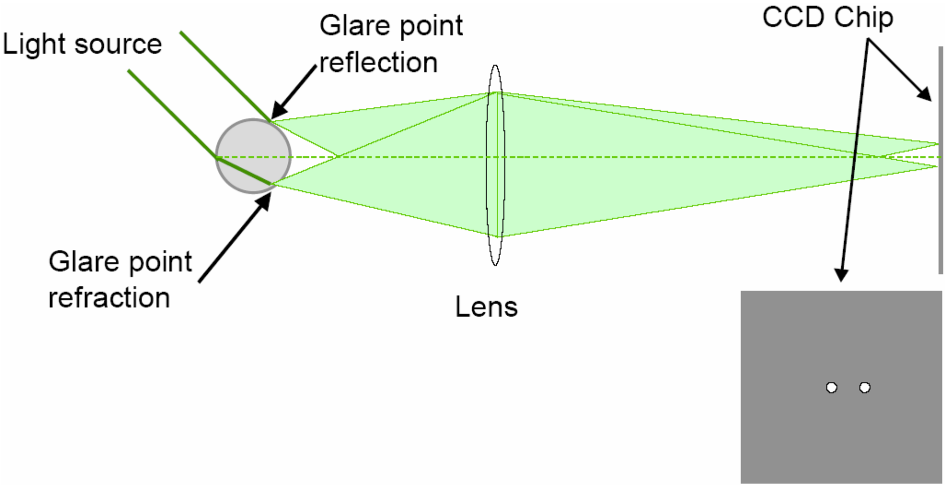

Figure 4.8: Schematic of the optical paths of reflection and refraction (Dantec, 2003*b*).

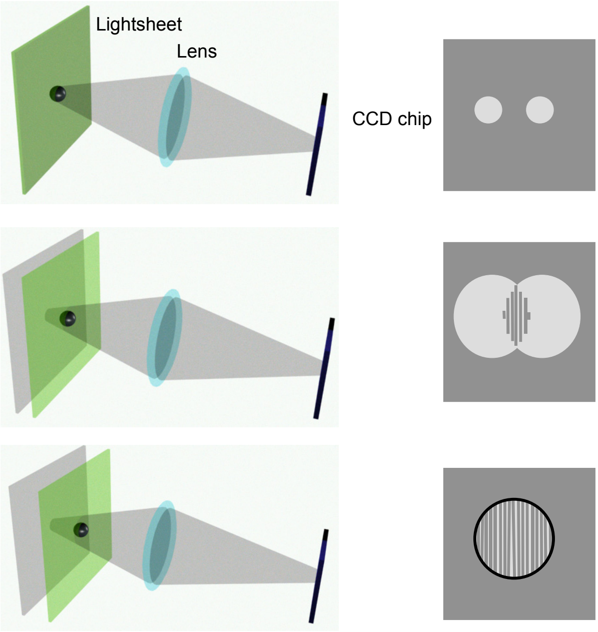

Figure 4.9: Effect of moving the focus plane of the camera away from the lightsheet on the captured particle image (Dantec, 2003*b*).

The IPI technique works best in scattering regimes where the intensities of the reflected and refracted light are relatively close. In the case of water droplets with parallel polarization the optimum angle is often stated as 68°, even though 90°, or orthogonal to the lightsheet, is a better angle. In practical terms, this orientation affords the best viewing of out-of-focus images. The size of the out-of-focused particle image is independent of particle size, but rather on particle position in the light sheet and the amount of user applied de-focusing.

Once the images are acquired, the diameter of a particle can be determined by measuring the size of the out-of-focus particle images and determining the fringe frequency, eventually resulting with a fringe count. The relationship between the number of fringes, N_f, and particle diameter, d_p, is linear, and is defined by Hesselbacher, *et al.* (1991) as:

$$N_f = \kappa d_p \tag{4.12}$$

where for a relative refractive index $m > 1$:

$$\kappa = \frac{\sin^{-1}\left(d_a/2z\right)}{\lambda}\left[\cos\left(\phi/2\right)+\frac{m\sin\left(\phi/2\right)}{\sqrt{m^2+1-2m\cos\left(\phi/2\right)}}\right] \tag{4.13}$$

and for $m < 1$ (Maeda, *et al.*, 2000):

$$\kappa = \frac{\sin^{-1}\left(d_a/2z\right)}{\lambda}\left[m\cos\left(\phi/2\right)-\frac{m\sin\left(\phi/2\right)}{\sqrt{m^2+1-2m\cos\left(\phi/2\right)}}\right] \tag{4.14}$$

where d_a is the aperture diameter, z is the distance to the lightsheet, λ is the wavelength, and ϕ is the off-axis angle.

The dynamic range of the measurement is dependent on a number of factors: the camera resolution, the size of the out-of-focus images, the laser intensity, the scattering angle and the properties of the particle and medium. As indicated by Damaschke, *et al.* (2002), the smallest measurable particle is defined by a fringe count of unity. This can be directly determined from Eq. (4.12). Increasing the magnification by reducing the distance to the lightsheet will reduce this value. The generally accepted minimum diameter that can be measured is 5-8 microns. The maximum particle size that can be measured will depend on the size of the out-of-focus particle image, the optic configuration, and the camera resolution.

There is a trade-off between de-focusing, which increases the size of the out-of-focus particle image, and image contrast. The larger the image, the more fringes can be defined, but resulting with a lower signal-to-noise ratio. The Nyquist Criteria requires that at least two pixels define a fringe. In practice, fringes exhibit gradients and are not perfectly straight, so a more reasonable requirement is three or four pixels per fringe. A representative image of fringes is shown in Figure 4.10. Note the range of fringes present; from approx 2 to 30 fringes are present.

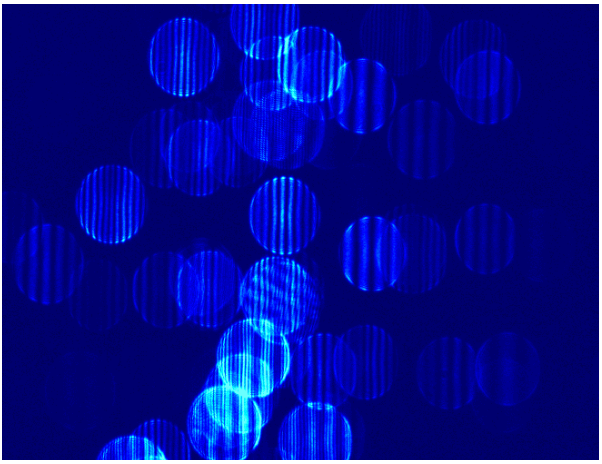

Figure 4.10: Out-of-focus image showing fringes.

4.3.2 Experimental setup

A series of measurements were conducted on a pressure-swirl atomizer. A Danfoss oil nozzle type OD was chosen because this nozzle series can be used in most types of oil burners for domestic heating. The capacity of the chosen nozzle is 0.75 gal/h at an atomization pressure of 700 kPa in test oil with a viscosity of 3.4 mm^2/s and a density of 820 kg/m^3. The spray angle is specified to 80° and the spray pattern is specified as solid. The nozzle was mounted in a test rig in such a way that the spray propagated downwards. The test rig consisted of a pump, a flow meter and a barometer. The nozzle was operated with tap water at atomization pressures ranging from 700 to 850 kPa. Here only results obtained with an atomization pressure of 850 kPa is presented. At this pressure the water flow rate was 3.2 L/h.

The droplet size and velocity of the produced spray was obtained using IPI and PTV techniques. The experimental setup consisted of a Dantec FlowMap Particle Sizer (FPS) system with a laser and two cameras. Using a beam splitter the cameras were placed orthogonal to one another and directed onto a common viewing area at a right angle to the light sheet, as shown in Figure 4.11. The laser source was a double-pulsed Nd:YAG laser at 532 nm in wavelength with a power of 100 mJ, repetition frequency of 15 Hz, and a laser sheet thickness of about 1.0 mm. The laser light was polarized perpendicular to the laser sheet. The cameras used were Kodak MegaPlus ES1.0 digital CCD cameras with 1008 × 1016 pixels. For the focused camera a 60 mm objective lens was used, whereas for the de-focused camera both a 60 mm and a 105 mm lens (with PK-11A extension tube attached) were used. The size of measurement areas were approximately 25 × 25 mm^2 and 10 × 10 mm^2, respectively. To measure velocity, double images were acquired and particle tracking carried out on the focused images.

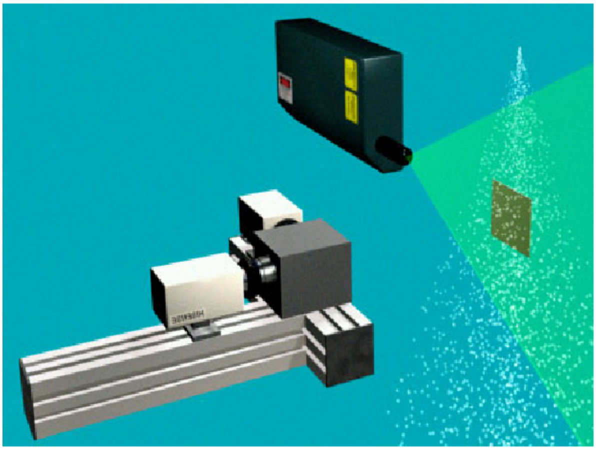

Figure 4.11: IPI measurement configuration with laser, two cameras, beam splitter and spray.

The location of the measurement planes in the spray were defined by the axial distance from the nozzle (z) and the radius (y) according to Figure 4.12, with the origin defined as the exit orifice of the nozzle. The 60 mm lens was used near the edge of the spray where it is diluted. Due to the smaller measurement area with the 105 mm lens, this lens was used in regions with a higher concentration of droplets. It was also tried to conduct measurements in the centre of the spray, but here the droplet concentration was too high and thus overlap between droplets makes the measurement difficult. Figure 4.12 also shows locations of PDA measurement points. All measurements were carried out in a vertical plane at x = 0.

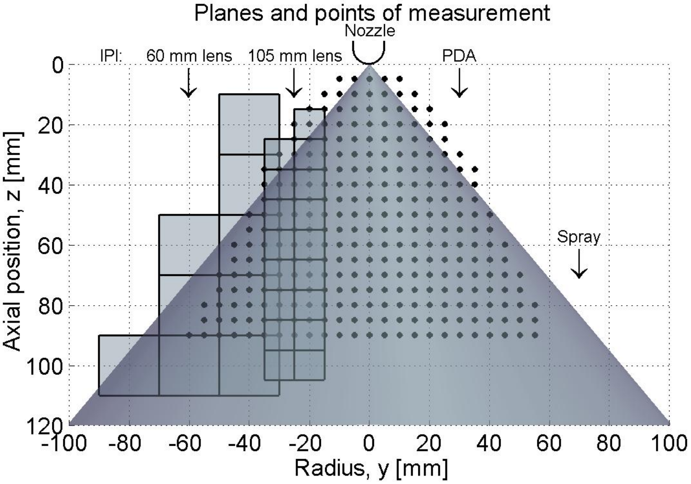

Figure 4.12: Location of IPI measuring planes and PDA measuring points.

For comparison, the droplet size and velocity were also measured using Phase Doppler Anemometry (PDA). The measurements were carried out using a 2D PDA from Dantec Dynamics. The system is described in Section 4.2.3. The measurements were conducted with a 30° scattering angle in refraction mode. The focal lengths of the transmitting and receiving lenses were 161.8 mm and 400 mm respectively. This setup made it possible to measure droplets within the range of diameters of 1 – 110 μm. The measurement volume had a length of 0.8 mm and a diameter of 0.1 mm. The locations of measuring points are shown in Figure 4.12. For each measuring point a sampling time of 120 seconds were used.

4.3.3 Results

In this section results are given for both PDA and IPI measurements of the same spray. PDA measurements were conducted both before and after IPI measurements to ensure consistency in the data.

PDA results

The contour plots in Figure 4.13 and Figure 4.14 show the length mean diameter, D_{10}, and the Sauter mean diameter (SMD), D_{32}, obtained from the PDA measurements, and the vector plot in Figure 4.15 represents mean velocity. The distributions of the two mean diameters are nearly identical in the spray where the smallest mean droplet diameters are found in the centre of the spray and as the radius increases the mean diameter increases. The d_{10} ranges from 9.5 μm to 68 μm whereas SMD ranges from 16.7 μm to 72 μm. In the vector plot, the highest axial and radial velocities are found near the nozzle with maximums of 17.2 and 14.4 m/s respectively. From the PDA results, it can be concluded that the spray is nearly symmetrical around the nozzle centre axis.

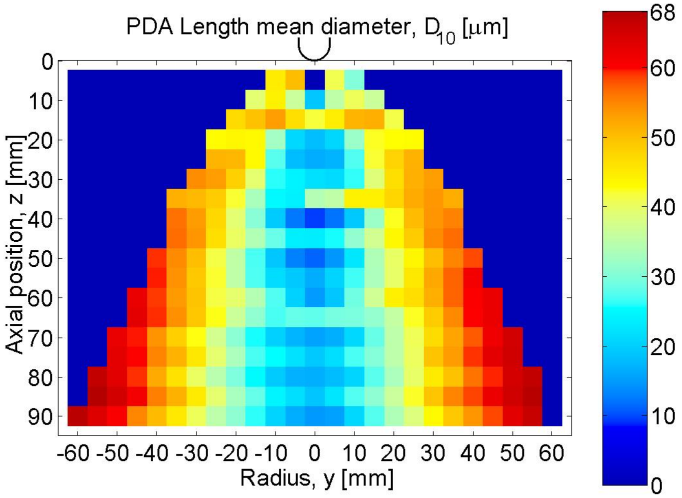

Figure 4.13: PDA length mean diameter, D_{10}.

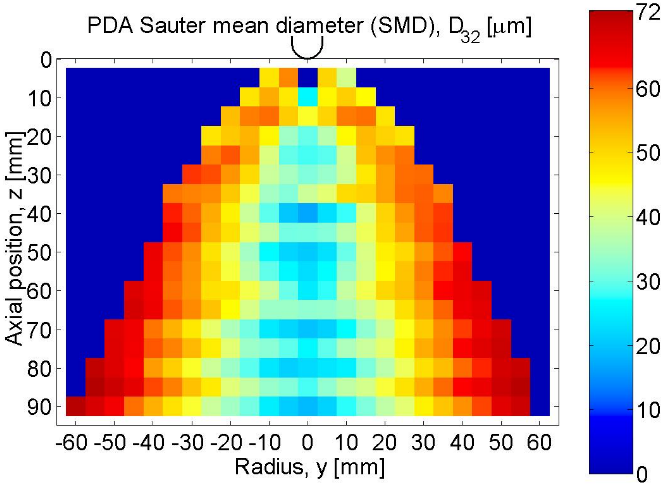

Figure 4.14: PDA Sauter mean diameter (SMD), D_{32}.

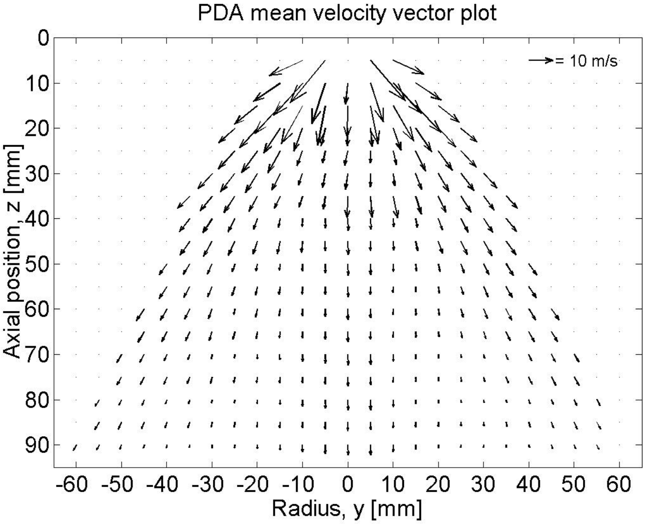

Figure 4.15: PDA 2D velocity vector plot.

IPI results

At each position the image raw image data was processed to produce a velocity and size map, as shown in Figure 4.16. Roughly 60% of the particles detected could be validated. 100 double images were then processed at each position and then averaged. The resulting data sets were then ensemble averaged to create the contour images in Figure 4.17 – Figure 4.19.

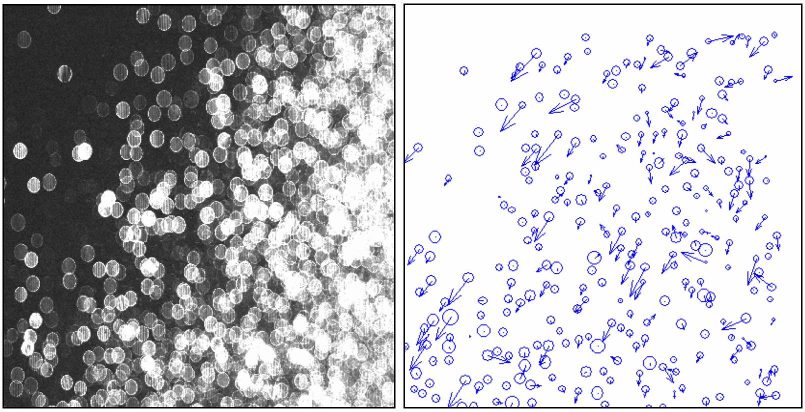

Figure 4.16: Instantaneous raw image and corresponding processed result showing relative particle size and velocity. (Position of center: y = 40 mm and z = 60 mm, Image area: 25x25 mm^2).

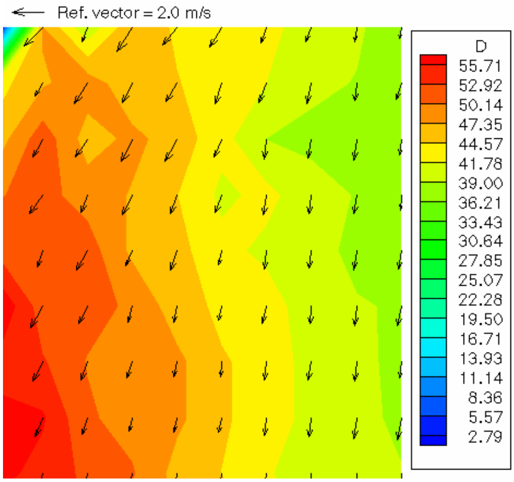

Figure 4.17: Ensemble averaged mean diameter and velocity at y = 40 mm and z = 60 mm.

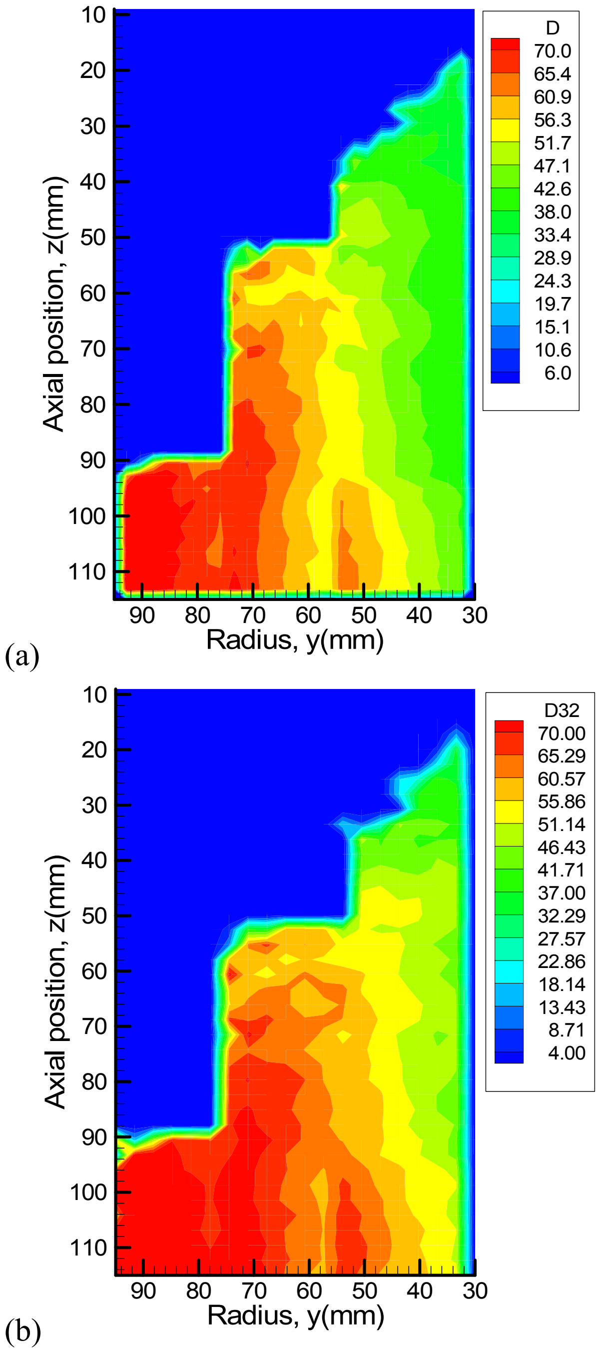

Figure 4.18: Ensemble averaged contour plot of (a) D_{10} and (b) D_{32}.

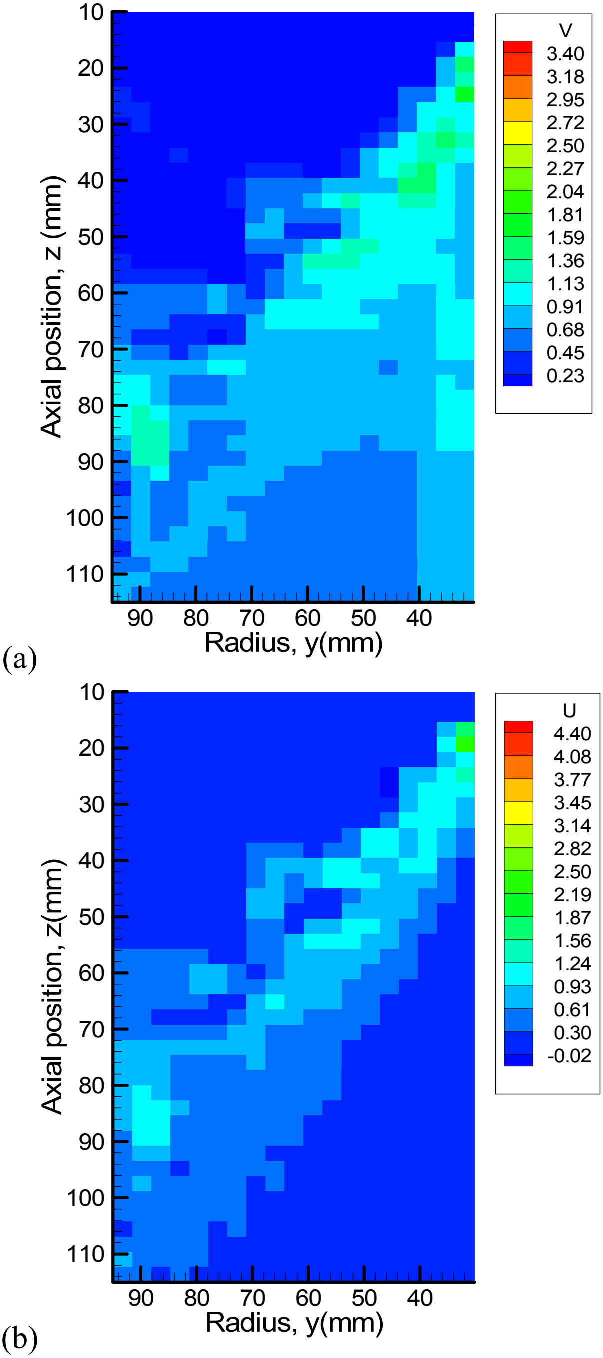

Figure 4.19: Contour plots of (a) mean axial and (b) mean radial velocity.

A comparison of mean diameters (D_{10} and D_{32}) at different axial positions obtained by IPI and PDA is shown in Figure 4.20 and Figure 4.21. The IPI yields smaller mean diameters than those indicated by PDA. These discrepancies arise from the two different methods of sampling employed by the measuring techniques. IPI employs *spatial sampling*, which describes the instantaneous measurement of droplets contained within a volume. PDA employs *temporal sampling*, which describes the measurement of droplets that pass through a fixed area during a specific time interval, with each droplet individually counted. With a pressure-swirl atomizer, the smaller droplets in the spray decelerate more rapidly than the larger droplets, and this leads to a high concentration of small droplets downstream of the atomizer. Thus, spatial sampling yields mean diameters smaller than those indicated by temporal sampling. Theoretically, if all droplets in the spray were moving at the same velocity, the results obtained by both methods should be the same.

A spatial DSD may be converted into a temporal distribution by multiplying the number of droplets of a given velocity by that velocity (Lefebvre, 1989), or temporal distribution may be converted into a spatial distribution by dividing by velocity. Which sampling method is best depends on the application. However spatial sampling might be advantageous in combustion applications, where ignition and burning rates are dependent on the instantaneous droplet population within a given volume.

The mean axial and radial velocities are presented in Figure 4.22 and Figure 4.23, respectively. It is seen that the two measurement techniques yield different velocities and the difference is largest at the axial position of $z = 50$ mm. As expected, the velocities follow the trend for the mean diameters with generally larger values from the PDA measurements, except for the axial velocity at $z = 80$ mm.

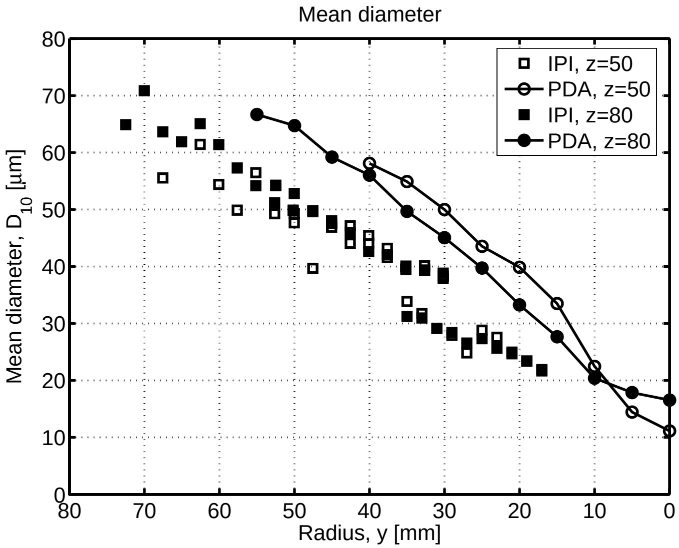

Figure 4.20: Comparison of length mean diameter, D_{10}, at different axial positions obtained from IPI and PDA.

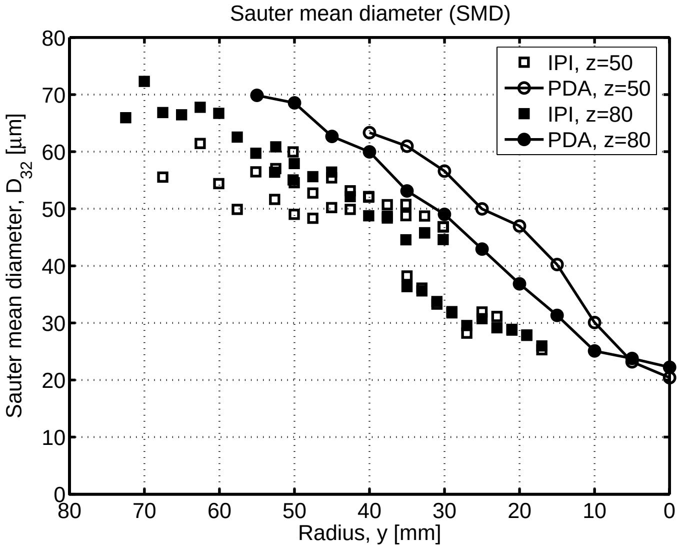

Figure 4.21: Comparison of SMD, D_{32}, at different axial positions obtained from IPI and PDA.

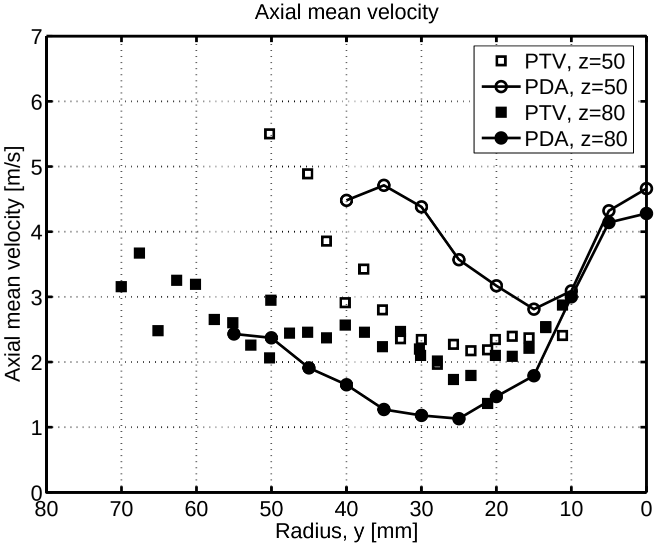

Figure 4.22: Comparison of mean axial velocity at different axial positions from PTV and PDA.

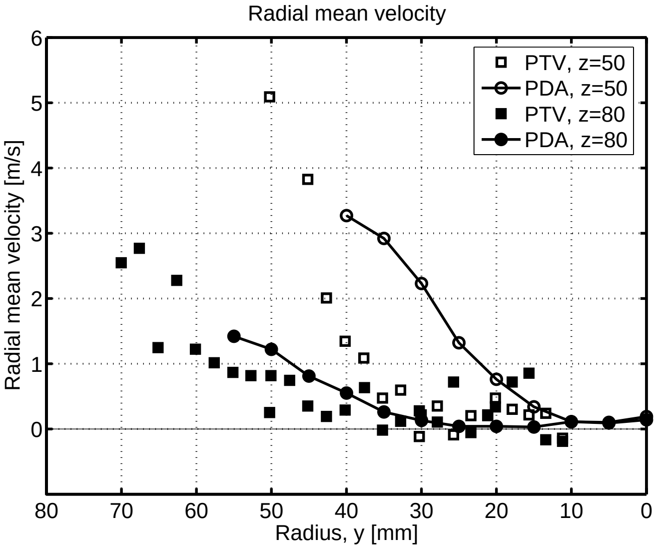

Figure 4.23: Comparison of mean radial velocity at different axial positions from PTV and PDA.

4.3.4 Summary

Spray measurements have been carried out using the IPI technique for determining the size of droplets, and using particle tracking for determining the velocity of each droplet. With different focal length optics for the de-focused camera, the IPI technique was adapted to the dilute part near the edge of the spray and to the more dense part closer to the centre axis. At the centre of the spray the concentration of droplets was too high and thus the resulting overlap reduced the validation. A solution to this problem is to magnify or reduce the measurement volume, thus spreading the particles farther apart, decreasing the overlap.

The IPI measurements have been compared to PDA measurements conducted on the same spray. In shape and trends the data acquired with IPI and PDA is very similar, however the comparison of mean diameters revealed that IPI yields smaller values than those measured by PDA. This discrepancy was expected due to the different sampling methods employed by the two measuring techniques.

Measurements with IPI have shown that the technique can be used effectively to map the spatial structure of a spray. Averaging many images revealed a consistent and repeatable structure. Even with the limitations of droplet concentration, the results show a marked improvement in spatial information over the PDA.

4.4 Experimental Characterization of Y-jet Atomizers

Y-jet atomizers are extensively used in oil fired utility boilers. Together with the burner aerodynamics, the atomizers represent the core of the combustion system and their good performance plays a major role to keep a low level of pollutant formation and to maintain the combustion efficiency as high as possible.

In this section, sprays from large-capacity Y-jet atomizers are investigated, and the effects of different design parameters and the loads are examined experimentally by using PDA. In what follows, the experimental setup and conditions will be presented, followed by the results.

4.4.1 Description of the Experiments

According to the requirement of oil fired boilers, nine single-hole Y-jet nozzles were designed. A schematic of the water/air Y-type atomizer used in this work is shown in Figure 4.24. The atomizer dimensions were calculated using the guidelines of Mullinger and Chigier (1974). The most important dimensions of the Y-jet nozzles are listed in Table 4.1, where D_a, D_f, and D_m represent the diameters of the air-injection orifice, the liquid-injection orifice, and the mixing chamber, respectively, and L_m represents the length of the mixing chamber. The liquid to mixing chamber angle θ was constant 60° throughout the experiments. The diameter of the mixing chamber was also constant D_m = 3.7 mm throughout all of the experiments.

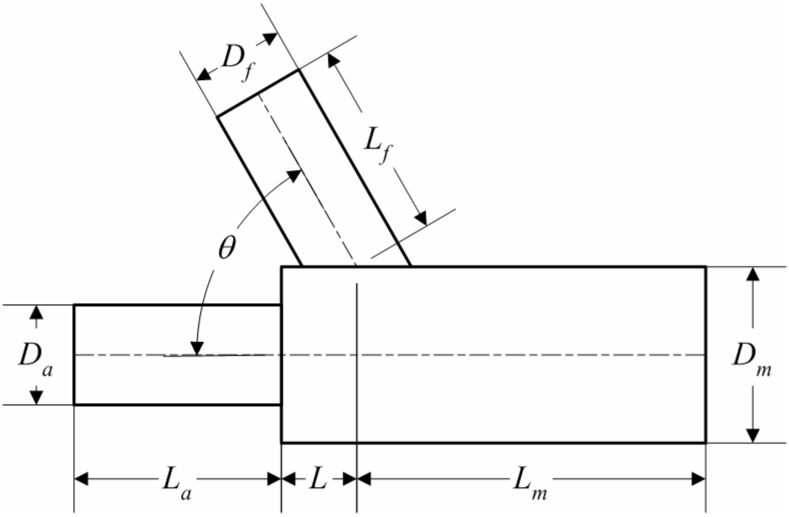

Figure 4.24: Y-jet atomizer.

Table 4.1: Dimensions of the Y-jet atomizers tested.

Nozzle No.	D_a [mm]	D_f [mm]	D_m [mm]	L_m [mm]	D_a/D_f	D_m/D_a	L_m/D_m
1	2.6	1.7	3.7	7.4	1.5	1.4	2
2	2.3	1.9	3.7	7.4	1.2	1.6	2
3	2.1	2.0	3.7	7.4	1.1	1.8	2
4	2.6	1.7	3.7	14.8	1.5	1.4	4
5	2.3	1.9	3.7	14.8	1.2	1.6	4
6	2.1	2.0	3.7	14.8	1.1	1.8	4
7	2.6	1.7	3.7	22.2	1.5	1.4	6
8	2.3	1.9	3.7	22.2	1.2	1.6	6
9	2.1	2.0	3.7	22.2	1.1	1.8	6

Compressed air and tap water were used to supply the gas-liquid spray system. The capacity of the designed atomizers is 190 kg/h. Experiments were performed with liquid mass flow rates of 76, 133, and 190 kg/h, and a ratio between the atomization air to the liquid flow rate (mass loading ratio $MLR = \dot{m}_g / \dot{m}_l$) of 3.75%, 5.00%, and 6.25%.

The test apparatus is schematically shown in Figure 4.25. It consisted of a Y-jet atomizer, as described earlier, positioned in the vertical direction with its tip pointed downward. Air was injected with a compressor and a centrifugal pump was used to supply the water. Both air and water flow rates were measured by float flow meters. Two manometers were also used to measure the gauge pressure for both air and water flows. The water droplets were collected by an open tank and then drained out.

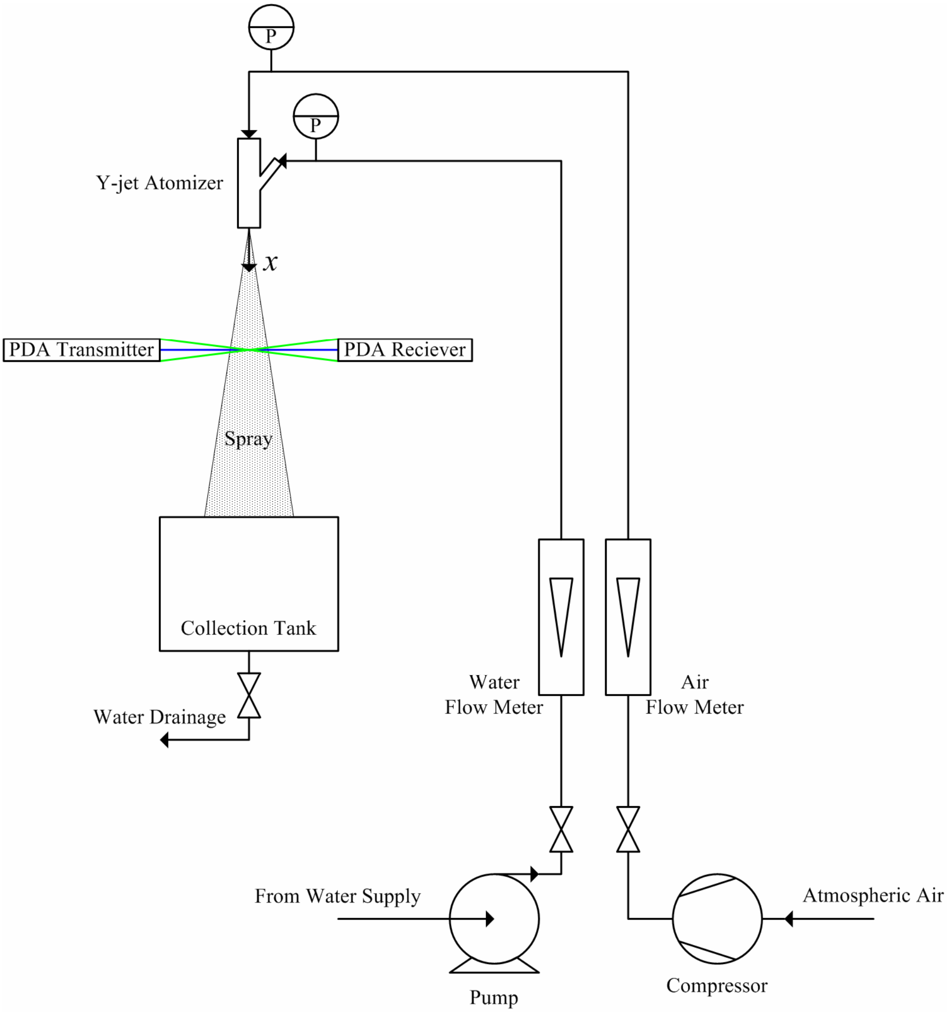

Figure 4.25: Schematic of experimental setup.

A two-component PDA system, from Dantec Dynamics, was used for the simultaneous measurements of droplet sizes and velocities. The four beams were focused by a transmitting lens with a focal length of 400 mm and a measurement volume was formed, which was around 190 µm in diameter and 4 mm in length. The receiving optics unit was mounted at a 70° scattering angle from the optical axis (see Figure 4.26), where the scattering of light by refraction is in the dominant mode and yields a linear relation of droplets size and phase between the photodetectors over the detectable range of the instrument. A receiving lens with a focal length of 300 mm was used in the present configuration, covering a droplet size range extending to 189 µm. The PDA transmitting and receiving optics were mounted on a three-dimensional traversing mechanism and the atomizer was fixed.

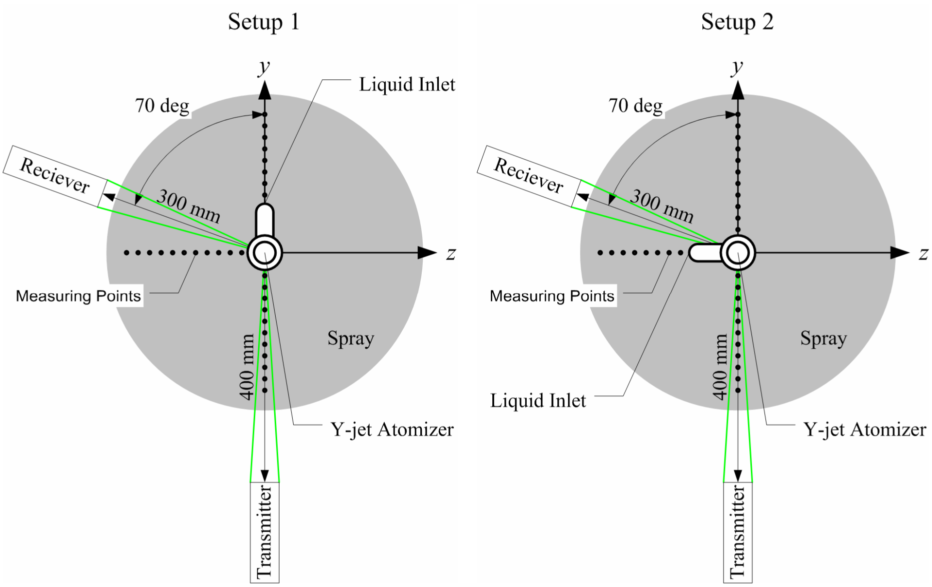

Figure 4.26: Optical arrangement of the PDA system, (left) Setup 1, (right) Setup 2.

4.4.2 Experimental Investigations

The droplet size and velocity distributions were measured at up to 25 different locations along the radial direction *r* at the cross sections located at the spray axial locations of x = 110, 150 and 190 mm, respectively. The coordinate *x* has its origin located at the nozzle exit, pointing to the downstream direction of the flow.

Three basic investigations were made during the experiments:

- First, measurements were done with the purpose to examine velocity and mean diameter symmetry of the spray.
- The effect of geometrical dimensions (D_a/D_f and L_m/D_m) was examined under the same liquid flow rate and mass loading ratio.
- The effect of liquid flow rate and mass loading ratio was examined for each atomizer in Table 4.1.

4.4.3 Spray Symmetry Assessment

First, measurements were made to examine the spray symmetry along one of the spray's radial direction *y* and its orthogonal direction *z* at the spray axial location of x = 150 mm for the water flow rate of 133 kg/h and the *MLR* of 5.00% for nozzle No. 4 in Table 4.1. Figure 4.27 and Figure 4.28 show the mean diameters (d_{32} and d_{10}) of droplets measured along the two orthogonal directions in Setup 1 and Setup 2 (see Figure 4.26), respectively. In both Setups, the variations of the mean diameters are asymmetric about the spray centerline *x*. From comparison it can be seen that the arithmetic mean (d_{10}) is less symmetrical than the SMD (d_{32}). It is clear that the SMD increases from the spray central region to the periphery. This increase is also seen in $+y$ direction for the arithmetic mean. In $-y$ and $-z$ directions, which represent the part of the spray where the laser beam blockage by the spray is low, the arithmetic mean is relatively low for both setups and the distributions are very flat.

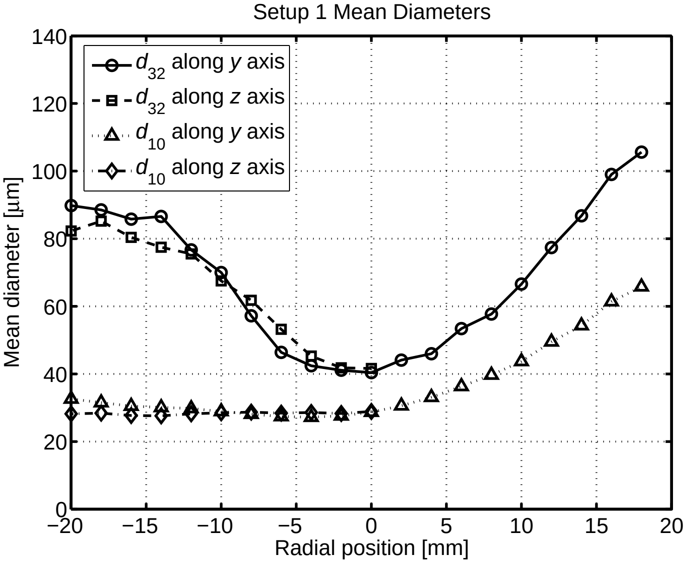

Figure 4.27: Distribution of d_{32} and d_{10} along two orthogonal directions y and z at $x = 150$ mm in Setup 1.

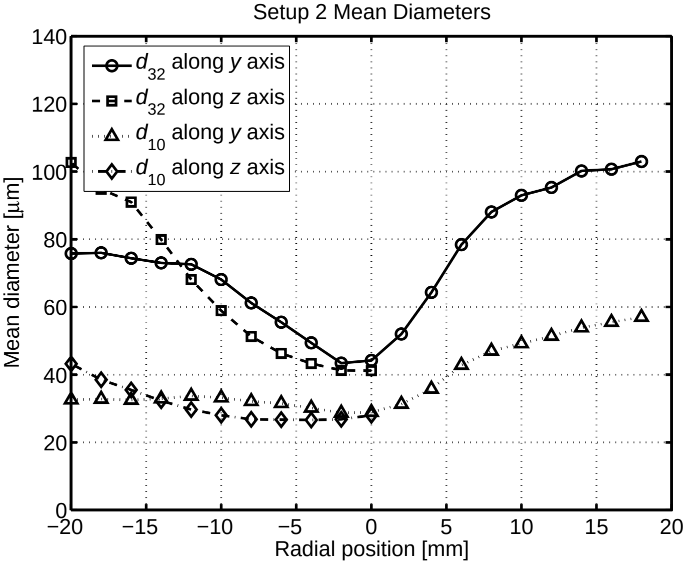

Figure 4.28: Distribution of d_{32} and d_{10} along two orthogonal directions y and z at $x = 150$ mm in Setup 2.

Asymmetry arises from the fundamental asymmetry of the Y-jet configuration itself. In Figure 4.27, the asymmetry is namely in the direction along the *y* axis, which is the plane drawn through the liquid and air inlets, see Setup 1 in Figure 4.26. On the side of the liquid inlet to the mixing chamber (+*y*), the mean diameters increase with a higher gradient than on the opposite side of the spray (–*y*). This trend is also seen in the –*z* direction for Setup 2 in Figure 4.28. This result on spatial variation confirms the Jedelsky, *et al.* (2003) observations for similar Y-jet sprays.

As shown in Figure 4.29, the measured data yield similar values of the droplet SMD profile on the side of the liquid inlet in both Setups. Figure 4.29 also indicates that the arithmetic mean diameter profiles are not the same. As a next step it is necessary to pay attention to the area where the transmitting and receiving light have to pass through the dense spray. This effect can be seen at the +*y* direction in both Setups. Here the transmitted light has to pass through the dense spray so that the laser beams are scattered by the cloud of droplets. This obscuration causes systematic errors in the measurements of mean diameters, because the small droplets do not generate signals, and especially the arithmetic mean diameters in the +*y* direction are increased compared to the –*y* and –*z* directions.

In the plane perpendicular to the plane drawn through the liquid and air inlets, the spray should be more symmetrical. The asymmetry in this plane seen along the *y* axis in Figure 4.28 may be attributed to the obscuration effect described above. The radial profiles of the mean diameters on the side perpendicular to the liquid inlet in Figure 4.30 represent the laser entrance where the obscuration by the spray is low. As shown, the profiles are very similar for both Setups.

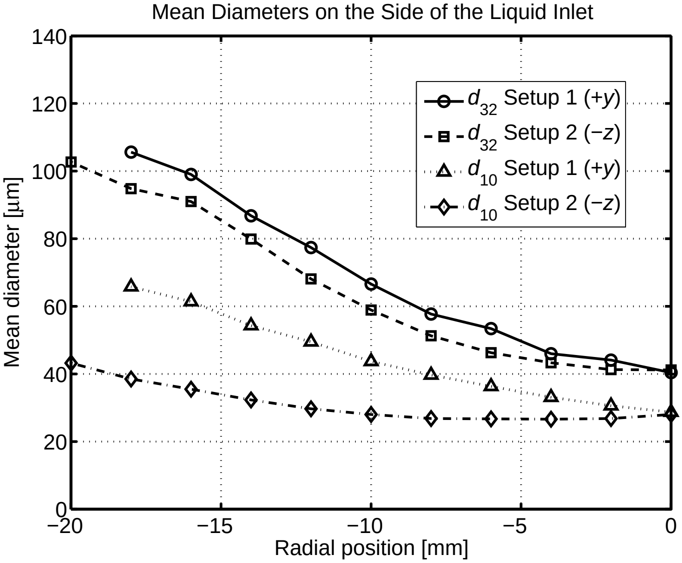

Figure 4.29: Distribution of d_{32} and d_{10} on the side of the liquid inlet in the +*y* direction in Setup 1 and the –*z* direction in Setup 2.

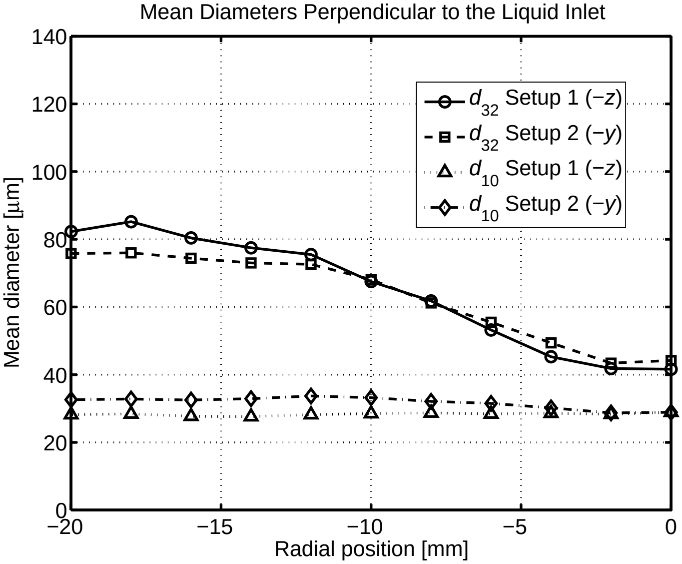

Figure 4.30: Distribution of d_{32} and d_{10} perpendicular to the liquid inlet in the –*z* direction in Setup 1 and the –*y* direction in Setup 2.

The variations of the arithmetic mean axial velocities of droplets in Setup 1 and Setup 2, shown in Figure 4.31 and Figure 4.32 respectively, are nearly symmetric about the spray axis. From comparison with the mean diameter profiles it can be seen that the axial mean velocity is less affected by the obscuration effect and the asymmetry of the Y-jet atomizer itself. The small differences between Setup 1 and Setup 2 may be attributed to the fact that the nozzle positions might not be the same before and after it was rotated 90° during the measurements, although much attention was paid to it. It is seen that the mean velocity reaches a maximum value at the spray centerline, and decreases toward the spray edges as the spray spreads out. The velocities exhibit a typical Gaussian-type variation, similar to those observed for sprays formed from annular sheet breakup (Lavergne, *et al.*, 1993; Li and Shen, 1999).

From the measurements it can be concluded that an asymmetry in mean diameters is seen due to the impact of liquid and air stream in the mixing chamber which is projected also outside the atomizer. Moreover, the obscuration by the dense spray has an effect on especially the arithmetic mean diameter, as the small droplets are not properly counted.

In the following sections, the radial profiles along the *y* axis in Setup 1 are presented. In this direction the effect of obscuration on mean axial velocity and SMD is low.

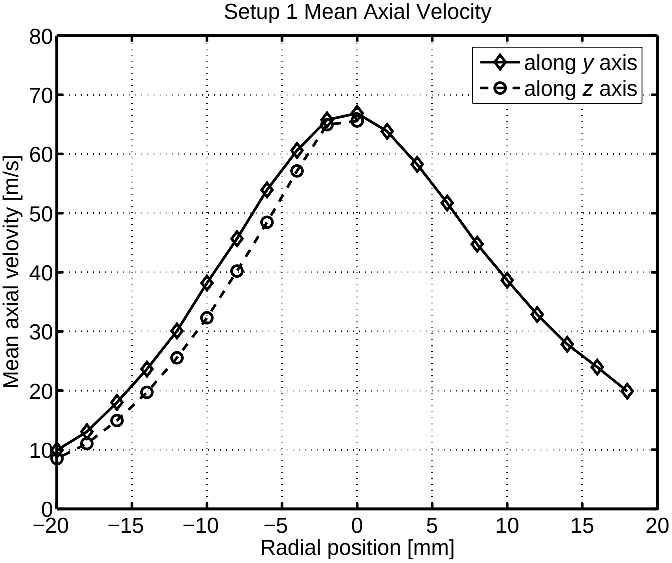

Figure 4.31: Distribution of droplet mean axial velocity along two orthogonal directions *y* and *z* at *x* = 150 mm in Setup 1.

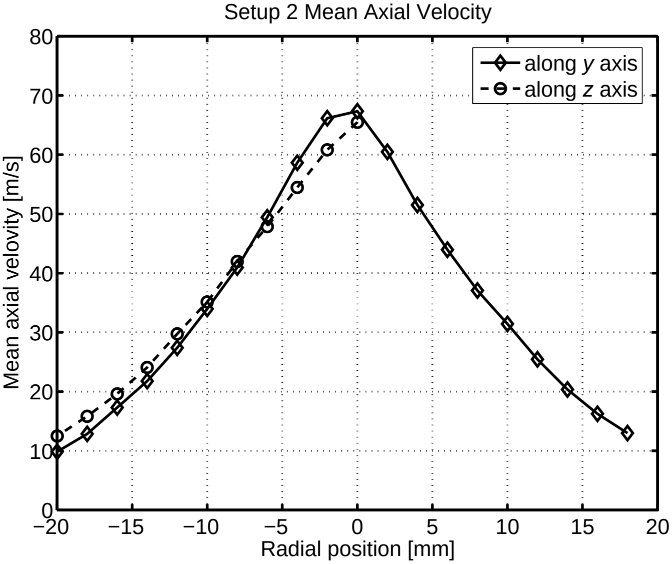

Figure 4.32: Distribution of droplet mean axial velocity along two orthogonal directions *y* and *z* at *x* = 150 mm in Setup 2.

4.4.4 The Effect of Atomizer Geometry

The effects of geometrical dimensions are presented below.

The Effect of Air and Liquid Injection Orifice Diameters

According to Mullinger and Chigier (1974) the optimal D_m/D_a ratio is 1.4 – 1.8, and D_m/D_a = 1.4, 1.6, and 1.8 are tested. The geometrical changes of D_m and D_f also change the air/liquid injection diameter ratio, and D_a/D_f = 1.1, 1.2, and 1.5 are tested. Figure 4.33 and Figure 4.34 show the effect of the D_a/D_f ratio on the mean axial velocity and the SMD, respectively, for L_m/D_m = 6. As might be expected, an increase in the liquid injection orifice diameter causes the maximum mean axial velocity to fall. Larger liquid injection orifice diameters results in thicker liquid films having lower axial velocity in the mixing chamber. As a result of the liquid film having a lower axial velocity, the spray axial velocity will be lower. Furthermore, there is a noticeable influence of the D_a/D_f ratio on the spray symmetry. The more symmetric spray with larger D_a/D_f indicates a more uniform film in the mixing chamber.

The Effect of Mixing Length

The results obtained at the axial location of x = 190 mm from changing the mixing length L_m are shown in Figure 4.35 and Figure 4.36 for D_a/D_f = 1.2, $\dot{m}_l$ = 133 kg/h, and MLR = 5.00%. Figure 4.36 shows that the spray becomes coarser as the length of the mixing chamber L_m is increased. This is in disagreement with the findings of Mullinger and Chigier (1974); but according to the authors the optimal L_m/D_m ratio is 4, which is in agreement with the present findings.

The longer nozzle mixing chamber gives a greater time for momentum transfer between the air and water; hence, the droplet velocity farther downstream of the nozzle exit is higher. Furthermore, the velocity profile is narrower and sharper. The variations of velocities and droplet sizes are consistent with each other in the sense that the larger droplets for L_m/D_m = 6, having larger inertia, tend to follow their own trajectories, and are less affected by the air entrainment motion.

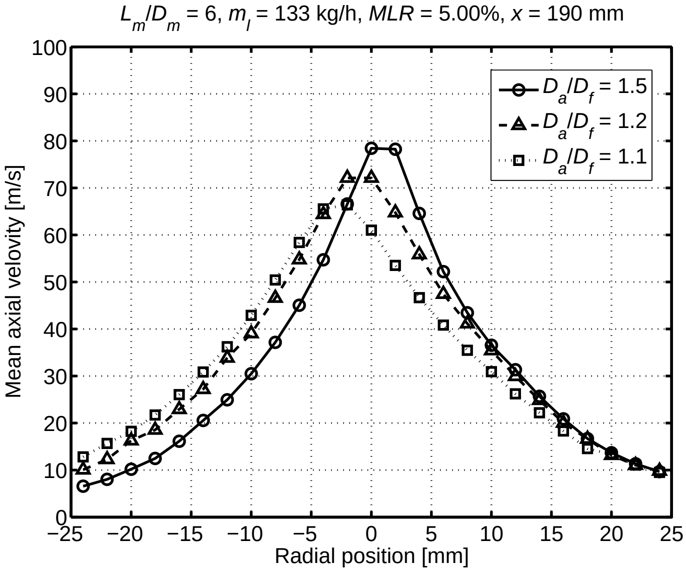

Figure 4.33: The effect of changing the ratio D_a/D_f on the mean axial velocity.

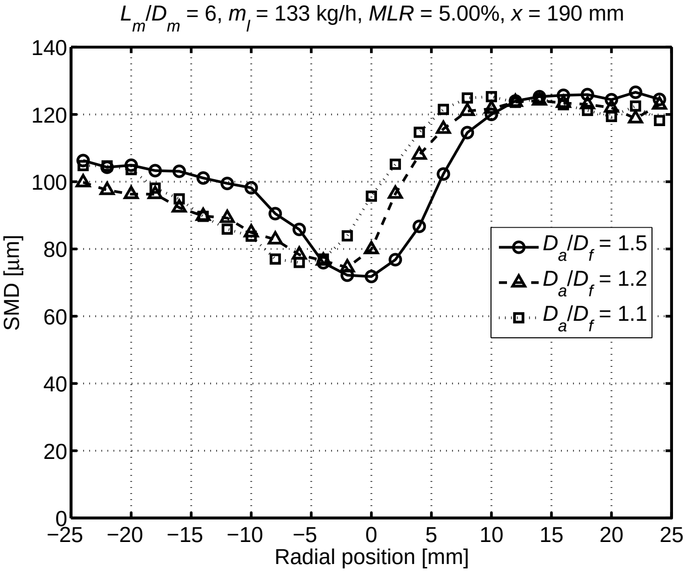

Figure 4.34: The effect of changing the ratio D_a/D_f on the SMD.

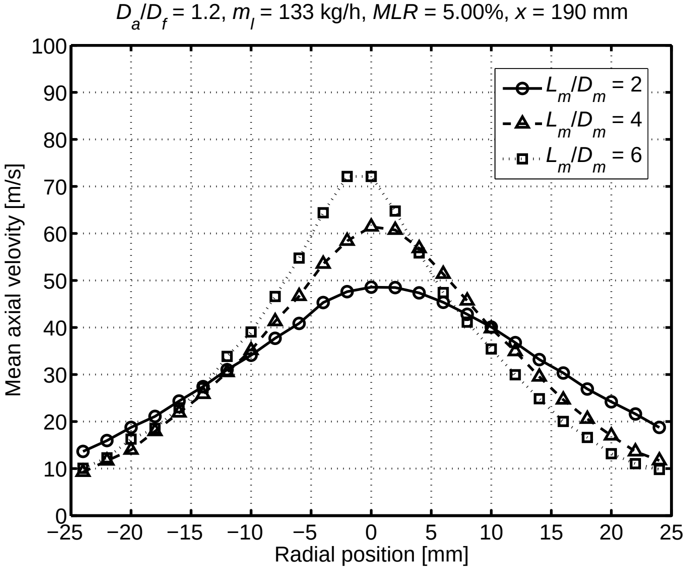

Figure 4.35: The effect of changing the ratio L_m/D_m on the mean axial velocity.

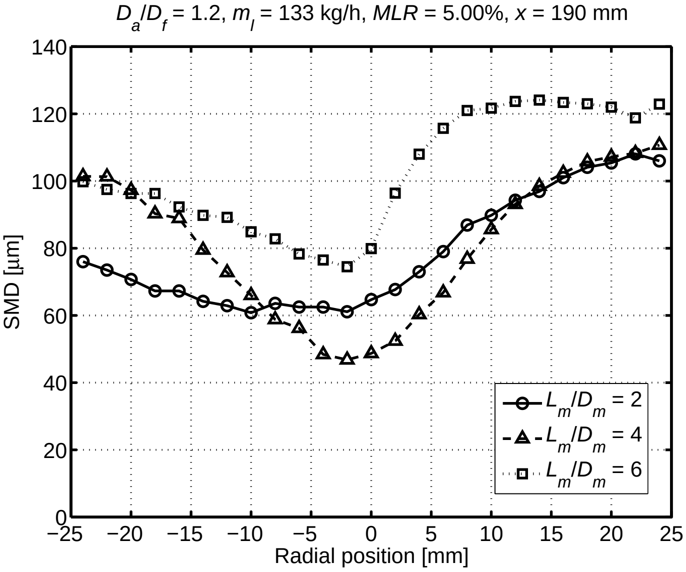

Figure 4.36: The effect of changing the ratio L_m/D_m on the SMD.

4.4.5 The Effect of Operating Conditions

Each of the Y-jet atomizers in Table 4.1 were used to study the effect of mass loading ratio (*MLR*) and liquid flow rate. Measurements for all atomizers show similar trends. Here only the results for nozzle No. 5 are presented.

The Effect of Mass Loading Ratio

The atomizers were operated at three different values of mass loading ratio *MLR* = 3.75%, 5.00%, and 6.25%. Results of mean axial velocity and SMD are in Figure 4.37 and Figure 4.38, respectively, for nozzle No. 5 operated at a liquid flow rate of 133 kg/h. The figures show that an increase in the mass loading ratio *MLR* causes an increase in mean axial velocity and a reduction in the SMD. As can be seen, the asymmetry in SMD is more apparent for higher mass loading ratios.

The Effect of Liquid Flow rate

Mean axial velocity and SMD were measured at three different liquid mass flows and the results are in Figure 4.39 and Figure 4.40 for *MLR* = 5.00%. As expected, an increase in liquid flow rate results in an increase of the mean axial velocity. A decrease in SMD would also be expected. In practice, as shown in Figure 4.40, an increase in liquid flow rate results in an increase of the SMD on the right side of the figure and a decrease on the left side. This asymmetry may be attributed to the obscuration effect by the dense spray described in Section 4.4.3. With increasing liquid flow rate, a more dense spray is generated and the SMD is more affected by the obscuration effect. Therefore the SMD at positive positions may be increased compared to the lower liquid flow rates.

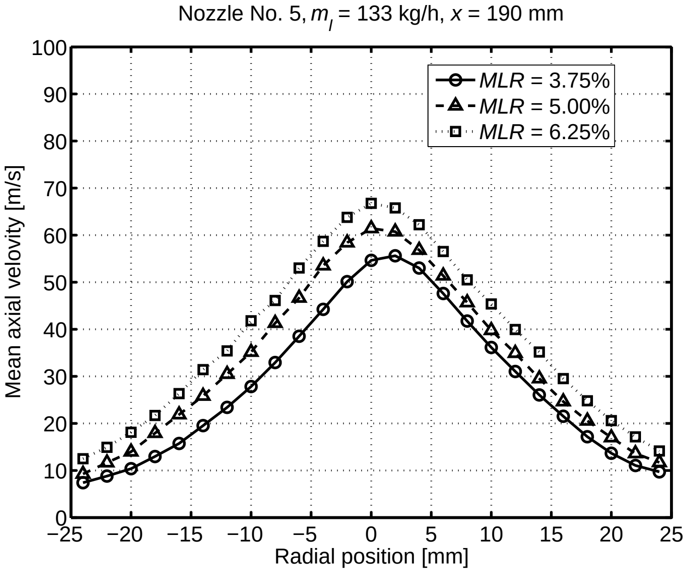

Figure 4.37: The effect of mass loading ratio *MLR* on the mean axial velocity for a liquid flow rate of $\dot{m}_l$ = 133 kg/h.

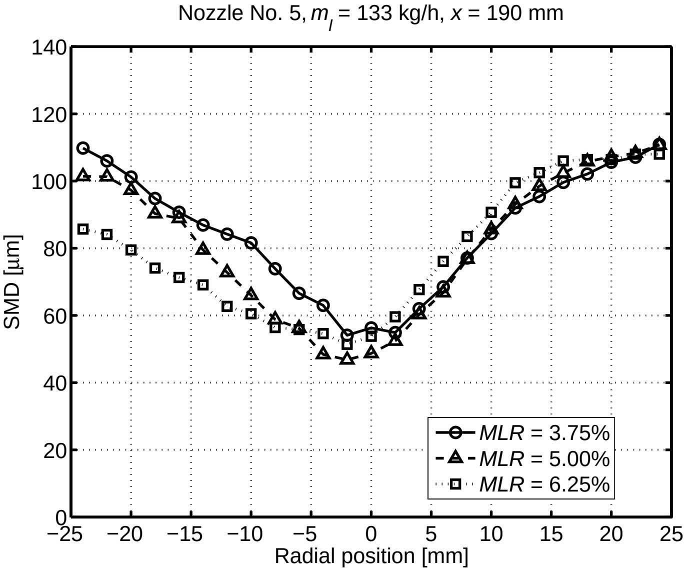

Figure 4.38: The effect of mass loading ratio *MLR* on the SMD for a liquid flow rate of $\dot{m}_l$ = 133 kg/h.

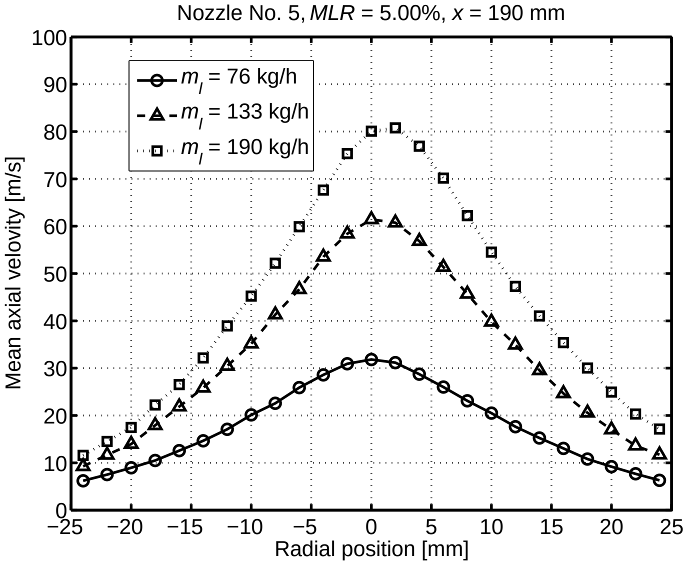

Figure 4.39: The effect of liquid flow rate $\dot{m}_l$ on the mean axial velocity for a mass loading ratio of $MLR = 5.00\%$.

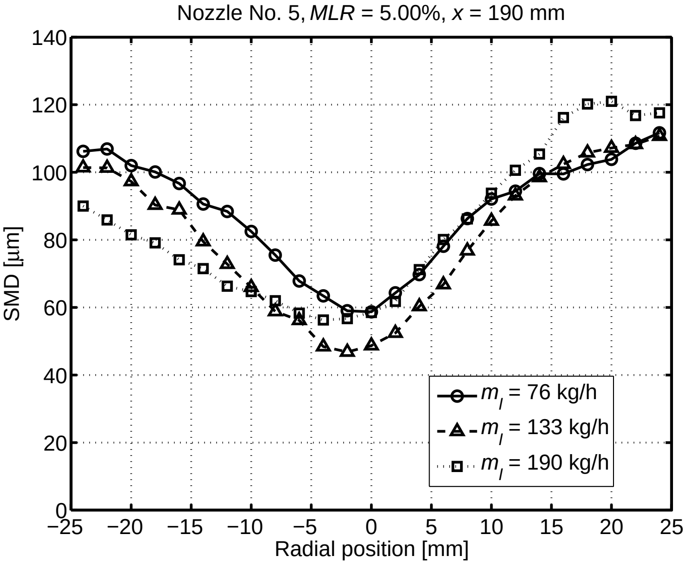

Figure 4.40: The effect of liquid flow rate $\dot{m}_l$ on the SMD for a mass loading ratio of $MLR = 5.00\%$.

4.4.6 Summary

The characteristics of sprays produced by nine different single-hole Y-jet atomizers have been investigated experimentally by using PDA. The spray characteristic parameters, such as droplet arithmetic and Sauter mean diameter and mean velocity have been measured for various radial and axial locations and under various liquid and air flow rates. The results indicate that the spray characteristic parameters are asymmetric about the spray axis due to the impact of liquid and air streams in the mixing chamber which is projected outside the atomizer. At each axial spray cross section, the droplet mean axial velocity reaches the maximum value in the spray center and decreases from the spray center to the edge. The mean diameter has a minimum value at the spray center and increases toward the spray periphery.

The guidelines of Mullinger and Chigier (1974) for the design of internal mixing twin fluid atomizers are found to agree with the present experimental results. The mixing length should be approximately four times the mixing chamber diameter, L_m/D_m = 4. Other geometrical variables (D_a and D_f) have relatively little effect except for the way in which they affect air and water gauge pressures.

From the results obtained in the PDA measurements, it can be concluded that increasing the liquid flow rate or the mass loading ratio both reduce the mean diameters and increase the axial velocity of the spray. The liquid flow rate is the key parameter determining the spray characteristics of the Y-jet atomizers. The spray is less affected by different mass loading ratios.

It should be emphasized that the PDA measurements are affected by the obscuration of the laser beams, and an error in the calculation of the mean diameter can be expected. For most of the experiments, the obscuration effect on droplet mean axial velocity and SMD is small. Only in a few cases for the maximum liquid flow rate, the values of SMD are overpredicted in the $+y$ direction.

For verification of the DQMOM-multi-fluid model computations, nozzle No. 4 in Table 4.1 is used for comparison in Chapter 9.

Chapter 5

Multiphase Flow Modeling

5.1 Introduction

Based on the level of description, multiphase models can be grouped in three classes:

- Inter-phase tracking models
- Eulerian/Lagrangian models
- Eulerian/Eulerian models

Inter-phase tracking methods include, among others, the volume of fluid (VOF) methods and the level-set methods. They give an accurate description of the interface between the two phases, but the proper application of the methods requires the resolution of all involved length scales. This results in very large computational efforts. Therefore, these methods are not able to solve dispersed two-phase flows.

A subcategory of two-phase flows is dispersed phase flows in which one phase dos not constitute a connected continuum, for instance gas-droplet flows. Two approaches have been used to model such flows: Lagrangian and Eulerian (Mostafa and Mongia, 1987).

In the Lagrangian formulation a large number of particles trajectories are calculated, whereas the continuous phase is described by standard Eulerian conservation equations (e.g., Rüger, *et al.*, 2000).

In the Eulerian approach, the two phases are treated as separate interpenetrating continua, and mean equations with interaction terms are solved for each phase (e.g., Mostafa and Elghobashi, 1985).

This chapter presents the VOF model for simulating internal nozzle flows, and the Lagrangian and Eulerian models for simulating gas-droplet flows.

5.2 Volume of Fluid (VOF) Model

In the VOF model, a single set of momentum equations is shared by the fluids, and the volume fraction of each of the fluids is tracked throughout the domain.

Governing Equations

The governing equations representing the conservation of mass and momentum in Cartesian coordinates assume the following form when written in tensor notation:

Equation of continuity (mass conservation):

$$\frac{\partial \rho}{\partial t}+\frac{\partial}{\partial x_i}\left(\rho u_i\right)=0 \tag{5.1}$$

Momentum conservation (Navier-Stokes equation):

$$\frac{\partial}{\partial t}\left(\rho u_i\right)+\frac{\partial}{\partial x_j}\left(\rho u_i u_j\right)=-\frac{\partial p}{\partial x_i}+\frac{\partial}{\partial x_j}\left[\mu\left(\frac{\partial u_i}{\partial x_j}+\frac{\partial u_j}{\partial x_i}\right)\right]+\rho g_i \tag{5.2}$$

Here the left hand side represents convection and the first term on the right hand side represents pressure. The remaining terms represent diffusion and the body force of gravity.

The VOF formulation relies on the fact that fluid phases are not interpenetrating. The tracking of the interface between the gas and liquid phases is accomplished by the solution of a continuity equation for the volume fraction of one of the phases. For the liquid phase, this equation has the form:

$$\frac{\partial}{\partial t}\alpha_l + \frac{\partial}{\partial x_i}\left(\alpha_l u_i\right) = S_{\alpha_l} \tag{5.3}$$

where α_l is the volume fraction of the liquid in the gas-liquid system. The source term on the right hand side of the equation is zero when there is no mass source or mass transfer between the phases. The volume fraction equation of the gas phase α_g is not solved; the gas phase volume fraction is computed based on the following constraint:

$$\alpha_g + \alpha_l = 1 \tag{5.4}$$

The properties appearing in the transport equations are determined by the presence of the component phases in each control volume. The density in each cell is given by

$$\rho = \alpha_l \rho_l + \alpha_g \rho_g = \alpha_l \rho_l + \left(1 - \alpha_l\right)\rho_g \tag{5.5}$$

The viscosity is computed in the same manner.

Interpolation near the Interface

When the volume fraction is between zero and one, there exists a fluid interface within the computational cell. The volume fraction equation can be solved using standard upwind differencing techniques, which tend to smear the surface over a few cells, or by Geometric Reconstruction of the two-phase interface, which ensures that the two-phase boundary is captured within one computational cell (Fluent, 2005). In this work the Geometric Reconstruction scheme computed in a time-accurate manner is used to keep the interface sharp.

5.3 Lagrangian Model

In the Lagrangian approach computational particles (droplet parcels) are released into the gas flow and their position and velocity are obtained by integrating the particle equation of motion. This force balance equates the particle inertia with the forces acting on the particle, and can be written in Cartesian coordinates as (Fluent, 2005)

$$\frac{\mathrm{d}u_{p,i}}{\mathrm{d}t} = \frac{\left(u_i - u_{p,i}\right)}{\tau_p} + \frac{g_i\left(\rho_p - \rho_g\right)}{\rho_p} + F_i \tag{5.6}$$

where particle relaxation time is given by

$$\tau_p = \frac{24}{C_D \operatorname{Re}_p} \frac{d_p^2 \rho_p}{18\mu_g} \tag{5.7}$$

and the particle Reynolds number is defined as

$$\operatorname{Re}_p = \frac{\rho_g d_p \left|\vec{u} - \vec{u}_p\right|}{\mu_g} \tag{5.8}$$

Here the index i indicates the three coordinates of the particle position and the three velocity components of the instantaneous gas velocity, u_i, at the particle position and the instantaneous particle velocity $u_{p,i}$, μ_g is the molecular viscosity of the gas, ρ_g is the gas density, ρ_p is the density of the particle, d_p is the particle diameter, and C_D is the drag coefficient. Equation (5.6) incorporates additional forces, F_i, that can be important under special circumstances, e.g. the virtual mass force and the Saffman's lift force.

The instantaneous gas phase velocity is given by

$$u_i = U_i + u_i' \tag{5.9}$$

where U_i is determined from the solution of the mean flow equations of the gas phase and u_i' is chosen randomly from an isotropic Gaussian distribution with mean square derivation $\frac{2}{3}k$ where k is the turbulent kinetic energy of the gas phase. For each particle, after a turbulent correlation time, τ, a new value of u_i' is chosen. τ is the minimum of two time scales, one being a characteristic turbulent eddy life time, τ_e, and the other the residence time of the particle in the eddy, τ_r. Prediction of τ_e and τ_r makes use of the concept of the fluid Lagrangian integral time, T_L. This time scale can be approximated as (Milojević, 1990)

$$T_L = C_T \frac{k}{\varepsilon} \tag{5.10}$$

where ε is turbulent kinetic energy dissipation rate of the gas phase. The constant C_T has to be determined and is not well known; values between 0.135 and 0.41 have been used.

The characteristic eddy lifetime is defined either as a constant:

$$\tau_e = 2T_L \tag{5.11}$$

or as a random variation about T_L:

$$\tau_e = -T_L \ln\left(r\right) \tag{5.12}$$

where r is a uniform random number between 0 and 1 (Graham and James, 1996).

The droplet residence time is defined as (Graham and James, 1996)

$$\tau_r = -\tau_p \ln\left(1 - \frac{l_e}{\tau_p \left|\vec{u} - \vec{u}_p\right|}\right) \tag{5.13}$$

where τ_p is the particle relaxation time and l_e is the eddy length scale defined by

$$l_e = \tau_e \sqrt{\tfrac{2}{3}k} \tag{5.14}$$

Hence

$$\tau = \min\left(\tau_e, \tau_r\right) \tag{5.15}$$

5.4 Eulerian Multi-Fluid Model

In the Eulerian multi-fluid model, the gas and droplet phases are treated as interpenetrating continua in an Eulerian framework. The gas phase is considered as the primary phase, whereas the droplet phases are considered as dispersed or secondary phases. The gas and droplet phases are characterized by volume fractions, and by definition, the volume fractions of all phases must sum to unity:

$$\alpha_g + \sum_{q=1}^{N} \alpha_q = 1 \tag{5.16}$$

where α_g is the gas volume fraction, α_q is the volume fraction of the q^{th} droplet phase, and N is the total number of droplet phases.

The governing equations of the multi-fluid model can be derived by conditionally ensemble averaging of the local instant conservation equations of single-phase flow (Drew, 1983; Drew and Passman, 1999). In the present case, the flow is assumed to be isothermal; hence, energy balances are not needed. Furthermore, there is no interfacial mass transfer between the gas and droplet phases.

5.4.1 Conservation Equations

The continuity equation for the gas phase is

$$\frac{\partial}{\partial t}\left(\alpha_g \rho_g\right) + \frac{\partial}{\partial x_i}\left(\alpha_g \rho_g U_{i,g}\right) = 0 \tag{5.17}$$

where $U_{i,g}$ is velocity and ρ_g is density of the gas.

The continuity equation for the q^{th} droplet phase is

$$\frac{\partial}{\partial t}\left(\alpha_q \rho_l\right) + \frac{\partial}{\partial x_i}\left(\alpha_q \rho_l U_{i,q}\right) = \sum_{p=1}^{N} \dot{m}_{pq} \tag{5.18}$$

where $\dot{m}_{pq}$ characterizes the mass transfer from the p^{th} to the q^{th} droplet phase due to breakup and coalescence.

The momentum equation for the gas phase is

$$\begin{aligned}&\frac{\partial}{\partial t}\left(\alpha_g\rho_g U_{i,g}\right)+\frac{\partial}{\partial x_j}\left(\alpha_g\rho_g U_{i,g}U_{j,g}\right)\\&=-\alpha_g\frac{\partial P}{\partial x_i}+\frac{\partial}{\partial x_j}\left(\alpha_g\tau_{ij,g}\right)+\alpha_g\rho_g g_i+\sum_{q=1}^{N}F_{i,qg}\end{aligned}\tag{5.19}$$

Likewise, for the droplet phases, the momentum balances are

$$\begin{aligned}&\frac{\partial}{\partial t}\left(\alpha_q\rho_l U_{i,q}\right)+\frac{\partial}{\partial x_j}\left(\alpha_q\rho_l U_{i,q}U_{j,q}\right)\\&=-\alpha_q\frac{\partial P}{\partial x_i}+\frac{\partial}{\partial x_j}\left(\alpha_q\tau_{ij,q}\right)+\alpha_q\rho_l g_i+F_{i,gq}+\sum_{p=1}^{N}\dot{m}_{pq}U_{i,pq}\end{aligned}\tag{5.20}$$

where $\tau_{ij,g}$ and $\tau_{ij,q}$ is the stress tensors for the gas and the droplet phases, respectively:

$$\tau_{ij}=\mu_t\left(\frac{\partial U_i}{\partial x_j}+\frac{\partial U_j}{\partial x_i}\right)-\frac{2}{3}\delta_{ij}\left(\rho k+\mu_t\frac{\partial U_k}{\partial x_k}\right)\tag{5.21}$$

where μ_t is the turbulent viscosity and k is the turbulent kinetic energy of the respective phase. P is the pressure shared by all phases and g_i is gravity in the i^{th} direction. The last term on the right-hand side of Eq. (5.20) takes into account momentum transfer due to mass transfer between the droplet phases, where $U_{i,pq}$ ($= U_{i,qp}$) is defined as follows:

$$U_{i,pq}=\begin{cases}U_{i,p} & \text{if}\,\dot{m}_{pq}>0\\ U_{i.q} & \text{if}\,\dot{m}_{pq}<0\end{cases}\tag{5.22}$$

$F_{i,qg}$ ($= -F_{i,gq}$) is the interfacial momentum transfer from the q^{th} droplet phase to the gas phase and accounts for drag, virtual mass effect, lift forces, etc. In most cases the lift force is insignificant compared to the drag force and the virtual mass force is insignificant when the secondary phase density is much larger than the primary phase density. Neglecting the influence of lift and virtual mass forces and only using the drag force as the interfacial momentum transfer mechanism, $F_{i,qg}$ reduces to

$$F_{i,qg} = C_{f,qg} U_{i,rel} \qquad (5.23)$$

where $C_{f,qg}$ (= $C_{f,gq}$) is the friction coefficient and $U_{i,rel}$ is the relative velocity (defined by Eq. (5.52) below). For gas-droplet flows, the friction coefficient between the q^{th} droplet phase and the gas phase is written in the following form:

$$C_{f,qg} = \frac{3}{4} \frac{\alpha_q \alpha_g \rho_g C_D}{d_q} U_{rel} \qquad (5.24)$$

where d_q is the diameter of the droplets of phase q and $U_{rel} = \left| \vec{U}_q - \vec{U}_g \right|$ is the relative velocity magnitude between the q^{th} droplet phase and the gas phase. The drag coefficient, C_D, is based on the Schiller-Naumann (Schiller and Naumann, 1933) and Newton drag correlations:

$$C_D = \max\left[\frac{24}{\mathrm{Re}_q} \left(1 + 0.15\,\mathrm{Re}_q^{0.687} \right), 0.44 \right] \qquad (5.25)$$

where Re_q is the relative Reynolds number for the gas phase and droplet phase q obtained from

$$\mathrm{Re}_q = \frac{\rho_g U_{rel} d_q}{\mu_g} \qquad (5.26)$$

5.5 Turbulence Models

To describe the effects of turbulent fluctuations of velocities and scalar quantities in a single phase, various types of closure models can be used (Ferziger, *et al.*, 2004). In comparison to single-phase flows, the number of terms to be modeled in the momentum equations in multiphase flows is large, and this makes the modeling of turbulence in multiphase simulations extremely complex (Crowe, *et al.*, 1996; Peirano and Leckner, 1998).

In the context of CFD modeling, turbulence in two-phase flow is more often modeled using an extension of the standard k-ε model, although other more sophisticated models using higher order moment closures also exist. This is because the k-ε model offers reasonable accuracy at low computational cost as well as being more stable to execute. It is therefore quite attractive in routine engineering computations.

For modeling turbulence in multiphase gas-droplet flows, three methods are considered within the context of the k-ε models: mixture turbulence model, dispersed turbulence model, and turbulence model for each phase. Descriptions of each method are presented below.

5.5.1 Mixture *k*-*ε* Turbulence Model

The mixture turbulence model represents the first extension of the single-phase k-ε model, and it is applicable for stratified multiphase flows and when the density ratio between phases is close to one.

The turbulent kinetic energy, k, and its dissipation rate, ε, are obtained from the following transport equations:

$$\frac{\partial}{\partial t}\left(\rho_m k\right)+\frac{\partial}{\partial x_j}\left(\rho_m k U_{j,m}\right)=\frac{\partial}{\partial x_j}\left(\frac{\mu_{t,m}}{\mathrm{Pr}_k}\frac{\partial k}{\partial x_j}\right)+G_{k,m}-\rho_m\varepsilon \tag{5.27}$$

and

$$\frac{\partial}{\partial t}\left(\rho_m \varepsilon\right)+\frac{\partial}{\partial x_j}\left(\rho_m \varepsilon U_{j,m}\right)=\frac{\partial}{\partial x_j}\left(\frac{\mu_{t,m}}{\mathrm{Pr}_\varepsilon}\frac{\partial \varepsilon}{\partial x_j}\right)+\frac{\varepsilon}{k}\left(C_{\varepsilon 1}G_{k,m}-C_{\varepsilon 2}\rho_m\varepsilon\right) \tag{5.28}$$

where the mixture density and velocity, ρ_m and $U_{i,m}$, are computed from

$$\rho_m=\alpha_g\rho_g+\sum_{q=1}^{N}\alpha_q\rho_l \tag{5.29}$$

and

$$U_{i,m}=\frac{\alpha_g\rho_g U_{i,g}+\sum_{q=1}^{N}\alpha_q\rho_l U_{i,q}}{\rho_m} \tag{5.30}$$

the turbulent viscosity, $\mu_{t,m}$, is computed by combining k and ε as

$$\mu_{t,m} = \rho_m C_\mu \frac{k^2}{\varepsilon} \tag{5.31}$$

and the term $G_{k,m}$, representing the production of turbulence kinetic energy, is computed from

$$G_{k,m} = \mu_{t,m} S_m^2 \tag{5.32}$$

where S_m is the modulus of the mixture mean strain rate tensor, defined as

$$S_m = \sqrt{2 S_{ij,m} S_{ij,m}} \tag{5.33}$$

where $S_{ij,m}$ is the mixture mean rate of strain tensor, defined as

$$S_{ij,m} = \frac{1}{2}\left(\frac{\partial U_{i,m}}{\partial x_j} + \frac{\partial U_{j,m}}{\partial x_i} \right) \tag{5.34}$$

The constants in these equations are the same as those for the single-phase k-ε model:

$$C_\mu = 0.09,\ C_{\varepsilon 1} = 1.44,\ C_{\varepsilon 2} = 1.92,\ \mathrm{Pr}_k = 1.0,\ \mathrm{Pr}_\varepsilon = 1.3 \tag{5.35}$$

It is well known that the standard k-ε model does not fit the data for single-phase axisymmetric jets. A common practice is to modify one of the contestants in the model $C_{\varepsilon 2}$ from 1.92 to 1.87 (Faeth, 1987).

5.5.2 Dispersed k-ε Turbulence Model

The extension of the single-phase standard k-ε model to dispersed two-phase flows has been the subject of study for many years, e.g. Elghobashi and Abou-Arab (1983), Kataoka and Serizawa (1989), and Lopez de Bertodano (1998).

A k-ε model for dispersed two-phase flow has been developed by Simonin and Viollet (1990). In the case of dilute sprays, interdroplet collisions are negligible and the dominant process in the random motion of the droplet phases is the influence of the gas-phase turbulence.

Fluctuating quantities of the droplet phases can therefore be given in terms of the mean characteristics of the gas phase and the ratio of the particle relaxation time and eddy-droplet interaction time (Simonin and Viollet, 1990).

The method for modeling turbulence involves the following assumptions:

- A modified *k*-ε model for the gas phase: Turbulent predictions for the gas phase are obtained using a *k*-ε model supplemented with extra terms that include the interphase turbulent momentum transfer.
- Tchen-theory correlations for the droplet phases: Predictions for turbulence quantities for the droplet phases are obtained using the Tchen theory of dispersion of discrete particles by homogeneous turbulence (Hinze, 1975).
- Interphase momentum transfer: In turbulent flows, the momentum exchange terms contain the correlation between the instantaneous distribution of the droplet phases and the gas-phase motion. It is possible to take into account the dispersion of the droplet phases transported by the turbulent gas-phase motion.
- A phase-weighted averaging process: When a two-step averaging process is used with a phase-weighted average for the turbulence, no turbulent volume fraction fluctuations are introduced into the continuity equations.

Turbulence in the Gas Phase

Turbulent predictions in the gas phase are carried out with the standard *k*-ε model supplemented with additional terms taking into account the interfacial turbulent momentum transfer.

The eddy viscosity $\mu_{t,g}$ is written in terms of the turbulent kinetic energy k_g and a characteristic time $\tau_{t,g}$:

$$\mu_{t,g} = \frac{2}{3}\rho_g k_g \tau_{t,g} \tag{5.36}$$

The characteristic time of the energetic turbulent eddies is defined as

$$\tau_{t,g} = \frac{3}{2} C_\mu \frac{k_g}{\varepsilon_g} \tag{5.37}$$

where ε_g is the dissipation rate.

The modeled transport equations for k_g and ε_g are

$$\begin{aligned} &\frac{\partial}{\partial t}\left(\alpha_g \rho_g k_g\right) + \frac{\partial}{\partial x_j}\left(\alpha_g \rho_g k_g U_{j,g}\right) \\ &= \frac{\partial}{\partial x_j}\left(\alpha_g \frac{\mu_{t,g}}{\mathrm{Pr}_k} \frac{\partial k_g}{\partial x_j}\right) + \alpha_g G_{k,g} - \alpha_g \rho_g \varepsilon_g + S_{k,g} \end{aligned} \tag{5.38}$$

and

$$\begin{aligned} &\frac{\partial}{\partial t}\left(\alpha_g \rho_g \varepsilon_g\right) + \frac{\partial}{\partial x_j}\left(\alpha_g \rho_g \varepsilon_g U_{j,g}\right) \\ &= \frac{\partial}{\partial x_j}\left(\alpha_g \frac{\mu_{t,g}}{\mathrm{Pr}_\varepsilon} \frac{\partial \varepsilon_g}{\partial x_j}\right) + \alpha_g \frac{\varepsilon_g}{k_g}\left(C_{\varepsilon 1} G_{k,g} - C_{\varepsilon 2} \rho_g \varepsilon_g\right) + S_{\varepsilon,g} \end{aligned} \tag{5.39}$$

Here $S_{k,g}$ and $S_{\varepsilon,g}$ represent the influence of the droplet phases on the gas phase. The term $S_{k,g}$ is modeled according to Simonin and Viollet (1990):

$$S_{k,g} = \sum_{q=1}^{N} C_{f,qg}\left(k_{qg} - 2k_g + U_{i,rel} U_{i,dr}\right) \tag{5.40}$$

where k_{qg} is the covariance of the velocities of the droplet phase q and the gas phase (calculated from Eq. (5.48) below), $U_{i,rel}$ is the relative velocity (defined by Eq. (5.52) below), and $U_{i,dr}$ is the drift velocity (defined by Eq. (5.53) below).

$S_{\varepsilon,g}$ is modeled according to Elghobashi and Abou-Arab (1983):

$$S_{\varepsilon,g} = C_{\varepsilon 3} \frac{\varepsilon_g}{k_g} S_{k,g} \tag{5.41}$$

where $C_{\varepsilon 3} = 1.2$.

Turbulence in the Droplet Phases

Three time scales that characterize the motion are used to evaluate dispersion coefficients, correlation functions, and the turbulent kinetic energy of each droplet phase.

The first one relates to inertial effects acting on the droplet. The characteristic droplet relaxation time connected with inertial effects acting on a droplet phase *q* is defined as

$$\tau_{F,qg} = \frac{\alpha_q \rho_g}{C_{f,qg}} \left(\frac{\rho_l}{\rho_g} + C_A \right) \tag{5.42}$$

where C_A is the added mass coefficient ($C_A = 0.5$).

The second time scale describes the loss of correlation due to the mean relative movement of the droplets (crossing-trajectories effects). The transient time required for the droplets to cross the large eddies of the gas-phase turbulent motion is given by

$$\tau_{T,qg} = \tau_{t,g} \frac{\sqrt{\frac{2}{3} k_g}}{\left| \vec{U}_{rel} \right|} \tag{5.43}$$

The characteristic time of the correlated turbulent motion, or eddy-droplet interaction time, is written following Picart, *et al.* (1986):

$$\tau_{t,qg} = \frac{\tau_{t,g}}{\sqrt{1 + C_\beta \xi_{qg}^2}} \tag{5.44}$$

where ξ_{qg} is the ratio between the characteristic time of the energetic turbulent eddies and the characteristic transient time required for the droplets to cross the large eddies:

$$\xi_{qg} = \frac{\tau_{t,g}}{\tau_{T,qg}} = \frac{\left| \vec{U}_{rel} \right|}{\sqrt{\frac{2}{3} k_g}} \tag{5.45}$$

The parameter C_β is set at 0.45 in the direction parallel to the mean relative velocity and to 1.80 in the perpendicular directions.

The ratio between the time of the correlated turbulent motion and the droplet relaxation time is written as

$$\eta_{qg} = \frac{\tau_{t,qg}}{\tau_{F,qg}} \tag{5.46}$$

Following Simonin and Viollet (1990), the turbulence quantities for droplet phase q are written as follows:

$$k_q = k_g \left(\frac{b^2 + \eta_{qg}}{1 + \eta_{qg}} \right) \tag{5.47}$$

$$k_{qg} = 2k_g \left(\frac{b + \eta_{qg}}{1 + \eta_{qg}} \right) \tag{5.48}$$

$$D_{t,qg} = \frac{1}{3} k_{qg} \tau_{t,qg} \tag{5.49}$$

$$\nu_{t,q} = D_{t,qg} + \left(\frac{2}{3} k_q - \frac{1}{3} b k_{qg} \right) \tau_{F,qg} \tag{5.50}$$

$$b = \frac{1 + C_A}{\rho_l / \rho_g + C_A} \tag{5.51}$$

In gas-droplet flows ($\rho_l \gg \rho_g$ and $b \ll 1$) inertial effects lead to decrease the kinetic energy of the droplet phase ($k_q < k_g$) and the additional source term $S_{k,g}$ in the k-equation is negative. The eddy diffusivity of the droplet phase, $\nu_{t,q}$, is primary affected by crossing-trajectories effects and is equal to the one of the gas phase when the mean relative velocity is negligible ($\xi_{qg} \approx 0$).

Interphase Turbulent Momentum Transfer

$U_{i,rel}$, the averaged relative velocity between the droplet phase and the gas phase, can be expressed in function of the total relative mean velocity, $U_{i,q} - U_{i,g}$, and a drifting velocity, $U_{i,dr}$, due to the correlation between the instantaneous distribution of droplets and the turbulent gas-phase motion at large scales with respect to droplet diameter:

$$U_{i,rel} = \left(U_{i,q} - U_{i,g}\right) - U_{i,dr} \tag{5.52}$$

$U_{i,dr}$ represents the dispersion of the droplets due to transport by the gas-phase turbulence. This is an important effect since the mass balances do not contain a diffusive term that would be responsible for dispersion of the droplets. The drift velocity is written as follows:

$$U_{i,dr} = -\frac{D_{t,qg}}{\mathrm{Pr}_\alpha}\left(\frac{1}{\alpha_q}\frac{\partial \alpha_q}{\partial x_i} - \frac{1}{\alpha_g}\frac{\partial \alpha_g}{\partial x_i}\right) \tag{5.53}$$

Here $D_{t,qg}$ is the binary diffusion coefficient defined by Eq. (5.49), and Pr_α is a dispersion Prandtl number, $\mathrm{Pr}_\alpha = 0.67$ (Simonin and Viollet (1990).

When using the mixture *k-ε* turbulence model in multiphase flows, it is assumed that $D_{t,qg} = \nu_{t,m}$.

5.5.3 Turbulence Model for Each Phase

In the dispersed *k-ε* model, turbulence is associated with the continuous phase, which is assumed to be the dominant phase, i.e. the dispersed phase is present in small quantities. Hence, the dispersed phase can only respond to or modify the continuous phase turbulence. When the phase fraction increases this assumption ceases to be valid as the dispersed phase fluctuations become intertwined with those of the continuous phase. In the limit, when the dispersed phase fraction approaches unity, turbulence becomes associated with the "dispersed" phase. Hence a model catering for the full range of phase fraction values is needed. Such a model, based on the solution of the *k* and *ε* transport equations for each phase, is presented here.

Since two additional transport equations are solved for each droplet phase, the per-phase turbulence is more computationally intensive than the mixture or dispersed turbulence models.

Transport Equations

The gas-phase turbulent kinetic energy k_g and its dissipation ε_g are computed using Eqs. (5.38) and (5.39). Likewise, for the droplet phases, the modeled transport equations for k_q and ε_q are

$$\begin{aligned}&\frac{\partial}{\partial t}\left(\alpha_q\rho_l k_q\right)+\frac{\partial}{\partial x_j}\left(\alpha_q\rho_l k_q U_{j,q}\right)\\ &=\frac{\partial}{\partial x_j}\left(\alpha_q\frac{\mu_{t,q}}{\mathrm{Pr}_k}\frac{\partial k_q}{\partial x_j}\right)+\alpha_q G_{k,q}-\alpha_q\rho_l\varepsilon_q+S_{k,q}+\sum_{p=1}^{N}\dot{m}_{pq}k_{pq}\end{aligned} \tag{5.54}$$

and

$$\begin{aligned}&\frac{\partial}{\partial t}\left(\alpha_q\rho_l\varepsilon_q\right)+\frac{\partial}{\partial x_j}\left(\alpha_q\rho_l\varepsilon_q U_{j,q}\right)\\ &=\frac{\partial}{\partial x_j}\left(\alpha_q\frac{\mu_{t,q}}{\mathrm{Pr}_k}\frac{\partial \varepsilon_q}{\partial x_j}\right)+\alpha_q\frac{\varepsilon_q}{k_q}\left(C_{\varepsilon 1}G_{k,q}-C_{\varepsilon 2}\rho_l\varepsilon_q\right)+S_{\varepsilon,q}+\sum_{p=1}^{N}\dot{m}_{pq}\varepsilon_{pq}\end{aligned} \tag{5.55}$$

Here, the last term on the right hand side of the equations takes into account turbulence transfer due to mass transfer between the droplet phases, where k_{pq} and ε_{pq} is defined according to Eq. (5.22). The source terms $S_{k,q}$ and $S_{\varepsilon,q}$ represent the influence of the gas phase on the q^{th} droplet phase. The term $S_{k,q}$ is modeled according to Eq. (5.40):

$$S_{k,q}=C_{f,qg}\left(C_{gq}k_g-C_{qg}k_q+U_{i,rel}U_{i,dr}\right) \tag{5.56}$$

Likewise, for the gas phase, the source term $S_{k,g}$ is

$$S_{k,g}=\sum_{q=1}^{N}C_{f,qg}\left(C_{qg}k_q-C_{gq}k_g+U_{i,rel}U_{i,dr}\right) \tag{5.57}$$

The terms C_{qg} and C_{gq} are approximated as (Fluent, 2005)

$$C_{qg}=2,\ C_{gq}=2\left(\frac{\eta_{qg}}{1+\eta_{qg}}\right) \tag{5.58}$$

where η_{qg} is defined by Eq. (5.46). The source terms $S_{\varepsilon,q}$ and $S_{\varepsilon,g}$ is modeled according to Eq. (5.41).

Rather than using the Tchen theory as in the dispersed turbulence model, the droplet turbulent diffusivity $\nu_{t,q}$ is computed directly from k_q and ε_q. The relative velocity $U_{i,rel}$ is defined by Eq. (5.52), and the drift velocity for droplet phase q is computed as

$$U_{i,dr} = -\left(\frac{\nu_{t,q}}{\alpha_q \Pr_{\alpha_q}} \frac{\partial \alpha_q}{\partial x_i} - \frac{\nu_{t,g}}{\alpha_g \Pr_{\alpha_g}} \frac{\partial \alpha_g}{\partial x_i} \right) \tag{5.59}$$

Chapter 6

Direct Quadrature Method of Moments

6.1 Introduction

Spray models have a common basis at what can be called "the kinetic level" under the form of a probability density function (PDF or distribution function) satisfying a Boltzmann type equation, the so-called Williams equation (Williams, 1985). The variables characterizing one droplet are the size, the velocity, and the temperature. Such a transport equation describes the evolution of the distribution function of the spray due to evaporation, to the drag force of the gaseous phase, to the heating of the droplets by the gas, to breakup phenomena, and finally to the droplet-droplet interaction such as collision. The spray transport equation is then coupled to the gas phase equations. The two-way coupling of the phases occurs first in the spray transport equations through the rate of evaporation, drag force, and the heating rate, which are functions of the gas phase variables, and second through exchange terms in the gas phase equations.

There are several strategies in order to solve the liquid phase. Currently the most common spray description is based on the Lagrangian discrete droplet method (DDM) (e.g., Rüger, *et al.*, 2000). While the continuous phase is described by the standard Eulerian conservation equations, the transport of the dispersed phase is calculated by tracking the trajectories of a certain number of representative parcels (particles). A parcel consists of a number of droplets and it is assumed that all the droplets within one parcel have the same physical properties and behave equally when they move, break up, or evaporate. The coupling between the liquid and the gaseous phases is achieved by source term exchange for mass, momentum, energy, and turbulence. Various submodels account for the effects of turbulent dispersion, coalescence, evaporation, and droplet breakup. The Lagrangian method is especially suitable for dilute sprays, but has shortcomings with respect to modeling of dense sprays. Further problems are reported connected with bad statistical convergence and also with dependence of the spray on grid size (Schmidt and Rutland, 2000).

These drawbacks make the use of an Eulerian formulation for the description of the disperse phase attractive. Until recently the Eulerian methods were dominated by the two-fluid approach in which a set of continuum equations representing conservation of mass, momentum, and energy are derived for each phase. The fact that no information is available on the droplet size distribution is generally too severe an assumption in most spray applications. An alternative approach is based upon adopting an Eulerian multiphase method treating different size classes of the spray droplets as separate, interpenetrating phases and solving conservation equations for each of them. von Berg, *et al.* (2005) developed a model based on this approach. For each phase mass, momentum, and energy conservation equations were solved. A disadvantage of the method is that the number of equations to be solved increases when the droplet size distribution becomes wider and therefore the number of droplet size classes increases. If the size distributions in the spray are to be fully captured, this leads to a computationally expensive scheme.

Several authors have proposed dispersed phase transport models that involve transportation of moments of the particle size distribution (Beck and Watkins, 2002; Yue and Watkins, 2004; Archambault, *et al.*, 2003; Marchisio, *et al.*, 2003*a*). These techniques are broadly known as "moment method" models. Moment transport models attempt to model polydispersed flow by transporting statistical moments of the droplet distribution (size, velocity, etc.) through physical space. The advantage of the moment methods is that the number of moments required is very small (about 4-6). When a moment approach is adopted to solve the phase space transport equation, problems are encountered because the governing equations for the k^{th} moment also depends on the $(k+1)^{th}$ moment. Previous work in this area has adopted two different methods for the reconstruction of the PDF. Beck and Watkins (2002) approximate the DSD using a presumed Gamma distribution, parameterized by two transported moments. Yue and Watkins (2004) extended the method by transporting four moments; however, a presumed size distribution is still needed to evaluate higher order moments. Archambault, *et al.* (2003) outline the use of the maximum entropy formulation to calculate the higher order moments, required for closure, using the transported moments of the droplet size-velocity joint-PDF.

As an alternative, McGraw (1997) developed the so-called quadrature method of moments (QMOM), which is based on the product-difference (PD) algorithm formulated by Gordon (1968). QMOM has been validated for small particles in the study of aerosols in chemical engineering. It provides a precise and efficient numerical method in order to follow the size distribution of particles, without inertia, experiencing some aggregation-breakage phenomena (Marchisio, *et al.*, 2003*b*). One of the main limitations of QMOM is that since the dispersed phase is represented through the moments of the size distribution, the phase-average velocity of different dispersed phases must be used to solve the transport equations for the moments. Thus, in order to use this method in the context of sprays for which the inertia determines the dynamical behavior of the droplets, it is necessary to extend QMOM to handle cases where each droplet size is convected by its own velocity. In order to address these issues, the direct quadrature method of moments (DQMOM) has been formulated and validated (Marchisio and Fox, 2005). Unlike the standard moment methods, with DQMOM the volume fractions and diameters are tracked directly, rather than the moments themselves.

The newly developed parallel parent and daughter classes (PPDC) method, which uses the PD algorithm for reducing the computational cost of the QMOM, is another effective numerical method to predict size distributions (Bove, *et al.*, 2005). The PPDC is shown to perform as well as QMOM and DQMOM and in some cases even better, by using only a few classes (2-3) (Bove, *et al.*, 2004). The advantage of the PPDC algorithm over the QMOM and DQMOM, when applied to CFD, consists in a reduction of the additional transport of scalars by a factor of two.

In the present chapter, mathematical and numerical aspects of the DQMOM-multi-fluid model are exposed. First, the model is derived and the governing equations are presented. Then, implementation of droplet breakup and coalescence models in the DQMOM-multi-fluid model is described. Finally, issues related to the numerical implementation of DQMOM in the CFD code Fluent are addressed.

6.2 Population Balance Equation

A polydisperse non-evaporating droplet phase can be modeled by a multivariate number distribution function defined as $n\left(d,U_i,x_i,t\right)$, where

$$n\left(d,U_i,x_i,t\right)\mathrm{d}d\mathrm{d}U_i\mathrm{d}x_i \tag{6.1}$$

denotes the average number of droplets, at time *t*, in the diameter range d*d* about *d*, with velocities in the range dU_i about U_i, and located in the spatial range dx_i about x_i. Here, the droplets are considered to be spherical and characterized by their diameter *d*.

Ramkrishna (2000) discusses the distribution and the population balance equation (PBE). Conservation of droplet numbers leads to the following equation, which governs the distribution function $n\left(d,U_i\right)$ for the droplets (spatial and time dependencies are suppressed for simplicity):

$$\frac{\partial}{\partial t}n\left(d,U_i\right)+\frac{\partial}{\partial x_i}\left[U_i n\left(d,U_i\right)\right]+\frac{\partial}{\partial U_i}\left[F_i n\left(d,U_i\right)\right]=S\left(d,U_i\right) \tag{6.2}$$

where $F_i=\mathrm{d}U_i/\mathrm{d}t$ is the force acting to accelerate the droplets, and $S\left(d,U_i\right)$ represents the rate of change of the distribution function caused by droplet formation or destruction processes such as nucleation, droplet breakup, or collisions. Both F_i and *S* depends on $\left(d,U_i,x_i,t\right)$ and the local properties of the gas. Eq. (6.2) is also known as the spray equation (Williams, 1985).

6.3 Direct Quadrature Method of Moments

The derivation of the DQMOM-multi-fluid model is conducted following two steps. The key idea, in a first step, is to reduce the size of the phase space $\left(d,U_i\right)$ and to consider only the mean velocity for a given droplet size, at a given time, and a given position. Integration of the distribution function gives the averaged values used in the multi-fluid approach. The droplet number distribution is given by the three-dimensional integral

$$n\left(d\right)=\int_{-\infty}^{\infty} n\left(d,U_i\right)\mathrm{d}U_i \tag{6.3}$$

U_i can be integrated to give the average velocity conditioned on d

$$U_i\left(d\right)=\frac{\int_{-\infty}^{\infty} U_i n\left(d,U_i\right)\mathrm{d}U_i}{n\left(d\right)} \tag{6.4}$$

Assuming that for a given droplet size, at a given time and location, there is only one characteristic averaged velocity and that the velocity variation around the averaged velocity is zero in each direction, the velocity distribution is a Dirac delta function and the distribution function is approximated as

$$n\left(d,U_i\right)=n\left(d\right)\delta\left[U_i-U_i\left(d\right)\right] \tag{6.5}$$

Integrating out the velocity in Eq. (6.2), the droplet-phase population balance equation is obtained as

$$\frac{\partial}{\partial t}n\left(d\right)+\frac{\partial}{\partial x_i}\left[U_i\left(d\right)n\left(d\right)\right]=S\left(d\right) \tag{6.6}$$

where $S\left(d\right)$ is the size-dependant source term for breakup and coalescence.

Instead of solving the droplet size distribution directly, the methods of moments aim to solve some of the DSD properties, for instance the lower order moments of the distribution. The generic k^{th} moment balance equation can be derived multiplying Eq. (6.6) by d^k and integrating over the droplet size domain:

$$\frac{\partial}{\partial t}\int_0^\infty d^k n(d)\,\mathrm{d}d+\frac{\partial}{\partial x_i}\int_0^\infty d^k U_i(d)\,n(d)\,\mathrm{d}d=\int_0^\infty d^k S(d)\,\mathrm{d}d \qquad (6.7)$$

Using DQMOM, the distribution function $n(d)$ is approximated by a summation of N Dirac delta functions (Marchisio and Fox, 2005):

$$n(d)=\sum_{q=1}^{N}\omega_q\delta\left[d-d_q\right] \qquad (6.8)$$

where ω_q is the weight of the delta function centered at the characteristic droplet diameter d_q. The transport equations for the N weights ω_q and the N abscissas d_q can be found from this representation of the droplet size distribution. Inserting Eq. (6.8) in Eq. (6.7) yields

$$\sum_{q=1}^{N}\left[\frac{\partial}{\partial t}\left(\omega_q d_q^k\right)+\frac{\partial}{\partial x_i}\left(U_{i,q}\omega_q d_q^k\right)\right]=\overline{S}_{m_k} \qquad k=0,\ldots,2N-1 \quad (6.9)$$

where $U_{i,q}=U_i\left(d_q\right)$ and the source term for the k^{th} moment is defined by

$$\overline{S}_{m_k}=\int_0^\infty d^k S(d)\,\mathrm{d}d \qquad (6.10)$$

The time derivative term can be written as

$$\frac{\partial}{\partial t}\left(\omega_q d_q^k\right)=(1-k)\,d_q^k\frac{\partial}{\partial t}\left(\omega_q\right)+kd_q^{k-1}\frac{\partial}{\partial t}\left(\omega_q d_q\right) \qquad (6.11)$$

and the convective term can be expressed as

$$\frac{\partial}{\partial x_i}\left(U_{i,q}\omega_q d_q^k\right)=(1-k)\,d_q^k\frac{\partial}{\partial x_i}\left(U_{i,q}\omega_q\right)+kd_q^{k-1}\frac{\partial}{\partial x_i}\left(U_{i,q}\omega_q d_q\right) \quad (6.12)$$

Introducing the weighted abscissas $\delta_q=\omega_q d_q$ and substituting the reformulated derivatives Eqs. (6.11) and (6.12) into Eq. (6.9), yields

$$\sum_{q=1}^{N}\left\{\left(1-k\right)d_q^k\left[\frac{\partial}{\partial t}\omega_q+\frac{\partial}{\partial x_i}\left(U_{i,q}\omega_q\right)\right]+kd_q^{k-1}\left[\frac{\partial}{\partial t}\delta_q+\frac{\partial}{\partial x_i}\left(U_{i,q}\delta_q\right)\right]\right\} \\ =\overline{S}_{m_k} \tag{6.13}$$

Defining S_{ω_q} and S_{δ_q} to be the source terms for the weights ω_q and the weighted abscissas δ_q, respectively, the DQMOM transport equations for the weights and the weighted abscissas can be written as

$$\begin{aligned} &\frac{\partial}{\partial t}\omega_q+\frac{\partial}{\partial x_i}\left(U_{i,q}\omega_q\right)=S_{\omega_q} \qquad q=1,\ldots,N \\ &\frac{\partial}{\partial t}\delta_q+\frac{\partial}{\partial x_i}\left(U_{i,q}\delta_q\right)=S_{\delta_q} \qquad q=1,\ldots,N \end{aligned} \tag{6.14}$$

Using these definitions, Eq. (6.13) can be written in a simpler form:

$$\left(1-k\right)\sum_{q=1}^{N}d_q^kS_{\omega_q}+k\sum_{q=1}^{N}d_q^{k-1}S_{\delta_q}=\overline{S}_{m_k} \qquad k=0,\ldots,2N-1 \tag{6.15}$$

As seen from this equation, the source terms of the transport equations for the N weights ω_q and the N weighted abscissas δ_q can be defined through a linear system found from the first $2N$ integer moments (i.e., $k = 0,\ldots, 2N-1$). This linear system can be written in matrix form as

$$\mathbf{Ax}=\mathbf{b} \tag{6.16}$$

where the $2N\times 2N$ coefficient matrix $\mathbf{A}=\left[\mathbf{A}_1\mathbf{A}_2\right]$ is defined by

$$\mathbf{A}_1=\begin{bmatrix} 1 & \cdots & 1 \\ 0 & \cdots & 0 \\ -d_1^2 & \cdots & -d_N^2 \\ \vdots & \ddots & \vdots \\ 2\left(1-N\right)d_1^{2N-1} & \cdots & 2\left(1-N\right)d_N^{2N-1} \end{bmatrix} \tag{6.17}$$

and

$$\mathbf{A}_2 = \begin{bmatrix} 0 & \cdots & 0 \\ 1 & \cdots & 1 \\ 2d_1 & \cdots & 2d_N \\ \vdots & \ddots & \vdots \\ (2N-1)d_1^{2N-2} & \cdots & (2N-1)d_N^{2N-2} \end{bmatrix} \tag{6.18}$$

The $2N$ vector of unknowns **x** is defined by

$$\mathbf{x} = \begin{bmatrix} S_{\omega_1} & \cdots & S_{\omega_N} & S_{\delta_1} & \cdots & S_{\delta_N} \end{bmatrix}^{\mathrm{T}} \tag{6.19}$$

and the known right-hand side is

$$\mathbf{b} = \begin{bmatrix} \overline{S}_{m_0} & \cdots & \overline{S}_{m_{2N-1}} \end{bmatrix}^{\mathrm{T}} \tag{6.20}$$

As shown below, with the DQMOM approximation, the right-hand side of Eq. (6.10) is closed in terms of N weights and abscissas. As N increases, the quadrature approximation will approach the exact value, although at a higher computational cost.

If the abscissas d_q are unique, then **A** will be full rank. For this case, the source terms for the transport equations of the weights ω_q and weighted diameters δ_q can be found by inverting **A** in Eq. (6.16):

$$\mathbf{x} = \mathbf{A}^{-1}\mathbf{b} \tag{6.21}$$

There are cases for which the matrix **A** is not full rank (the matrix is singular). These cases can occur when one or more of the abscissas d_q are non-distinct. In general this problem occurs due to initial conditions and must be addressed in order to formulate a stable numerical algorithm. To overcome this problem, a small perturbation can be added to the abscissas to make **A** full rank. Note that it is not necessary to perturbate d_q when computing the right hand side of Eq. (6.16), and that the perturbations will leave the weights ω_q unchanged. Another important case where **A** can be singular is when the weights ω_q and weighted abscissas δ_q are zero. Thus, the abscissas d_q are undefined, the matrix **A** is not invertible, and therefore the source terms S_{ω_q} and S_{δ_q} cannot be found. A possible solution is to force the abscissas d_q to be equal to non-zero values. The choice of the numerical values for the abscissas is not unique, but usually the computation of $\overline{S}_{m_k}$ provide a useful hint. Another more efficient way to get around the problem is to use the moments of the droplet size distribution to build a quadrature approximation and then use the abscissas in the definition of **A**. If, for example, breakup produces droplets with a general distribution the corresponding moments can be determined. By using the first 2*N* moments it is possible to determine the *N* abscissas by means of the PD algorithm (Gordon, 1968).

6.3.1 DQMOM-Multi-Fluid Model

In order to be consistent with the variables used in the multi-fluid model, the weights and abscissas need to be related to the droplet volume fraction α_q and the effective diameter $\alpha_q d_q$ for each droplet phase. For spherical droplets, the volume fraction of each droplet phase is related to the abscissas d_q and weights ω_q by

$$\alpha_q = \frac{\pi}{6}\omega_q d_q^3 = \frac{\pi}{6}\frac{\delta_q^3}{\omega_q^2} \tag{6.22}$$

and the effective diameter of the droplet phase is

$$\alpha_q d_q = \frac{\pi}{6}\omega_q d_q^4 = \frac{\pi}{6}\frac{\delta_q^4}{\omega_q^3} \tag{6.23}$$

Using Eqs. (6.22) and (6.23), the transport equations for α_q and d_q can be written as

$$\frac{\partial}{\partial t}\left(\alpha_q \rho_l\right) + \frac{\partial}{\partial x_i}\left(\alpha_q \rho_l U_{i,q}\right) = \frac{\pi}{2}\rho_l d_q^2 S_{\delta_q} - \frac{\pi}{3}\rho_l d_q^3 S_{\omega_q} \tag{6.24}$$

and

$$\frac{\partial}{\partial t}\left(\alpha_q \rho_l d_q\right) + \frac{\partial}{\partial x_i}\left(\alpha_q \rho_l U_{i,q} d_q\right) = \frac{2\pi}{3}\rho_l d_q^3 S_{\delta_q} - \frac{\pi}{2}\rho_l d_q^4 S_{\omega_q} \tag{6.25}$$

Previous validation studies of DQMOM have demonstrated that by using as few as N = 2 or 3 nodes, the lower order moments of the size distribution are tracked with small errors (Marchisio and Fox, 2005). The DQMOM approach has been tested for predicting aggregation, breakage, and molecular growth. It has been shown that the nodes of the quadrature approximation can be thought of as different dispersed phases with characteristic diameter d_q and velocity $U_{i,q}$, and that the quadrature approximation actually resembles the shape of the underlying size distribution (Marchisio and Fox, 2005). Each node of the quadrature approximation is calculated in order to guarantee that the moments of the size distribution are tracked with high accuracy but, at the same time, each node is treated as a distinct dispersed phase. The DQMOM approach has been applied for the simulation of polydisperse gas-solid systems using the Eulerian multi-fluid model to compute the phase velocities (Fan, *et al.*, 2004).

6.4 Implementation of Breakup and Coalescence

In this work, changes in the DSD due only to breakup (*bu*), coalescence (*coal*), collision-induced breakup (*frag*) are considered. For this case, the moment transform of the breakup and coalescence source terms is (Marchisio and Fox, 2005)

$$\overline{S}_{m_k} = \overline{B}_k^{bu} - \overline{D}_k^{bu} + \overline{B}_k^{coal} - \overline{D}_k^{coal} + \overline{B}_k^{frag} - \overline{D}_k^{frag} \tag{6.26}$$

where the moments of the birth (B) and death (D) rates are defined by

$$
\begin{aligned}
\overline{B}_k^{bu} &= \int_0^\infty \int_0^\infty d^k b\left(d \middle| d_q\right) a\left(d_q\right) n\left(d_q\right) \mathrm{d}d_q \mathrm{d}d \\
\overline{D}_k^{bu} &= \int_0^\infty d_q^k a\left(d_q\right) n\left(d_q\right) \mathrm{d}d_q \\
\overline{B}_k^{coal} &= \frac{1}{2} \int_0^\infty \int_0^\infty \left(d_p^3 + d_q^3\right)^{k/3} c\left(d_p, d_q\right) n\left(d_p\right) n\left(d_q\right) \mathrm{d}d_p \mathrm{d}d_q \\
\overline{D}_k^{coal} &= \int_0^\infty \int_0^\infty d_q^k c\left(d_p, d_q\right) n\left(d_p\right) n\left(d_q\right) \mathrm{d}d_p \mathrm{d}d_q \\
\overline{B}_k^{frag} &= \frac{1}{2} \int_0^\infty \int_0^\infty \int_0^\infty d^k f\left(d \middle| d_p, d_q\right) e\left(d_p, d_q\right) n\left(d_p\right) n\left(d_q\right) \mathrm{d}d_p \mathrm{d}d_q \mathrm{d}d \\
\overline{D}_k^{frag} &= \int_0^\infty \int_0^\infty d_q^k e\left(d_p, d_q\right) n\left(d_p\right) n\left(d_q\right) \mathrm{d}d_p \mathrm{d}d_q
\end{aligned}
\tag{6.27}
$$

In these expressions, $a\left(d_q\right)$ is the breakup kernel, which is the frequency of breakup of a droplet of diameter d_q, $b\left(d \middle| d_q\right)$ is the breakup daughter distribution function, which contains information about the diameter d of the droplets produced during the breakup of a droplet of diameter d_q, $c\left(d_p, d_q\right)$ is the coalescence kernel, $e\left(d_p, d_q\right)$ is the collision induced breakup kernel, and $f\left(d \middle| d_p, d_q\right)$ is the fragmentation daughter distribution function, which contains information about the size d of the droplets produced during the collision-induced breakup of two droplets of diameters d_p and d_q.

DQMOM is based on the quadrature approximation reported in Eq. (6.8). Thus, using this approximation, the source term in Eq. (6.26) is closed:

$$
\begin{aligned}
\overline{S}_{m_k} = &\sum_{q=1}^{N} \overline{b}_q^{(k)} a_q \omega_q - \sum_{q=1}^{N} d_q^k a_q \omega_q \\
&+ \frac{1}{2} \sum_{p=1}^{N} \sum_{q=1}^{N} \left(d_p^3 + d_q^3\right)^{k/3} c_{pq} \omega_p \omega_q - \sum_{p=1}^{N} \sum_{q=1}^{N} d_q^k c_{pq} \omega_p \omega_q \\
&+ \frac{1}{2} \sum_{p=1}^{N} \sum_{q=1}^{N} \overline{f}_{pq}^{(k)} e_{pq} \omega_p \omega_q - \sum_{p=1}^{N} \sum_{q=1}^{N} d_q^k e_{pq} \omega_p \omega_q
\end{aligned}
\tag{6.28}
$$

where

$$\begin{aligned}
a_q &= a\left(d_q\right) \\
\overline{b}_q^{(k)} &= \int_0^\infty d^k b\left(d \middle| d_q\right) \mathrm{d}d \\
c_{pq} &= c\left(d_p, d_q\right) \\
e_{pq} &= e\left(d_p, d_q\right) \\
\overline{f}_{pq}^{(k)} &= \int_0^\infty d^k f\left(d \middle| d_p, d_q\right) \mathrm{d}d
\end{aligned} \tag{6.29}$$

Submodels for simulating the physical processes of the droplets such as breakup and droplet-droplet collision were presented in Chapter 3. However, to solve the PBE using DQMOM, these models must be translated into the DQMOM frame. The expressions below describe how the models have been transformed to the kernels and daughter distribution functions in Eq. (6.29).

6.4.1 Breakup Daughter Distribution Function

The breakup daughter distribution function corresponding to an erosion type breakup mechanism is given by Eq. (3.14). Using this, the moment transform of the daughter distribution function becomes

$$\overline{b}_q^{(k)} = \gamma d_{st}^k + \left(d_q^3 - \gamma d_{st}^3\right)^{k/3} \qquad \text{for erosion type breakup} \tag{6.30}$$

If symmetric breakup is considered, the breakup mechanism is given by Eq. (3.15). The moment transform of the daughter distribution function corresponding to this mechanism is

$$\overline{b}_q^{(k)} = 2^{(3-k)/3} d_q^k \qquad \text{for symmetric breakup} \tag{6.31}$$

6.4.2 Breakup Kernel

The WAVE breakup model was given in Section 3.2.3. To implement the WAVE model, it is of interest to make sure that the droplet sizes are consistent with the original DDM model of Reitz and Diwakar (1987). In that model, the change in the Sauter mean diameter (SMD), $d_{32} = m_3/m_2$, is calculated as follows:

$$\frac{\mathrm{d}\, m_3/m_2}{\mathrm{d}t} = -\frac{d_q - d_{st}}{\tau_{bu}} \tag{6.32}$$

The breakup kernel $a_q = a\left(d_q\right)$ is chosen to make sure that the size distribution after breakup corresponds to that given by Eq. (6.32) since that result is based on experimental findings. The breakup process must obey liquid mass conservation, $\mathrm{d}m_3/\mathrm{d}t = 0$, and conservation of SMD. For the DDM model, the conservation of the second order moment due to the breakup of a single droplet parcel is given by

$$\frac{\mathrm{d}m_2}{\mathrm{d}t} = \omega_q d_q \frac{d_q - d_{st}}{\tau_{bu}} \tag{6.33}$$

For the DQMOM model, the moment transform of the breakup source term for the second order moment, $\overline{S}_{m_2}$, due to breakup of droplets of diameter d_q is given by

$$\overline{S}_{m_2} = \overline{b}_q^{(2)} a_q \omega_q - d_q^2 a_q \omega_q \tag{6.34}$$

Thus, Eqs. (6.33) and (6.34) are rewritten as follows:

$$\omega_q d_q \frac{d_q - d_{st}}{\tau_{bu}} = \overline{b}_q^{(2)} a_q \omega_q - d_q^2 a_q \omega_q \tag{6.35}$$

and the solution of this equation yields a_q:

$$a_q = \frac{1 - d_{st}/d_q}{\left(\overline{b}_q^{(2)}/d_q^2 - 1\right)\tau_{bu}} \tag{6.36}$$

As seen, a_q depends on the breakup daughter distribution function $\overline{b}_q^{(k)}$. This is because the original DDM model only gives a diameter reduction rate for a droplet parcel. If the daughter distribution function corresponding to an erosion type breakup mechanism, Eq. (6.30), is chosen, the breakup kernel becomes

$$a_q = \frac{1 - d_{st}/d_q}{\left(\frac{\gamma d_{st}^2}{d_q^2} + \left(1 - \frac{\gamma d_{st}^3}{d_q^3}\right)^{2/3} - 1\right)\tau_{bu}} \quad \text{for erosion type breakup} \tag{6.37}$$

Assuming that the number of droplets of droplets of diameter d_{st} produced is equal to the ratio between the parent drop surface area and the stable droplet surface area, $\gamma = d_q^2/d_{st}^2$, the breakup kernel reduces to

$$a_q = \frac{\left(1 - d_{st}/d_q\right)^{1/3}}{\tau_{bu}} \quad \text{for erosion type breakup with } \gamma = \frac{d_q^2}{d_{st}^2} \tag{6.38}$$

If instead the daughter distribution function corresponding to the symmetric breakup mechanism, Eq. (6.31), is considered, the breakup kernel becomes

$$a_q = \frac{1 - d_{st}/d_q}{\left(2^{1/3} - 1\right)\tau_{bu}} = \frac{1 - d_{st}/d_q}{0.26\tau_{bu}} \quad \text{for symmetric breakup} \tag{6.39}$$

These breakup kernels ensure that the SMD reduction rate is consistent with the original DDM model. However, other breakup models using the rate approach can easily be implemented.

6.4.3 Coalescence and Droplet Collision Induced Breakup Kernels

A composite droplet-droplet collision model was given in Section 3.3. The model takes coalescence and bounce into account, as well as collision-induced breakup (fragmentation). The collision coefficient was given by

$$\beta_{pq} = \pi d_{pq}^2 U_{rel} \tag{6.40}$$

where $d_{pq} = \left(d_p + d_q\right)/2$ and $U_{rel} = \overline{\left|\vec{u}_p - \vec{u}_q\right|}$ is the average relative velocity between the two droplet classes obtained from

$$U_{rel} = \sqrt{\left|\vec{U}_p - \vec{U}_q\right|^2 + 2\left(1 - \rho_{pq}\right)\left(k_p + k_q\right)} \tag{6.41}$$

where $\vec{U}$ is mean droplet phase velocity, k is the droplet phase turbulent kinetic energy, and ρ_{pq} is the correlation coefficient obtained from

$$\rho_{pq} = 1 - \frac{3.6\left(\frac{\varepsilon_p + \varepsilon_q}{2} d_{pq}\right)^{2/3}}{k_p + k_q} \tag{6.42}$$

where ε is the droplet turbulent kinetic energy dissipation rate.

With the collision coefficient β_{pq}, the expression for the coalescence kernel becomes

$$c_{pq} = \min\left(E_{boun}, E_{coal}\right)\beta_{pq} \tag{6.43}$$

where the probability of coalescence at low collisional Weber numbers, E_{boun}, is given by Eq. (3.26), and the probability of coalescence at higher collisional Weber numbers, E_{coal}, is given by Eq. (3.24). The collisions undergoing the bounce regime are ignored in this model because the diameter and momentum of the droplets are conserved during a bounce collision.

The third possible outcome of droplet-droplet collisions is the breakup of the original droplets into smaller droplets. The collision-induced breakup kernel is expressed as

$$e_{pq} = \left(1 - E_{coal}\right)\beta_{pq} \tag{6.44}$$

and the moment transform of the fragmentation daughter distribution function corresponding to this collision induced breakup mechanism is

$$\overline{f}_{pq}^{(k)} = \left(d_p^3 + d_q^3\right) d_{frag}^{k-3} \tag{6.45}$$

where the diameter of the droplet fragments, d_{frag}, is given by the correlation in Eq. (3.27).

6.5 Solution Method

DQMOM is implemented in the CFD code Fluent 6.2 by representing each node of the quadrature approximation as a distinct droplet phase. In the Eulerian multi-fluid model each droplet phase has its own momentum balance, giving the DQMOM-multi-fluid model the ability to treat polydispersed droplets, which have their own inertia and size-conditioned dynamics. Equation (6.25) is solved in the multi-fluid model as a set of user-defined scalars.

In the finite-volume calculation of the droplet flow Eqs. (6.24) and (6.25) govern the droplet size evolution at a cell centre due to convection and breakup and coalescence. It is important to appreciate the different timescales involved in the different processes. The characteristic convection time can be expressed as

$$\tau_{conv} = \frac{\Delta x}{U} \tag{6.46}$$

where Δx is the cell length and U is the cell velocity. The characteristic time of the breakup process can be expressed as

$$\tau_{bu} = \frac{1}{a_q} \tag{6.47}$$

and the characteristic time of the collision process can be expressed as

$$\tau_{co} = \frac{1}{\beta_{pq}\omega_q} = \frac{\pi}{6}\frac{d_q^3}{\beta_{pq}\alpha_q} \tag{6.48}$$

6.5.1 Splitting Method

Equations (6.24) and (6.25) are solved by a simple splitting method, so that different processes are treated in separate fractional steps. Equations (6.24) and (6.25) are split into a pure convection system:

$$\begin{gathered}\frac{\partial}{\partial t}\left(\alpha_q\rho_l\right)+\frac{\partial}{\partial x_i}\left(\alpha_q\rho_l U_{i,q}\right)=0\\\frac{\partial}{\partial t}\left(\alpha_q\rho_l d_q\right)+\frac{\partial}{\partial x_i}\left(\alpha_q\rho_l U_{i,q} d_q\right)=0\end{gathered}\tag{6.49}$$

and a pure breakup and coalescence system:

$$\begin{gathered}\frac{\partial}{\partial t}\left(\alpha_q\rho_l\right)=\frac{\pi}{2}\rho_l d_q^2 S_{\delta_q}-\frac{\pi}{3}\rho_l d_q^3 S_{\omega_q}\\\frac{\partial}{\partial t}\left(\alpha_q\rho_l d_q\right)=\frac{2\pi}{3}\rho_l d_q^3 S_{\delta_q}-\frac{\pi}{2}\rho_l d_q^4 S_{\omega_q}\end{gathered}\tag{6.50}$$

In the first fractional step, the pure convection system is integrated over a time step Δt, to get $\alpha_q^*\left(t+\Delta t\right)$ and $\alpha_q^* d_q^*\left(t+\Delta t\right)$. Then in the second fractional step, the pure breakup and coalescence system is integrated (from initial conditions $\alpha_q^*\left(t+\Delta t\right)$ and $\alpha_q^* d_q^*\left(t+\Delta t\right)$) over a time step Δ$t$ to get $\alpha_q\left(t+\Delta t\right)$ and $\alpha_q d_q\left(t+\Delta t\right)$.

The overall fractional time-stepping is represented as

$$\begin{gathered}\alpha_q\left(t\right)\xrightarrow{\text{transport}}\alpha_q^*\left(t+\Delta t\right)\xrightarrow{\substack{\text{breakup and}\\\text{coalescence}}}\alpha_q\left(t+\Delta t\right)\\\alpha_q d_q\left(t\right)\xrightarrow{\text{transport}}\alpha_q^* d_q^*\left(t+\Delta t\right)\xrightarrow{\substack{\text{breakup and}\\\text{coalescence}}}\alpha_q d_q\left(t+\Delta t\right)\end{gathered}\tag{6.51}$$

The breakup and coalescence source terms are decoupled from the transport terms. Thus, the problem statement of solving breakup and coalescence source terms is based on a given droplet distribution (volume fractions and diameters) at time t for determining the droplet distribution at time $t + \Delta t$ resulting from breakup and coalescence.

An analysis shows that, in the limit as Δt tends to zero, the error on each time step is $O\left(\Delta t^2\right)$ so that the error for a fixed time interval is $O\left(\Delta t\right)$, i.e. the method is first-order accurate. Numerical tests confirm that the method is first-order accurate (Yang and Pope, 1998). In practice, the time step is selected to be small compared to the characteristic convection timescale (e.g. $\Delta t=\frac{1}{10}\tau_{conv}$), but this may be several orders of magnitude larger than the smallest breakup or coalescence timescale.

In the numerical implementation in Fluent, Eq. (6.49) is implicitly integrated at every time step and Eq. (6.50) is explicitly integrated at the end of every time step.

Implicit Time Integration

In the numerical implementation in Fluent, Eq. (6.49) is implicitly integrated at every time step. In this method, all of the fluxes and source terms are evaluated in terms of the unknown variable values at the new time level:

$$\phi^{n+1} = \phi^{n} + F\left(\phi^{n+1}\right)\Delta t \tag{6.52}$$

where ϕ is a scalar quantity, superscripts ^{n} and $^{n+1}$ refer to values at the current time level t and time level $t + \Delta t$, respectively. The function $F\left(\phi^{n+1}\right)$ represents the sum of convective, diffusive, and source terms. This implicit equation can be solved iteratively by initializing ϕ^{i} to ϕ^{n} and iterating the equation

$$\phi^{i} = \phi^{n} + F\left(\phi^{i}\right)\Delta t \tag{6.53}$$

until ϕ^{i} stops changing. At this point, ϕ^{n+1} is set to ϕ^{i}.

The shortcomings of this method are the need to solve a large coupled set of equations at each time step (requires intermediate iterative stages). The advantage is that it is unconditionally stable with respect to time step size.

Explicit Time Integration

Equation (6.50) is explicitly integrated at the end of every time step. In this method sources are evaluated using known values at t. Thus the new value of the unknown for a control volume can be explicitly calculated:

$$\phi^{n+1} = \phi^{n} + F\left(\phi^{n}\right)\Delta t \tag{6.54}$$

The advantage is that explicit time stepping is less expensive than the implicit time stepping method. However, the time step Δt is restricted to the stability limit. For Eq. (6.50) with no convection and diffusion, the time step should satisfy the following conditions:

$$\Delta t < \begin{cases} -\dfrac{6\alpha_q}{\pi d_q^3 S_{\omega_q}} & \text{if } S_{\omega_q} < 0 \\ -\dfrac{6\alpha_q}{\pi d_q^2 S_{\delta_q}} & \text{if } S_{\delta_q} < 0 \end{cases} \tag{6.55}$$

This problem must be addressed in order to formulate a stable numerical algorithm. For the computational cell where a stability problem happens, the time step used for the DQMOM calculation, Eq. (6.50), will not be the same as the time step Δt_{Fluent} used for the rest of the transport equations in Fluent. Based on the restrictions in Eq. (6.55), the time step Δt_{DQMOM} for Eq. (6.50) is refined automatically:

$$\Delta t_{\text{DQMOM}} = \frac{\Delta t_{\text{Fluent}}}{2^n} \tag{6.56}$$

where n is an integer. The maximum allowed n is chosen to be 10. If this approach does not "solve" the stability problem, the source vector **x**, Eq. (6.19), is set to zero and Eq. (6.50) is not solved. In this case, convection in physical space will solve the stability problem. However, it is important to highlight that the frequency of this event is very low in the simulations.

6.5.2 Flow Chart

The flow chart for simulation of polydispersed gas-droplet flows is shown in Figure 6.1.

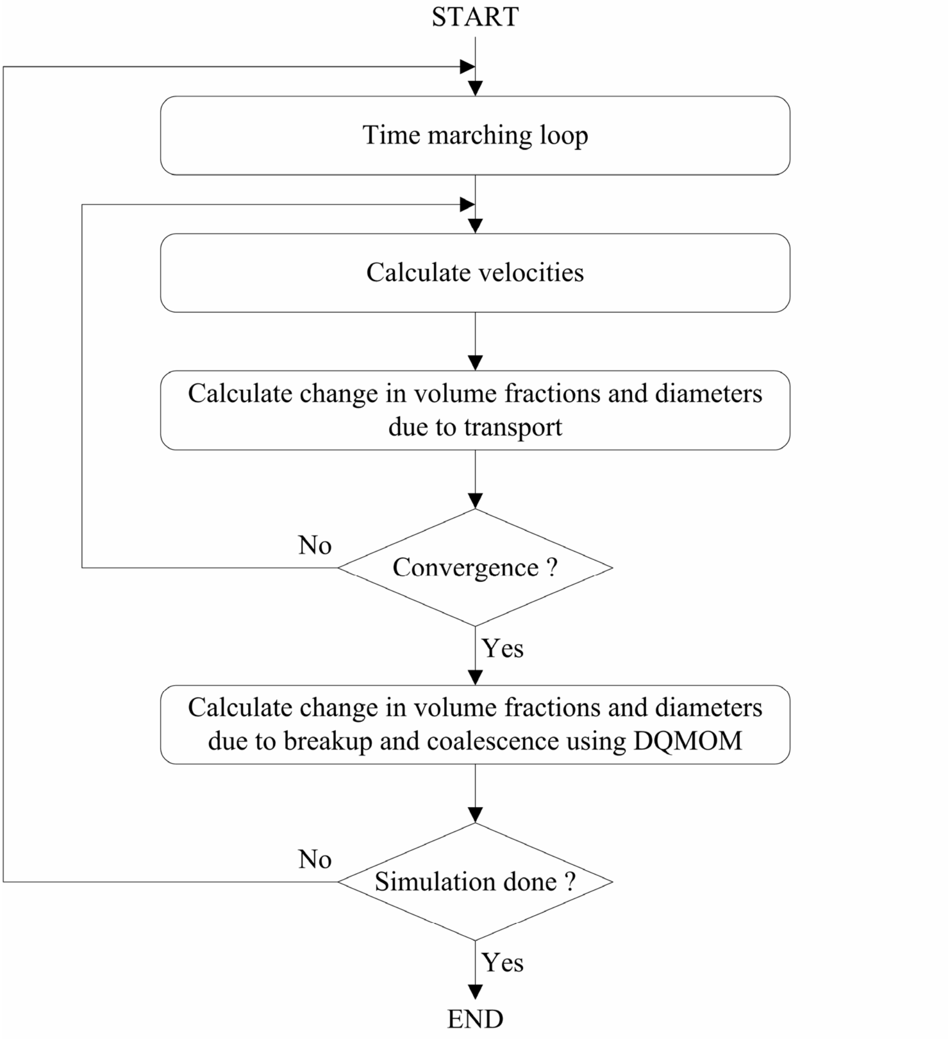

Figure 6.1: The flow chart of Fluent with DQMOM.

Chapter 7

Numerical Simulation of Internal Flow in a Large-Scale Pressure-Swirl Atomizer[*]

7.1 Introduction

The performance characteristics of an atomizer are directly influenced by geometrical parameters, fluid properties, and operational conditions. This needs a physical understanding of both the internal flow of the atomizer and the mechanisms of spray formation outside the nozzle. In this chapter, the focus is on the internal flow in a pressure-swirl atomizer.

Historically, studies of atomization have been focused on breakup of simple forms of bulk fluids (e.g., jets and planar sheets), on the statistical nature of sprays (e.g., droplet size distribution), and on the development of correlations that relate some atomizer characteristic dimensions and operating parameters to relevant spray characteristics, e.g. see Lefebvre (1989). Less attention has been given to the internal flow in atomizers most likely due to the small size of practical atomizers which makes measurements difficult. Nonetheless, internal flows in atomizers are of interest due to their potential effect on the external atomization. It is, for

---

[*] Partly based on Madsen, *et al.* (2004).

example, well established that minor geometrical changes internally can greatly impact the characteristics of the spray that is produced. Unsteadiness of the flow inside the atomizer also has the potential to influence the breakup of the bulk liquid and droplet dispersion.

Many studies of liquid sheet atomization have shown that the mean droplet size is directly related to the thickness of the liquid film emanating from the atomizer. Therefore, the film thickness is considered as an important parameter governing atomizer performance. For a given mass-flow rate, studies have shown that geometrical design of the pressure-swirl atomizer is the primary factor that determines the internal flow-field and influences the atomizer performance parameters (Lefebvre, 1989). Despite the simple geometry of the pressure-swirl atomizer, the flow phenomena within the atomizer are complex.

One way to study internal flows in atomizers is to use large-scale models in experimental investigations. Studies reported by Jeng, *et al.* (1998), Cooper, *et al.* (1999), Ma, *et al.* (2000), Yule and Chinn (2000), and Cooper and Yule (2001) used large-scale pressure-swirl atomizers to enable measurements of air-core size and velocity fields inside the swirl chambers and orifices of the atomizers. Such studies are difficult to perform for production-scale atomizers.

As a compliment to the limitations of the experimental techniques, computational fluid dynamics (CFD) provide additional insight into the dynamics of the internal flow of pressure-swirl atomizers. However, when applying CFD in a new way to model fluid-dynamic behavior, some form of validation is necessary for reliable results. The main difficulty in the numerical simulation of the flow in a pressure-swirl atomizer is the accurate tracking of the liquid/air interface. Jeng, *et al.* (1998) and Sakman, *et al.* (2000) performed two-dimensional turbulent numerical simulations using moving grids to represent the free surface. Yule and Chinn (2000) used Fluent to solve for the liquid flow field. They determined the position of the interface with an approximate method and restricted their simulation to laminar flow. Steinthorsson and Lee (2000) used the Volume of Fluid (VOF) method in Fluent 5 to simulate three-dimensional flow, while a Reynolds stress model was used to model turbulence. More recently, von Lavante, *et al.* (2002) performed numerical simulations of internal flow in both two- and three-dimensional models using the VOF-method, and Buelow, *et al.* (2003)

used a two-phase VOF technique to simulate the flow through a small-scale pressure-swirl atomizer.

Hansen and Madsen (2001 and 2002) performed both experimental and computational studies of a large-scale pressure-swirl atomizer. The experimental values of tangential and axial velocities were obtained using laser Doppler anemometry. Radial profiles of axial and tangential velocities at five axial locations in the swirl chamber were measured. The gas-liquid flow was simulated using the homogeneous two-phase model in CFX-4.3. The flow-field was simulated using both a laminar flow assumption (QLES) and large eddy simulation (LES) turbulence modeling. It was found that the CFD models could capture the features of the internal flow of the atomizer. Trends of tangential velocity were predicted very well; however, magnitudes were underpredicted. Some of this discrepancy may be due to the grid used for the numerical simulations. The flow field was computed on a three-dimensional structured grid; however, the three feed slots were not included in the model, and therefore, the interaction between the feed slots and the swirl chamber was not captured.

In the present study, Fluent 6.1 is used to simulate the flow through the large-scale atomizer investigated by Hansen and Madsen (2001 and 2002). The primary focus of the analysis is on the internal flow characteristics in the swirl chamber, the resulting liquid film properties at the exit of the atomizer as well as the near-field spray-cone prior to film breakup. Where possible, comparisons are made with measured velocity profiles and photographs of the air-core and the spray-cone from the atomizer.

7.2 Atomizer Geometry and Flow Characteristics

The atomizer used in this study was scaled up from a production scale Danfoss atomizer. The atomizer shown in Figure 7.1 was manufactured from Plexiglas. Three feed slots (grooves) are positioned on top of a conical swirl chamber, which leads to the outlet via a cylindrical orifice. The top diameter of the swirl chamber is d_s = 100 mm and the length is $L - L_o$ = 40 mm. The orifice has a diameter of d_o = 20 mm and a length of L_o = 30 mm. In this atomizer, water flow axially into the swirl chamber through the tangential feed slots. The tangential inlet flow sets up a strong swirling flow inside the swirl chamber. Due to the strong swirl, an air core forms along the axis of the atomizer as seen in Figure 7.2. As the liquid leaves the orifice and the flow is no longer constrained by the atomizer walls, a swirling conical liquid sheet is formed as seen in Figure 7.3.

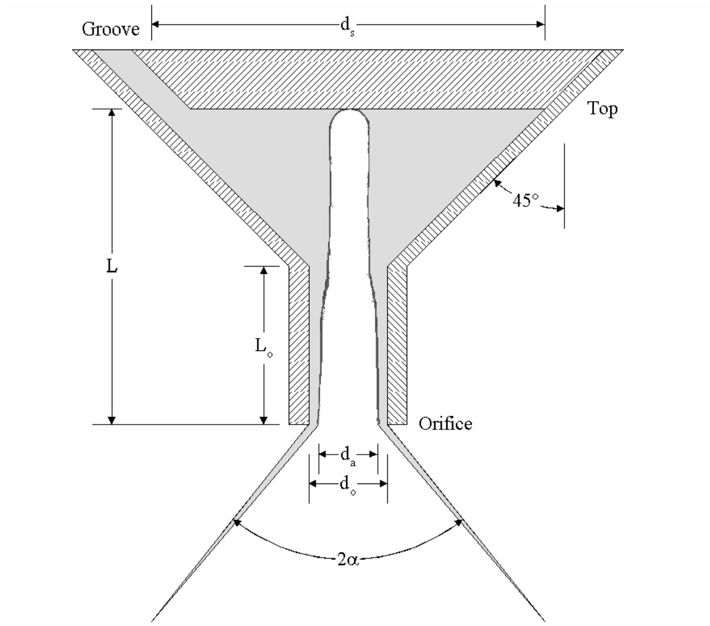

Figure 7.1: Geometry of the swirl camber.

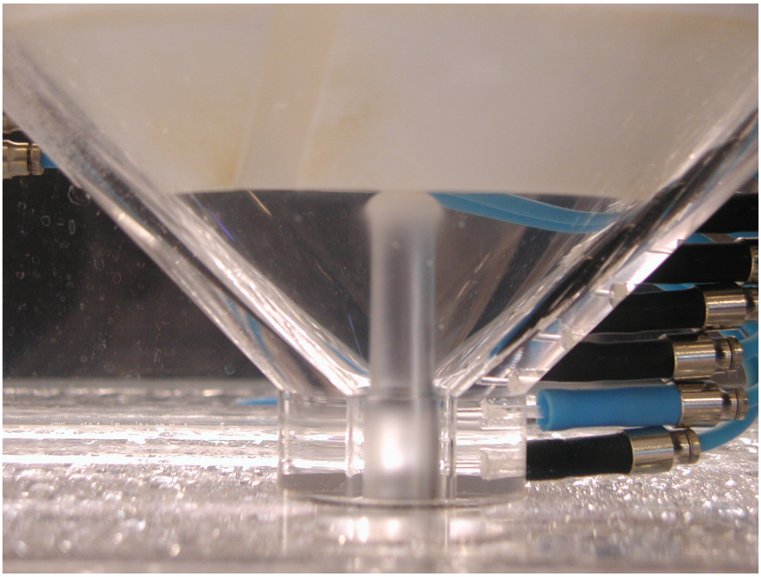

Figure 7.2: Photograph of the air-core in the large-scale atomizer.

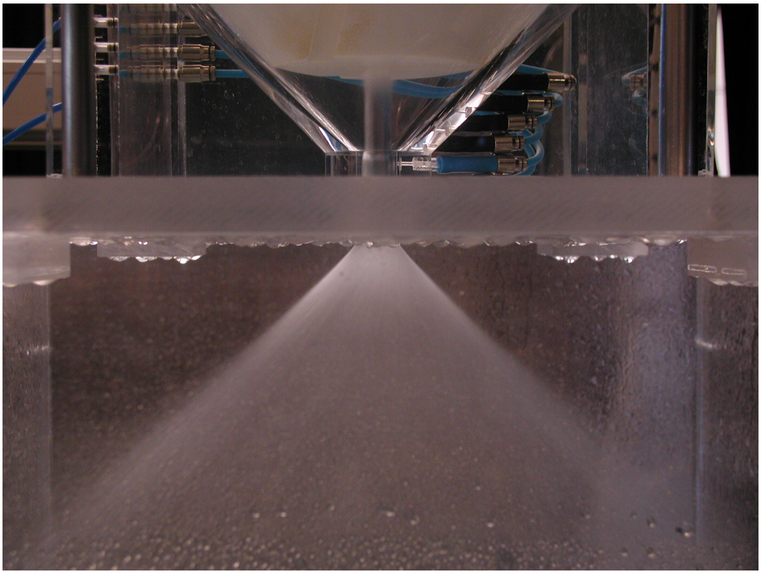

Figure 7.3: Photograph of the spray section of the large-scale atomizer.

7.3 Numerical Methods

Two grids are constructed for the present study. Initially, the numerical simulations are performed using a three-dimensional grid of hexahedral, tetrahedral and prismatic cells, consisting of the three feed slots, the conical swirl chamber, and the cylindrical orifice; see Figure 7.4. The tetrahedral and prismatic cells are located in the swirl chamber downstream the feed slots; the remaining cells are all hexahedral. Furthermore, cells are tightly spaced near the walls. When the solution is close to steady state, the mesh around the fluid interface is refined. This allows sharp velocity gradients and the interface itself to be captured more sharply. The original grid consists of 297,446 cells and the adapted consists of about 600,000 cells.

The second grid includes the three feed slots, the swirl chamber, the orifice, and the near field spray-cone 25 mm downstream of the atomizer; see Figure 7.5. This grid is constructed to model the liquid film cone exiting from the atomizer. As described above, the mesh around the interface is refined. The original grid consists of 553,549 cells, and the adapted of about 1.1 million cells.

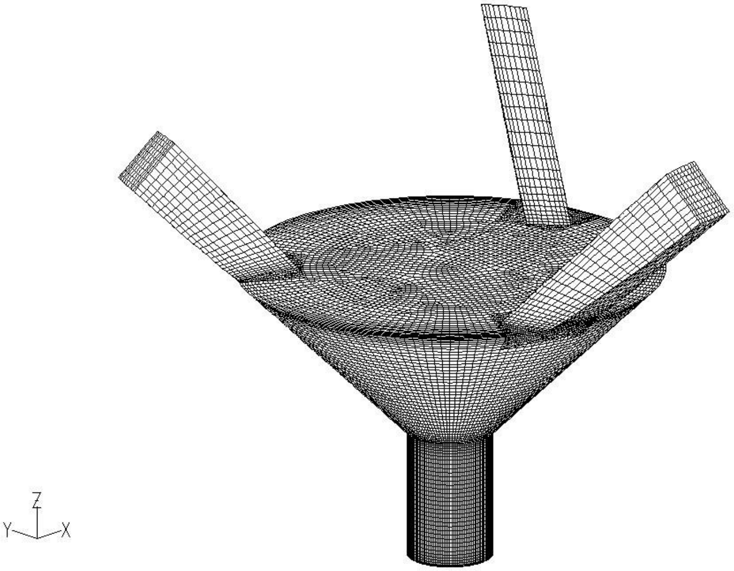

Figure 7.4: Grid consisting of three feed slots, swirl chamber, and orifice.

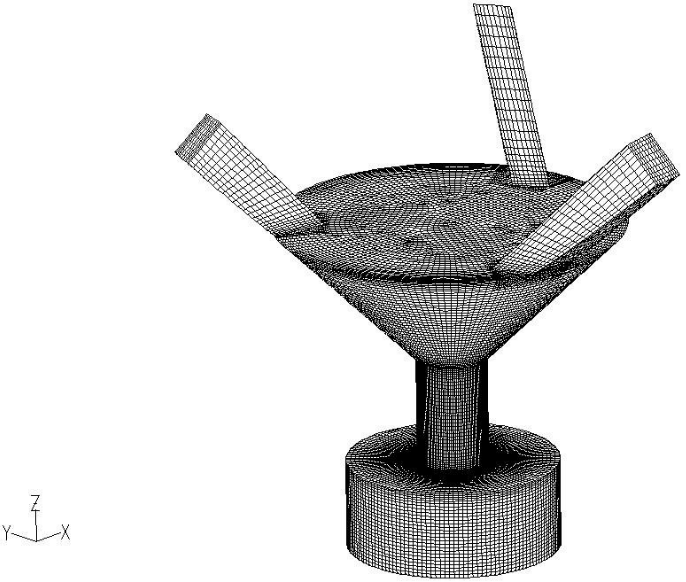

Figure 7.5: Grid consisting of three feed slots, swirl chamber, orifice, and near field spray-cone domain.

The two-phase flow simulations are carried out using the two approaches described below.

7.3.1 Volume of Fluid (VOF) Model

Many inter-phase tracking methods exist to simulate two-phase flow-fields and a brief examination of the currently available techniques can be found in Steinthorsson and Lee (2000). In this study, the VOF method, implemented in the commercially available CFD code Fluent 6.1, is used to simulate the flow of water and air in the large-scale pressure-swirl atomizer. The model was presented in Section 5.2.

In the light of the fact that the Reynolds number for this flow-field is in the order of 12,000 to 41,000 (based on the conditions in the feed slots and the hydraulic diameter of the feed slots), the flows within the feed slots and swirl chamber may be turbulent. It was attempted to make use of the standard, the RNG, and the realizable two-equation k-ε turbulence models in Fluent 6.1. However, for this particular flow-field these turbulence models were unable to predict the air-core. Therefore, the flow-field is simulated using both a quasi-LES (QLES) flow assumption and LES subgrid-scale turbulence modeling.

In the LES methodology one solves only those eddies that are large enough to contain information about the geometry and dynamics of the specific problem under investigation, and regards all structures on a smaller scale as "universal" following the viewpoint of Kolmogorov. The LES equations are derived by applying a filter function to the time-dependent Navier-Stokes equations. Whereas LES of single-phase flows has reached a sophisticated standard, applications of LES formalism to two-phase flows with moving interfaces are harder to find in the literature. A concern for two-phase simulations is the ability to correctly model the turbulence in the presence of liquid and air.

The effect of the unresolved small-scale fluctuations on the resolved larger-scale motion needs to be modeled. The QLES approach leaves this simply to the diffusion effect of the numerical scheme used for discretizing the convection terms using the laminar viscosity only.

In most LES calculations, the effect of the unresolved small-scale motion is modeled with a subgrid-scale model. In this work, the standard Smagorinsky-Lilly model (Smagorinsky, 1963; Lilly, 1967) is considered. The influence of the unresolved motion on the resolved scales is treated as an additional viscosity, μ_t, modeled by

$$\mu_t = \rho L_S^2 \sqrt{2\bar{S}_{ij}\bar{S}_{ij}} \tag{7.1}$$

where $\bar{S}_{ij}$ is the rate-of-strain tensor for the resolved scale and L_S is the mixing length for subgrid-scales computed using

$$L_S = \min\left(\kappa d_w, C_S V_{cell}^{1/3}\right) \tag{7.2}$$

where κ is the von Kármán constant, d_w is the distance to the closest wall, and V_{cell} is the volume of the computational cell. C_S is the Smagorinsky constant and a value of $C_S = 0.1$ is used.

The work represents a first step in applying subgrid-scale modeling in a VOF simulation, and the issue of additional terms due to the interface is not considered.

7.3.2 Two-Fluid Euler/Euler Model

Instead of switching from a VOF method inside the atomizer to an Eulerian multiphase method downstream the nozzle, a two-fluid Euler/Euler method is considered for the flow inside the atomizer also.

The Eulerian multiphase approach, as discussed in Chapter 5, Section 5.4, treats the liquid and air as separate interpenetrating phases. For each phase mass and momentum equations are solved as well as an equation for volume fraction. In this study, momentum exchange between the gas and liquid is modeled through a symmetrical drag model. The gas-liquid momentum exchange coefficient, $C_{f,gl}$, is written in terms of mixture density, ρ_{gl}, and mixture interfacial area density, A_{gl}:

$$C_{f,gl} = \frac{1}{8} C_D \rho_{gl} A_{gl} U_{rel} \tag{7.3}$$

where $U_{rel} = \left|\vec{u}_g - \vec{u}_l\right|$ is the relative velocity between the two phases and

$$\rho_{gl} = \alpha_g \rho_g + \alpha_l \rho_l \qquad \text{and} \qquad A_{gl} = \frac{6\alpha_g \alpha_l}{d_{gl}} \tag{7.4}$$

where $d_{gl} = \alpha_g d_l + \alpha_l d_g$ is an interfacial length scale, α_g and α_l are the volume fraction of gas and liquid, d_g and d_l are the diameter of bubbles and droplets. For this first step a value of $d_g = d_l = 1.0$ mm is used.

The drag coefficient, C_D, is based on the Schiller-Naumann and Newton particle drag correlations:

$$C_D = \max\left[\frac{24}{\mathrm{Re}_{gl}}\left(1 + 0.15\,\mathrm{Re}_{gl}^{0.687}\right), 0.44\right] \tag{7.5}$$

where Re_{gl} is the relative mixture Reynolds number obtained from:

$$\mathrm{Re}_{gl} = \frac{\rho_{gl} U_{rel} d_{gl}}{\mu_{gl}} \tag{7.6}$$

where $\mu_{gl} = \alpha_g \mu_g + \alpha_l \mu_l$ is the mixture viscosity of gas and liquid. This symmetrical drag model gives correct behavior for particle flow with vanishing volume fractions.

The turbulence in the two phases is described with the QLES approach presented above.

7.4 Results and Discussion

The flow simulations are done for the two domains shown in Figure 7.4 and Figure 7.5. The boundary condition for the inlets is taken to be a specified volume flow rate normal to the boundary. The downstream pressure boundary is set to ambient pressure (101325 Pa). All wall boundaries are taken as no-slip. For all cases, the fluids are air and water at an operating temperature of 50°C. For air and water respectively, the densities are $\rho_g = 1.04$ kg/m^3 and $\rho_l = 988$ kg/m^3, the viscosities are $\mu_g = 1.84\times10^{-5}$ kg/m·s and $\mu_l = 5.44\times10^{-4}$ kg/m·s, and surface tension is $\sigma = 0.068$ N/m.

Two operating conditions are computed, with water volume flow rates of 15 and 50 L/min, respectively. The simulations are run as time-dependent, and the time steps used for the two cases are $\Delta t = 1.0\times10^{-4}$ and 2.5×10^{-5} s, respectively. The choice of the time-step interval used in the computations is based on a Courant number of 1, and it was found that these intervals were sufficient to display the time dependency and to ensure convergence for each time step. Obtaining a converged steady-state solution was found to be impossible.

In both the VOF and Two-Fluid cases, the interface between the liquid and the gas becomes unsteady, displaying waves of small magnitude along its surface; see Figure 7.6. The waves originate at the atomizer top, at the stagnation point on the wall, and propagate toward the exit. The stagnation point leads to the formation of a crest at the atomizer top. The resulting flows are of highly three-dimensional character, where the air-core is rotating, generating a spiraling disturbance on its surface. The qualitative agreement of the experimentally obtained flow visualization data in Hansen and Madsen (2001 and 2002) with the present numerical simulations is good; see Figure 7.2. For both flow rates, the air-core has a near-constant mean diameter throughout the conical swirl chamber. Over a distance of approximately 10 mm in the cylindrical orifice, the air core is seen to expand to a second near-constant mean diameter. The drawback of the Two-Fluid approach is that the interface is poorly resolved compared to the VOF approach. Therefore, the volume fraction and velocity gradients become smeared out over several cells.

The velocity and thickness of the liquid film at orifice exit, as well as the downstream variations, are of interest because they govern the breakup of the film. Unfortunately, grid resolution requirements for the VOF simulation restrict the simulation to 25 mm downstream from the exit of the atomizer, see Figure 7.7. The liquid film thins out so rapidly that an additional 2-3 million cells within the film would be required to resolve the film. However, the CFD model does provide adequate grid resolution to resolve the liquid film in the orifice and at the exit of the atomizer. The film properties here are important, because they can provide the boundary conditions for film breakup models.

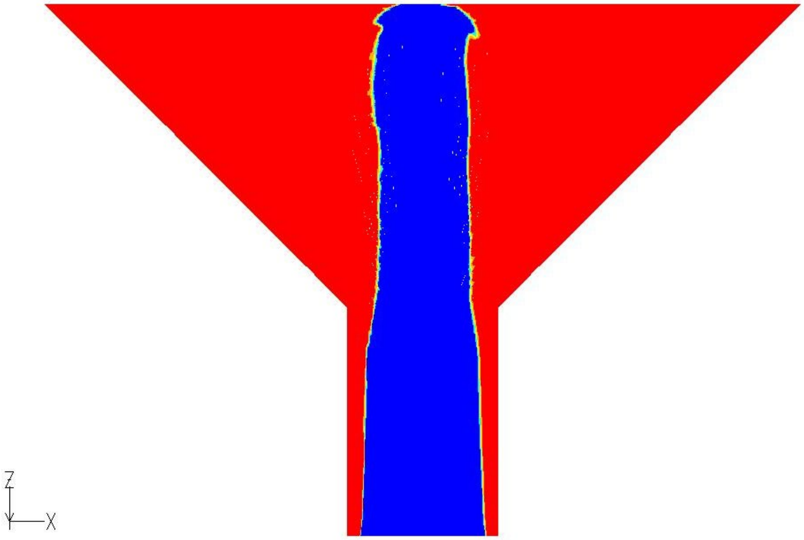

Figure 7.6: Volume fraction for the VOF-QLES case at 50 L/min (water in red and air in blue) for the internal domain.

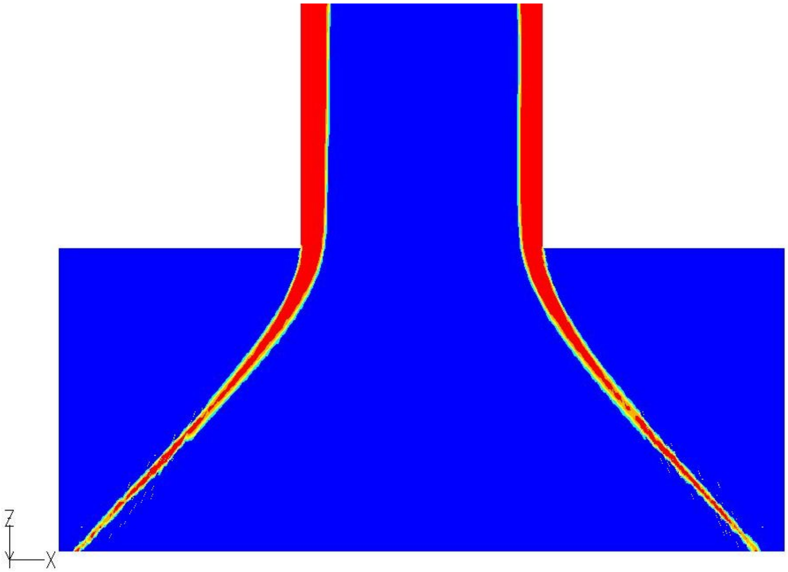

Figure 7.7: Volume fraction for the VOF-QLES case at 50 L/min (water in red and air in blue) for the near field spray-cone.

In the experiments, the tangential velocity profiles in the conical swirl chamber were found to be essentially independent of the axial position. This is also found in the simulations. The velocity distributions in the swirl chamber are similar for both grids. For the region close to the orifice exit, the results show little difference between the two grids. This suggests that the downstream flow field only affects the internal flow field of the atomizer in a region close to the exit. In the following figures the results are plotted for the grid in Figure 7.4.

Figure 7.8 and Figure 7.9 show a comparison of tangential velocity measurements and predictions at an axial position 10 mm below the top of the swirl chamber, with volume flow rates of 15 and 50 L/min, respectively. The general agreement between the experiment (Hansen and Madsen, 2001) and the three present cases (Two-Fluid-QLES, VOF-QLES, and VOF-LES) is good. It is seen that the tangential velocity component exhibits the $1/r$ variation for the irrotational region of a free vortex for most of the chamber width. The flow simulations carried out in Hansen and Madsen (2001) using the homogeneous two-phase model in CFX-4.3 and the QLES approach deliver similar qualitative behavior. However, the tangential velocity is underpredicted by as much as 20-40%. This underprediction is due to the grid used where the three feed slots were not included in the model, and therefore, the interaction between the feed slots and the swirl chamber was not captured.

Figure 7.10 and Figure 7.11 show mean axial velocity at an axial position 10 mm below the top of the swirl chamber. Both the present computations and measurements show that the axial component of the velocity is concentrated within a region surrounding the air-core, and in this region this gives a deviation in the tangential velocity profile from the free vortex shape. A peak in axial velocity is also seen next to the wall at r = 0.4 mm, and everywhere else both the axial and radial velocities are very small compared with the tangential. Between the wall and the air-core the axial velocity contains both positive and reverse flow. The negative peaks in axial velocity profile near the air-core and next to the wall are not obtained in the predictions of Hansen and Madsen (2001).

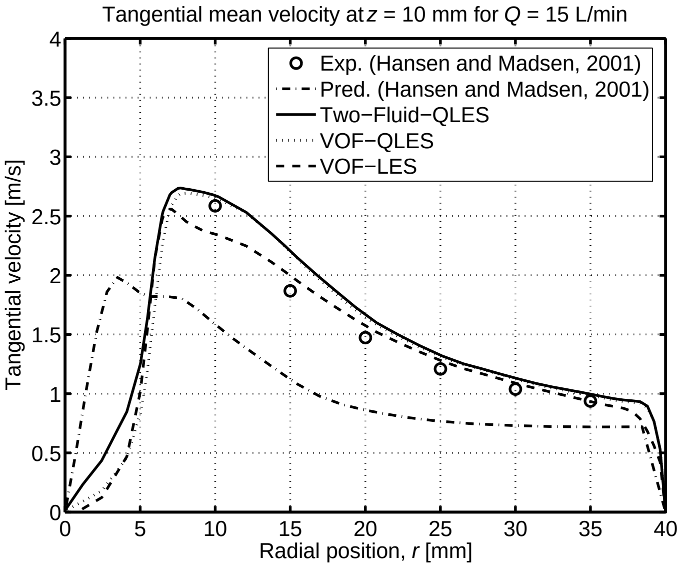

Figure 7.8: Mean tangential velocity profiles for flow rate of 15 L/min.

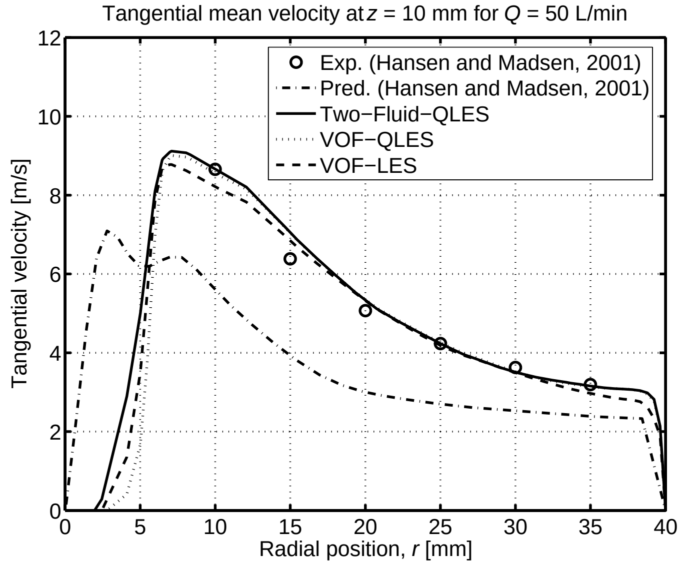

Figure 7.9: Mean tangential velocity profiles for flow rate of 50 L/min.

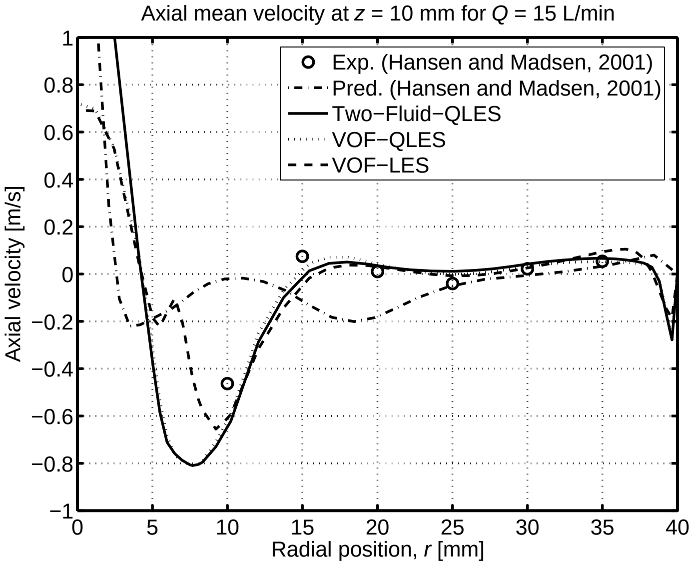

Figure 7.10: Mean axial velocity for flow rate of 15 L/min.

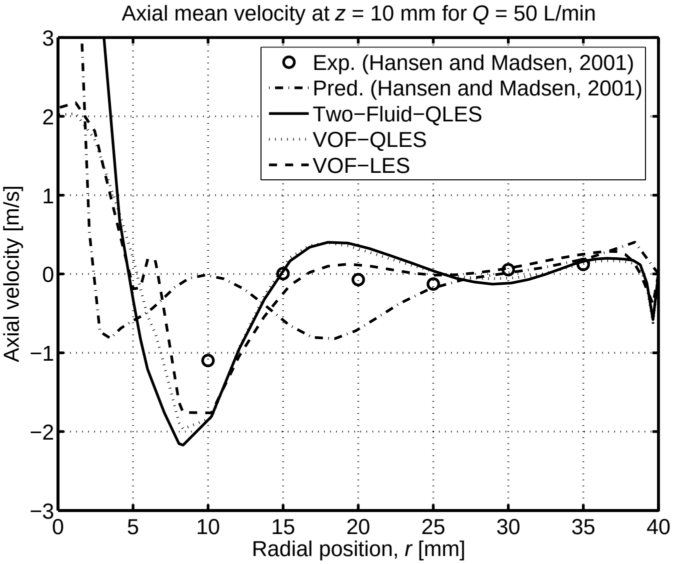

Figure 7.11: Mean axial velocity for flow rate of 50 L/min.

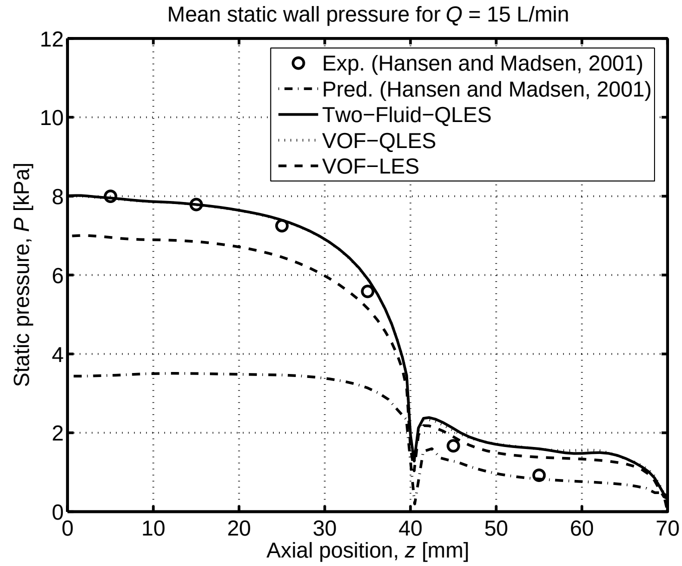

Figure 7.12: Mean static wall pressure (gauge) for flow rate of 15 L/min.

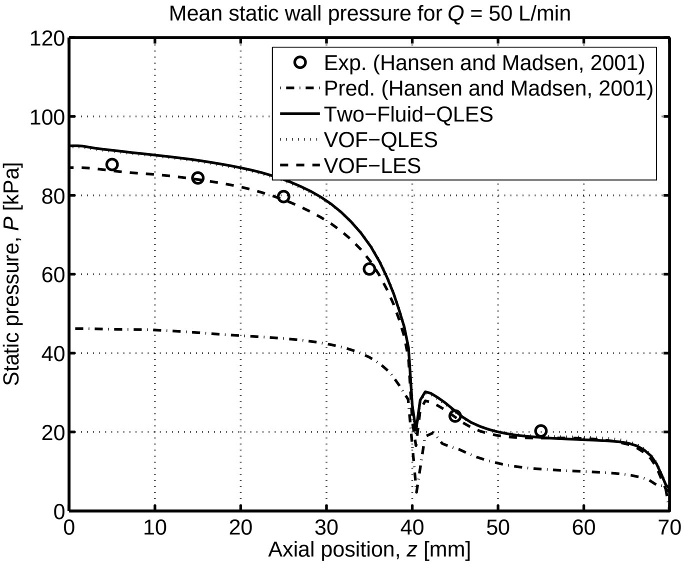

Figure 7.13: Mean static wall pressure (gauge) for flow rate of 50 L/min.

Figure 7.12 and Figure 7.13 compare the predicted and measured static wall pressures for the two flow rates. Generally the agreement between the present predictions and experiment is seen to be good. The pressures predicted by Hansen and Madsen (2001) are 40-50% lower than measured. This discrepancy is due to the underprediction of tangential velocity.

The VOF-QLES and Two-Fluid-QLES approaches show very similar results comparing velocity profiles and static wall pressure, whereas the VOF-LES approach dampens the flow and reduces the static wall pressure. The best general agreement is seen for the QLES approaches. The drawback to the Two-Fluid approach is that the interface becomes smeared out over several cells, and due to the extra set of momentum equations and more iteration needed per time step, it requires more computation time. Therefore, the results of this study suggest that the use of VOF-QLES modeling is the best choice for the cases examined here.

7.5 Summary

The applicability of two-phase CFD modeling of the internal flow in a large-scale pressure-swirl atomizer is investigated using three approaches: 1) the VOF-QLES method using the laminar viscosity only, 2) the VOF-LES method using subgrid-scale turbulence modeling, and 3) the two-fluid Euler/Euler method using the QLES approach. All simulations show similar results and produce the characteristic air-core that matches those observed in the experiments. Likewise, tangential and axial velocity profiles in the conical swirl chamber and static wall pressure are found to favorably match with the measured profiles. For the two flow rates considered here, the VOF-QLES and Two-Fluid-QLES approaches appear to give the best agreement.

For more accurate predictions, some refinements of the approaches are needed. For instance, finer mesh may be needed, and a refinement in the subgrid-scale model may be needed to capture the turbulence in presence of the liquid/air interface correctly. The ability of the two-fluid model to predict the flow-field should also be further assessed especially the drag correlation and the two diameters d_g and d_l.

The liquid film cone exiting from the atomizer is modeled in a region 25 mm downstream the atomizer prior to film breakup. The atomizer and near-field spray-cone is simulated using 1.1 million cells; however, the resolution is insufficient. To include the breakup of the liquid film, an even finer grid resolution would be required.

This study presents a first part of a larger effort to incorporate two-phase CFD analysis into the design process of pressure-swirl atomizers. The focus has been to assess the ability of a commercial CFD code (Fluent) to model the two-phase flow of a large-scale pressure-swirl atomizer. The results of this study suggest that the use of two-phase CFD modeling can be used to gain valuable insight into the dynamics of the internal flow of production-scale pressure-swirl atomizers.

The analysis of the internal flow in the mixing chamber of a Y-jet atomizer is an even more complex problem due to the violent mixing of the liquid and gas and a wider range of physical processes occurring over a broader range of length- and time-scales. The VOF model may be incapable of describing the flow because the phases are not separated as in the pressure-swirl atomizer. In order to model the mixing of liquid and gas, the two-fluid (or multi-fluid) model should be used. Because of these difficulties, the modeling of the internal flow in twin-fluid atomizers is practically non-existent; however, Bertel and Lavsen (2002) conducted numerical simulations of the flow inside a large-scale Aalborg Industries Y-jet atomizer. LDA data was used to validate the simulation data, and observed trends from the experiments were captured in the simulations.

Chapter 8

Numerical Simulation of Diesel-Type Sprays by the DQMOM-Multi-Fluid Model[*]

8.1 Introduction

Before applying the DQMOM-multi-fluid model to Y-jet and pressure-swirl water sprays, some computations are performed on a diesel-type spray.

8.2 Measurement Details

Measurements of axial droplet velocities in steady sprays were made by Wu, *et al.* (1984). Liquid n-hexane was injected into quiescent nitrogen at room temperature but at high pressure so that the ratio of the gas density to the injected fuel density is similar to that in a diesel engine cylinder at the top dead center. The experimental conditions are summarized in Table 8.1.

---

[*] Partly based on Madsen, *et al.* (2005).

Table 8.1: Test conditions for the measurements (Wu, *et al.*, 1984). Nozzle diameter: D = 127 μm. Liquid: n-hexane, ρ_l = 665 kg/m^3, μ_l = 3.2×10^{-4} kg/m s, σ= 1.84×10^{-2} N/m. Gas: nitrogen. Room temperature.

Case	P [MPa]	ρ_g / ρ_l	ρ_g [kg/m^3]	U_{inj} [m/s]
A	1.48	0.0256	17.0	127
B	4.24	0.0732	48.7	127
C	4.24	0.0732	48.7	194

These data consist of measurements of axial drop velocity in steady sprays at various stations downstream of the nozzle.

8.3 Computational Domain and Conditions

The comparison with the experimental data is performed in an axisymmetric half chamber. The computations are performed using the CFD code Fluent 6.2. The computational grid is shown in Figure 8.1. The total number of cells is 218×55. There are two cells along the radius of the injector hole, and the aspect ratio of the cells near the orifice is close to one in order to achieve good numerical accuracy.

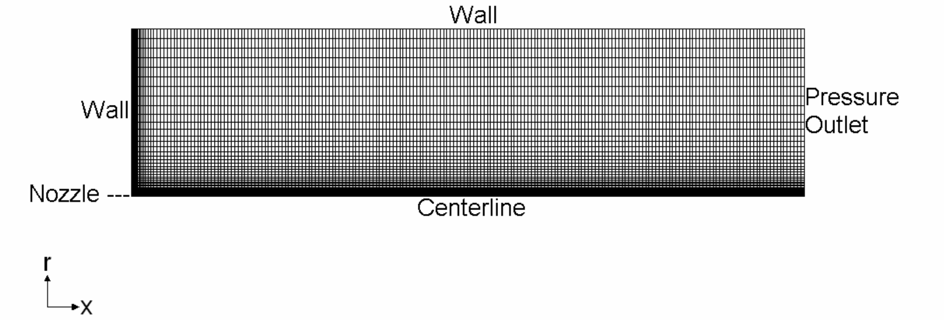

Figure 8.1: Computational grid.

The model is tested with N = 3 nodes (droplet phases). The blob atomization model is employed, in which liquid blobs are injected with a diameter equal to the nozzle diameter $d_{inj} = D$. The computations are carried out using the erosion type breakup mechanism, where in Eqs. (3.14) and (6.30), the number γ of droplets of diameter d_{st} produced is assumed to be equal to the ratio between the parent drop surface area and the stable droplet surface area. Using $\gamma = d_q^2 / d_{st}^2$, the breakup kernel a_q is given by Eq. (6.38). The WAVE breakup model is employed with the model constant B_1 = 10. Computations were also performed with B_1 = 1.73 and 20, but the overall trend is closer to the measurements with B_1 = 10. The droplet-droplet collisions have a large effect in the near nozzle region but have little effect on the downstream SMD values. For the results presented here collision effects are not included.

8.4 Results and Discussion

Figure 8.2 shows the computed (CFD) and measured (Exp.) steady axial liquid velocity as a function of the radial distance from the centerline at axial locations of x/D = 400 and 600 for Case A. The computations overpredict the axial velocities near the centerline at both axial locations. The agreement between the computed and measured values is better beyond a radial position of 5 mm. Figure 8.3 and Figure 8.4 show the results for Cases B and C, respectively. In these cases, the ambient density is higher than that for Case A. The computed velocities are somewhat lower than the measurements near the centerline for both these cases.

Overall, there is a reasonably good agreement between the computed and the measured velocity profiles for the three cases considered. This confirms that momentum transfer rates, which also influences the turbulent diffusivity, are computed accurately in the model.

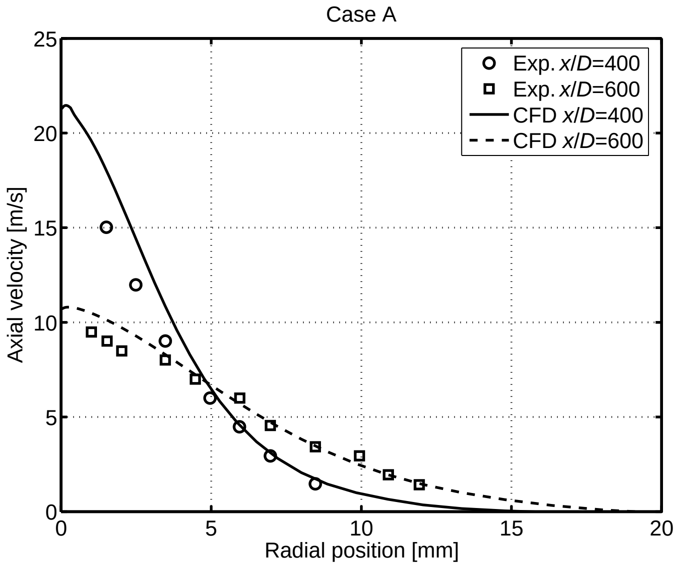

Figure 8.2: Axial liquid velocity for case A.

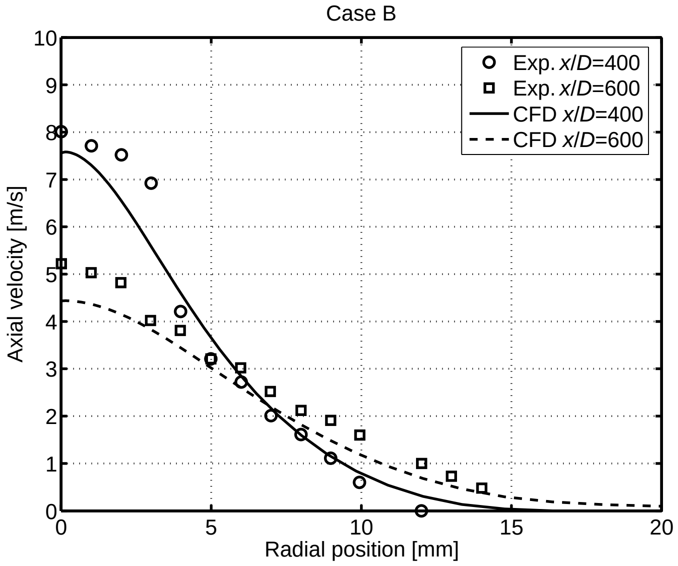

Figure 8.3: Axial liquid velocity for case B.

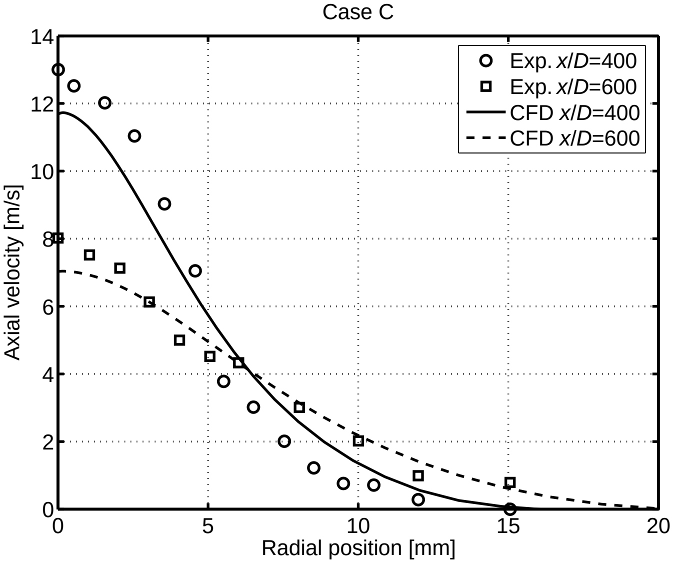

Figure 8.4: Axial liquid velocity for case C.

The main difference with the most common multi-fluid models is that in the DQMOM the "classes" are moving along the droplet size axis and are changing their volume fractions in order to mimic the evolution of the DSD. As already mentioned, the DQMOM is based on a presumed functional form of the DSD that allows solving the closure problem. In Figure 8.5, volume-fraction versus droplet-size diagrams are used to report on the position of the 3 delta functions. This can give some insight into the shape of the underlying DSD. The approximated DSD for Case A is shown at the axial distances x = 45 mm and x = 90 mm along the centerline and at the radial position r = 2 mm. Due to droplet breakup and convection, the DSD at different positions are different.

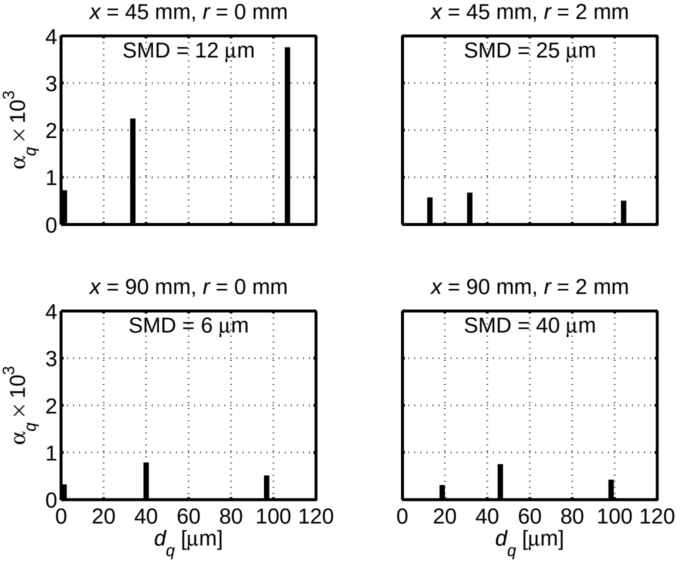

Figure 8.5: DSD at different positions for case A.

8.5 Summary

A new spray model based on the Eulerian multi-fluid model has been developed which removes the need to discretize the DSD into fixed size classes. The evolution of the DSD due to breakup and coalescence is simulated using the DQMOM. In the model each droplet phase has its own momentum balance, giving the DQMOM-multi-fluid model the ability to treat the polydisperse nature of the flow field.

The first application of this model for non-evaporating diesel-type sprays performed with three droplet phases yields promising results. Applications of the DQMOM-multi-fluid model to Y-jet and pressure-swirl water sprays are investigated in the next chapters.

Chapter 9

Application of the DQMOM-Multi-Fluid Model to Y-jet Water Sprays[*]

9.1 Introduction

In this Chapter, two-dimensional axisymmetric computations of the atomization process of Y-jet water spray are presented. The aim is to provide a complete description of the spray from a Y-jet atomizer, including the modeling of the liquid sheet atomization and secondary breakup and coalescence of droplets. The analysis of the atomization process of a Y-jet nozzle is a highly complex problem due to the gas-liquid flow interactions, which cause violent mixing of the liquid and the gas. To predict the performance of a Y-jet atomizer, both the gas-liquid flow within the nozzle and the atomization process of the liquid sheet shed from it have to be modeled. According to the experimental investigation of Mullinger and Chigier (1974), the annular flow regime can be assumed for the two-phase flow in the mixing chamber of the nozzle.

---

[*] Partly based on Madsen, *et al.* (2006).

9.2 The DQMOM-Multi-Fluid Model

The multi-fluid model that is employed here for Y-jet sprays has been described in Chapter 5. The essential idea behind the modeling approach is to solve continuum Eulerian equations for the gas phase and N droplet (liquid) phases. For each phase mass and momentum balances are solved as well as corresponding equations for turbulent kinetic energy and its dissipation rate. The DQMOM representation of the DSD involves the solution of an equation for the diameter for each droplet phase.

Submodels are employed for the following physics:

- The interfacial momentum transfer between gas and droplet phases includes drag, Eq. (5.23), and turbulent dispersion forces, Eq. (5.52).
- The drag force is modeled through the Schiller-Naumann drag correlation, Eq. (5.25).
- Balance equations for both turbulent kinetic energy k, Eq. (5.54) and its dissipation rate ε, Eq. (5.55), are solved for each phase where corresponding interfacial transfer terms, Eq. (5.56), are included.

9.2.1 Droplet Breakup

To model atomization, the blob injection model is employed, in which liquid blobs are injected with a diameter equal to the sheet thickness. The primary breakup of these blobs and secondary breakup of droplets is modeled using the standard WAVE breakup model. In this work symmetric fragmentation is considered, i.e. the breakup of an unstable droplet with diameter d_q produces two droplets of diameter $2^{-1/3}d_q$. The daughter distribution function $b\left(d\middle|d_q\right)$ corresponding to this breakup mechanism is given by Eq. (3.15) and the moment transform $\overline{b}_q^{(k)}$ of this function is given by Eq. (6.31). The WAVE model has been transformed to the breakup kernel a_q by Eq. (6.39).

9.2.2 Droplet-Droplet Collision

Collision rates are expressed by the collision coefficient β_{pq} given by Eq. (6.40), where the average relative velocity $U_{rel} = \left|\vec{u}_p - \vec{u}_q\right|$ between colliding droplets is obtained from Eq. (6.41).

The model takes coalescence and bounce into account, as well as collision-induced breakup (fragmentation). With the collision coefficient, the expression for the coalescence kernel c_{pq} is given by Eq. (6.43). The collision-induced breakup kernel e_{pq} is expressed as Eq. (6.44), and the diameter of the droplet fragments d_{frag} is given by the correlation in Eq. (3.27).

9.3 Computation Details

Nozzle No. 4 in Table 4.1 is used for comparison in this work. A schematic view of the Y-type atomizer used in this work is shown in Figure 4.24. The most important dimensions of the Y-jet nozzle tested are the diameters of the air-injection orifice D_a = 2.6 mm, the liquid-injection orifice D_f = 1.7 mm, the mixing chamber D_m = 3.7 mm, and the length of the mixing chamber L_m = 14.8 mm.

Computations are performed with a liquid mass flow rate of 190 kg/h, and a ratio between the atomization air to the liquid flow rate (mass loading ratio $MLR = \dot{m}_g / \dot{m}_l$) of 3.75%, 5.00%, and 6.25%. For all cases, the fluids are air and water at room temperature and atmospheric pressure. For air and water respectively, the densities are ρ_g = 1.225 kg/m^3 and ρ_l = 998.2 kg/m^3, the viscosities are $\mu_g = 1.79\times10^{-5}$ kg/m·s and $\mu_l = 1.00\times10^{-3}$ kg/m·s, and surface tension is σ = 0.0719 N/m.

The computations are performed on two two-dimensional axisymmetric computational grids using the CFD code Fluent 6.2. Figure 9.1 shows the grids (A and B) for the Y-jet atomizer. The nozzle and spray regions are represented within a single calculation domain. The spray domain is the same for both grids and 422.6 mm long by 100 mm in radius with 170×63 cells. In Grid A, the nozzle mixing chamber is 14.8 mm (= L_m) long by 1.85 mm in radius with 15×9 cells. In Grid B, the nozzle mixing chamber is reduced to 1 cell in the axial direction with a length of 1 mm.

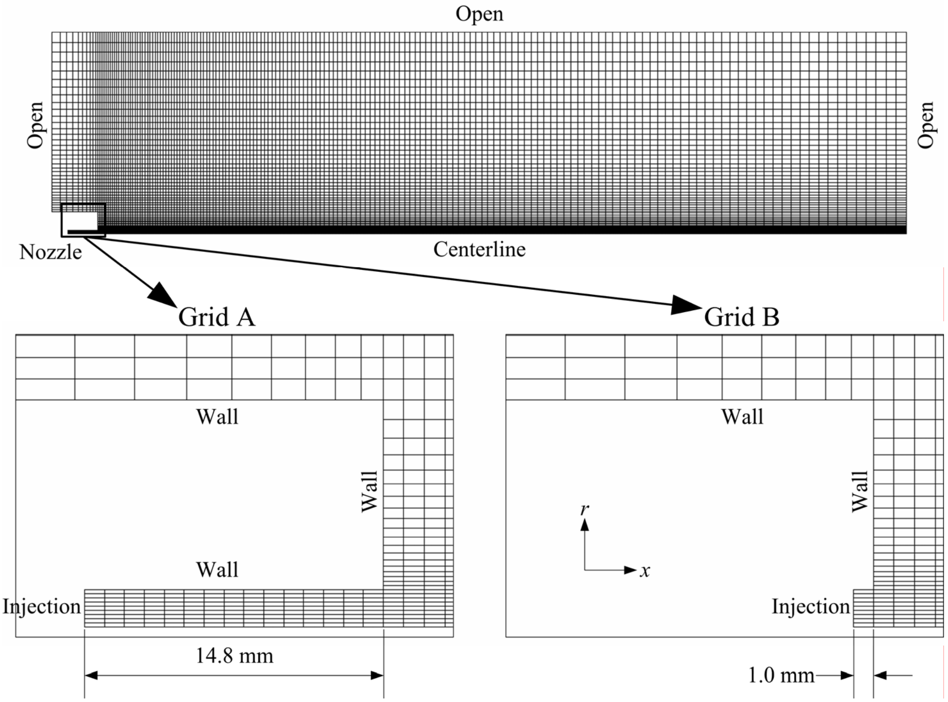

Figure 9.1: Computational grids. Spray domain together with a close-up view near the nozzle of Grid A and Grid B.

The liquid injection is comprised of the wall-adjacent cell and the air injection is comprised of the central 8 cells. The liquid film injection is modeled by specifying a uniform droplet size equal to the film thickness d_{inj} = 206 μm and a velocity of $U_{inj,l}$ = 23.4 m/s at the boundary. The core airstream has a flat velocity profile with velocities of $U_{inj,g}$ = 190, 254, and 317 m/s for the three mass loading ratios, respectively. These parameters can then be used to solve the dispersion relation for short waves, Eq. (2.5), obtained in the linear instability analysis for a liquid sheet in Chapter 2. The liquid and gas injection velocities $U_{inj,l}$ and $U_{inj,g}$, the momentum flux ratio *MFR*, Eq. (2.31), and the estimated droplet diameter d_D, Eq. (2.20), are shown in Table 9.1.

Table 9.1: Parameters for the three cases.

MLR [%]	*MFR* [-]	$U_{inj,l}$ [m/s]	$U_{inj,g}$ [m/s]	d_D [μm]
3.75	0.081	23.4	190	199
5.00	0.144	23.4	254	147
6.25	0.225	23.4	317	117

The flow in the mixing chamber of the nozzle and in the near-field is sensitive to the injection boundary values of k and ε. To assess the effect of the assumed boundary conditions for turbulence intensities, I_l and I_g, and turbulent length scales, ℓ_l and ℓ_g, computations are performed for Grid B with different sets of turbulence boundary values. Table 9.2 shows a summary of the runs made.

Table 9.2: Description of the simulations made. D_f = 1.7 mm, D_a = 2.6 mm, and d_{inj} = 206 μm.

Run #	Grid	B_1	Turbulence boundary values				We_{coll}
			I_l [%]	I_g [%]	ℓ_l	ℓ_g	
1	A	10	4	6	$0.07D_f$	$0.07D_a$	12
2	B	10	4	6	$0.07D_f$	$0.07D_a$	12
3	B	1.73	4	6	$0.07D_f$	$0.07D_a$	12
4	B	1.73	10	10	$0.07D_f$	$0.07D_a$	73
5	B	1.73	10	10	$0.14d_{inj}$	$1.12d_{inj}$	94
6	B	1.73	5	4	$0.14d_{inj}$	$1.12d_{inj}$	23

The computations are performed with two values of the WAVE model constant B_1. Reitz (1987) used B_1 = 10 and based on comparisons to the TAB model B_1 has been set as $B_1 = \sqrt{3} = 1.73$.

The outcome of droplet collisions is described by the collisional Weber number $\mathrm{We}_{coll} = \rho_l U_{rel}^2 d / \sigma$. In Table 9.2, We_{coll} is shown as function of liquid injection boundary values for the 6 Runs. These values act to determine what proportion of the collisions occurring between droplets in the liquid film injection result in each collision regime. Thus Figure 3.8 shows that the injection boundary values in all the Runs result in coalescence and fragmentation. The effect of the predicted collisions on the droplet mean diameter can be approximated by Figure 3.11. The high collisional Weber numbers of Runs #4 and #5 result in a decrease of the mean diameter, whereas the lower Weber numbers of Runs #1 - #3 result in almost unchanged mean diameters.

It is well known that the standard k-ε model does not fit the data for single-phase axisymmetric jets. A common practice is to modify one of the constants in the model, $C_{\varepsilon 2}$, form 1.92 to 1.87. This correction is applied in the present simulations.

The nozzle and spray regions are treated with the same DQMOM-multi-fluid model where the droplet breakup and coalescence models are applied in both regions. The model is tested with $N = 3$ droplet phases.

The measurements were made in steady sprays whereas the computational model solves the time-dependent governing equations. The time step used for all Runs is $\Delta t = 2.5\times10^{-7}$ s, corresponding to a maximum Courant number of 0.1.

9.4 Results and Discussion

This section demonstrates the capabilities of the DQMOM-multi-fluid model applied to Y-jet water sprays. It is split into four sections. The first section deals with the basic structure of the computational spray. The second deals with comparisons between the experimental and the predicted results. The third considers parametric tests performed to ensure that the model is producing qualitatively the correct effects. The fourth is concerned with droplet size distributions, as found in experiments and predictions.

9.4.1 Basic Structure

Figure 9.2 shows the SMD contours within the spray. The iso-lines corresponding to liquid volume fractions of 10^{-4} and 10^{-3}, also shown in the figure, show that the majority of the liquid remains near the axis of the spray. The centre of the spray contains small droplets, as they are entrained into the centre of the spray more easily. The very small droplet sizes in the centre of the spray near the nozzle are due to droplet breakup. Outside the dense regions of the spray, the droplet size rises towards the spray edge due to droplet coalescence, and the sizes are seen to increase with the distance from the nozzle. The larger droplets have smaller drag, which allows them to travel further radially, which results in their making up the spray edge. The predicted spray structure is physically reasonable, and captures the essence of the spray.

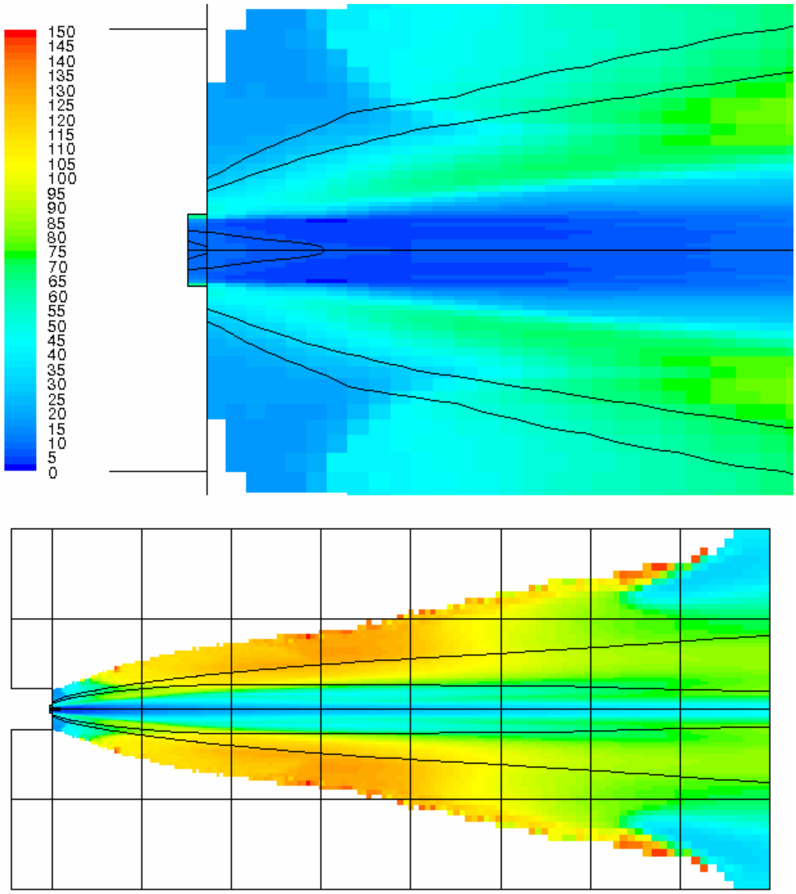

Figure 9.2: Contours of SMD and iso-lines corresponding to liquid volume fractions of 10^{-4} and 10^{-3} of the computation Run #4 for *MLR* = 6.25% at time *t* = 50 ms. The top image is a close-up view near the nozzle. The grid superimposed on the images has a spacing of 50 mm.

The subsequent discussion in the next sections focuses on the steady axial velocities and SMD values.

9.4.2 Comparison with Experiment

The radial profiles of the axial droplet velocity calculated with the DQMOM-multi-fluid approach (Run #4) are compared with the measured ones (Exp.) in Figure 9.3, and the radial distribution of the droplet SMD is shown in Figure 9.4. The profiles are determined at three axial locations for *MLR* = 5.00%. For all the radial profiles presented, the experimental data represents the $-z$ direction in Setup 1 in Figure 4.26, where the laser beam blockage by the spray is low. In this plane perpendicular to plane drawn through the liquid and air inlets, the spray is nearly symmetrical.

It is seen that the measured mean velocity reaches a maximum value at the spray centerline, and decreases toward the spray edges as the spray spreads out. The air entrainment from the surroundings to the spray region is responsible for this behavior of the mean velocity distribution. The variation of the velocity profile along the spray axis x in the downstream direction indicates the expansion of the spray region caused by the effect of spray-air interaction and air entrainment. Along the downstream direction, the variation of the droplet velocity near the central region is just opposite to that near the edge. Near the center, the axial mean velocity decreases as the distance from the nozzle increases, whereas close to the edge it increases downstream. At the nozzle exit, the initial large velocity difference between the liquid and the airflow results in high velocities of the droplets because of the strong momentum transfer and the small sizes of the droplets. After a certain distance downstream of the nozzle exit, the droplets are accelerated to the velocity of the air, which slows down as a result of the loss of its momentum to the droplets and the entrained surrounding air. Then as the droplets and the co-flowing air are transported further downstream and spread out, they are decelerated because of the air entrainment from the surroundings. Thus, the velocity profile flattens as the spray region expands downstream along the spray axis.

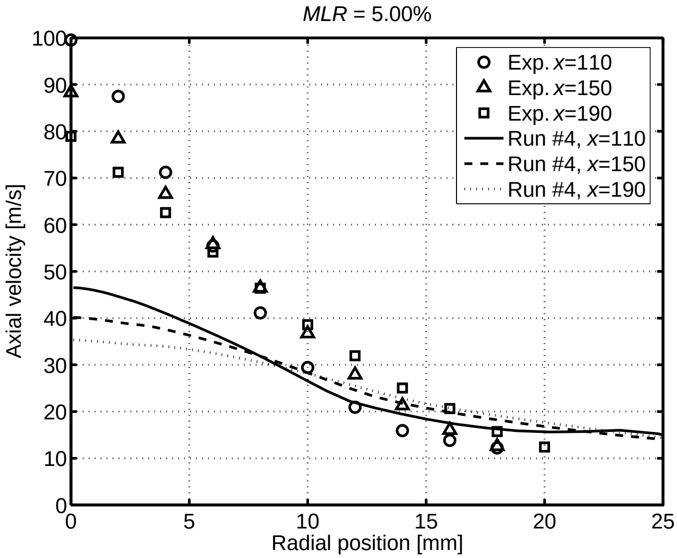

Figure 9.3: Comparison of the calculated and measured radial profiles of the axial droplet velocity for *MLR* = 5.00%.

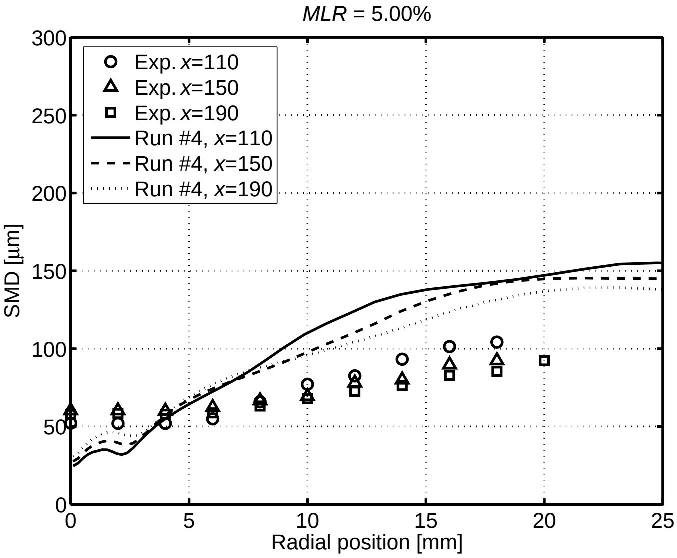

Figure 9.4: Comparison of the calculated and measured radial profiles of the SMD for *MLR* = 5.00%.

The measured SMD increases slightly from the spray central region to the spray periphery. Referring back to the variation of the axial mean velocity shown in Figure 9.3, it is evident that the variations of the droplet sizes and velocities are consistent with each other in the sense that the high air velocity and the high fluctuating component of the droplet velocities in the spray central region results in small droplets there because of aerodynamic breakup and collision-induced breakup. The small droplets are entrained by the high-velocity core airstream and are accelerated to higher velocities in the central region of the spray. The larger droplets, having larger inertia, tend to follow their own trajectories, and are less affected by the air entrainment motion near the spray edges. It is also seen that some increase in the SMD with the axial distance occurs near the central region, whereas close to the edge the SMD decreases downstream, similar to that observed by Li and Shen (1999). This is mainly because of relatively large droplets migrating toward the central region.

The predicted radial distribution of axial velocity is shown for Run #4 in Figure 9.3. The centerline axial velocity is predicted to low, and the droplet velocities at larger radial distances are overpredicted. This is a phenomenon that is seen in all runs made on Grid B, suggesting that this may be an injection condition problem.

Radial distributions of predicted droplet SMD are shown in Figure 9.4. The trend of increasing droplet size with radial distance is correct, but the rate of change is too large, with SMD of the small droplets on the centerline underpredicted and the SMD of the large droplets toward the periphery overpredicted. There are two main reasons for this. The first is that the sheet breakup in the computation results in large droplets from the injected blobs with many surrounding smaller droplets, especially between the "sheet" and the spray axis. This results in small values of the axis SMD and large values of the periphery SMD. The other reason is that the collision rate of droplets in the spray may be overpredicted. The rate of change of droplet size with axial distance is approximately correct.

9.4.3 Parametric Tests

The influence of grid, droplet breakup, and turbulence boundary conditions on the spray will be discussed next. Computations for all mass loading ratios show similar trends.

Grid

The results obtained at the axial location of $x = 190$ mm from running the simulation on two different grids are shown in Figure 9.5 and Figure 9.6 for $MLR = 6.25\%$. The long nozzle mixing chamber in Grid A cause the droplets to be accelerated to the velocity of the air, hence the droplet velocity further downstream of the nozzle exit is overpredicted. At the nozzle exit in Grid B the lower droplet velocities result in a faster slow down of the air velocity and lower droplet velocities downstream. The smallest downstream SMD values are predicted when using Grid A. This is due to the large region within the nozzle with high velocity difference between the phases, resulting in small droplets there because of droplet breakup and thus smaller downstream SMD values.

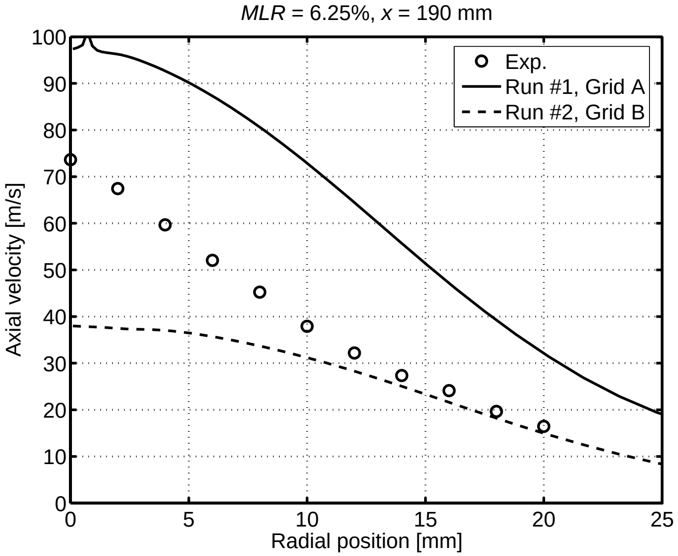

Figure 9.5: Effect of grid on predicted axial velocity at the axial distance $x = 190$ mm for $MLR = 6.25\%$.

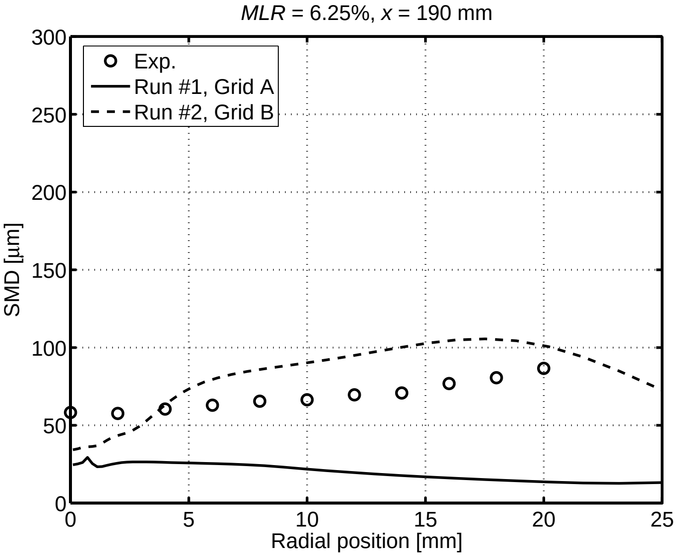

Figure 9.6: Effect of grid on predicted SMD at the axial distance $x = 190$ mm for $MLR = 6.25\%$.

WAVE Droplet Breakup Constant B_1

In Figure 9.7 the spray droplet size is seen to be sensitive to the value of the WAVE model breakup constant B_1. Smaller droplet sizes result as B_1 is lowered because of faster droplet breakup. The droplet axial velocity is not sensitive to the reduced droplet breakup time, so this figure is not presented here.

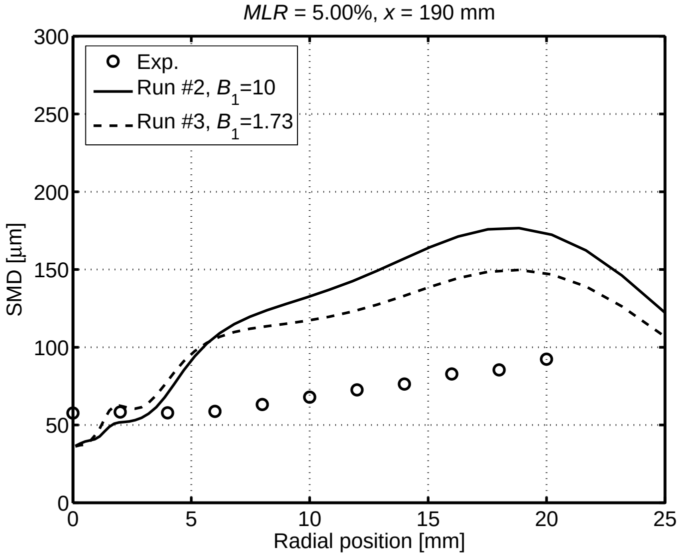

Figure 9.7: Effect of constant B_1 on predicted SMD at the axial distance x = 190 mm for *MLR* = 5.00%.

Turbulence Injection Boundary Conditions

Figure 9.8 shows the computed and measured SMD for *MLR* = 3.75% as a function of radial distance at the axial distance x = 190 mm. Computed results of the SMD for the four sets of injection boundary turbulence values given in Table 9.2, Runs #3 - #6, are shown. It may be seen that in all Runs, the computed values of SMD are greater than the measured ones. The results show that the submodel for coalescence and collision-induced breakup has a noticeable effect with the SMD being larger in the case of low gas turbulent intensities I_g. For Runs #3 and #6, the submodel for droplet-droplet collision leads to the formation of droplets larger than the injected ones (d_{inj} = 206 μm). For Runs #4 and #5, the higher fluctuating component of the droplet velocities results in small droplets because of collision-induced breakup. These results imply that, if even higher gas turbulence intensities were employed, the computed results may come closer to the measured ones.

Figure 9.9 shows the effect of adjusting the injection turbulence values on axial velocity for MLR = 3.75%. The spray is spread more in the radial direction as the gas turbulence intensity I_g is decreased. This is the opposite effect to that seen in single-phase jets and two-phase particle laden jets in which the jets are spread more as the turbulence intensity is increased. This demonstrates that the effect is due to the breakup and coalescence of the droplets. In the case of Run #3 and #6, the larger droplets, having larger inertia, tend to follow their own trajectories, and are less affected by the air entrainment motion near the spray edges. As a result the spray spreads more.

Runs #4 and #5 show that the values of the SMD and the axial velocity are not very sensitive to the injection boundary values of turbulent length scales ℓ_l and ℓ_g.

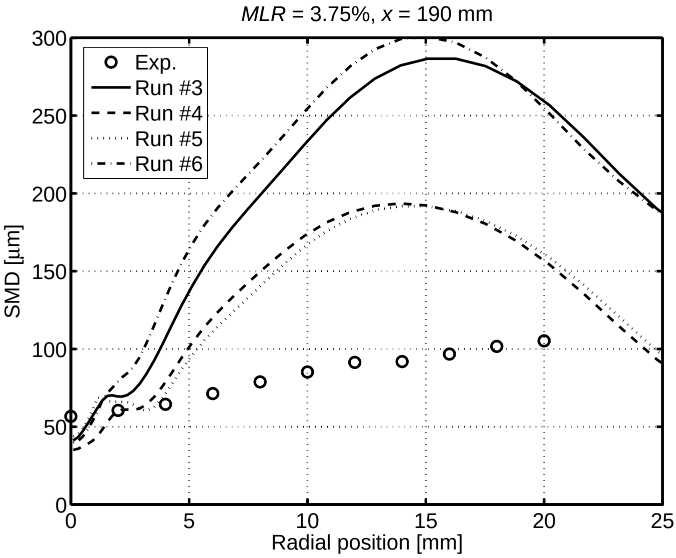

Figure 9.8: Effect of different injection turbulence boundary values (Table 9.2) on predicted SMD for *MLR* = 3.75%.

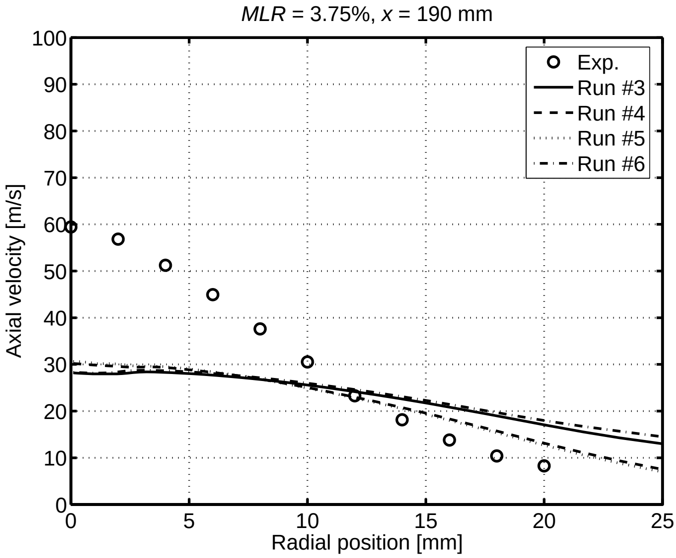

Figure 9.9: Effect of different injection turbulence boundary values (Table 9.2) on predicted axial velocity for *MLR* = 3.75%.

The parametric tests suggest that the error is in the injection boundary values, and that the conditions computed in the near-nozzle region are inaccurate. Unfortunately, it is not possible to perform rigorous tests since the experimental values in the near-nozzle region are not known.

9.4.4 Droplet Size Distribution

The DQMOM does not directly give information about the DSD since it tracks only its moments. Nevertheless, the droplet diameters d_q and weights ω_q can be seen as an approximation of the real DSD. The calculated droplet number distribution in comparison with the experimental data for MLR = 5.00% is given in Figure 9.10. Four measured DSDs at different positions are shown and the differences between them are small, only a higher amount of small droplets can be observed for the distributions nearest to the spray centerline (r = 6 mm). Towards the spray edges (r = 12 mm) existence of larger droplets can be observed. Additionally, the results of droplet size predictions of Run #4 are shown. A certain correspondence between droplet diameters and number densities and the measured DSD is evident. The same shape of the DSD is predicted. Only the existence of larger droplets and the SMD is somewhat overpredicted.

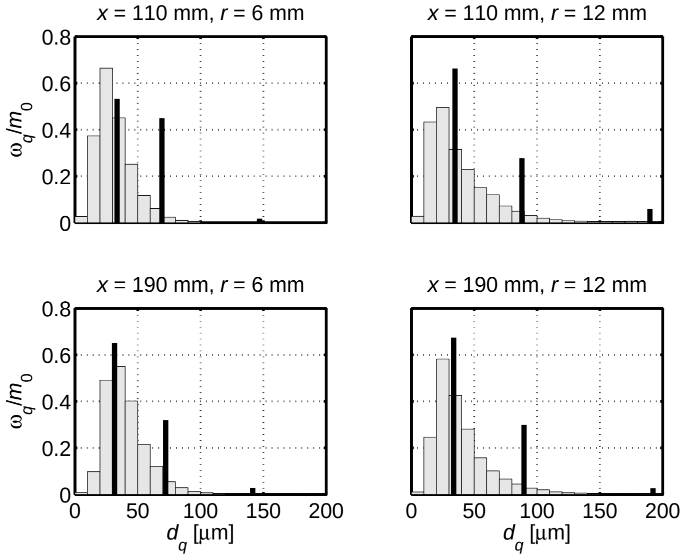

Figure 9.10: Normalized DSDs (number density function) at four different positions for *MLR* = 5.00%. The gray bars represent the experimental data. The DQMOM prediction of Run #4 is represented by the vertical black peaks centered on the respective droplet phase diameter d_q, whose height is the corresponding number density ω_q normalized by the total number density m_0.

9.5 Summary

The performance of the DQMOM-multi-fluid model for Y-jet water sprays has been discussed. It has been shown that the model is able to reproduce measured trends in steady droplet SMD and axial velocities. The parametric explorations have served to demonstrate that the model reacts in the correct qualitative manner to changes in input parameters. However, the measured values are not reproduced quantitatively with adequate accuracy.

The accuracy of the calculations strongly depends on the consistent modeling of the nozzle flow characteristics and the models adopted for breakup and collision processes. Hence, careful validation of the individual models and the availability of proper boundary conditions at the nozzle exit serve as major prerequisites for the successful analysis and optimization of Y-jet sprays.

Chapter 10

Application of the DQMOM-Multi-Fluid Model to a Hollow-Cone Spray

10.1 Introduction

Much recent research has gone into the production of well-atomized hollow-cone sprays using pressure-swirl atomizers. These have been used extensively in spray combustion applications, medical sprays, and for many other industrial purposes (Nasr, *et al.*, 2002), and more recently have become the foundation of the majority of gasoline direct-injection (GDI) systems (Rotondi and Bella, 2006).

In order to predict the behavior of pressure-swirl atomizers, the near-field region of hollow-cone sprays must be understood. This region includes the liquid sheet as it leaves the atomizer and breaks up. The spray near the atomizer is initially very dense and difficult to observe using optical methods.

At the atomizer exit, the flow through the orifice becomes a free sheet that later forms the spray. This important boundary, along with the aerodynamic interaction with the ambient gas, determines the behavior of the spray. Thus knowledge of the flow-field at the atomizer exit is necessary for spray prediction. Ideally, the flow at the exit would be known from simulation. In Chapter 7, the Fluent CFD code was used to simulate the flow through a large-scale atomizer. This approach is valid also for production-scale atomizers, but is too computational expensive for inclusion into a polydisperse spray model. Instead, the zero-dimensional model presented in Section 2.2.2 is used in the current approach to represent the internal atomizer flow.

In the computations, a model is needed to provide the droplet size and size distribution information of the atomized liquid sheet. To model hollow-cone sprays used in GDI engines Xu and Markle (1998) applied an approach, in which "blobs" were injected with a size equal to the initial sheet thickness and the subsequent breakup of the blobs and droplets were calculated using the TAB model. Schmehl, *et al.* (2000) applied a similar computational approach for the simulation of the spray of an air-assisted pressure-swirl atomizer; however, the subsequent droplet breakup was calculated using the correlations of Pilch and Erdman (1987).

In the above models, it is assumed that the liquid sheet has been atomized into discrete droplets at the exit of the nozzle. Hence, a size distribution has to be used with the mean droplet size given by the sheet thickness. A Rosin-Rammler distribution was used by Schmehl, *et al.* (2000). This assumption needs experimental validation, and the effects of initial size distribution on downstream spray calculations should be tested.

Instead of assuming sheet atomization at the nozzle exit, Han, *et al.* (1997) employed Lagrangian equations to solve for the motion of an intact sheet outside the nozzle and initial SMD was set equal to the sheet thickness. Because the initial droplets represented an intact liquid sheet, they were not subject to the effects of drag and turbulent dispersion. Once these drops had traveled a distance from the nozzle greater than the breakup length, L_{bu}, they were treated as normal droplets.

In studies of GDI hollow-cone sprays, Schmidt, *et al.* (1999) and Senecal, *et al.* (1999) used the LISA method (see Section 2.2) to give the initial droplet size, d_D, at the breakup location. Nagaoka and Kawamura (2001) and Rotondi and Bella (2006) used another sheet atomization model for GDI hollow-cone injectors based on the linear sheet instability argument. They estimated the initial droplet sizes and the breakup length from the stability analysis performed by Dombrowski and Johns (1963).

In these models, it is assumed that after the liquid sheet breaks up, the sizes of the droplets are distributed according to a Rosin-Rammler distribution with a spread parameter of $q = 3.5$.

Lee, *et al.* (2004) compared various models for the primary and secondary breakups of a GDI spray. For the primary breakup, the LISA sheet model or the WAVE "blob" injection model was used, whereas the TAB, DDB, or RT model (see Section 3.2.2) was utilized for secondary breakup. It turned out that all six combinations of breakup models were capable of reproducing measured data, as long as model constants were properly chosen.

In the current approach, the sheet breakup model (LISA) presented in Section 2.2.1 is used to predict how the liquid sheet develops into droplets. It is assumed that the liquid sheet has been atomized into droplets at the exit of the nozzle. Finally, the droplets are modeled using the DQMOM-multi-fluid model or a DDM model.

The GDI sprays, high-pressure diesel-type jets (Chapter 8), and Y-jet sprays (Chapter 9) have high relative velocities. The high velocities result in much droplet breakup and the narrow diesel-type jet and Y-jet sprays are relatively dense, resulting in many collisions. With secondary droplet breakup and coalescence, the downstream results are dependant on the breakup and collisions modeling and insensitive to the initial droplet size. In the present hollow-cone spray, no droplet breakup downstream of the nozzle is observed, and very few collisions occur due to the dilute nature of this spray. Therefore, the droplet sizes produced by the model give an indication of the performance of the sheet breakup model.

In this chapter, a Danfoss pressure-swirl atomizer hollow-cone water spray is modeled using the DQMOM-multi-fluid model and a DDM model. Since the spray of interest is essentially axisymmetric, a two-dimensional grid is used to keep computer usage time to a minimum. For the DDM model the standard submodels in Fluent 6.2 are used (Fluent, 2005). The numerical results obtained from the models are compared with the experimental PDA results obtained in Section 4.3.

10.2 Computation Details

The injection velocity and inlet sheet thickness are approximated using the measured inlet mass flow rate of $\dot{m}_l$ = 3.2 kg/h, and an injection pressure of ΔP = 850 kPa. The nozzle has an exit diameter of D_0 = 436 μm. The nominal spray cone angle is taken as $2\theta = 80°$, as the quoted nozzle design figure. The density, viscosity, and surface tension of water are given as $\rho_l = 998$ kg/m^3, $\mu_l = 1.00\times10^{-3}$ kg/m·s, and $\sigma = 0.0719$ N/m, respectively. The calculated liquid sheet thickness δ_0 and velocity U_l under the considered conditions are listed in Table 10.1. The most unstable sheet wave length Λ_S and the most probable droplet size d_D at the sheet breakup time τ_{bu} are calculated using the equations derived in Section 2.2.1. These parameters are used as the initial conditions for the droplets at the atomizer exit. The characteristics of the Danfoss pressure-swirl atomizer are shown in Table 10.1.

Table 10.1: Boundary conditions for the Danfoss pressure-swirl atomizer.

Exit diameter	D_0	μm	436
Injection pressure	ΔP	kPa	850
Mass flow rate	$\dot{m}_l$	kg/h	3.2
Cone angle	2θ	deg.	80
Injection velocity	U_l	m/s	28.9
Film thickness	δ_0	μm	31.6
Sheet thickness parameter	K	μm^2	3809
Sheet breakup time	τ_{bu}	μs	227
Sheet wave length	Λ_S	μm	884
Droplet diameter	d_D	μm	48.6

The spray boundary conditions are given at the nozzle exit. Instead of assuming an intact sheet, droplets are injected that have a SMD equal to the most probable droplet size d_D. The actual droplet size is chosen from a prescribed distribution function. The DSDs used in the present study are presented in section 10.2.4.

It should be mentioned that the liquid sheet will possibly keep some of its angular momentum after it exits the nozzle orifice. However, this is simplified in the present model, and the angular velocity component of the sheet is converted into a radial component of velocity.

The possibility of secondary droplet breakup is examined in the calculations. Taking Eq. (3.5) and a maximum relative velocity of $U_{rel} = U_l = 28.9$ m/s and a critical Weber number of $\mathrm{We}_{g,critt} = 12$, it is found that the stable droplet diameter d_{st} is above 844 μm in the entire spray, so secondary breakup is not important.

10.2.1 Computational Domain

To save computational time, axisymmetry is assumed. For the unstructured grids shown in Figure 10.1, the cylindrical domain has a radius of 200 mm and a length of 237 mm. The mesh spacing is non-uniform, with fine resolution close to the atomizer exit.

The fineness of grid with which the DQMOM-multi-fluid model is able to work allows the atomizer exit to be comprised of a number of cells. For example, seven radial cells have been used here for the Danfoss pressure-swirl atomizer spray simulations. The size of the cells is chosen such that the liquid sheet, δ_0, is exactly fitted into one cell. In the DDM approach the atomizer exit, $\frac{1}{2}D_0$, is comprised of one cell, yet the cell size is smaller than the cell size used in most DDM calculations. For the DQMOM, a 30×30 μm grid with 20×20 cells is used near the exit. For the DDM, a larger cell size of 200×200 μm is used. Beyond a radius and a length of 4 mm from the exit, the spray domain is the same for both grids. The DQMOM grid contains 5,424 cells, and the DDM grid has 3,944 cells.

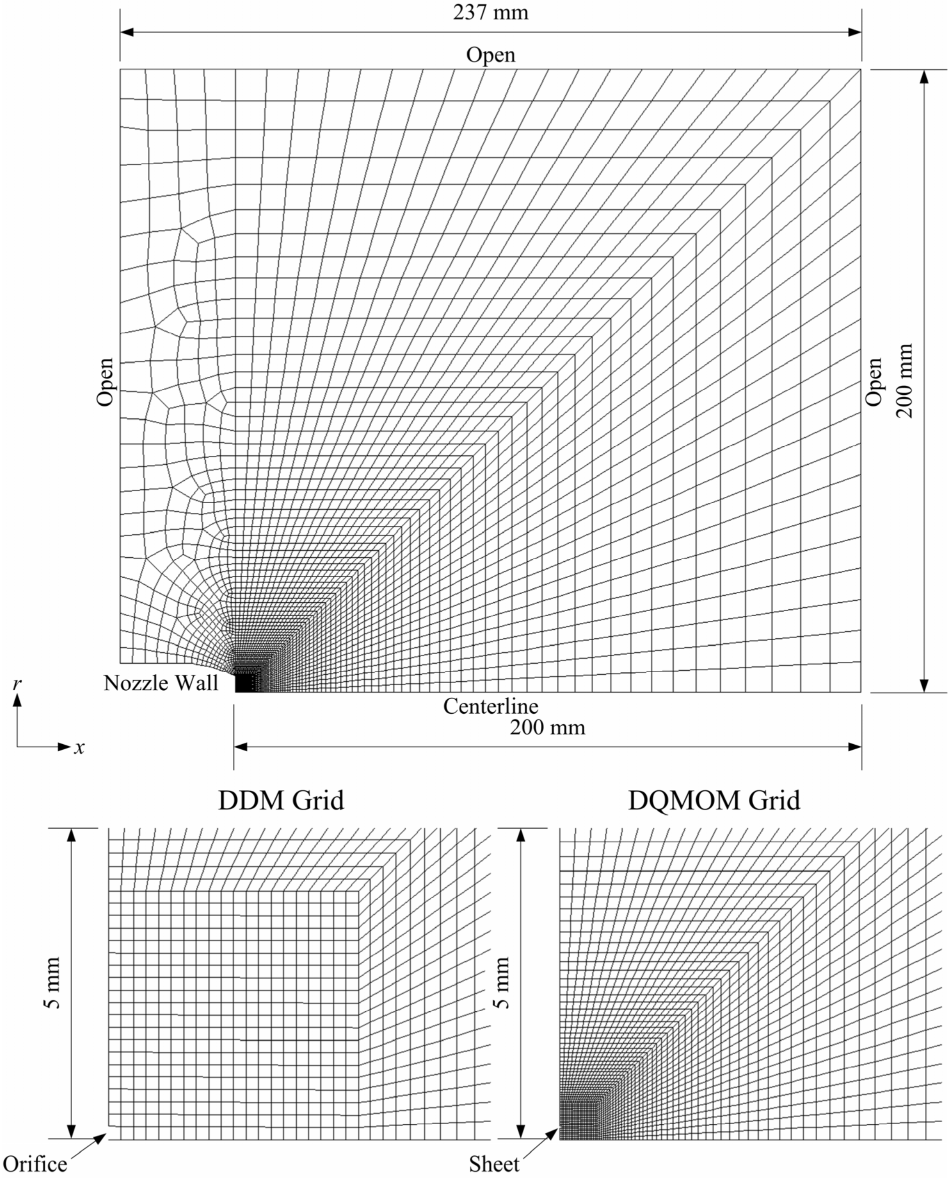

Figure 10.1: Axisymmetric computational grids. The bottom left image is a close-up view near the atomizer exit of the DDM grid, and the bottom right image is the corresponding DQMOM grid. The downstream domain is the same for both grids.

The specification of spray boundary conditions (DQMOM-multi-fluid model) and droplet initial conditions (DDM model) depends on the inherent characteristics of the disperse phase modeling approaches.

10.2.2 DQMOM-Multi-Fluid Model

The DQMOM-multi-fluid model that is employed here for the pressure-swirl atomizer spray has been described in Section 9.2.

The liquid injection is comprised of one cell, where the liquid volume fraction is set to 1.0. The radial and axial velocity components are calculated from the sheet velocity, U_l, and the direction, θ. The turbulence quantities for the k-ε model are specified in terms of turbulent length scale, ℓ, and turbulent time scale, τ_t. These turbulent scales are estimated based on the following two hypotheses.

The turbulent length scale is proportional to the wavelength, Λ_S, which breaks up the sheet:

$$\ell = C_\ell \Lambda_S \tag{10.1}$$

where C_ℓ is a coefficient set to ¼ on the assumption that the eddy diameter which is twice the turbulent length scale, 2ℓ, is equal to half of the sheet wave length, Λ_S.

The turbulent time scale is proportional to the sheet breakup time, τ_{bu}:

$$\tau_t = C_\tau \tau_{bu} \tag{10.2}$$

where the coefficient C_τ is set to 1.0.

The liquid turbulence kinetic energy, k_l, and its dissipation rate, ε_l, are linked to ℓ and τ_t by:

$$k_l = \frac{\ell^2}{\tau_t^2} \tag{10.3}$$

$$\varepsilon_l = C_\mu^{3/4} \frac{\ell^2}{\tau_t^3} \tag{10.4}$$

where C_μ is a coefficient of the k-ε turbulence model (see Section 5.5).

In this spray, higher levels of turbulence are generated by the spray than enter the domain at the injection boundary, making the result of the calculations relatively insensitive to the injection boundary values.

The time step used is $\Delta t = 1$ μs, and the simulations are run for 1 s, when steady conditions have been reached

10.2.3 DDM Model

The Fluent DDM model treats the spray droplets as parcels. Each parcel represents a group of droplets which all have the same characteristics (size, velocity, etc.). All of the parcels have the same amount of mass, and are followed by the code using a Lagrangian approach. The number of parcels injected at every time step is chosen to be 3. The parcels are injected with the sheet velocity, U_l, without swirl. The parcels are injected at a radial distance between $D_0/2$ and $D_0/2-\delta_0$ with a mean angle of θ from the spray axis. The angle of each parcel is randomly distributed over a range of $\theta \pm \Delta\theta$, where $\Delta\theta$ is assumed to be 7.5 degrees.

A discussion of the basic Lagrangian tracking method and turbulent spray dispersion is given in Section 5.3.

The trapezoidal method (Fluent, 2005), which is second accurate in time is employed for the time stepping scheme of the spray equations. For the calculations, the time step used is $\Delta t = 10$ μs.

The DDM computations are carried out with and without consideration of droplet coalescence to asses the influence of the coalescence in the DDM model.

10.2.4 Initial Droplet Size Distribution

Several empirical relationships have been proposed to characterize the distribution of droplet sizes in a spray, e.g. Rosin-Rammler, Nukiyama-Tanasawa, log-normal, root-normal, and log-hyperbolic, etc. (Lefebvre, 1989; Babinsky and Sojka, 2002).

As an alternative to the empirical approach, several analytical approaches to address the problem of modeling DSDs have been developed. Characterization of sprays is presently possible through the maximum entropy formalism (MEF) (Li, *et al.*, 1991; van der Geld and Vermeer, 1994; Semião, *et al.*, 1996; Dumouchel and Boyaval, 1999; Dumouchel, *et al.*, 2003).

In the present study, two correlations for the DSD are adopted to define the DSD at the atomizer exit. In the DDM model the Rosin-Rammler correlation is used, and in the DQMOM-multi-fluid model both the Rosin-Rammler correlation and the model of Li and Tankin (1987) are used.

Nukiyama-Tanasawa Distribution

As far as the size distribution of polydisperse droplets is concerned, several functions can be found in the literature. A possible distribution that is used in the present work is the Nukiyama-Tanasawa function (see e.g. Lefebvre, 1989)

$$f_0(d) = a d^p \exp\left(-b d^q\right) \tag{10.5}$$

where p, q and b are adjustable parameters controlling the width of the distribution and the location of the mean, and a is a normalizing constant given by

$$a = \frac{q b^{(p+1)/q}}{\Gamma\left(\dfrac{p+1}{q}\right)} \tag{10.6}$$

where $\Gamma(x)$ is the gamma function defined as (Spiegel and Liu, 1999)

$$\begin{aligned} \Gamma(x) &= \int_0^\infty t^{x-1} e^{-t} \mathrm{d}t \qquad && \text{for } x > 0 \\ \Gamma(x) &= \frac{\Gamma(x+1)}{x} && \text{for } x < 0 \end{aligned} \tag{10.7}$$

Defining a characteristic diameter $d_c = b^{-q}$, it is possible to rewrite the Nukiyama-Tanasawa distribution, Eq. (10.5), in a more convenient form

$$f_0(d) = \frac{q}{d_c \Gamma\left(\frac{p+1}{q}\right)} \left(\frac{d}{d_c}\right)^p \exp\left[-\left(\frac{d}{d_c}\right)^q\right] \tag{10.8}$$

Converted into a volume distribution the preceding equation becomes

$$f_3(d) = \frac{q}{d_c \Gamma\left(\frac{p+4}{q}\right)} \left(\frac{d}{d_c}\right)^{p+3} \exp\left[-\left(\frac{d}{d_c}\right)^q\right] \tag{10.9}$$

Physically meaningfully results are produced if $p > 0$ and $q > 0$.

Moments of Nukiyama-Tanasawa distribution can be calculated in the following manner:

$$m_k = \int_0^\infty d^k f_0(d) \mathrm{d}d = d_c^k \frac{\Gamma\left(\frac{k+p+1}{q}\right)}{\Gamma\left(\frac{p+1}{q}\right)} \tag{10.10}$$

and mean diameters can be calculated from the following equation:

$$d_{jk} = \left[\frac{\int_0^\infty d^j f_0(d) \mathrm{d}d}{\int_0^\infty d^k f_0(d) \mathrm{d}d}\right]^{1/(j-k)} = d_c \left[\frac{\Gamma\left(\frac{j+p+1}{q}\right)}{\Gamma\left(\frac{k+p+1}{q}\right)}\right]^{1/(j-k)} \tag{10.11}$$

Rosin-Rammler Distribution

Most commonly used size distribution functions represent simplifications of modifications of the Nukiyama-Tanasawa function (Lefebvre, 1989). One example is the normalized form of the Rosin-Rammler distribution in which $d_c = d_{RR}$ and $p = q - 4$:

$$f_0(d) = \frac{q}{d_{RR}\Gamma(1-3/q)}\left(\frac{d}{d_{RR}}\right)^{q-4} \exp\left[-\left(\frac{d}{d_{RR}}\right)^{q}\right] \tag{10.12}$$

where d_{RR} represents the mean of the distribution, and q indicates the value of the width of the distribution. Small values of q are associated with broad sprays, and large values of q are associated with narrow sprays. Usually $1.5 < q < 4$ (Lefebvre, 1989). The Rosin-Rammler distribution gives a good fit to droplet volume distributions for sprays; however, it often gives a rather poor fit to the droplet number distribution (Nasr, *et al.*, 2002). Note that if $q < 4$, the number distribution does not go to zero as the drop diameter approaches zero because the probability of small droplet sizes is overestimated, and if $q < 3$ the probability becomes negative. The Rosin-Rammler distribution is widely used in DDM spray applications, to determine the post breakup sizes of the primary parcels

Li & Tankin Model

The two shape parameters of the Nukiyama-Tanasawa distribution have been determined by Li and Tankin (1987) using the concept of MEF. The resulting number DSD is

$$f_0(d) = \frac{\pi}{2}\frac{\rho_l \dot{n}}{\dot{m}_l} d^2 \exp\left(-\frac{\pi}{6}\frac{\rho_l \dot{n}}{\dot{m}_l} d^3\right) \tag{10.13}$$

where $\dot{n}$ is the total number of droplets produced per unit time, and $\dot{m}_l$ is the liquid mass flow rate. Using Eq. (10.11) the SMD becomes

$$\text{SMD} = d_{32} = \left(\frac{6}{\pi}\frac{\dot{m}_l}{\rho_l \dot{n}}\right)^{1/3} \frac{\Gamma(2)}{\Gamma(5/3)} \tag{10.14}$$

Substituting Eq. (10.14) into Eq. (10.13), the expression for the number DSD, as shown by Semião, *et al.* (1996), becomes

$$f_0(d) = \frac{3}{\text{SMD}\,\Gamma(5/3)}\left(\frac{d}{\text{SMD}\,\Gamma(5/3)}\right)^{2} \exp\left[-\left(\frac{d}{\text{SMD}\,\Gamma(5/3)}\right)^{3}\right] \tag{10.15}$$

This distribution is a form of the Nukiyama-Tanasawa function, where the distribution parameters are no longer variable, but equal to $p = 2$ and $q = 3$. The characteristic droplet size is $d_c = \mathrm{SMD}\,\Gamma(5/3)$. It is seen that the knowledge of the SMD is sufficient to obtain the DSD. Li and Tankin (1987) compare the volume distribution with experimental data and the agreement is reasonable.

Initial Diameter Selection

There are many ways to obtain a specified size distribution when injecting droplets. The method used in the DDM model, samples most frequently those portions of the size distribution where the most mass (or volume) occurs. The total droplet mass associated with each parcel is constant. This constant is determined by dividing the input total spray mass to be injected, $\dot{m}_l \Delta t$, by the number of parcels to be injected. Best resolution of the DSD is obtained where the values of $f_3(d)$ are largest. The actual droplet size is selected randomly from a Rosin-Rammler volume distribution with d_D assumed to be the SMD and with a spread parameter of $q = 3.5$. This choice of distribution and spread parameter is based on past modeling experience (Han, *et al.*, 1997). The corresponding volume distribution, $f_3(d)$, of Eq. (10.12) is illustrated in Figure 10.2.

The smallest and largest diameter considered in the size distribution corresponds to $d_{v0.005}$ and $d_{v0.995}$, respectively. They are the diameters such that 0.5% and 99.5%, respectively, of the total liquid volume is in droplets of smaller diameter, and are defined for a Rosin-Rammler distribution as

$$\begin{aligned} d_{v0.005} &= d_{RR}\left[-\ln(1-0.005)\right]^{1/q} \\ d_{v0.995} &= d_{RR}\left[-\ln(1-0.995)\right]^{1/q} \end{aligned} \tag{10.16}$$

The result of the sampling procedure for the initial droplet diameter is given in Figure 10.2 and Figure 10.3, where histograms of the droplet volume distribution and number distribution, respectively, are plotted.

With respect to the DQMOM method, the representation of the spray boundary conditions has to be limited to a few droplet phases. Each phase is described by a specific combination of fixed numerical values for droplet diameter and volume fraction. The boundary conditions are calculated by using the moments of the number distribution. Starting from the first $2N$ moments m_k ($k = 0,\ldots,2N-1$) the N volume fractions α_q and the N diameters d_q are calculated by using the PD algorithm (Gordon, 1968). The model is tested with $N = 3$ droplet phases.

The DQMOM representation of the Rosin-Rammler volume distribution and number distribution is shown in Figure 10.2 and Figure 10.3, respectively. The position of the three nodes (phases) are represented as vertical black peaks centered on the corresponding droplet phase diameter d_q, whose height is proportional to the corresponding volume fraction α_q and number density ω_q, respectively. Because the smallest droplet class is very small $d_1 = 4.5$ μm, it represents a very small fraction of the volume of the liquid and thus it is not visible in the volume distribution plot. However, as it possible to see in Figure 10.3, the corresponding weight ω_1 (number density) is large.

It is clearly seen that the DQMOM representation gives more small droplets and less large droplets in comparison with the DDM sampling procedure. Computations of the present hollow-cone spray indicate that the DDM sampling procedure results in an underestimated population of small-size droplets, and this directly influences the spray structure.

One of the major advantages of the DDM is the possibility of a large number of different droplet initial conditions for a high-resolution discretization of the DSD.

The DQMOM representation of the Li and Tankin (1987) volume distribution and number distribution, Eq. (10.15), is shown in Figure 10.4 and Figure 10.5, respectively. The corresponding Rosin-Rammler distributions are also shown graphically in the figures. It is seen that the Li and Tankin model gives more medium droplets in comparison with the Rosin-Rammler distribution.

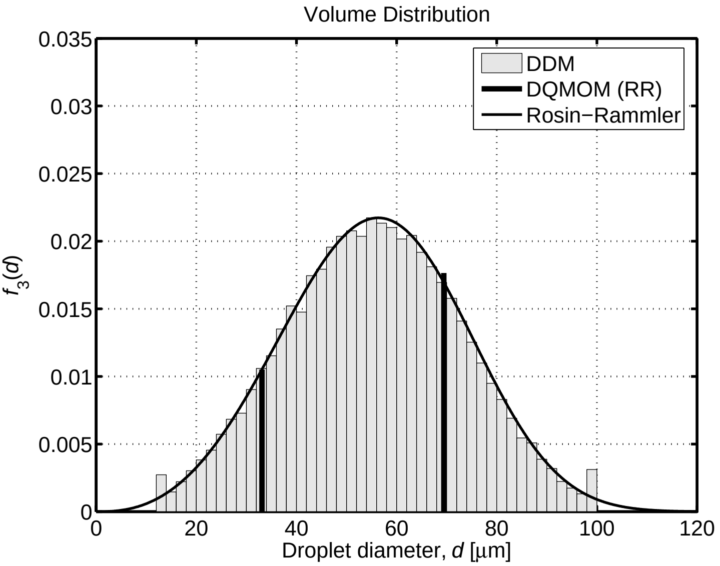

Figure 10.2: Initial Rosin-Rammler volume distribution for SMD = 48.6 μm and q = 3.5. The gray bars represent the DDM sampling. The vertical black peaks represent the DQMOM representation.

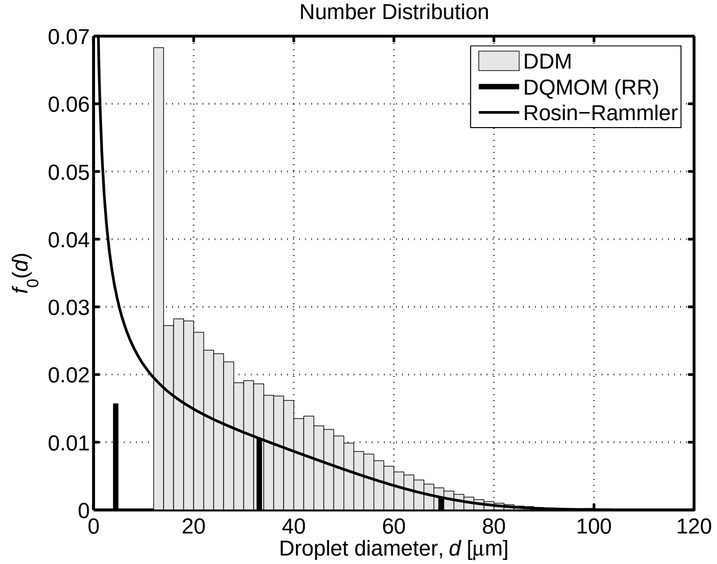

Figure 10.3: Initial Rosin-Rammler number distribution.

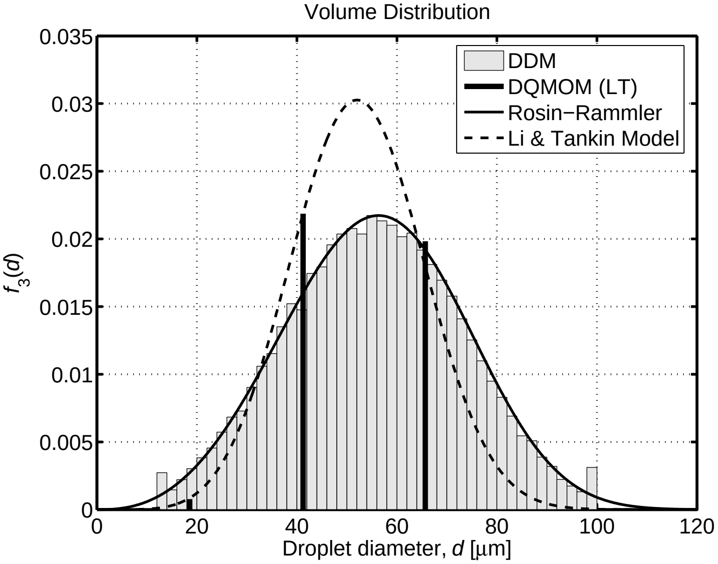

Figure 10.4: Comparison of the Rosin-Rammler and Li and Tankin (1987) volume distributions for SMD = 48.6 μm. The vertical black peaks represent the DQMOM representation of the Li and Tankin model.

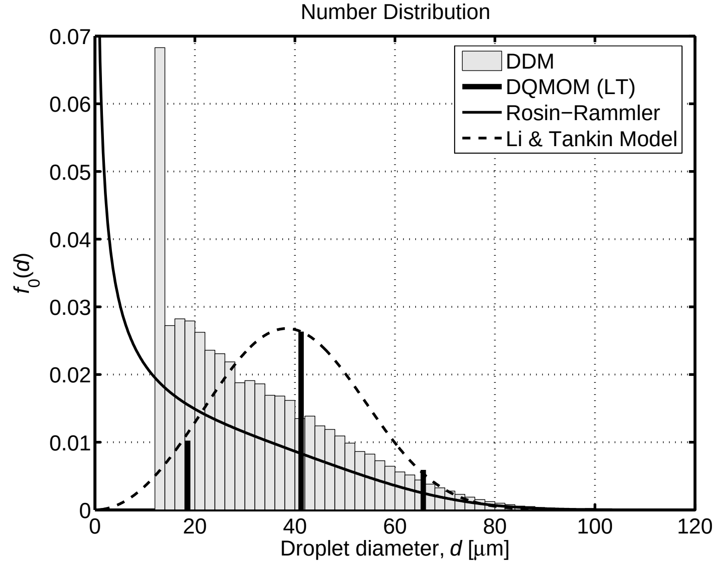

Figure 10.5: Rosin-Rammler and Li and Tankin number distributions.

The droplet boundary conditions used in the two DQMOM cases and the droplet initial conditions used in the DDM case are reported in Table 10.2. Three representative diameters (d_{10}, d_{32}, and d_{43}) are also reported in the table.

Table 10.2: Boundary values of droplet diameters, droplet number fractions, and droplet volume fractions for the DQMOM model for the Rosin-Rammler distribution with q = 3.5 and for the Li and Tankin model, and initial conditions for the DDM model.

Model	DQMOM			DQMOM			DDM
DSD	Rosin-Rammler (RR)			Li and Tankin (LT)			RR
Droplet phase, q	1	2	3	1	2	3	
Diameter, d_q [μm]	4.4	33.1	69.4	18.6	41.2	65.7	$d_{v0.005}$ = 13.7
Number fraction, ω_q / m_0 [-]	0.558	0.374	0.068	0.241	0.620	0.139	$d_{v0.995}$ = 99.9
Volume fraction, $\alpha_q = \frac{\pi}{6}\omega_q d_q^3$ [-]	0.001	0.373	0.626	0.018	0.515	0.467	
Mean diameters:							
d_{10} [μm]	19.6			39.2			31.9
d_{32} [μm]	48.6			48.6			48.6
d_{43} [μm]	55.8			52.2			55.5

By using the DQMOM, the first six moments (m_0 – m_5) of the Rosin-Rammler distribution are correctly represented, and thus the mean diameters are equal to the diameters calculated form Eq. (10.11).

The Rosin-Rammler distribution used in the DDM model is truncated at $d_{v0.005}$ and $d_{v0.995}$. This truncated distribution is obtained by matching the $\text{SMD} = m_3/m_2$ as d_D. The other moments (m_0, m_1, m_4, etc.) are then found from this truncated distribution, and thus those moments do not match the moments of the non-truncated Rosin-Rammler distribution calculated from Eq. (10.10). Therefore, the value of d_{10} is overestimated, and the d_{43} value is slightly underestimated. The comparison of the number distribution produced by this truncation with the Rosin-Rammler distribution is made in Figure 10.3. This shows that the number of very small droplets is underestimated; however, the distributions match for large droplets.

The Li and Tankin model decreases the range of initial droplet sizes. Since the range is smaller, the d_{10} is increased and d_{43} is decreased in comparison with the Rosin-Rammler distribution with $q = 3.5$.

10.2.5 Other Boundary Conditions

For completeness a short discussion of the boundary conditions being employed is included here. For the nozzle wall, the wall-function method of Launder and Spalding (1974) for turbulent fluids is used. For the air-core in the DQMOM computations (6 cells) and the orifice in the DDM computations (1 cell), a slip wall (zero shear stress) is applied.

The other boundary conditions employed are for the centerline and the pressure-outlets (open). The centerline condition is one of symmetry, such that all fluid properties have zero radial gradients across the centerline. Hence there is no flow across the symmetry axis. The pressure-outlet condition is similar in that the fluid properties all have zero normal gradients at the outlet.

10.2.6 Initial Conditions

At the start of the computation the domain consists of quiescent air at atmospheric pressure and room temperature. The initial values of the gas phase turbulent kinetic energy and the dissipation rate are selected such that the initial gas turbulence is small relative to that generated by the spray. The computations are performed with initial values of $k_g = 0.0148$ m^2/s^2 and $\varepsilon_g = 0.198$ m^2/s^3 yielding a turbulent diffusivity of $\nu_{t,g} = 1.0\times10^{-4}$ m^2/s. The initial values of k_g and ε_g influence the transient results when the DDM approach is used to model the spray. However, the steady state results are not sensitive to the initial turbulence values. The DQMOM-multi-fluid computations are insensitive to these initial values.

10.3 Results and Discussion

This section demonstrates the capabilities of the DQMOM-multi-fluid model applied to the hollow-cone spray. It is split into three sections. The first deals with the basic structure of the spray. The second considers comparisons between experimental data and the predicted results in order to quantitatively show the capability of the model. The third in concerned with local DSDs.

10.3.1 Basic Structure

Figure 10.6 shows the structure of the spray in terms of contours of the droplet SMD. The iso-lines corresponding to liquid volume fractions of 10^{-6} and 10^{-5}, also shown in the figure, show the hollow-cone shape, especially in the near-nozzle region of the spray. Here a very narrow high flux region is predicted along the hollow-cone sheet path. Beyond an axial distance of 30 mm, the spray region becomes much thicker, and it can be observed that the hollow-cone spray tends to collapse. The reason why the spray collapses is that droplets loose the momentum of radial direction due to dynamic drag. The spray motion causes the air flow to re-circulate through the spray. The small droplets loose their momentum quickly against the air drag force and are therefore easily carried by the air flow.

Higher droplet SMD values can be seen at the periphery of the spray than elsewhere due to the large droplets experiencing less drag than the smaller droplets, which are entrained along the spray centerline. The experimental comparisons will demonstrate that this is done with a reasonable degree of accuracy.

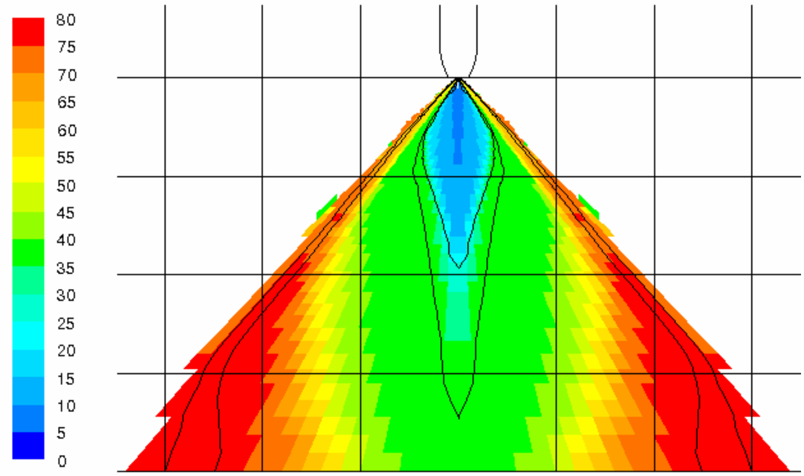

Figure 10.6: Contours of SMD together with iso-lines corresponding to liquid volume fractions of 10^{-6} and 10^{-5} of the DQMOM computation with the Rosin-Rammler initial DSD. The grid superimposed on the image has a spacing of 50 mm.

10.3.2 Comparison with Experiment

Radial profiles of arithmetic mean diameter d_{10}, SMD d_{32}, and mean axial and radial velocities are evaluated at axial positions of $x = 10, 20, 40$, and 80 mm. Since PDA droplet sizing is based on the presence of spherical droplets, measurements can only be taken in a certain distance from the liquid sheet breakup. Therefore comparisons at closer axial distances are meaningless. Computed results obtained by the DQMOM-multi-fluid model are shown for two initial DSDs: the Rosin-Rammler (RR) and the Li and Tankin (LT) distributions. Results obtained from running the DDM model with (coll. on) and without (coll. off) consideration of droplet collision are also shown.

Droplet Size

Figure 10.7 presents radial evolutions of droplet arithmetic mean diameter, d_{10}, and Figure 10.8 presents radial evolutions of SMD, d_{32}, at axial distances 10, 20, 40, and 80 mm from the nozzle for the experiment and all computations realized. The measurements give a minimum droplet size at the spray axis and an increase of the size towards the edges of the spray. General trends of the local mean diameter are in good agreement between models and experiment as shown in Figure 10.7. Concerning the SMD, the agreement between measurement and calculations is also reasonably good as shown in Figure 10.8.

What is immediately noticeable is that, at x = 10 and 20 mm, the droplets in the DDM calculations are detected only beyond the radius of approximately 5 mm, whereas the measurements have detected droplets over the entire range from 0 mm. Figure 10.7 shows that a mean diameter in the range between 8 and 14 μm is found in the experiments. Such small droplets are not present in the DDM calculations at these locations in the spray. This is a result of the truncation of the initial Rosin-Rammler DSD in the DDM calculations. In the case with the Li and Tankin (LT) initial DSD, the DQMOM-multi-fluid model also misses this main feature due to the initial distribution approximation. At the spray axis the DQMOM (RR) calculation gives nearly the same mean diameter values as the measurements.

The effect of the DDM collision model is pointed out by a comparison between DDM computations with and without collision. The droplet sizes reported by the DDM with consideration of collision are significantly larger in the outer radial locations than that produced by the DDM without consideration of collision, although they are nearly equal at shorter radial distances. The agreement improves, if the DDM computations are carried out without consideration of collisions and coalescence.

The agreement between the experimental and DQMOM (RR) distributions at 10 mm downstream of the nozzle is good. The trend of increasing droplet size with radial distance is correct, but the rate of change is too large, with the mean diameter of the small droplets on the centerline well predicted and the mean diameter of the large droplets at the periphery overpredicted.

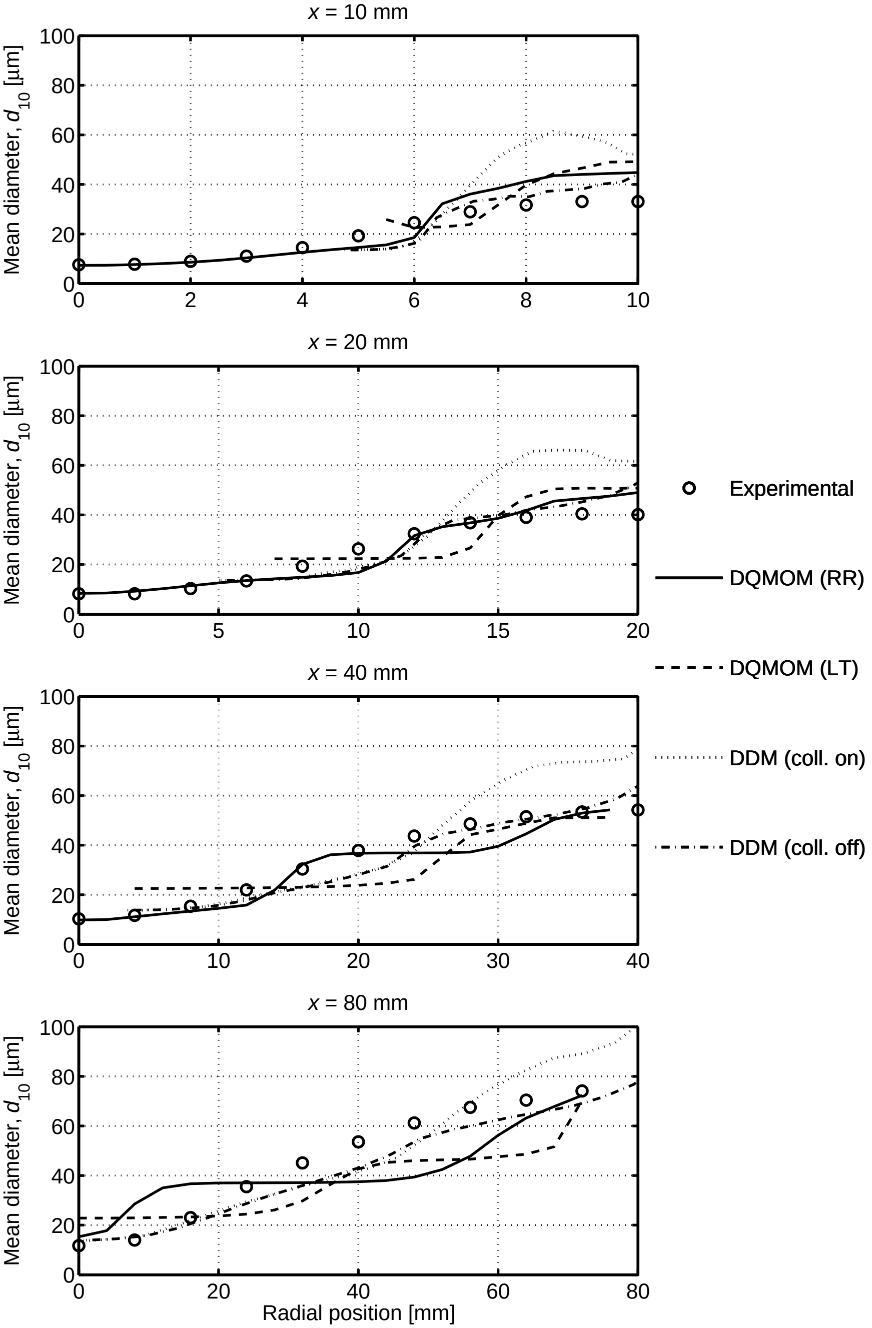

Figure 10.7: Profiles of droplet arithmetic mean diameter, comparison of calculations and measurement.

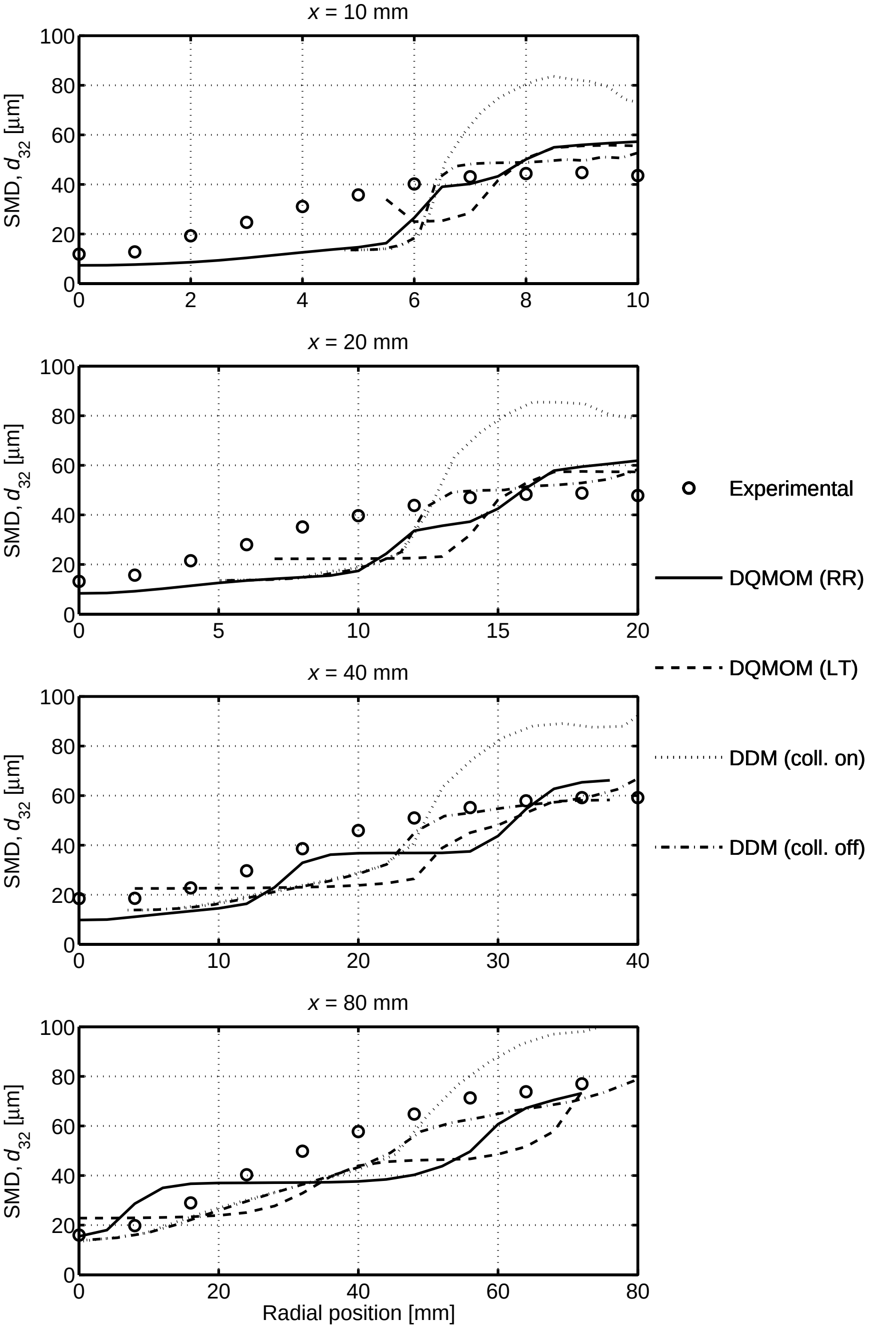

Figure 10.8: Profiles of droplet SMD, comparison of calculations and measurement.

By 20 mm downstream of the nozzle, the agreement between the DQMOM (RR) and experimental radial droplet mean diameter distributions is closer. The droplet size at the spray periphery is still overpredicted, but is closer than the value predicted at 10 mm axial distance. The rate of increase of droplet size with radial distance is approximately correct and the size of the smallest droplets on the centerline is again in good agreement with experiment.

The agreement between the distributions at 40 mm downstream of the nozzle is again good, the predicted mean diameter having now reduced to a level below the experimental values. The droplet mean diameter increases at similar rates with radial distance. The droplet sizes at the centerline are again in good agreement with experiment.

The predicted radial distribution at 80 mm axial distance is the least accurate in comparison with the experiment. The trend of increasing droplet size with radial distance is correct, but whereas the experimental results and the DDM (coll. off) predict a continuously increasing mean diameter with radial distance, slope changes are predicted by the DQMOM-multi-fluid model. The mean diameter of the small droplets at the centerline is overpredicted and the mean diameter of the large droplets at radial distances from 30 – 60 mm is underpredicted. The main reason for this disagreement is that the DQMOM-multi-fluid model predicts nearly monodisperse local DSDs, especially at larger downstream distances. At shorter axial distances the DQMOM (RR) predicted droplet sizes agree with the measured experimental data. Then, it can be assumed that the three nodes used to represent the distribution of droplet sizes are appropriate. The continuously increasing mean diameter with radial distance of the DDM (coll. off) model is due to the finer discretization of the droplet conditions.

The experimental mean diameter values increase in axial distance, possibly due to the coalescence of smaller droplets. Despite disregarding coalescence, the DDM (coll. off) mean diameter values also increase with axial distance suggesting that coalescence is not significant as regards the present spray. Also, the DQMOM-multi-fluid model results show that the effect of collisions on the mean diameter values is small.

Droplet Velocity

Figure 10.9 compares the experimental results with the DQMOM-multi-fluid and DDM predictions of the axial mean velocity profiles of droplets at various axial locations downstream of the nozzle. Both models predict reasonable accurate decay rates for the axial mean velocity. Figure 10.10 shows that the radial mean velocity of droplets is also predicted accurately by the DQMOM-multi-fluid and DDM models. Thus, both modeling approaches are able to predict the main features of the hollow-cone spray.

The comparison of the experimental and numerical data reveals some discrepancies. Generally speaking, the larger size droplets are less affected by the air flow and tend to follow a more independent path, whereas smaller size droplets tend to follow the air flow field. The measured axial mean velocity profiles reveal the effect of air entrainment into the spray core and the resulting transport of small droplets. This entrainment causes the high droplet velocities on the centerline (see Figure 10.9). The DQMOM-multi-fluid model with the Rosin-Rammler initial DSD produces a droplet distribution covering the entire width of the spray. The other computations demonstrate that there is a concentration of droplets in the outer radial locations corresponding with the spray angle. All in all the DQMOM (RR) simulation deliver a more accurate description of the droplet velocity field in the spray. The trend of changing droplet axial velocity with radial distance is correct, but the velocity of the small droplets on the centerline is underpredicted and the velocity of the large droplets at the periphery is overpredicted. Hence it seems that the air entrainment by the spray is underpredicted. The difference may also be due to an underestimate of turbulent droplet dispersion in the model. As a result of the lesser dispersion or air entrainment, the computed mean diameters shown in Figure 10.7 and Figure 10.8 behave somewhat differently than the experimental results.

The DDM model without consideration of collision underpredicts both droplet velocity components. The DQMOM-multi-fluid model is slightly better, generally underpredicting the velocities at short radial distances and overpredicting them at further radial distances. One possible reason for the better performance of the DQMOM-multi-fluid model compared to the DDM model could be the use of finer grid resolution near the nozzle compared to the DDM model.

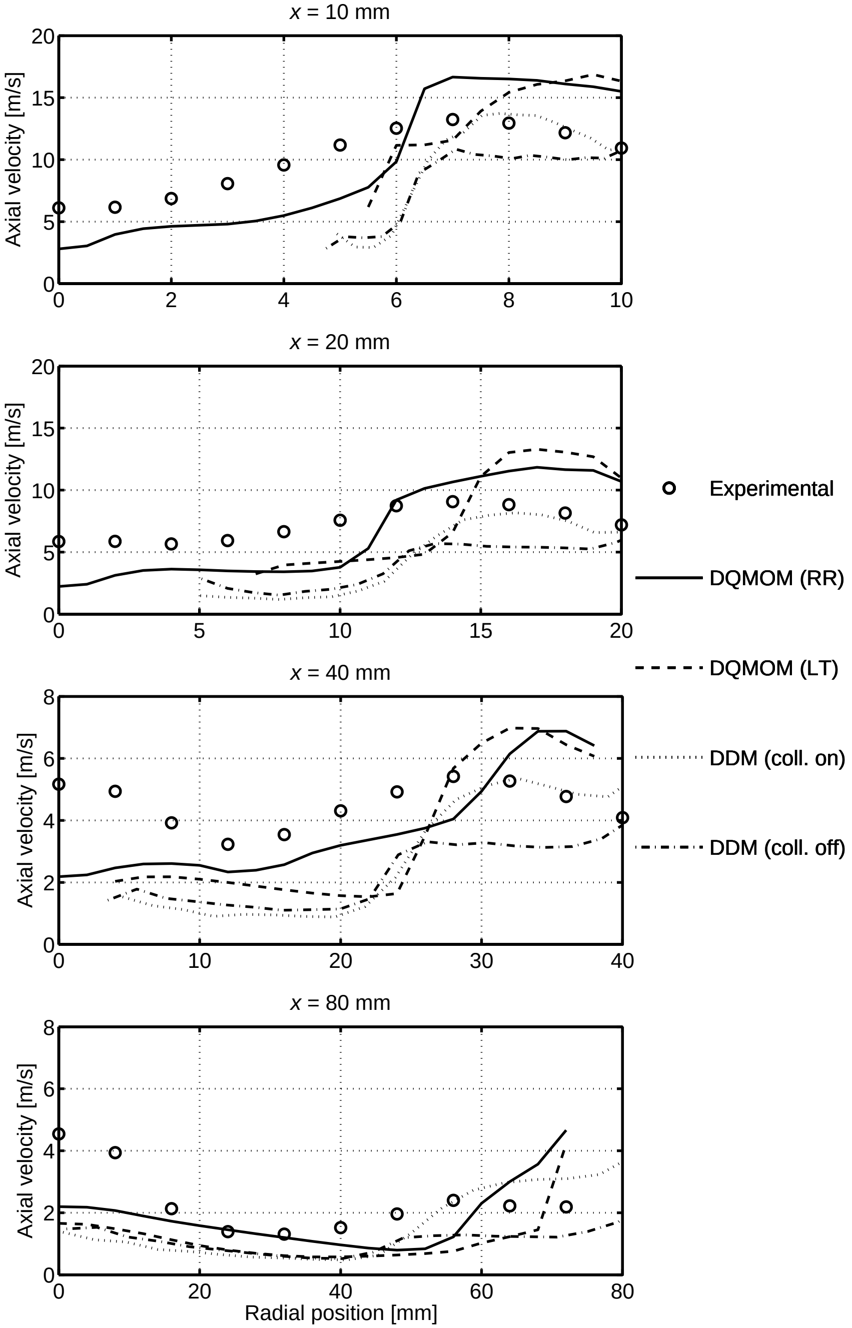

Figure 10.9: Profiles of axial droplet mean velocity, comparison of calculations and measurement.

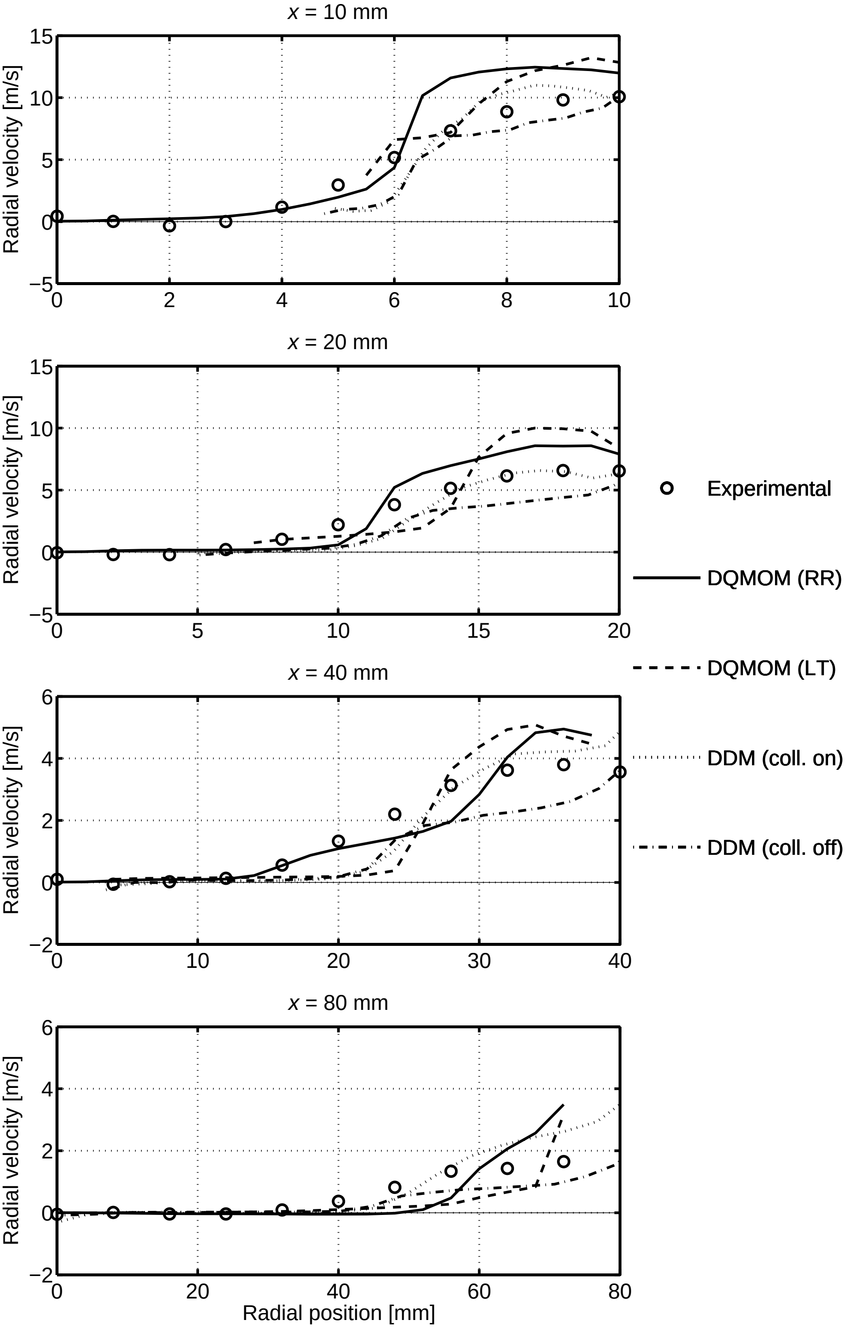

Figure 10.10: Profiles of radial droplet mean velocity, comparison of calculations and measurement.

To compare the gas phase flow field, the predicted velocity vectors are shown in Figure 10.11 with superimposed iso-lines indicating a liquid volume fraction of 1%. Shown are only the steady state results of the DQMOM-multi-fluid model for the Rosin-Rammler initial DSD and of the DDM model without considering collision. The two images represent $x = 0 - 2.0$ mm by $r = 0 - 1.4$ mm areas of the computational grids.

The large-scale gas velocity fields of both models appear similar. However, there are differences in the velocity fields, especially in the region close to the atomizer. Due to the much finer spatial resolution of the DQMOM grid, the maximum velocity and the velocity gradients are higher there. The DDM simulations show a smoother velocity field. All in all the DQMOM-multi-fluid simulations deliver a more accurate description of the gas velocity field in the dense spray region. The atomizer exit is fully resolved by the DQMOM mesh; however, the mesh has a wall at the position of the air-core, which definitely affects the gas velocity field.

The air is initially accelerated through aerodynamic drag interaction with the spray droplets, which decelerate and give up their momentum. The spray motion causes the air flow to re-circulate through the spray, which is responsible for the high droplet velocities on the centerline at downstream locations. The inward-directed velocity vector at the edges of the spray will certainly influence the smaller droplets, which have a smaller aerodynamic relaxation time (Crowe, *et al.*, 1998). These smaller droplets will be preferentially swept toward the centerline of the spray, which explains the previously observed increase in mean droplet size in the radial direction.

DQMOM (RR)

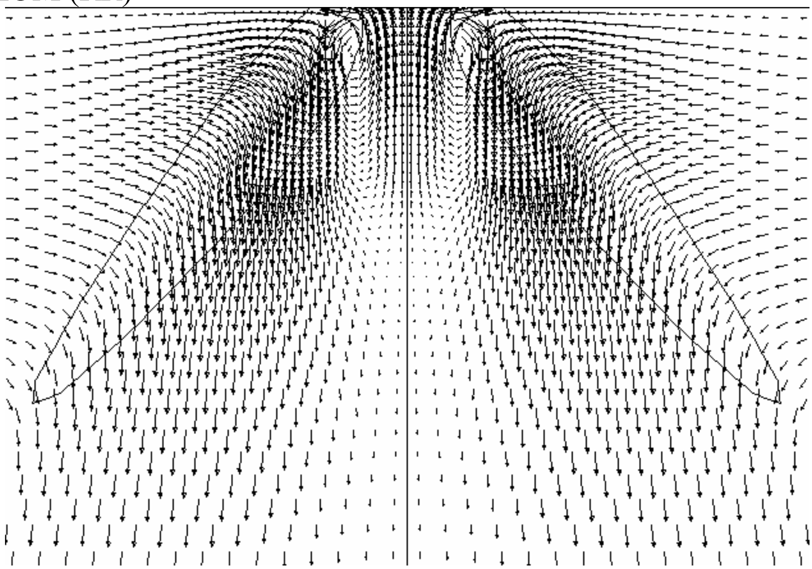

DDM (coll. off)

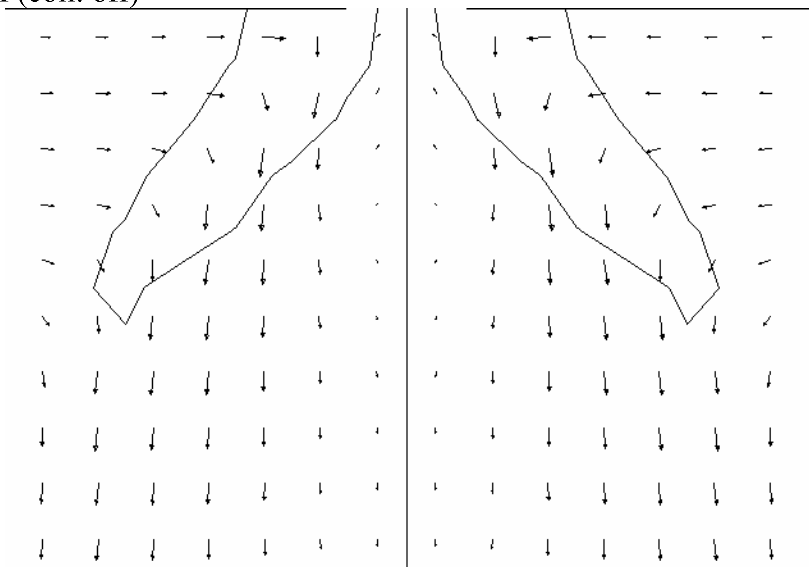

Figure 10.11: Computed air velocity vectors of two models, indicating the centrally directed entrainment. The superimposed iso-line indicates a liquid volume fraction of 1%.

Liquid Volume Fraction

Another quantity that can be used to validate a spray model is the predicted volume fraction distribution. In order to successfully validate the spray models, the measured volume fraction of droplets must be known accurately, which implies that the diameter and velocity of every droplet that contributes to the overall droplet flow must be recorded. However, this measurement is notoriously difficult to take accurately using PDA due to high data rejection rates, which are caused by weak and ambiguous signals as the droplets pass through the detection volume. The PDA instrument was not able to detect every droplet in the vicinity of the atomizer where the spray is relatively dense and the velocity is high, although it was better able to handle sparse, low-velocity conditions that develop further downstream. Thus, there is some uncertainty about the PDA data, which is not suitable for a quantitative comparison with simulations.

Comparison of the computed radial distributions of volume fraction of the spray liquid is given in Figure 10.12, which illustrates the typical hollow-cone structure of the spray and its increasing dispersion in the downstream region. The comparison of the numerical data reveals some disagreements. Both DQMOM computations and the DDM computation with consideration of collision agree well at $x = 10$ mm. The profiles of the droplet volume fraction are typical for a hollow-cone spray with a local minimum in the core region and a maximum at the edge of the spray. Further downstream, droplet transport, from the edge of the spray into the core region by air entrainment, results in an increase of the volume fraction in the core of the spray especially for the DDM case without consideration of collision. The DQMOM results, and especially the case with the Li and Tankin initial DSD, retain the hollow-cone shape longer and show higher volume fractions and less dispersion than the DDM data. This difference may be due to an underestimate of turbulent droplet dispersion in the DQMOM-multi-fluid model. The dispersion effect of the air flow is less significant sine the air flow has a smaller impact on larger droplets representing the major fraction of liquid volume, whereas number averaged flow variables such as mean droplet velocities are more sensitive to the dynamics of smaller droplets.

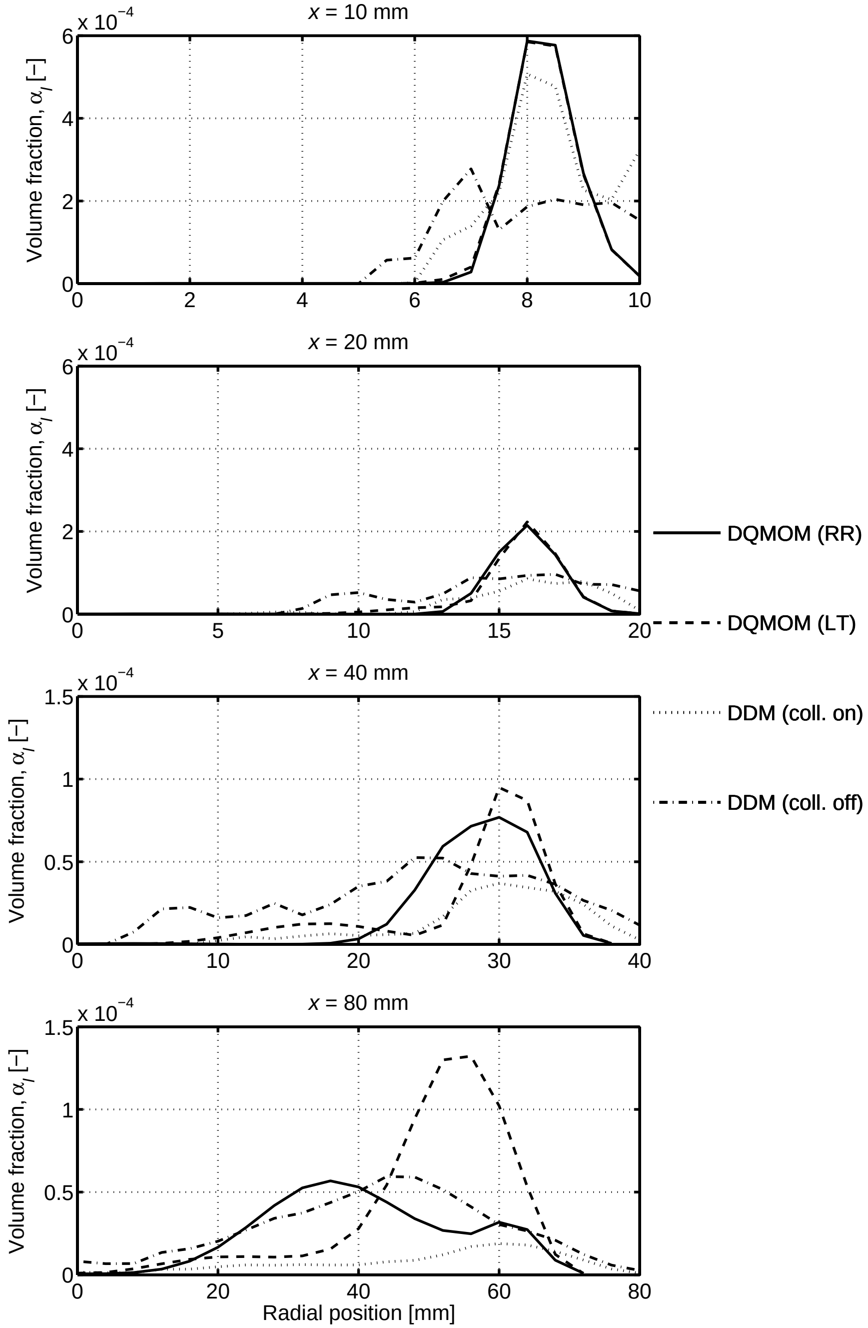

Figure 10.12: Profiles of liquid volume fraction, comparison of calculations.

Fluctuations, which can be seen in the DDM results, are due to the statistical nature of the Monte Carlo sampling method. They could be damped by increasing the number of parcels used to evaluate mean liquid volume fractions.

Limitations of the Fluent DDM Droplet Collision Model

Results for the DDM model show that the submodel for collisions and coalescence of droplets has a noticeable effect with the droplet sizes and velocities being smaller in the absence of collisions and coalescence. These results are consistent with the findings of Aneja and Abraham (1998). They showed that the models do not give converged results with larger droplets resulting from increased grid resolution in the presence of collisions and coalescence. Such larger droplets are less effective in transferring momentum to the air, and hence the velocity is larger.

In the Fluent DDM droplet collision model, the collision frequency β_{12} is estimated according to the kinetic theory of gases (Fluent, 2005)

$$\beta_{12} = \frac{\pi}{4} \frac{n_2}{V_{cell}} \left(d_1 + d_2\right)^2 U_{rel}, \qquad \left(d_2 < d_1\right) \tag{10.17}$$

where n_2 is the number of droplets in the parcel with the smaller diameter and V_{cell} is the volume of the continuous-phase cell containing the parcel.

However, there are at least three limitations in the Fluent model. The first is that the Fluent model assumes that a given parcel may collide with another parcel only if these two parcels lie in the same computational cell. As indicated by Schmidt and Rutland (2000) and Nordin (2001), this assumption may be inappropriate. Under this assumption, the collision between two spatially very close parcels is a priori ignored if they reside in different computational cells. Contrary to this, the collision may occur for a pair of possibly far distant parcels in the same computational cell. As a result, the collision model strongly depends on the computational cell sizes. The second limitation is linked with non-uniformity of the spatial distribution of parcels in the domain. Aneja and Abraham (1998) indicated that the Fluent approach is not suitable for sprays, where the variation in number density is large even inside one cell. Finally, the Fluent model considers only two collision regimes such as separation and permanent coalescence. In the separation regime the colliding droplets loose only their momentum, but retain their sizes after impact. As referred by Georjon and Reitz (1999), this could lead to an overprediction of the coalescence phenomenon because the collision-induced breakup process is ignored. Collision-induced breakup occurs when the relative velocity of colliding droplets is high, and since a low velocity spray is under consideration here, the phenomena almost never occurs in this investigation. In contrast, since bounce and coalescence appear at low velocities, it is expected that their effect is significant as regards this spray.

The grid size employed is finer than the resolution typically employed in DDM computations (Han, *et al.*, 1997; Schmidt, *et al.*, 1999; Lee, *et al.*, 2004; Rotondi and Bella, 2006). Support is thus lent to the suggestion that the number of large droplets produced in coalescence near the atomizer is too high, which results in the prediction of high droplet sizes at all positions further downstream.

Although the collision models developed by Schmidt and Rutland (2000), Nordin (2001), and Ko and Ryou (2005*a*) are more accurate, they have not been implemented in the Fluent code.

10.3.3 Droplet Size Distribution

In order to gain a more resolved assessment of the DQMOM-multi-fluid model, a closer look into the local DSDs reveals some additional information. Calculated DSDs in comparison with measurements is illustrated in Figure 10.13 for four radial locations at x = 80 mm. The agreement of the calculated DSDs with the PDA measurements is reasonably good. The experimental results show a wider range of droplet sizes than is predicted. At r = 0, the DDM model without consideration of collision predicts less numerous small droplets, and at r = 20, 40, and 80 mm, it predict less numerous large droplets. The DQMOM-multi-fluid model predicts even more monodisperse distributions. These results agree with the trends shown in Figure 10.7 and Figure 10.8.

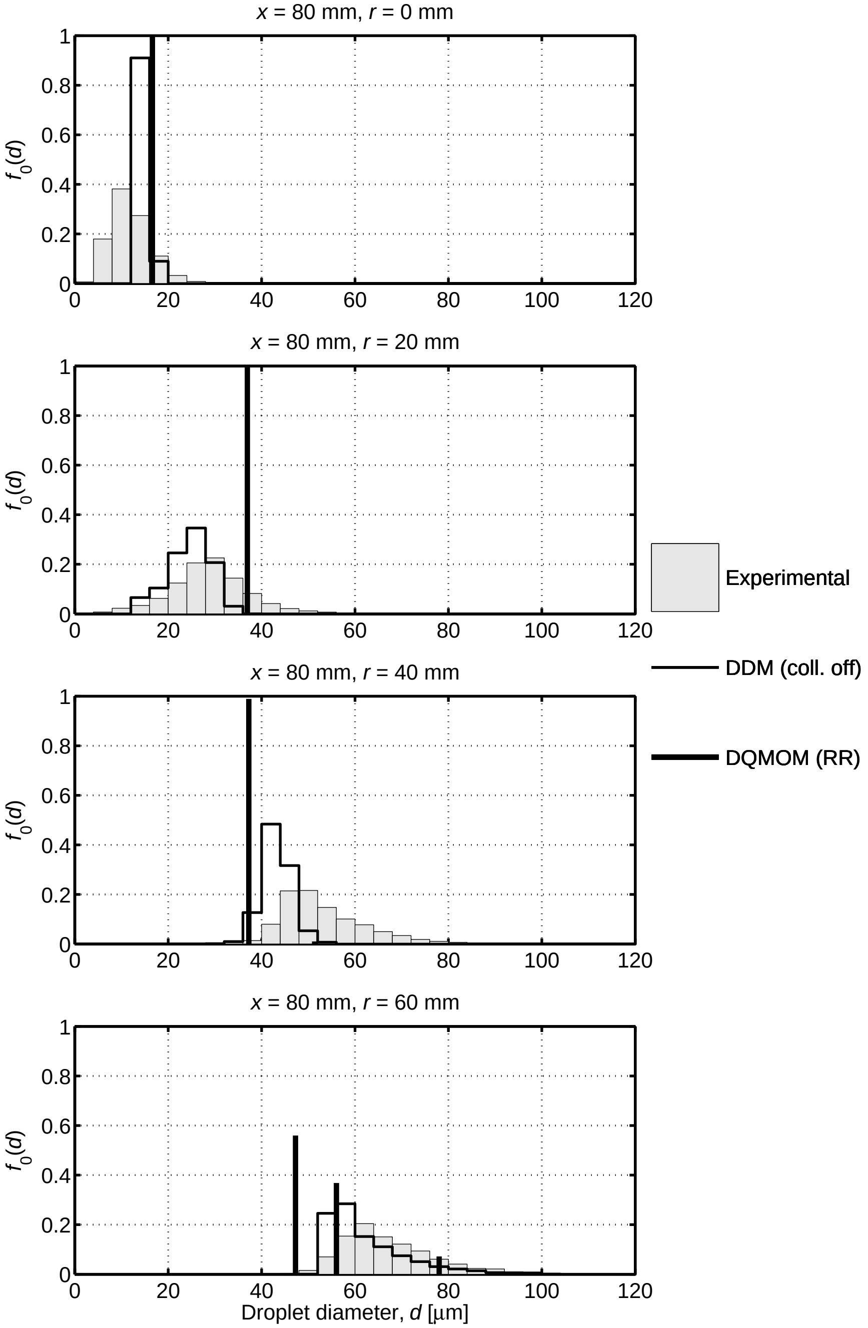

Figure 10.13: Comparison of measured and computed local DSDs.

As the DQMOM-multi-fluid model allows the three droplet phases to be transported at different velocities, the polydisperse nature of the flow can be simulated. However, this causes its own problems. Unless droplet breakup or coalescence occurs, the droplet classes in the DQMOM representation will not move along the droplet size axis. In the present hollow-cone spray, no droplet breakup downstream of the nozzle is observed, and very few collisions occur in the dilute region of this spray. Therefore, the change in the DSD is due to only larger droplets being convected into some regions of the spray and only small droplets reaching other regions. Unless the droplet phases tend toward having similar velocities, the local DSD will quickly become monodisperse. This means that the DSD is not represented by three droplet phases at all locations.

With a more realistic representation of the local DSDs in the spray, the model would be able to predict satisfactorily the segregation of droplets in the spray. However, the size distributions cannot be fully captured, unless a large number of droplet phases are considered, and this leads to a computationally expensive scheme.

At shorter axial distances the predicted droplet sizes agree closer with the measured experimental data, and here the three nodes (droplet phases) used to represent the distribution of droplet sizes are appropriate.

10.4 Computational Effort

The efficiency of the two approaches used to calculate the given two-phase flow can be characterized by the CPU times required by the different calculations.

Discretization of the DSD and solution of the momentum equations for each droplet phase (at least 3) is considered necessary in the DQMOM-multi-fluid approach in order to predict the velocity differences that develop among droplets of different sizes. In the DDM approach, the spray is modeled by tracking a large number (approximately 60,000) of representative parcels. On the other hand, fewer transport equations are required for the DDM approach. In addition, fewer cells are used for the DDM approach, so that it is only slightly more computationally expensive per time step compared with the DQMOM-multi-fluid approach. However, the time step in the DDM solution is ten times larger than the DQMOM-multi-fluid time step, so that the DQMOM-multi-fluid method needs about ten times more computationally effort than the DDM model.

The results support the concept of the DQMOM-multi-fluid scheme, showing that it reaches a solution of the two-phase flow field. However, this flow field is only of restricted quality due to the limitations imposed on the discretization of the polydisperse spray. The method can handle only a limited number of droplet phases. Taking advantage of the stochastic nature of the tracking approach, the DDM model on the other hand is highly accurate due to a refined discretization of droplet initial conditions. Although well established for the numerical calculation of complex disperse two-phase flows, the DDM model for droplet tracking shows a poor convergence behavior for this kind of flow.

Due to the much finer spatial resolution of the DQMOM grid, the DQMOM-multi-fluid treatment has the potential to deliver a more accurate description of the two-phase field in the dense spray region than the DDM counterpart.

10.5 Summary

The DQMOM-multi-fluid model has been applied to the calculation of a low-speed hollow-cone spray. For validating the calculations experimental data obtained by PDA have been used. The DQMOM-multi-fluid model predictions have also been compared to the computational results obtained using the Fluent DDM model. Good levels of agreement between the experiment and computations in spray characteristics such as local droplet velocities, droplet sizes, and DSDs have been obtained.

The droplet sizes of this low-speed hollow-cone spray are determined mainly by the breakup of the liquid sheet. However, it is important to note that the present comparisons with experimental measurements validate the spray models as a whole, i.e. the effects of primary atomization, droplet drag and collision, and do not directly validate the primary breakup expressions presented in Section 2.2 (LISA model).

It has been found that the size distribution of the droplets after the sheet breaks up is very influential on the overall spray characteristics. The truncated Rosin-Rammler distribution used in the DDM model and the Li and Tankin distribution used in the DQMOM-multi-fluid model results in an underestimated population of small droplets, which leads to inaccurate predictions of spray structure. The Rosin-Rammler distribution used in the DQMOM-multi-fluid model is found to increase the range of droplet sizes in the spray and improves the predictions substantially.

Only two assumed distributions have been used in the course of this work. Future work should consider a number of functions and compare the behavior of the model with different assumed distributions.

The DQMOM-multi-fluid model with the Rosin-Rammler initial DSD displays good velocity results in comparison with experimental data suggesting that the interphase drag model is performing well. The droplet sizes predicted are reasonable in comparison with both experiment and results produced by the DDM model without considering collision. The comparisons of results are found to be best at the initial stations close to the atomizer but gets worse downstream. Due to the use of finer grid resolution near the nozzle compared to the DDM model, the DQMOM-multi-fluid model performs better in the dense spray region. However, the model suffers from bad statistics in the thin spray region, due to the limited number of size classes that can be employed.

The influence of the consideration of collision and coalescence in the DDM model has been discussed. The results show that the consideration of collision leads to a wrongly predicted spray behavior. The major problem is that the droplet sizes predicted in the near-nozzle zone are too large, which suggests that an improvement in the DDM collision model will be required in order to more accurately predict these collision effects.

The overall agreement between the predicted and measured droplet sizes is good, suggesting that the droplet formation in the LISA model is valid, as well as the description of the collisions with the DQMOM model. The predictions of both DQMOM-multi-fluid and DDM approaches are consistent with each other, which points to the validity of the DQMOM-multi-fluid model, so that the approach can be used with more confidence for future predictions of hollow-cone sprays.

Future work could include more accurate modeling of the flow through the atomizer and thus a better estimate of the sheet thickness and exit velocity. The inclusion of transient and three-dimensional behavior could also improve the model. Additionally, the assumed aerodynamic breakup process is speculative and would benefit from a better understanding of primary atomization physics.

Chapter 11

Conclusions and Future Work

11.1 Summary and Conclusions

In this work, the DQMOM-multi-fluid model has been developed for sprays. The primary objective of developing this model was to overcome the numerical resolution limitations of the traditionally employed DDM approach for sprays and thereby employ the model to study the physical processes in sprays with adequate accuracy. The evaluation of the model was conducted by comparing with experimental findings obtained from production-scale pressure-swirl and Y-jet atomizers operated with water. In this Section, the work is summarized and the important conclusions are drawn.

11.1.1 Experimental Work

In Section 4.3, interferometric particle imaging (IPI) and particle tracking velocimetry (PTV) measurements were performed in the hollow-cone spray from a Danfoss pressure-swirl atomizer. With different focal length optics for the de-focused camera, the IPI technique was adapted to the dilute part near the edge of the spray and to the more dense part closer to the centre axis. At the centre of the spray the concentration of droplets was too high and thus the resulting overlap reduced the validation. The measurement results were compared to PDA measurements. It was found that the shape and trends of the data acquired with IPI and PDA were very similar. However the comparison of mean diameters revealed that IPI yields smaller values than those measured by PDA most likely due to different averaging techniques rather than measurement techniques. Measurements with IPI and PTV have shown that the technique can be used effectively to map the spatial structure of a spray. The main limitation of the technique is that it cannot be used at high droplet concentrations.

In Section 4.4, experimental studies were conducted in sprays produced by nine different single-hole Y-jet atomizers with different operating conditions. The PDA system was used to measure droplet velocity and size. The results indicated that the spray characteristic parameters are asymmetric about the spray axis due to the impact of liquid and air streams in the mixing chamber which is projected outside the atomizer. The guidelines of Mullinger and Chigier (1974) for the design of internal mixing twin-fluid atomizers were found to agree with the present experimental results. The mixing length should be approximately four times the mixing chamber diameter. Other geometrical variables had relatively little effect except for the way in which they affected air and water gauge pressures. From the results obtained in the PDA measurements, it can be concluded that increasing the liquid flow rate or the mass loading ratio both reduce the mean diameters and increase the axial velocity of the spray. The liquid flow rate is the key parameter determining the spray characteristics of the Y-jet atomizers. The spray is less affected by different mass loading ratios.

11.1.2 Numerical Simulation of Internal Atomizer Flow

In Chapter 7, the applicability of two-phase CFD modeling of the internal flow in a large-scale pressure-swirl atomizer was investigated using three approaches: 1) the VOF-QLES method using the laminar viscosity only, 2) the VOF-LES method using subgrid-scale turbulence modeling, and 3) the Two-Fluid Euler/Euler method using the QLES approach. All simulations delivered similar results and produced the characteristic air-core that matched those observed in the experiments. Likewise, tangential and axial velocity profiles in the conical swirl chamber and static wall pressure were found to match favorably with the measured profiles. For the two flow rates considered here, the VOF-QLES and Two-Fluid-QLES approaches appeared to give the best agreement.

The liquid film cone exiting from the atomizer was modeled in a region 25 mm downstream the atomizer prior to film breakup. The atomizer and near-field spray-cone was simulated using 1.1 million cells; however, the resolution was insufficient. To include the breakup of the liquid film, an even finer grid resolution would be required.

The results of this study suggest that the use of two-phase CFD modeling can be used to gain valuable insight into the dynamics of the internal flow of production-scale pressure-swirl atomizers.

The analysis of the internal flow in the mixing chamber of a Y-jet atomizer is an even more complex problem due to the violent mixing of the liquid and gas and a wider range of physical processes occurring over a broader range of length- and time-scales. The VOF model may be incapable of describing the flow because the phases are not separated as in the pressure-swirl atomizer. In order to model the mixing of liquid and gas, the two-fluid (or multi-fluid) model should be used.

11.1.3 Development of the DQMOM-Multi-Fluid Model

The DDM approach is, in principle, valid only for dilute sprays when the local gas volume fraction is greater than 90%. This criterion is not satisfied in the region close to the nozzle orifice where the presence of an intact liquid sheet and the dense spray regime results in relatively small gas volume fractions. To enforce the criterion, the smallest grid size that may be employed in the near-nozzle region has to be much greater than the sheet thickness. This grid size is insufficient to resolve the sharp gradients in the near-nozzle region. Furthermore, the Lagrangian approach cannot be employed to represent the intact liquid sheet. These numerical limitations are minimized with the DQMOM-multi-fluid approach.

The Eulerian treatment of the liquid phase has the potential to be more efficient than its Lagrangian counterpart. However, multi-size Eulerian treatments have hitherto been employed by similar discretization of the DSD and considering each size group as a completely separate phase.

This leads to a scheme involving many phases and is also computationally expensive.

The DQMOM model used in this thesis originated in the research work of Marchisio and Fox (2005) and is based on an alternative approach to the modeling of population balances. The concept is to model both the liquid and the gas in the potentially more efficient Eulerian formulation, but to capture the full polydisperse nature of the spray flow while only considering the liquid as a few ($N = 3$) phases. The DQMOM representation of the DSD involves the solution of an equation for the volume fraction and an equation for the diameter for each droplet phase. Source terms in these equations are derived in the model in terms of source terms of the first $2N$ moments of the size distribution. In the DQMOM-multi-fluid model each droplet phase has its own momentum balance giving the model the ability to treat the polydispersed nature of the flow field. The number of equations being solved is significantly less than in previous polydisperse Eulerian spray models, making the scheme more computationally efficient than its predecessors.

The governing equations of the multi-fluid model were presented in Section 5.4. The governing equations are written for both the liquid phases and the gas phase and the equations are coupled through interfacial transfer terms. The interfacial forces between the liquid phases and the gas phase arise from drag and turbulent dispersion. The modeling of drag and turbulent dispersion was discussed in Sections 5.4.1 and 5.5.2, respectively. Turbulence is modeled using the k-ε model with additional source terms due to turbulence modulation as discussed in Section 5.5.

The evolution of droplet sizes due to breakup and coalescence is predicted using the DQMOM as described in Chapter 6. The WAVE atomization and droplet breakup model considered in this work was described in Section 3.2. The model for collisions and coalescence was described in Section 3.3.

11.1.4 Comparison of Computed Droplet Size and Velocity Profiles with Measurements

The DQMOM-multi-fluid model has been applied to calculate local values of the droplet sizes produced by diesel-type sprays, Y-jet water sprays, and a hollow-cone spray.

Computation of Diesel-Type Sprays

The computed liquid velocity profiles for non-evaporating diesel-type sprays were compared with measurements of Wu, *et al.* (1984) for three cases, each with a different combination of injection velocity and ambient density. Good agreement were obtained by comparing the computed velocity profiles for the three cases at two axial locations of 400 and 600 nozzle diameters downstream, refer to Figure 8.2 – Figure 8.4.

Computation of Y-jet Water Sprays

The droplet size and velocity results for the Y-jet sprays have been less satisfactory. However, it has been shown that the model is able to reproduce measured trends as shown in Figure 9.3 and Figure 9.4. Parametric explorations have served to demonstrate that the model reacts in the correct qualitative manner to changes in input parameters. This suggests that the boundary conditions at the nozzle were incorrect in these cases. The accuracy of the calculation results strongly depends on the consistent modeling of the nozzle flow characteristics. Hence, the availability of proper boundary conditions at the nozzle exit serve as major prerequisites for the successful analysis and optimization of Y-jet sprays; and numerical assessment of the Y-jet nozzle to provide internal distributions of liquid and gas should be performed.

Computation of a Hollow-Cone Spray

The DQMOM-multi-fluid model has been applied to the calculation of a low-speed hollow-cone spray. For validating the calculations experimental data obtained by PDA have been used. The DQMOM-multi-fluid model predictions have also been compared to the computational results obtained using the Fluent DDM model. Good levels of agreement between the experiment and computations in spray characteristics such as local droplet velocities (Figure 10.9), droplet sizes (Figure 10.7), and DSDs (Figure 10.13) have been obtained.

It has been found that the size distribution of the droplets after the sheet breaks up is very influential on the overall spray characteristics. The truncated Rosin-Rammler distribution used in the DDM model and the Li and Tankin distribution used in the DQMOM-multi-fluid model resulted in an underestimated population of small droplets, which lead to inaccurate predictions of spray structure. The Rosin-Rammler distribution used in the DQMOM-multi-fluid model was found to increase the range of droplet sizes in the spray and improved the predictions substantially.

Due to the use of finer grid resolution near the nozzle compared to the DDM model, the DQMOM-multi-fluid model performs better in the dense spray region. However, the model suffers from bad statistics in the thin spray region, due to the limited number of size classes that can be employed.

11.1.5 The DQMOM-Multi-Fluid Model in General

These simulations have mainly served as tests for carrying out DQMOM-multi-fluid spray simulations. Making a more "realistic" spray simulation may require time accurate calculations, e.g. LES. A realistic spray simulation would also require rigorous argumentation of the role of breakup and hypothesis testing using different types of breakup scenarios.

Based on the present study, it is concluded that the present DQMOM-multi-fluid model would be useful in spray simulations. The use of one model to predict diesel-like jets behavior, Y-jet spray behavior, and hollow-cone spray behavior will simplify atomization submodels and improve confidence in spray modeling.

Maybe the most physical situation of using the DQMOM-multi-fluid technique near the nozzle is in the case of very high relative velocities when aerodynamic secondary breakup has a major role in contrast to primary breakup.

The present Eulerian multi-fluid model is computationally limited for practical reasons, because impinging sprays can never be simulated properly using this approach. Droplets in the same phase originating from different nozzles that point towards each other, cannot pass each other and cross-over the central axis of the impinging spray system in an Eulerian simulation, because of the inherent flaw in the assumption that each droplet phase is represent by a continuum. The Lagrangian approach is not limited in this manner, so that droplets of similar size originating from different nozzles that point towards each other can cross-over the central axis of the impinging spray system, provided they have sufficient inertia.

11.2 Future Work

In this section, the possibilities for further improvements to the DQMOM-multi-fluid model for sprays, presented in this work, and related challenges are discussed.

It should be noted that, although the DQMOM-multi-fluid model devised in this work is designed for gas-droplet flow and in particular for sprays, it is quite general and can be applied to other classes of multiphase systems. For instance, the model can be employed in the solution of gas-particle, liquid-particle, liquid-liquid, and liquid-bubble multiphase systems.

11.2.1 Improvements to Nozzle Exit Boundary Conditions

Future work could include more accurate modeling of the flow through the Y-jet atomizers and the Danfoss pressure-swirl atomizers and thus a better estimate of the sheet thickness and exit velocity. The inclusion of transient and three-dimensional behavior could also improve the model. Additionally, the assumed aerodynamic breakup process (LISA model) is speculative and would benefit from a better understanding of primary atomization physics.

11.2.2 Improvements to the Droplet Breakup Model

One of the biggest challenges in spray modeling is the accurate prediction of droplet sizes. Special emphasis should be put on modeling the physics of the breakup, which requires assumptions about the daughter droplet distributions. If secondary breakup due to aerodynamics is of a minor role, which is the case in the low-velocity Danfoss pressure-swirl atomizer, it is enough to only have the information of the DSD from the primary breakup of the liquid sheet. In this case it is possible to neglect the secondary breakup.

The WAVE atomization and droplet breakup model used in this work predicts the droplet sizes and the breakup rate based on a linear stability analysis of liquid jets. One of the drawbacks of the WAVE model is that there are two adjustable constants that have to be calibrated to match with measurements. In the model, there is a constant, B_1, in the expression for the breakup time as given by Eq. (3.11). The computed droplet size values are sensitive to the value of B_1 as shown in Figure 9.7.

In this work a framework to include atomization and breakup in a multi-fluid spray computation is provided. Improved models if available can be included in this framework. Mechanisms for breakup, other than the Kelvin-Helmholtz mechanism that is considered in this work, are employed by other researchers. Patterson and Reitz (1998) and Beale and Reitz (1999) have used the Rayleigh-Taylor breakup mechanism in conjunction with the Kelvin-Helmholtz mechanism. The Rayleigh-Taylor accounts for droplet acceleration effects on the breakup process. Bianchi, *et al.* (2001) has developed a model for diesel spray atomization that considers nozzle exit turbulence conditions. Both these models have been employed in the context of Lagrangian calculations. It may be worthwhile extending them to DQMOM spray computations.

Besides further studies on the droplet breakup submodels of the DQMOM-multi-fluid model, the focus of future works should be on the modeling of the liquid sheet primary breakup and the very dense spray.

The values of injected droplet diameter depend on the atomizer geometry and conditions upstream of the atomizer. This will change with different atomizers. To address these issues, more fundamental studies on internal atomizer flows are required.

11.2.3 Improvements to the Droplet Collisions Model

In this work, a droplet-droplet collisions model for the multi-fluid approach has been formulated as discussed in Section 3.3. The collision rate takes into account the size of the colliding droplets and the relative velocity between the droplets. The choice of average relative velocity can be discussed. In the employed formulation, the relative velocity is assumed to be proportional to the local droplet turbulent kinetic energy. The correlation between fluctuating droplet velocities is obtained by using the droplet turbulent kinetic energy dissipation rate, a quantity that is not very well modeled. Hence, a simpler approach could be more reliable. The need to model the average relative velocity is not required in Lagrangian models and can be considered a weakness of using an Eulerian approach.

According to literature, there are four distinct collision regimes, refer to Figure 3.7. Each regime corresponds to a different outcome of collision. The coalescence probability of the employed model accounts only for the transition between the regimes of coalescence, bounce, and fragmentation based on the theory of Brazier-Smith, *et al.* (1972). Other researchers have developed other criteria for the transition between regimes (Estrade, *at al.*, 1999; Ko and Ryou, 2005*b*). Ko and Ryou (2005*a*) has also incorporated the different transition criteria in a spray computation using a Lagrangian approach.

In this work, a framework to incorporate coalescence and collision-induced breakup models in an Eulerian multi-fluid approach is provided. More work is required to extend the different collisions regimes in this framework.

11.2.4 Improvements to Turbulence Modeling

If turbulence is not a well understood physical problem in single-phase flows it is even less understood in multiphase flows. Research should focus on the mechanisms of turbulence production and dissipation due to the interaction between the phases. In the dense spray region near the orifice, there is a possibility that turbulence is generated in the liquid and transferred to the gas. When the liquid phase fraction decreases, turbulence becomes associated with the gas phase and the dispersed droplets respond to or modify the gas phase turbulence. So the application of models for turbulence poses physical and numerical challenges. To overcome the challenges, separate k-ε transport equations for each of the droplet phases are solved in this work. The models for turbulence modulation act as interfacial coupling terms between the liquid and the gas turbulence. The employed model needs further testing and validation. The simulations of the Y-jet sprays indicate that the choice of the turbulence model and turbulence injection boundary conditions has a large impact on the outcome of the simulations. In order to resolve the energetic large scale fluctuating motion, a large eddy simulation (LES) would probably be a better choice for a turbulence model, than the k-ε turbulence model.

11.2.5 Extension to Evaporating Sprays

Modeling of the physical processes that lead to the evaporation of the liquid is very important to make the DQMOM-multi-fluid model applicable to compute real combustion systems. For modeling evaporation, heat and mass transfer must be added to the CFD model proposed in this work. However, the conceptual framework of the DQMOM-multi-fluid model needs not to be changed to accommodate these additional features.

Modeling fuel combustion is a complicated problem and is a topic of active research especially from the point of view of accurate prediction of toxic pollutants. The problems become more challenging when combustion is combined with multiphase flows. Though the chemical reactions are believed to occur primarily in the gas phase, the evaporation of the liquid in fuel sprays can lead to changes in the combustion chemistry as a result of changes in temperature. In the case of reacting sprays, the gas phase would consist of the fuel vapor as well as the products of the combustion of the fuel vapor.

11.2.6 Experimental Work

In order to evaluate the performance of the DQMOM-multi-fluid model and submodels more experimental data is needed for different atomizers, geometries, and operating conditions. Especially, more precise dense spray measurements are needed.

Bibliography

Albrecht, H.-E., M. Borys, N. Damaschke and C. Tropea (2003). *Laser Doppler and Phase Doppler Measurement Techniques*. Springer, Berlin.

Alhassid, Y., N. Agmon and R.D. Levine (1978). An upper bound for the entropy and its applications to the maximal entropy problem. *Chemical Physics Letters* **53**, pp. 22-26.

Amsden, A.A., P.J. O'Rourke and T.D. Butler (1989). KIVA-II: A computer program for chemically reactive flows with sprays. Los Alamos National Laboratory, Rep. LA-11560-MS.

Aneja, R. and J. Abraham (1998). How far does the liquid penetrate in a Diesel engine: computed results vs. measurements? *Combust. Sci. and Tech.* **138**, pp. 233-255.

Archambault, M.R., C.F. Edwards and R.W. MacCormack (2003). Computation of spray dynamics by moment transport equations I: Theory and development. *Atomization and Sprays* **13**, pp. 63-87.

Babinsky, E. and P.E. Sojka (2002). Modeling drop size distributions. *Prog. Energy Combust Sci.* **28** , pp. 303-329.

Beale, J.C. and R.D. Reitz (1999). Modeling spray atomization with the Kelvin-Helmholtz/Rayleigh-Taylor hybrid model. *Atomization and Sprays* **9**, pp. 623-650.

Beau, P.-A., R. Lebas and F.-X. Demoulin (2005). The Eulerian-Lagrangian spray atomization model - contribution to the mean liquid/gas interface transport equation. *Proc. ILASS-Europe 2005*, pp. 201-206.

Beck, J.C. and A.P. Watkins (2002). On the development of spray submodels based on droplet size moments. *Journal of Computational Physics* **182**, pp. 586-621.

Beck, J.E., A.H. Lefebvre and T.R. Koblish (1991). Airblast atomization at conditions of low air velocity. *J. Propulsion* **7**, pp. 207-212.

Beheshti, N. and A.A. Burluka (2004). Eulerian modelling of atomization in turbulent flows. *Proc. ILASS-Europe 2004*, pp. 207-212.

Bertel, S.N. and T.A. Lavsen (2002). Internal Mixing of Air and Water in a Scaled Y-jet Atomiser. M.Sc. Thesis, Aalborg University Esbjerg, Denmark.

Bianchi, G.M., P. Pelloni, F.E. Corcione, L. Allocca and F. Luppino (2001). Modeling atomization of high-pressure diesel sprays. *Journal of Engineering for Gas Turbines and Power* **123**, pp. 419-427.

Bove, S., T. Solberg and B.H. Hjertager (2004). Evaluation of the parent and daughter classes technique (PPDC) for solving population balance equations by discretization: aggregation and breakage. *Proc. ASME Heat Transfer/Fluids Engineering Summer Conference HT-FED2004-56726*.

Bove, S., T. Solberg and B.H. Hjertager (2005). A novel algorithm for solving population balance equations: the parallel parent and daughter classes. Derivation, analysis and testing. *Chemical Engineering Science* **60**, pp. 1449-1464.

Brazier-Smith, P.R., S.G. Jennings and J. Latham (1972). The interaction of falling water drops: coalescence. *Proc. R. Soc. Lond. A.* **326**, pp. 393-408.

Brenn, G., D. Valkovska and K.D. Danov (2001). The formation of satellite droplets by unstable binary drop collisions. *Phys. Fluids* **13**, pp. 2463-2477.

Buelow, P.E.O., C.-P. Mao and S. Smith (2003). Two-phase CFD modeling of a simplex atomizer. *Proc. ILASS-Americas 2003*, p. No. 09A3.

Chiu, H.H. (2000). Advances and challenges in droplet and spray combustion. I. Toward a unified theory of droplet aerothermochemistry. *Prog. Energy Combust Sci.* **26**, pp. 381-416.

Cooper, D., A.J. Yule and J.J. Chinn (1999). Experimental measurements and computational predictions of the internal flow field in a pressure swirl atomizer. *Proc. ILASS-Europe '99*.

Cooper, D. and A.J. Yule (2001). Waves on the air core/liquid interface of a pressure swirl atomizer. *Proc. ILASS-Europe 2001*, pp. 625-629.

Couderc, F. and J.L. Estivalezes (2004). Numerical simulation of the air-blasted liquid sheet: development of a DNS solver based on the level-set method. *Proc. ILASS-Europe 2004*, pp. 124-129.

Crowe, C.T., T.R. Troutt and J.N. Chung (1996). Numerical models for two-phase turbulent flows. *Annu. Rev. Fluid Mech.* **28**, pp. 11-43.

Crowe, C.T., M. Sommerfeld and T. Yutaka (1998). *Multiphase Flows with Droplets and Particles*. CRC Press, Boca Raton, Fla.

Damaschke, N., H. Nobach and C. Tropea (2002). Optical limits of particle concentration for multi-dimensional particle sizing techniques in fluid mechanics. *Experiments in Fluids* **32**, pp. 143-152.

Damaschke, N., D. Kalantari, I.V. Roisman and C. Tropea (2005). Characterization of spray transport and spray/wall interactions using the IPI technique. *Proc. ILASS-Europe 2005*, pp. 379-384.

Dantec (2003*a*). *BSA Flow Software v. 2.1 Installation & User's guide*. Dantec Dynamics A/S, Skovlunde, Denmark.

Dantec (2003*b*). *FlowMap Particle Sizer Installation & User's guide*. Dantec Dynamics A/S, Skovlunde, Denmark.

Delichatsios, M.A. and R.F. Probstein (1975). Coagulation in turbulent flow: Theory and experiment. *Journal of Colloid and Interface Science* **51**, pp. 394-405.

Deux, E. and M. Sommerfeld (2004). Modelling of spray atomisation and dispersion. *Proc. ILASS-Europe 2004*, pp. 195-200.

Dombrowski, N. and R.P. Fraser (1954). A photographic investigation into the disintegration of liquid sheets. *Phil. Trans. R. Soc. Lond. A* **247**, pp. 101-130.

Dombrowski, N., D. Hasson and D.E. Ward (1960). Some aspects of liquid flow through fan spray nozzles. *Chemical Engineering Science* **12**, pp. 35-50.

Dombrowski, N. and P.C. Hooper (1962). The effect of ambient density on drop formation in sprays. *Chemical Engineering Science* **17**, pp. 291-305.

Dombrowski, N. and W.R. Johns (1963). The aerodynamic instability and disintegration of viscous liquid sheets. *Chemical Engineering Science* **18**, pp. 203-214.

Drew, D.A. (1983). Mathematical modeling of two-phase flow. *Ann. Rev. Fluid Mech.* **15**, pp. 261-291.

Drew, D.A. and S.L. Passman (1999). *Theory of Multicomponent Fluids*. Springer, New York.

Dumouchel, C. and S. Boyaval (1999). Use of the maximum entropy formalism to determine drop size distribution characteristics. *Part. Part. Syst. Charact.* **16**, pp. 177-184.

Dumouchel, C., D. Sindayihebura and L. Bolle (2003). Application of the maximum entropy formalism on sprays produced by ultrasonic atomizers. *Part. Part. Syst. Charact.* **20**, pp. 150-161.

Elghobashi, S.E. and T.W. Abou-Arab (1983). A two-equation turbulence model for two-phase flows. *Phys. Fluids* **26**, pp. 931-938.

Estrade, J.-P., H. Carentz, G. Lavergne and Y. Biscos (1999). Experimental investigation of dynamic binary collision of ethanol droplets - a model for droplet coalescence and bouncing. *Int. J. Heat and Fluid Flow* **20**, pp. 486-491.

Faeth, G.M. (1983). Evaporation and combustion of sprays. *Prog. Energy Combust Sci.* **9**, pp. 1-76.

Faeth, G.M. (1987). Mixing, transport and combustion in sprays. *Prog. Energy Combust Sci.* **13**, pp. 293-345.

Faeth, G.M., L.-P. Hsiang and P.-K. Wu (1995). Structure and breakup properties of sprays. *Int. J. Multiphase Flow* **21**, pp. 99-127.

Faeth, G.M. (1996). Spray combustion phenomena. *Proc. Twenty-Sixth Symposium (International) on Combustion/The Combustion Institute*, pp. 1593-1612.

Faeth, G.M. (2002). Dynamics of secondary drop breakup—a rate controlling process in dense sprays. *Proc. ILASS-Europe 2002*, p. Invited Lecture.

Fan, R., D.L. Marchisio and R.O. Fox (2004). Application of the direct quadrature method of moments to polydisperse gas-solid fluidized beds. *Powder Technology* **139**, pp. 7-20.

Ferziger, J.H., B. Aupoix, M. Peric, K. Hanjalic, U. Piomelli and D. Laurence (2004). *Introduction to Turbulence Modeling, VKI LS 2004-06*. von Karman Institute for Fluid Dynamics, Belgium.

Fluent (2005). *Fluent 6.2 User's Guide*. Fluent Inc., Lebanon, NH.

Fulgosi, M., D. Lakehal, S. Banerjee and V. De Angelis (2003). Direct numerical simulation of turbulence in a sheared air-water flow with a deformable interface. *J. Fluid Mech.* **482**, pp. 319-345.

Georjon, T.L. and R.D. Reitz (1999). Drop-shattering collision model for multidimensional spray computations. *Atomization and Sprays* **9**, pp. 231-254.

Gidaspow, D. (1994). *Multiphase Flow and Fluidization*. Academic Press, Boston.

Glover, A.R., S.M. Skippon and R.D. Boyle (1995). Interferometric laser imaging for droplet sizing: a method for droplet-size measurement in sparse spray system. *Applied Optics* **34**, pp. 8409-8421.

Gordon, R.G. (1968). Error bounds in equilibrium statistical mechanics. *Journal of Mathematical Physics* **9**, pp. 655-663.

Graham, D.I. and P.W. James (1996). Turbulent dispersion of particles using eddy interaction models. *Int. J. Heat Mass Transfer* **22**, pp. 157-175.

Hallmann, M., M. Scheurlen and S. Wittig (1995). Computation of turbulent evaporating sprays: Eulerian versus Lagrangian approach. *Journal of Engineering for Gas Turbines and Power* **117**, pp. 112-119.

Han, Z., S. Parrish, P.V. Farrell and R.D. Reitz (1997). Modeling atomization processes of pressure-swirl hollow-cone fuel sprays. *Atomization and Sprays* **7**, pp. 663-684.

Hansen, K.G. and J. Madsen (2001). A Computational and Experimental Study of the Internal Flow in a Scaled Pressure-Swirl Atomizer. M.Sc. Thesis, Aalborg University Esbjerg, Denmark.

Hansen, K.G., J. Madsen, C.M. Trinh, C.H. Ibsen, T. Solberg and B.H. Hjertager (2002). A computational and experimental study of the internal flow in a scaled pressure-swirl atomizer. *Proc. ILASS-Europe 2002*, pp. 351-356.

Hesselbacher, K.H., K. Anders and A. Frohn (1991). Experimental investigation of Gaussian beam effects on the accuracy of a droplet sizing method. *Applied Optics* **30**, pp. 4930-4935.

Hinze, J.O. (1975). *Turbulence*. McGraw-Hill, New York.

Ibrahim, E.A., H.Q. Yang and A.J. Przekwas (1993). Modeling of spray droplets deformation and breakup. *J. Propulsion* **9**, pp. 651-654.

Iyer, V. and J. Abraham (2003). An evaluation of a two-fluid Eulerian-liquid Eulerian-gas model for diesel sprays. *Journal of Fluids Engineering* **125**, pp. 660-669.

Iyer, V. and J. Abraham (2005). Two-fluid modeling of spray penetration and dispersion under diesel engine conditions. *Atomization and Sprays* **15**, pp. 249-269.

Jedelsky, J., M. Jicha and J. Slama (2003). Characterization of spray generated by multihole effervescent atomizer and comparison with standard Y-jet atomizer. *Proc. ICLASS 2003*, p. No. 0311.

Jeng, S.M., M.A. Jog and M.A. Benjamin (1998). Computational and experimental study of liquid sheet emanating from simplex fuel nozzle. *AIAA Journal* **36**, pp. 201-207.

Kataoka, I. and A. Serizawa (1989). Basic equations of turbulence in gas-liquid two-phase flow. *Int. J. Multiphase Flow* **15**, pp. 843-855.

Klein, M. (2005). Direct numerical simulation of a spatially developing water sheet at moderate Reynolds number. *Int. J. Heat and Fluid Flow* **26**, pp. 722-731.

Ko, G.H. and H.S. Ryou (2005*a*). Droplet collision processes in an inter-spray impingement system. *Aerosol Science* **36**, pp. 1300-1321.

Ko, G.H. and H.S. Ryou (2005*b*). Modeling of droplet collision-induced breakup process. *Int. J. Multiphase Flow* **31**, pp. 723-738.

König, G., K. Anders and A. Frohn (1986). A new light-scattering technique to measure the diameter of periodically generated moving droplets. *J. Aerosol Sci.* **17**, pp. 157-167.

Lasheras, J.C., E. Villermaux and E.J. Hopfinger (1998). Break-up and atomization of a round water jet by a high-speed annular air jet. *J. Fluid Mech.* **357**, pp. 351-379.

Launder, B.E. and D.B. Spalding (1974). The numerical computation of turbulent flows. *Computer Methods in Applied Mechanics and Engineering* **3**, pp. 269-289.

Lavergne, G., P. Trichet, P. Hebrard and Y. Biscos (1993). Liquid sheet disintegration and atomization process on a simplified airblast atomizer. *Journal of Engineering for Gas Turbines and Power* **115**, pp. 461-466.

Lee, C.S., H.J. Kim and S.W. Park (2004). Atomization characteristics and prediction accuracies of hybrid break-up models for a gasoline direct injection spray. *Proc. Instn Mech. Engrs Part D: J. Automobile Engineering* **218**, pp. 1041-1053.

Lefebvre, A.H. (1989). *Atomization and Sprays*. Hemisphere, New York.

Li, X. and R.S. Tankin (1987). Droplet size distribution: A derivation of the Nukiyama-Tanasawa type distribution function. *Combust. Sci. and Tech.* **56**, pp. 65-76.

Li, X., L.P. Chin, R.S. Tankin, T. Jackson, J. Stutrud and G. Switzer (1991). Comparison between experiments and predictions based on maximum entropy for sprays from a pressure atomizer. *Combustion and Flame* **86**, pp. 73-89.

Li, X. and R.S. Tankin (1991). On the temporal instability of a two-dimensional viscous liquid sheet. *J. Fluid Mech.* **226**, pp. 425-443.

Li, X. and J. Shen (1999). Experimental study of sprays from annular liquid jet breakup. *J. Propulsion* **15**, pp. 103-110.

Lilly, D.K. (1967). The representation of small-scale turbulence in numerical simulation experiments. *Proc. IBM Scientific Computing Symposium on Environmental Sciences*, pp. 195-210.

Lopez de Bertodano, M.A. (1998). Two fluid model for two-phase turbulent jets. *Nuclear Engineering and Design* **179**, pp. 65-74.

Lozano, A. and F. Barreras (2001). Experimental study of the gas flow in an air-blasted liquid sheet. *Experiments in Fluids* **4**, pp. 367-376.

Lozano, A., F. Barreras, G. Hauke and C. Dopazo (2001). Longitudinal instabilities in an air-blasted liquid sheet. *J. Fluid Mech.* **437**, pp. 143-173.

Ma, Z., D. Wang, S.-M. Jeng and M.A. Benjamin (2000). On the internal flow of pressure-swirl atomizer at two different density ratios. *Proc. ICLASS 2000*, pp. 1206-1213.

Madsen, J., J. Harbo, T.I. Nonn, D. Blondel, B.H. Hjertager and T. Solberg (2003). Measurement of droplet size and velocity distributions in sprays using Interferometric Particle Imaging (IPI) and Particle Tracking Velocimetry (PTV). *Proc. ICLASS 2003*, p. No. 0906.

Madsen, J., B.H. Hjertager and T. Solberg (2004). Numerical simulation of internal flow in a large-scale pressure-swirl atomizer. *Proc. ILASS-Europe 2004*, pp. 183-188.

Madsen, J., T. Solberg and B.H. Hjertager (2005). Numerical simulation of sprays by the direct quadrature method of moments. *Proc. ILASS-Europe 2005*, pp. 179-184.

Madsen, J., B.H. Hjertager, T. Solberg, P. Nørskov and J. Ruså s (2006). Application of the direct quadrature method of moments to Y-jet water sprays. *Proc. ICLASS 2006*, p. ID 103.

Maeda, M., T. Kawaguchi and K. Hishida (2000). Novel interferometric measurement of size and velocity distributions of spherical particles in fluid flows. *Meas. Sci. Technol.* **11**, p. L13-L18.

Mansour, A. and N. Chigier (1990). Disintegration of liquid sheets. *Phys. Fluids A* **2**, pp. 706-719.

Mansour, A. and N. Chigier (1991). Dynamic behavior of liquid sheets. *Phys. Fluids A* **3**, pp. 2971-2980.

Marchisio, D.L., R.D. Vigil and R.O. Fox (2003*a*). Implementation of the quadrature method of moments in CFD codes for aggregation-breakage problems. *Chemical Engineering Science* **58**, pp. 3337-3351.

Marchisio, D.L., R.D. Vigil and R.O. Fox (2003*b*). Quadrature method of moments for aggregation-breakage processes. *Journal of Colloid and Interface Science* **258**, pp. 322-334.

Marchisio, D.L. and R.O. Fox (2005). Solution of population balance equations using the direct quadrature method of moments. *J. Aerosol Sci.* **36**, pp. 43-73.

Mathieu, J. and J. Scott (2000). *An Introduction to Turbulent Flow*. Cambridge University Press, Cambridge.

McGraw, R. (1997). Description of aerosol dynamics by the quadrature method of moments. *Aerosol Science and Technology* **27**, pp. 255-265.

Milojevic, D. (1990). Lagrangian stochastic-deterministic (LSD) predictions of particle dispersion in turbulence. *Part. Part. Syst. Charact.* **7**, pp. 181-190.

Mostafa, A.A. and S.E. Elghobashi (1985). A two-equation turbulence model for jet flows laden with vaporizing droplets. *Int. J. Multiphase Flow* **11**, pp. 515-533.

Mostafa, A.A. and H.C. Mongia (1987). On the modeling of turbulent evaporating sprays: Eulerian versus Lagrangian approach. *Int. J. Heat Mass Transfer* **30**, pp. 2583-2593.

Mullinger, P.J. and N.A. Chigier (1974). The design and performance of internal mixing multijet twin fluid atomizers. *Journal of the Institute of Fuel* **47**, pp. 251-261.

Nagaoka, M. and K. Kawamura (2001). A deforming droplet model for fuel spray in direct-injection gasoline engines. *SAE Paper* **2001-01-1225**.

Nasr, G.G., A.J. Yule and L. Bendig (2002). *Industrial Sprays and Atomization*. Springer, London.

Nordin, P.A.N. (2001). Complex Chemistry Modeling of Diesel Spray Combustion. Ph.D. Thesis, Chalmers University of Technology, Sweden.

O'Rourke, P.J. and A.A. Amsden (1987). The TAB method for numerical calculation of spray droplet breakup. *SAE Paper* **872089**.

Orme, M. (1997). Experiments on droplet collisions, bounce, coalescence and disruption. *Prog. Energy Combust Sci.* **23**, pp. 65-79.

Patterson, M.A. and R.D. Reitz (1998). Modeling the effects of fuel spray characteristics on diesel engine combustion and emission. *SAE Paper* **980131**.

Peirano, E. and B. Leckner (1998). Fundamentals of turbulent gas-solid flows applied to circulating fluidized bed combustion. *Prog. Energy Combust Sci.* **24**, pp. 259-296.

Picart, A., A. Berlemont and G. Gouesbet (1986). Modelling and predicting turbulence fields and the dispersion of discrete particles transported by turbulent flows. *Int. J. Multiphase Flow* **12**, pp. 237-261.

Pilch, M. and C.A. Erdman (1987). Use of breakup time data and velocity history data to predict the maximum size of stable fragments for acceleration-induced breakup of a liquid drop. *Int. J. Multiphase Flow* **13**, pp. 741-757.

Post, S.L. and J. Abraham (2002). Modeling the outcome of drop-drop collisions in Diesel sprays. *Int. J. Multiphase Flow* **28**, pp. 997-1019.

Qian, J. and C.K. Law (1997). Regimes of coalescence and separation in droplet collision. *J. Fluid Mech.* **331**, pp. 59-80.

Ramkrishna, D. (2000). *Population Balances*. Academic Press, San Diego, CA.

Reitz, R.D. and F.V. Bracco (1982). Mechanism of atomization of a liquid jet. *Phys. Fluids* **25**, pp. 1730-1742.

Reitz, R.D. (1987). Modeling atomization processes in high-pressure vaporizing sprays. *Atomisation and Spray Technology* **3**, pp. 309-337.

Reitz, R.D. and R. Diwakar (1987). Structure of high-pressure fuel sprays. *SAE Paper* **870598**.

Rotondi, R. and G. Bella (2006). Gasoline direct injection spray simulation. *International Journal of Thermal Sciences* **45**, pp. 168-179.

Rüger, M., S. Hohmann, M. Sommerfeld and G. Kohnen (2000). Euler/Lagrange calculations of turbulent sprays: The effect of droplet collisions and coalescence. *Atomization and Sprays* **10**, pp. 47-81.

Sakman, A.T., M.A. Jog, S.M. Jeng and M.A. Benjamin (2000). Parametric study of simplex fuel nozzle internal flow and performance. *AIAA Journal* **38**, pp. 1214-1218.

Schiller, L. and A. Naumann (1933). Über die grundlegenden Berechnungen bei der Schwerkraftaufbereitung. *Zeitschrift des Vereines deutscher Ingenieure* **77**, pp. 318-320.

Schmehl, R., G. Maier and S. Wittig (2000). CFD analysis of fuel atomization, secondary droplet breakup and spray dispersion in the premix duct of a LPP combustor. *Proc. ICLASS 2000*, pp. 918-925.

Schmidt, D.P., I. Nouar, P.K. Senecal, J. Hoffman, C.J. Rutland, J. Martin and R.D. Reitz (1999). Pressure-swirl atomization in the near field. *SAE Paper* **1999-01-0496**.

Schmidt, D.P. and C.J. Rutland (2000). A new droplet collision algorithm. *Journal of Computational Physics* **164**, pp. 62-80.

Scholz, J., K. Roetmann and V. Beushausen (2003). Influence of the internal flow conditions of slit nozzles on the stability of liquid sheets: Experimental results. *Proc. ICLASS 2003*, p. No. 0303.

Semião, V., P. Andrade and M. da Craça Carvalho (1966). Spray characterization: Numerical prediction of Sauter mean diameter and droplet size distribution. *Fuel* **75**, pp. 1707-1714.

Senecal, P.K., D.P. Schmidt, I. Nouar, C.J. Rutland, R.D. Reitz and M.L. Corradini (1999). Modeling high-speed viscous liquid sheet atomization. *Int. J. Multiphase Flow* **25**, pp. 1073-1097.

Simonin, O. and P.L. Viollet (1990). Prediction of an oxygen droplet pulverization in a compressible subsonic coflowing hydrogen flow. *Proc. Numerical Methods for Multiphase Flows ASME FED91*, pp. 73-82.

Sirignano, W.A. (1983). Fuel droplet vaporization and spray combustion theory. *Prog. Energy Combust Sci.* **9**, pp. 291-322.

Sirignano, W.A. and C. Mehring (2000). Review of theory of distortion and disintegration of liquid streams. *Prog. Energy Combust Sci.* **26**, pp. 609-655.

Smagorinsky, J. (1963). General circulation experiments with the primitive equations. I. The basic experiment. *Monthly Weather Review* **91**, pp. 99-165.

Sommerfeld, M. (1998). Analysis of isothermal and evaporating turbulent sprays by phase-Doppler anemometry and numerical calculations. *Int. J. Heat and Fluid Flow* **19**, pp. 173-186.

Spiegel, M.R. and J. Liu (1999). *Schaum's mathematical handbook of formulas and tables*. McGraw-Hill, New York.

Squire, H.B. (1953). Investigation of the instability of a moving liquid film. *British Journal of Applied Physics* **4**, pp. 167-169.

Stapper, B.E., W.A. Sowa and G.S. Samuelsen (1992). An experimental study of the effects of liquid properties on the breakup of a two-dimensional liquid sheet. *Journal of Engineering for Gas Turbines and Power* **114**, pp. 39-45.

Steinthorsson, E. and D.M. Lee (2000). Numerical simulations of internal flow in a simplex atomizer. *Proc. ICLASS 2000*, pp. 324-331.

Tolpadi, A.K., D.L. Burrus and R.J. Lawson (1995). Numerical computation and validation of two-phase flow downstream of a gas turbine combustor dome swirl cup. *Journal of Engineering for Gas Turbines and Power* **117**, pp. 704-712.

Tryggvason, G., B. Bunner, A. Esmaeeli, D. Juric, N. Al-Rawahi, W. Tauber, J. Han, S. Nas and Y.-J. Jan (2001). A front-tracking method for the computations of multiphase flow. *Journal of Computational Physics* **169**, pp. 708-759.

Vallet, A., A.A. Burluka and R. Borghi (2001). Development of a Eulerian model for the "atomization" of a liquid jet. *Atomization and Sprays* **11**, pp. 619-642.

van der Geld, C.W.M. and H. Vermeer (1994). Prediction of drop size distributions in sprays using the maximum entropy formalism: the effect of satellite formation. *Int. J. Multiphase Flow* **20**, pp. 363-381.

von Berg, E., W. Edelbauer, A. Alajbegovic, R. Tatschl, M. Volmajer, B. Kegl and L.C. Ganippa (2005). Coupled simulations of nozzle flow, primary fuel jet breakup, and spray formation. *Journal of Engineering for Gas Turbines and Power* **127**, pp. 897-908.

von Lavante, E., U. Maatje and F.-O. Albina (2002). Investigation of unsteady effects in pressure swirl atomizers. *Proc. ILASS-Europe 2002*.

Wigley, G., M. Goodwin, G. Pitcher and D. Blondel (2004). Imaging and PDA analysis of a GDI spray in the near-nozzle region. *Experiments in Fluids* **36**, pp. 565-574.

Williams, F.A. (1985). *Combustion Theory*. Addison-Wesley, Redwood, CA.

Wu, K.-J., D.A. Santavicca, F.V. Bracco and A. Coghe (1984). LDV measurements of drop velocity in diesel-type sprays. *AIAA Journal* **22**, pp. 1263-1270.

Wu, K.-J., R.D. Reitz and F.V. Bracco (1986). Measurements of drop size at the spray edge near the nozzle in atomizing liquid jets. *Phys. Fluids* **29**, pp. 941-951.

Xu, M. and L.E. Markle (1998). CFD-aided development of spray for an outwardly opening direct injection gasoline injector. *SAE Paper* **980493**.

Yang, B. and S.B. Pope (1998). An investigation of the accuracy of manifold methods and splitting schemes in the computational implementation of combustion chemistry. *Combustion and Flame* **112**, pp. 16-32.

Yue, B. and A.P. Watkins (2004). Mathematical development and numerical analysis of further transport equations for the droplet size moment theory. *Proc. ILASS-Europe 2004*, pp. 130-135.

Yule, A.J. and J.J. Chinn (2000). The internal flow and exit conditions of pressure swirl atomizers. *Atomization and Sprays* **10**, pp. 121-146.

Zaleski, S., J. Li, R. Scardovelli and G. Zanetti (1997). Direct simulation of multiphase flows with density variations. *Proc. IUTAM Symposium on Variable Density Low-Speed Turbulent Flows*, pp. 51-58.